Multiband Superconductivity in the Heavy Fermion compounds PrOs4Sb12 and CeCoIn5

Gabriel Seyfarth

THÈSE

présentée par

Gabriel F.D. SEYFARTH

pour obtenir le titre de

DOCTEUR DE L'UNIVERSITÉ JOSEPH FOURIER - GRENOBLE 1

Spécialité : Physique

Supraconductivité Multibande dans les composés à Fermions Lourds $PrOs_4Sb_{12}$ et $CeCoIn_5$

Date de soutenance : 21 décembre 2006

Composition du Jury :

Claude BERTHIER, LCMI Grenoble (Président)

Jean-Pascal BRISON, SPSMS-CEA Grenoble (Directeur de thèse)

Prof. Michael HUTH, Universität Frankfurt am Main

Didier JACCARD, Université de Genève (Rapporteur)

Dimitri RODITCHEV, INSP Paris (Rapporteur)

Thèse préparée au
Centre de Recherches sur les Très Basses Températures – CNRS
Laboratoire associé à l'Université Joseph Fourier et
à l'Institut National Polytechnique de Grenoble
Polygone Scientifique Grenoble – France

THESIS

submitted by

Gabriel F.D. SEYFARTH

in conformity with the requirements
for the Doctor's degree of the

Graduate Department of Physics

UNIVERSITÉ JOSEPH FOURIER - GRENOBLE 1

Multiband Superconductivity in the Heavy Fermion compounds $PrOs_4Sb_{12}$ and $CeCoIn_5$

Defense date: December 21, 2006

Committee :

Claude BERTHIER, GHFML Grenoble (President)

Jean-Pascal BRISON, SPSMS-CEA Grenoble (Supervisor)

Prof. Michael HUTH, Universität Frankfurt am Main

Didier JACCARD, Université de Genève (Referee)

Dimitri RODITCHEV, INSP Paris (Referee)

Thesis prepared at
Research Center for Very Low Temperatures – CRTBT/CNRS
Université Joseph Fourier and Institut National Polytechnique de Grenoble
Polygone Scientifique Grenoble – France

to my parents

Truth is what stands the test of experience.

Albert Einstein

Acknowledgements / Merci ! / Danke !

First of all, I am very indebted towards Didier Jaccard and Dimitri Roditchev for having accepted to referee this thesis, and towards Claude Berthier and Prof. Michael Huth for joining the defense committee.

More particularly, I hereby express my gratitude to my supervisor, Jean-Pascal Brison, who introduced me (with enthusiasm and patience) to the wide field of heavy fermion superconductivity and the techniques at very low temperatures. During all my time at CRTBT lab, I have benefited from both his professional and human qualities: his deep, physical understanding, his experience, his accuracy, his efficiency, his discipline and his sincerity. Furthermore, I particularly appreciated his confidence, his versatility, his availability and his continuous interest in all our experimental (more or less important) difficulties, so that he never got disconnected from the work I did on the setup or the fridge. Even more, it is really a great chance, pleasure and also a challenge to work with someone whose thoughts are regularly one step ahead, so that sometimes Jean-Pascal already suggested a solution for a (experimental) problem while I even had not fully realized the scope of the difficulties! I still admire this capability of quick and 100% correct apprehension, and also still wonder how he managed all his duties at the lab so successfully, even so the situation at home was not always easy for him. Finally, I want to thank him for sending me to ICM 2006 in Kyoto: it was a particularly rich (on all levels) expansion of my horizons.

Bien sûr, afin de mener à bien un projet de mesures thermiques près du zéro absolu, il faut également le savoir-faire, l'infrastructure et le soutien de tout un laboratoire spécialisé dans les basses températures. Je tiens donc à remercier de tout coeur l'ensemble du personnel du CRTBT pour son soutien constant. Plus particulièrement, j'adresse mes remerciements à Henri Rodenas (la "force d'intervention" du bâtiment M, toujours prêt à donner un coup de main si nécessaire), Pierre Chanthib (vivent ses nems!) et tout le service cryogénie-mécanique, à toute l'équipe du liquéfacteur (si vitale pour l'approvisionnement en hélium de ma dilution), à Jean-Louis Bret avec tout le service électronique pour leur aide rapide et efficace en cas de besoin. S'y ajoute Thierry Crozes (NanoFab) à qui je dois les dépôts d'or sur les échantillons. A ne pas oublier les chercheurs du laboratoire, notamment Philippe Gandit (merci pour le service dépannage trmc2, même tard le soir!) ainsi que Christine Opagiste, Gerard Vermeulen, Pierre-Etienne Wolf, Christopher Bauerle, Jacques Bossy, Jean-Claude Lasjaunias et Jean-Jacques Préjean: merci pour toutes sortes de conseils (cryogéniques surtout) et des discussions plus ou moins scientifiques.

Evidemmment, l'unique ambiance dans le hall du bâtiment M (et au labo) ne pourrait s'expliquer sans la présence des chers collègues stagiaires et thésards, d'abord Séverine, Elsa, Félicien, Sorin, Voicu, et puis Pascale, Valerie, Johannes, Jerry, Julien, Patrick, Thomas et surtout Francois sur la manip d'en face: merci beaucoup pour vos conseils, vos aides et coups de main, vos blagues, les repas communs et vos mots de soutien! C'est important de ne pas se sentir seul, surtout dans les moments difficiles quand la manip ne fait pas ce que l'on veut!

Merci également aux "bonnes âmes" du laboratoire, Danièle, Nathalie, Laurence, Patricia et

Martine pour l'accompagnement dans toutes les démarches administratives et les missions.

La physique des fermions lourds étant très complexe, il faut s'en approcher à plusieurs, en équipes plus précisément, afin de progresser. Au CRTBT, j'aimerais donc remercier les collègues qui nous ont accompagnés dans cette perspective: Pierre Haen, Klaus Hasselbach et particulièrement Pierre Rodière. Merci pour toutes les explications, conseils et discussions, et mille mercis à Pierre R. pour son dynamisme, sa disponibilité, sa bonne humeur et sa curiosité, qui aident toujours à avancer. Merci également à Albin DeMuer du LCMI pour ses conseils et son aide précieuse dans la mise en forme des échantillons. De l'autre côté de la "grille", au SPSMS-CEA, il y a un autre pôle fermions lourds de Grenoble, et je remercie chaleureusement Marie-Aude Méasson (la pro des micro-soudures et des échantillons minuscules), Daniel Braithwaite, Georg Knebel, Koichi Izawa, Florence Lévy, Julien Derr et Jacques Flouquet de leur collaboration fructueuse. Mais toutes nos recherches ne seraient pas possibles sans des échantillons de très bonne qualité, qui nous ont été fournis par le groupe de Gérard Lapertot et Dai Aoki, également au SPSMS-CEA, et par le groupe de Hitoshi Sugawara au Japon: un très grand merci à eux!

Even if not always easy to reconcile, life outside the lab did exist, especially in the beautiful surrounding mountains, both in winter and summer, and through unforgettable "soirées". A great "thank you!" to Aurore, Blandine, Caroline, Diane, Eva, Florence, Marion, Martina, Virginie, Alain, Christian, François, Gael, Gatien, Jan, JB, Jérôme, Max, Sébastien, Thomas and to all other friends for sharing their time with me in Grenoble. Il y avait également un peu de travail en dehors du labo: quelques vacations à mon ancienne école, l'ENSPG. Merci également à mes étudiants qui parfois m'ont fait repenser quelques fondamentaux de la physique, ce qui est important afin de ne pas rester fixé seulement sur le sujet de thèse tellement pointu.

Last, but not least, a big "Danke! / Merci!" goes to my parents in Munich (good old Bavaria) for supporting me in all my plans and projects during the whole period of my physics studies, first in Ilmenau, then in Karlsruhe (thanks to Prof. Engelhardt!) and now in Grenoble.

Contents

1. French summary

1.1. Introduction

$PrOs_4Sb_{12}$ et $CeCoIn_5$ font partie des composés à fortes corrélations électroniques (composés dits à fermions lourds). Dans cette thèse, on s'intéresse plus particulièrement à leur phase supraconductrice, étudiée par des mesures de transport thermique à basse température et sous champ magnétique, afin d'en analyser la symétrie du paramètre d'ordre.

En effet, dans $PrOs_4Sb_{12}$, des mesures de la dépendance angulaire de la conduction thermique dans un champ magnétique tournant prédisent des noeuds dans le gap supraconducteur, et l'apparition d'une double transition dans la chaleur spécifique (similaire à celle mesurée dans UPt_3) indique également la possibilité d'une supraconductivité non-conventionnelle. Cependant, nos mesures ne confirment pas ce scénario, au profit d'un gap complètement ouvert sur toute la surface de Fermi. En revanche, elles mettent en évidence le caractère multibande de la supraconductivité. Ce phénomène est bien connu du composé MgB_2, et attribué à un couplage électron-phonon qui varie selon les différentes bandes électroniques. Dans $PrOs_4Sb_{12}$, le mécanisme microscopique de la formation des paires de Cooper n'a pas encore été identifié, et l'effet multibande est probablement lié au fait que toutes les bandes n'ont pas un caractère f : cela explique notamment la présence simultanée de quasiparticules de masse effective légère et lourde, mais aussi peut-être une différence de force du mécanisme d'appariement sur chacune de ces bandes.

Dans $CeCoIn_5$, une grande diversité dans la masse effective des quasiparticules est constatée par des mesures d'effet de Haas–van Alphen. Par ailleurs, de nombreuses experiences indiquent la présence de noeuds dans le gap supraconducteur. Nos premières mesures de transport thermique à très basse température et à (faible) champ magnétique révèlent l'existence d'une échelle de champ caractéristique beaucoup plus petite que H_{c2}, ce qui s'interprète dans le cadre d'une supraconductivité multibande, similaire à MgB_2 et $PrOs_4Sb_{12}$.

1.2. Techniques experimentales

Le montage de conduction thermique utilisé correspond aux modèles standards avec un chauffage et deux thermomètres, et il permet la mesure de la resistivité électrique de l'échantillon avec le même facteur géométrique. De grands efforts expérimentaux ont été engagés afin d'adapter le montage aux très basses températures. En particulier, nous avons ajouté un dispositif qui permet le contrôle *quantitatif* des resistances de contact électriques *et* thermiques sur le montage, ce qui nous a permis d'optimiser notre procédure d'élaboration des contacts (micro-soudure à arc $\rightarrow$ bandes d'or évaporées + laque Ag). La fiablilité de l'ensemble a été vérifiée à travers la validité de la loi de Wiedemann–Franz dans la limite $T \rightarrow 0$ en phase normale (sous champ magnétique).

1.3. $PrOs_4Sb_{12}$

Après un premier cycle de mesures sur un échantillon en forme de barette et moins homogène (nommé A, cf. fig. 4.5b), nous avons effectué des mesures sur un échantillon de haute qualité, nommé B2. Il s'agit d'une petite plaquette obtenue à partir d'un monocristal de $PrOs_4Sb_{12}$ en forme de petit cube. Contrairement aux mesures sur ce dernier, la chaleur spécifique $C_p(T)$ de la plaquette ne présente pas de double transition, mais un saut unique à la température de transition inférieure (cf. fig. 4.4), ce qui montre que la double transition trouvée auparavant (sur le petit cube) est probablement liée à des problèmes d'inhomogénéité. En revanche, l'apparition simultanée de la transition supraconductrice en résitivité électrique, conduction thermique et chaleur spécifique témoigne de la bonne homogénéité de la plaquette B2 (cf. fig. 4.5a).

La figure 4.10 montre toutes les rampes en température de la conduction thermique κ/T. On remarque d'abord une rupture de pente très nette à T_c (cf. également fig. 4.17), même à champ nul. En baissant la température, $\kappa/T(T)$ présente un maximum local vers 1 K (qui disparaît rapidement avec le champ), puis chute finalement vers les plus basses températures pour atteindre un régime $\kappa \propto T^3$ en dessous de 100 mK (à champ nul, fig. 4.12). A ces températures, un très faible champ magnétique $\sim 0.04H_{c2}$ suffit pour rétablir environ 40% de la conduction thermique en phase normale (cf. fig. 4.15) et un régime métallique ($\kappa/T(T) = \text{const}$). Cette forte augmentation de $\kappa/T(H, T \to 0)$ sur une petite échelle de champ ne correspond pas à ce qui est attendu pour un supraconducteur "classique" de type II (en limite propre) ou un supraconducteur non-conventionnel comme UPt_3. Ce comportement resemble plutôt à ce qui a été mesuré dans le supraconducteur MgB_2 (cf. fig. 4.16). Dans ce composé, l'existence d'une échelle de champ beaucoup plus faible que H_{c2} est expliquée par la présence d'une bande électronique associée à un petit (par rapport à $1.764 \cdot k_B T_c$) gap, entrainant un champ caractéristique (ou de cross-over) $H_{c2}^S \ll H_{c2}$, à partir duquel les vortex se recouvrent pour rétablir la phase normale liée à cette bande. A ce jour, seul un scenario similaire permet d'expliquer la petite échelle de champ observé dans $PrOs_4Sb_{12}$. Les différentes masses éffectives (densités d'états) pourraient être responsables d'un couplage différent dans chaque bande (la bande aux faibles masses effectives serait par exemple associée au petit gap). Cependant, comme le champ caractéristique H_{c2}^S dépend à la fois de l'amplitude du gap et de la vitesse de Fermi, des mesures supplémentaires sont nécessaires afin de déterminer l'échelle d'énergie (le gap) correspondante.

Afin d'obtenir ces informations, et d'accéder à la topologie du gap supraconducteur, il faut analyser de près la dépendence en température de κ à champ nul. A très basse température, le régime $\kappa \propto T^3$ peut être attribué de façon consistente à la contribution des phonons, κ^{ph}, donnant un libre parcours moyen l_0^{ph} qui correspond environ à la plus petite dimension de l'échantillon (cf. fig. 4.22). Un raccord avec les données à haute température de κ^{ph} (estimées à partir des mesures de résitivité électrique avec la loi de Wiedemann–Franz) est possible en supposant une augmentation du libre parcours moyen des phonons pour $T < T_c$ à cause de la "condensation" des électrons qui les diffusaient (cf. équation (4.9) et fig. 4.23). Ainsi, on obtient une estimation de la contribution électronique au transport thermique, κ^{el}, fiable pour les plus basses temperatures: $\kappa^{el}(T)$ chute exponentiellement, reflétant ainsi l'ouverture d'un gap sur l'ensemble de la surface de Fermi. En outre, une analyse simple dans le cadre de la théorie BCS montre que $\kappa^{el}(T)$ ne peut pas être décrit avec un gap correspondant à $T_c \sim 1.75$ K ($\kappa^{el}(T)$ augmente à des températures plus faibles qu'attendu). Par contre, en supposant deux canaux de conduction parallèles, selon $\kappa^{el}/T = n_s \cdot \kappa^{el}_{\Delta_s}/T + (1 - n_s) \cdot \kappa^{el}_{\Delta_l}/T$ avec un rapport de gaps $\Delta_\mathrm{l}/\Delta_\mathrm{s}(T \to 0) \sim 3$ et un poids du petit gap $n_s \sim 0.35$ (comparable avec le niveau du "plateau" de $\kappa/T(H, T \to 0)$), il est possible de reproduire les données expérimentales (cf. fig.

4.25).

En résumé, nos mesures de la conduction thermique révèlent le caractère multibande de la supraconductivité dans $PrOs_4Sb_{12}$ à travers la manifestation expérimentale d'une petite échelle de champ et d'énergie. Quant à la topologie du gap supraconducteur, nos mesures indiquent clairement l'existence d'un gap ouvert sur toute la surface de Fermi, résultat qui correspond à l'observation d'une forte augmentation de la résistance des contacts thermiques (entre l'échantillon et les thermomètres) à très basse température (qui disparaît sous un faible champ, cf. figures 4.27 et 4.28).

1.4. $CeCoIn_5$

L'étude de la conduction thermique à très basse température et à faible champ magnétique de $CeCoIn_5$ est motivée par la possibilité d'effets multibandes, similaires à ceux observés sur $PrOs_4Sb_{12}$, évoquée dans la littérature et justifiée par sa structure électronique (distribution large des valeurs des masses effectives). Il s'agit de mesures "préliminaires" qui ne portent que sur la configuration $\vec{H} \parallel \vec{c} \perp \vec{j}$. Cependant, les résultats révèlent des propriétés remarquables:

- A champ nul, la conduction thermique augmente fortement en dessous de T_c, et à basse température, $\kappa/T(10\,\mathrm{mK}) \sim 2\kappa/T(T_c)$ (cf. fig. 5.7), ce qui est probablement dû à la suppression de collisions inélastiques dans la phase supraconductrice, similaire aux observations dans les cuprates à haute température critique.

- Aux plus basses températures, on constate une grande divergence entre les différentes mesures de la conduction thermique déjà publiées (cf. fig. 5.11), et une extrapolation fiable pour $T \to 0$ semble difficile à partir de la gamme de température accessible expérimentalement. Il est donc impossible d'extraire des informations sur la topologie du gap. Cependant, nous pouvons donner une limite supérieure pour $\kappa/T(T \to 0) \approx 2000\ \mu\mathrm{WK}^{-2}\mathrm{cm}^{-1}$ et ainsi exclure la présence d'électrons non-appariés comme proposé par d'autres auteurs.

- Le plus étonnant: un champ de seulement 8 mT ($\sim 0.002 H_{c2}$) est suffisant pour rétablir un régime $\kappa/T(T) = \mathrm{const}$ avec $\kappa/T(T \to 0) \sim 0.4\kappa/T(T \to 0, B = 6\ \mathrm{T})$ (cf. figures 5.7 et 5.12a). Cette forte augmentation ne peut pas seulement être expliquée par une densité d'états modifiée par le shift Doppler (dans le cas de présence de noeuds dans le gap) à cause de la petite échelle de champ sur laquelle elle se produit. Comme dans MgB_2 ou $PrOs_4Sb_{12}$, ce résultat est la signature d'une supraconductivité multibande dans $CeCoIn_5$, avec une échelle de champ caractéristique de l'ordre de H_{c1} seulement.

1.5. Conclusion

Notre étude sur le transport thermique dans la phase supraconductrice de $PrOs_4Sb_{12}$ et $CeCoIn_5$ montre que la supraconductivité multibande pourrait être plus répandue parmi les composés à fortes corrélations électroniques qu'initialement prévu. Cependant, par rapport au cas bien étudié et compris de MgB_2 (un composé *non* fermion lourd), l'origine microscopique de l'aspect multibande de la supraconductivité reste encore indéterminée (ainsi que le mécanisme d'appariement), et nécessite plus de recherches tant sur le plan expérimental que théorique, notamment en ce qui concerne l'influence des bandes à fort et à faible caractère f.

2. Introduction and Background

The research on heavy fermion (HF) systems constitutes the physical framework of this thesis. Hence we will start with some general remarks on these systems and their superconductivity, before introducing two of their representatives, $PrOs_4Sb_{12}$ and $CeCoIn_5$, the compounds under investigation. In particular, the main properties of their superconducting states will be reviewed. Finally, we include a short description of the concept of multiband superconductivity (MBSC) in order to allow a more straightforward argumentation in the following chapters, and a statement on the purpose of this work.

2.1. Heavy Fermion materials

2.1.1. Heavy Fermion materials – normal state properties

Even if this thesis is focussed on the examination of the *superconducting* state of heavy fermions, the natural starting point should be the normal ground state of these systems, from which the superconducting state emerges. Of course, there exist several review articles on both experimental and theoretical aspects in the rich and complex field of heavy fermion behavior [21, 43, 56, 71, 109, 110, 188, 208]. This section only intended to remind some basic ideas on the formation of the heavy fermion ground state, for the simplest case of f^1-based (Ce-based) systems. Some aspects on heavy fermion superconductivity will be addressed in the next section.

Typically, strongly correlated or "heavy fermion" systems involve intermetallic compounds, containing f electrons of actinide (like U) or rare earth elements (such as Ce, Pr, Yb, etc.), together with lower-orbital electrons contributed also by the lighter elements. Their name reflects the fact that, below a characteristic temperature (of the order of $10 - 100$ K), the conduction electrons acquire large *effective* masses (up to 100 or 1000 times the bare electron mass). Experimental evidence for these high effective mass values can be obtained by measurements of the electronic specific heat (Sommerfeld coefficient), of the upper critical field $H_{c2}(T)$ at low fields or more microscopically by measurements of the de Haas-van Alphen effect (see fig. 2.1). Hereby, the electrons of the partially filled $4f$ or $5f$ shell play a key role. The f state wave-functions are rather localized (close to the nucleus), typically $r_{4f} \approx 0.5$ Å. At high temperatures, these compounds may behave like conventional metals containing *localized* f electrons which carry a magnetic moment, giving rise to a Curie–Weiss-like susceptibility. The "light" s and d conduction electrons and the localized f electrons interact by a standard exchange coupling. In fact, the hybridization Γ of the f level with the conduction band is small, (~ 0.1 eV) while the intrasite Coulomb correlation U is large ($5 - 10$ eV). Under these circumstances, localized spin magnetism might be expected, i.e. the occurrence of some long range magnetic order at low temperature, as is generally observed for a lattice with sites carrying magnetic moments.

However, in heavy fermion systems, experimental results speak another language: one measures ordered magnetic moments per lattice site that are very small compared to the high

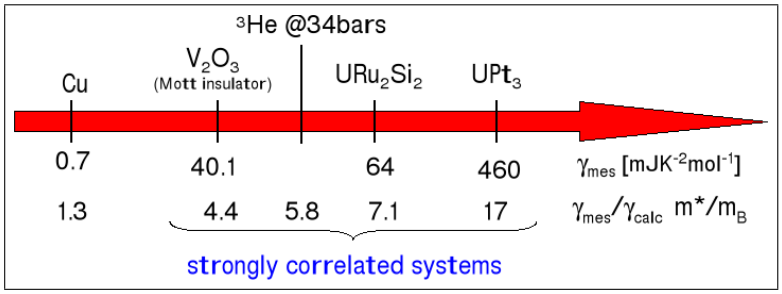

Figure 2.1. Comparison of copper with some strongly correlated systems. The impact of the correlations on the effective mass can be quite important. As usual, γ denotes the specific heat (SOMMERFELD) coefficient $\gamma^{el} = n(\pi k_B)^2 m^*/(\hbar k_F)^2 \propto m^*$, and m_B the (calculated) band mass.

temperature values, and sometimes the complete absence of a long range magnetic order. The magnetic properties of heavy fermions are therefore completely altered at low temperatures. It seems that the system changes continuously, without any phase transition, from a state where the conduction electrons and the f electrons are more or less decoupled into a low temperature state exhibiting FERMI liquid [108] properties with very heavy *quasiparticles*[1] and, if at all, very small magnetic moments ($< 0.1\mu_B$) localized at the Ce or U ion sites. From the experiments, one finds a specific heat linear with temperature, a PAULI-like spin susceptibility corresponding to a large density of states and an electric resistivity $\rho = \rho_0 + AT^2$ with a large A term. $CeAl_3$ [5] was the first specimen where LANDAU's *quasiparticle* picture was shown to hold quite well below ~ 1 K. However, different very low temperature ground states of heavy fermions have been uncovered, such as semiconducting, superconducting or anti-ferromagnetic. A so-called "Non-FERMI liquid" (NFL) behavior occurs in another class of heavy fermion materials, exhibiting physical properties that do not find explanation within a FERMI liquid picture at low temperatures[2] (for the first time discovered on $Y_{1-x}U_xPd_3$ [174]).

The high-temperature ground state in heavy fermions is reasonably well understood on the basis of extensions of the single-ion KONDO theory [99]. How the variety of low temperature ground states (paramagnetic, magnetic, semiconducting or superconducting) evolves from the high temperature normal state is, however, only partially understood, although the following considerations are generally agreed upon. There is a cross-over from local-moment behavior at higher temperatures to a reduced-moment regime at low temperatures, where the f-electron moments are reduced to a small fraction of their high-temperature values. This compensation occurs through an anti-ferromagnetic exchange interaction, like in the single-ion case.

In fact, KONDO's original paper [99][3] deals with the interaction between a single magnetic impurity implanted in a metal. Calculations in the framework of the ANDERSON hamiltonian [3] show that the correlations between the isolated spin of the impurity and the conduction electrons lead, below the KONDO temperature $T_K \ll T_F$, to the formation of a collective *singlet* state. This is a ground state where the conduction electrons screen locally the impurity spin [58], and the energy scale $k_B T_K$ corresponds to the gain in energy of the system. Due to the singlet formation, the density of states of the $4f$ electrons, as resulting from the ANDERSON picture, will be modified. To compensate the loss of degrees of freedom of the spin and the

[1] see for example the first chapters of the textbook of Pines and Nozières [155] as an introduction to the notions of FERMI liquid and *quasiparticle*.
[2] We will come back on that point later on when discussing $CeCoIn_5$.
[3] ZIMAN describes the KONDO effect in a particular simple and clear manner in chapter 10 of his textbook [219].

orbital moment, an extra density of states peak (narrow many body resonance) develops in the vicinity of the FERMI energy. This peak is responsible for the unusual low temperature behavior of the ion for $T < T_K$ and is known as the KONDO or ABRIKOSOV–SUHL resonance (see fig. 2.2). Alternatively, one can speak of an entropy transfer from the ion to the conduction electrons. The single impurity KONDO effect gives a contribution to $\rho(T)$ which has a logarithmic increase towards lower temperatures, with a saturation at $T \to 0$. Combined with the decreasing electron-phonon contribution, it results in characteristic minimum of $\rho(T)$ at a certain temperature. It corresponds very well to experimental observations on dilute alloys, for example in $Nb_{1-x}Mo_x$ [170].

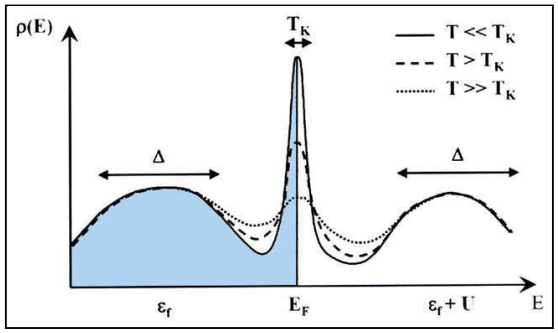

Figure 2.2. Schematic illustration of the formation of the KONDO- or ABRIKOSOV–SUHL resonance (one single impurity coupled to the conduction electrons), see text. ρ denotes the electronic density of states, E_F the FERMI level and ε_f the energy of the f-level.

In heavy fermion systems, we have at least one f electron per unit cell, i.e. a *periodic* arrangement of magnetic moments (so-called "KONDO lattice"). At high temperatures ($T > T_K$) all the physical properties are accounted for by models developed for isolated single impurity systems. However, for low temperatures (in particular for transport properties) significant deviations from the single impurity KONDO model are observed, most easily in electric resistivity. While dilute impurity systems show the "KONDO resistance minimum", the lattice systems are also characterized by a pronounced maximum below a certain characteristic temperature ($\propto T_K$) and by a strong drop of $\rho(T)$ below this temperature. This is explained as follows: at high temperatures, the KONDO centers on each site resonantly scatter electrons. But for $T \to 0$, when magnetic fluctuations disappear, a "perfect lattice" should be recovered, with propagating BLOCH waves. The picture at $T \to 0$ is that of highly *renormalized* bands, of width $\sim k_B T_K$: correlations between the different scatterers allow the conduction electrons to pass through in a *coherent* fashion (i.e. in form of BLOCH waves). As to the heavy quasiparticles (large mass enhancement), COLEMAN [43] proposes the following scenario : contrary to the "screening cloud" picture involving low energy electrons that form the KONDO singlet, the binding process takes place between local moments and *high energy* electrons (spanning decades of energy from the KONDO temperature to the bandwidth), forming a sort of "composite f-electron". The KONDO mechanism affects the temporal correlation between spin-flips of the conduction sea and spin-flips of the local moments, and one can show that it is localized in space, but extremely non-local in time and energy. So it is more convenient to speak of *temporal* (rather than of spatial) bound states, which is conceptually important to overcome such dilemmas as the "exhaustion problem" [43] when extending the KONDO effect from single to lattice impurities.

However, the transition from the initial KONDO problem to a lattice of magnetic ions is quite more subtle. Owing to the high concentration of magnetic moments in KONDO lattices, the intersite interactions can no longer be neglected. Such interactions are, in the case of f electron systems, of RKKY-type (according to RUDERMANN, KITTEL, KASUYA and YOSIDA) and promoted by the conduction electrons. In dense systems, the RKKY interaction typically

gives rise to a (long-range) ordered anti-ferromagnetic state. Hence the formation of a KONDO lattice regime (leading to heavy fermions) depends on the competition between the KONDO screening of the array of local moments and the RKKY interactions, as first proposed by DONIACH [51]: one needs $T_K > T_{\mathrm{RKKY}}$. As the renormalized mass m^* is proportional to $1/T_K$, heavy fermion systems are found at the verge of a paramagnetic-magnetic order instability.

2.1.2. Heavy Fermion materials – superconducting state properties

As mentioned before, in this thesis, we are essentially interested in the superconducting phase of heavy fermion compounds. In 1979, STEGLICH et al. [187] discovered that $CeCu_2Si_2$, which has a large $\gamma \approx 1$ J mol^{-1}K^{-2}, was superconducting around 0.6 K. Since then, many other heavy fermions (UBe_{13}, UPt_3, UPd_2Al_3, UNi_2Al_3, etc.) have been found to become superconducting ($T_c \leq 2$ K), at ambient or under pressure. From measurements of the specific heat and the initial slope of $H_{c2}(T)$ it can be concluded that the heavy quasiparticles themselves condensate into COOPER pairs. Additionally, in the case of $CeCu_2Si_2$ it was observed that the non-magnetic isostructural compounds with lanthanum or thorium do not show superconductivity. At first sight, it is astonishing to find superconductivity in systems exhibiting permanent magnetic moments, which in classical superconductors undermine the superconducting ground state (pair-breaking by paramagnetic impurities [1]). However, since KONDO screening is observed in these compounds at higher temperatures (for example seen from resistivity), it follows that the magnetic moments of the cerium or uranium ions are already compensated. Nevertheless, some of these compounds exhibit weak magnetic order above T_c, and the coexistence of magnetism and superconductivity in heavy fermion materials remains a central challenge for the understanding of these materials: some recent topics are superconductivity and anti-ferromagnetic instability in cerium compounds ($CeIn_3$, $CeRh_2Si_2$ and $CeRhIn_5$) with their corresponding phase diagrams (H, T, p), or the interplay of superconductivity and ferromagnetism in UGe_2 and URhGe [112].

As a general feature, most known heavy fermion superconductors are of type II with transition temperatures in the K- or sub-K-range, have magnetic field penetration depths λ in excess of several thousand Å and coherence lengths ξ of the order $100 - 200$ Å. This is in contrast to elemental superconductors which have significantly lower λ and higher ξ. These differences are a direct consequence of the very large effective masses m^* (corresponding to low FERMI velocities): $\lambda \propto (m^*/n_s)^{1/2}$ and $\xi \propto n^{1/3}/(m^*T_c)$ (n conduction electron density and n_s superconducting pair density). This leads to anomalously small values of $H_{c1} \propto 1/\lambda^2$ and large values of $H_{c2} \propto 1/\xi^2$ (typically several T) when compared to the thermodynamic critical fields H_c of ordinary type I superconductors (for example Al: $T_c \approx 1.2$ K and $H_c \approx 0.01$ T). Heavy fermions are large κ ($\kappa \sim \lambda/\xi$) superconductors.

Now, two major aspects have to be addressed:

- Which is the symmetry of the superconducting order parameter (which pair state) ?
- What is the attractive force between the quasiparticles (pairing mechanism) ?

BCS-theory [16] has been very successful for describing ordinary metals where the attractive mechanism is due to electron-phonon coupling, yielding an $l = 0$ ("s-wave") or "singlet" ground state. In fact, for the case of heavy fermions, there are several arguments implying that the situation might be quite different:

- Heavy fermions exhibit strong band structure and spin-orbit effects that make the early theory very oversimplified.

- There might be important strong-coupling corrections. In ordinary superconductors, they scale with a power series of $T_c/T_F < 10^{-4}$, but in the case of heavy electrons, the characteristic temperature is T_K and $T_c/T_K > 10^{-2}$.

- In BCS theory, the temperature characterizing the energy scale of the superconducting interaction is much smaller than the degeneracy temperature, $\theta_D/T_F < 10^{-2}$, meaning that the time scale of the phonons is much longer than that of the electrons, so that the COULOMB repulsion can be avoided. But in heavy fermion systems $\theta_D/T_K \sim 1$, and the strong COULOMB repulsion makes it difficult to imagine a resulting attractive electron-phonon interaction.

Indeed, heavy fermion superconductors have attracted considerable interest due to the *possibility* of a pairing mechanism not due to phonon exchange, but to electron-electron interactions. The arguments supporting this hypothesis rest primarily on the analogy with superfluid ^{3}He, where spin-triplet ($l = 1$) pairing must arise because of largely repulsive hard-core He-He interactions, the attractive mechanism then being mediated by spin fluctuations [111]. Even more interesting, this non-isotropic p-wave–state breaks the $SO(3)$-symmetry of the fluid, classifying it as *unconventional* superconductor. In heavy fermions, one can imagine that the strong repulsive COULOMB interaction, in conjunction with the generally small ξ (small expansion of the COOPER pairs) might also favor a state with non-zero angular momentum, in order to keep the electrons as far from each other as possible. As to the attractive pairing interaction, something similar to the spin fluctuations scenario in ^{3}He cannot be excluded, but the question still remains open and probably depends on the compound under consideration.

Under these circumstances, heavy fermions might also be hosts of unconventional superconductivity. The classification in a solid involves gauge symmetry, time reversal symmetry and the elements of the symmetry group of the crystal lattice. Due to the lack of rotational symmetry in spin space, and spin-orbit coupling, one has to introduce "pseudo-spin" if the crystal has an inversion center. Then the only general symmetry classification for the order parameter is *parity* (permitted combinations are singlet pseudo-spin and even parity or triplet pseudo-spin and odd parity). In any case, the order parameter can be classified according to the *irreducible representations* [72] of the point group, and expressed by the basis functions of this representation[4] (or by a linear combination in the case of degeneracy). Since the characterization of the pairing mechanism from first principles is extremely difficult, the preliminary, experimental determination of the order parameter symmetry might help to deduce the nature of the pairing interaction. So, for example, the symmetry of an order parameter belonging to the B_{1g} irreducible representation within the tetragonal point group (so-called "d-wave", observed in the high-T_c cuprates and $CeCoIn_5$) might be correlated with superconductivity mediated by anti-ferromagnetic fluctuations.

The importance of this symmetry classification is that symmetry breaking often implies nodes of the superconducting gap and phase changes which monitor the unusual physical properties of the superconducting state. Inversely, studying these properties is a first step towards identification of the pairing state. Thermal conductivity has been very successful for that purpose in the case of UPt_3 for example [189, 80, 38], and this thesis reports on work done with the same probe on the "new" systems $PrOs_4Sb_{12}$ and $CeCoIn_5$.

Since its discovery, heavy fermion superconductivity has revealed to be one of the most intriguing and exciting areas of modern condensed matter physics, and is far from being entirely

[4] For a more detailed discussion of this topic examples, see for example ref. [189] and the references therein.

understood – new observations regularly enrich the puzzle, as for example the recently discovered superconductivity in the heavy fermion $CePt_3Si$ [20] which has no inversion center. In this thesis, we will show that another feature, namely multiband superconductivity (first discovered in materials other than heavy fermions), might be more wide-spread in heavy fermions than previously thought, and may have considerable influence on their properties.

2.2. Some properties of $PrOs_4Sb_{12}$ and $CeCoIn_5$

Now, let us switch more specifically to the topic of this work, namely $PrOs_4Sb_{12}$ and $CeCoIn_5$. This section is intended to give a short, not exhaustive overview on the compounds' features, notably those related to the crystallographic and electronic structure, and to the superconducting phase. Each topic will be treated "in parallel" for both compounds, in order to better highlight similarities and differences. Let us start with the "families" each compound belongs to and the corresponding crystallographic structures.

2.2.1. Filled skutterudites and the $CeMIn_5$ (115) family – generalities and crystal structure

Filled or ternary skutterudites RT_4X_{12} (R = rare earth, U, Th; T = transition metal like Fe, Ru, Os; X = pnictogen like P, As, Sb) were first synthesized in 1977 [85] and are derivatives of the binary skutterudites MX_3 (M = Co, Ni and X = P, As, Sb). For applications filled skutterudites are very promising, due to their excellent thermoelectric properties at high temperatures [168]. Their low temperature characteristics are not less exciting, since a large variety of magnetic and electric states have been observed within these compounds: ferromagnetic, antiferromagnetic, antiferroquadrupolar, semiconductor, semi-metal, metal-insulator transition, intermediate valence, heavy fermion, Non-Fermi Liquid and superconductor[5].

The rich physics garnered in the 115 compounds finds its roots in the discovery in 1997 of pressure-induced superconductivity in the so-called "parent" compound $CeIn_3$, a material of simple cubic crystal structure which develops commensurate antiferromagnetic order below $T_N = 10.1$ K. The ordering temperature can be driven to absolute zero by increasing applied pressure to $p_c \approx 26$ kbar, where (eventually magnetically-mediated) superconductivity appears below $T_c \approx 200$ mK [212, 127]. Since it was believed that such a superconducting phase could be enhanced by reduced dimensionality (reduced dispersion along one crystal axis), superconductivity was quickly discovered in the tetragonal version of $CeIn_3$, namely $CeRhIn_5$ [135]. In this system, superconductivity also appears above a critical pressure, but at a temperature ($T_c \approx 2.1$ K) approximately one order of magnitude larger than in $CeIn_3$. This immediately prompted further searches for superconductivity in other quasi-2D variants of the cubic "parent" compound, and led to the discovery of superconductivity at *ambient* pressure in $CeIrIn_5$ [153] and subsequently in $CeCoIn_5$ [154] and in $PuCoIn_5$ (with $T_c \approx 18.5$ K [171]).

Filled skutterudites crystalize in a cubic lattice (bcc structure) belonging to the space group $Im\overline{3}$ (T_h^5, #204), as shown in fig. 2.3. In the case of $PrOs_4Sb_{12}$, the lattice constant is 9.31 Å. The rare earth atoms fill the icosahedral pnictogen cages, and their local point symmetry is T_h, which differentiates from more common, ordinary O_h symmetry by the lack of the following two symmetry operations: rotations of $\pi/2$ about the fourfold symmetry axis and rotations of π

[5] More details on general properties of rare earth filled skutterudites can be found in the corresponding literature [169, 168].

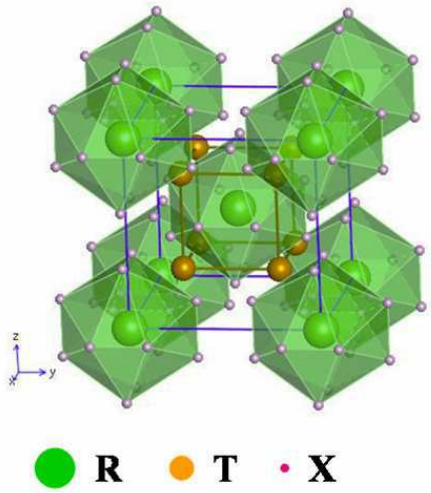

Figure 2.3. Crystal structure of the filled skutterudite RT_4X_{12} with the body-centered cubic lattice.

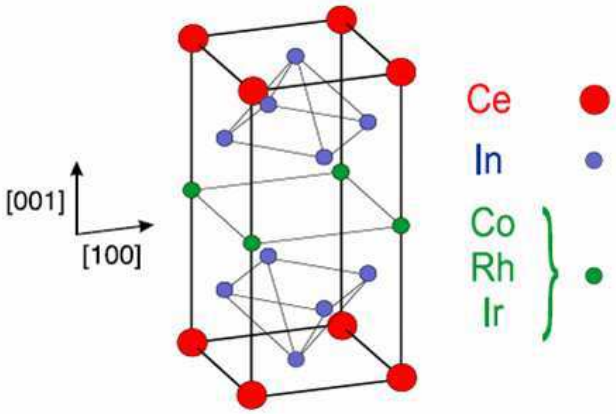

Figure 2.4. Crystal structure of the 115 compounds. Along the c axis, it can be viewed as an alternating stack of $CeIn_3$ and MIn_2 units.

perpendicular to the principal rotation axis [199]. Hence, if one of the principal crystal axes is fixed (for example by an external magnetic field), the other two axes are no longer equivalent.

$CeMIn_5$ has a primitive tetragonal $HoCoGa_5$ crystal structure (space group P4/mmm (# 123) or D_{4h}) which is composed of alternating layers of $CeIn_3$ and MIn_2 stacked sequentially along the [001] axis [65], as shown in fig. 2.4. For $CeCoIn_5$, the lattice parameters are $a = 4.614$ Å and $c = 7.552$ Å.

2.2.2. Low temperature $PrOs_4Sb_{12}$ and $CeCoIn_5$ – generalities and intriguing features

$PrOs_4Sb_{12}$

$PrOs_4Sb_{12}$ was first synthesized by Braun et al. [33] in 1980, and then revisited by Bauer et al. [19] in 2002, reporting superconductivity below $T_c = 1.85$ K (see fig. 2.5), according to specific heat and resistivity measurements. The superconducting state appears to involve *heavy fermion* quasiparticles with an effective mass up to $m^* \sim 50m_e$, as was inferred from the the electronic specific heat (Sommerfeld) coefficient $\gamma^{el} = n(\pi k_B)^2 m^*/(\hbar k_F)^2 \sim 450 - 700$ mJ mol^{-1}K^{-2} (n: electron number per mole) and the initial slope of the upper critical field $H_{c2}(T)$ [19, 125]. $PrOs_4Sb_{12}$ is therefore the first Pr-based compound exhibiting both *heavy fermion* behavior and superconductivity. Even more, the crystal electric field (CEF) level scheme of the Pr^{3+}-ion[6] in $PrOs_4Sb_{12}$ seems also quite unusual. A peculiarity of the structure of this system is that Pr ions in the Sb_{12} cages have lots of space: rattling motion is allowed down to low temperature ($\sim$ 30 K), and CEF levels should be well defined (small hybridization with the conduction band). Following a group theoretical analysis, the CEF[7] (respecting T_h symmetry) splits the

[6] The valence of the Pr-ion in $PrOs_4Sb_{12}$ was determined by XAFS studies [36].

[7] [72] contains a brief introduction to the application of group theory to solid state physics, and [113] a general introduction to CEF effects.

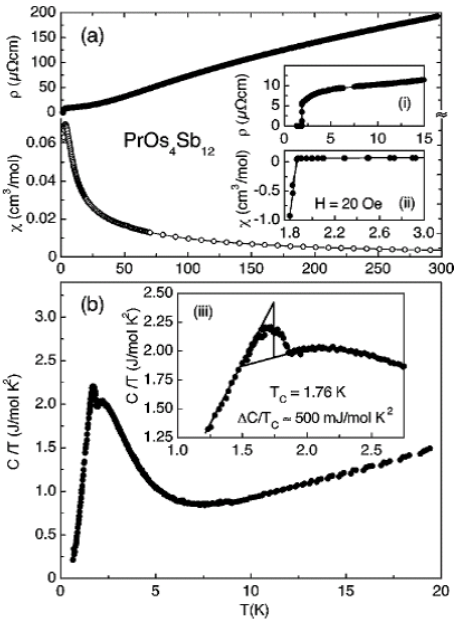

Figure 2.5. Resistivity $\rho(T)$, susceptibility $\chi(T)$ and specific heat $C_p/T(T)$ of $PrOs_4Sb_{12}$ as reported by BAUER et al. [19]. Here the superconducting anomaly in specific heat is quite broad.

$2 \times 4 + 1 = 9$ degenerate states (electronic configuration of the free Pr^{3+} ion: $[Xe]4f^2$ with total angular momentum $J = 4$) into 4 sub-levels [199]. Inelastic neutron scattering measurements [125, 63, 107, 106, 97] established the complete CEF level scheme, supporting a *singlet* ground state (no internal degrees of freedom) with the first excited state at only ≈ 0.7 meV, i.e. ~ 8.5 K. This outcome has profound impact on the low temperature properties of $PrOs_4Sb_{12}$.

- The first low-lying excited state explains the observed SCHOTTKY anomaly in specific heat (maximum in $C_p/T(T)$ at about 2 K, see figures 2.5 and 2.6).
- Moreover, at low temperatures and in magnetic fields above 4.5 T, a antiferro-quadrupolar field-induced ordered phase was detected [167, 210, 9, 77, 203, 165]. Neutron diffraction experiments [97] revealed that within this phase a small antiferromagnetic moment appears on the Pr^{3+} ions. These moments are induced by the ordering of O_{yz}-type quadrupolar moments produced from a pseudo-doublet state formed by CEF level crossing under magnetic field.
- The fundamental questions "what is the physical origin of the conduction electron mass enhancement?", and "what is the driving force of pair formation in the superconducting state?" are of particular interest for $PrOs_4Sb_{12}$, as in better known *heavy fermion* superconductors (U or Ce-based), these phenomena are thought to be related to magnetic interactions and magnetic fluctuations respectively, which are forbidden in the case of $PrOs_4Sb_{12}$ because of the *non-magnetic* ground state (of the Pr^{3+} ion).

In relation with the last point mentioned above, various scenarios for the *heavy fermion* behavior and the superconducting pair formation can be found in the literature. The *singlet* ground state of the Pr-ion prohibits a static electric quadrupole moment. Hence the "quadrupolar KONDO lattice" scenario, due to the interaction of a localized electric quadrupole moment with the charge of the conduction electrons ("electric quadrupolar KONDO effect" [45]) can probably be ruled out. Nevertheless, this does not exclude other models in which the quadrupolar degrees of freedom of the rare earth f electrons are important, especially because of the observation of

the antiferro-quadrupolar FIOP, suggesting the presence of quadrupolar fluctuations within the superconducting phase [106, 181]. Hence these quadrupolar fluctuations could be at the origin of the attractive pair potential. As to the mass enhancement in the normal phase, it could arise from inelastic exchange scattering of the conduction electrons by the low-lying crystal field levels [63]. Then, for the superconducting phase, the scenario could be as follows: although the above *s-f* exchange that is responsible for the mass enhancement tends to suppress superconductivity by magnetic pair-breaking, the relatively high transition temperature of $PrOs_4Sb_{12}$ (compared to the case of $LaOs_4Sb_{12}$) could be due to inelastic quadrupolar scattering (known as aspherical COULOMB scattering), enhancing pair formation [63]. At present, all the – admittedly innovative and attractive – proposed concepts remain speculative in the sense that they are backed by few experimental facts, both as regards the *heavy fermion* behavior in the normal phase and the pairing mechanism in the superconducting phase. During this thesis, we concentrated our efforts on the comprehension of the properties of the superconducting phase, so we will not go into more detail as to the possible mechanisms of mass enhancement or pairing.

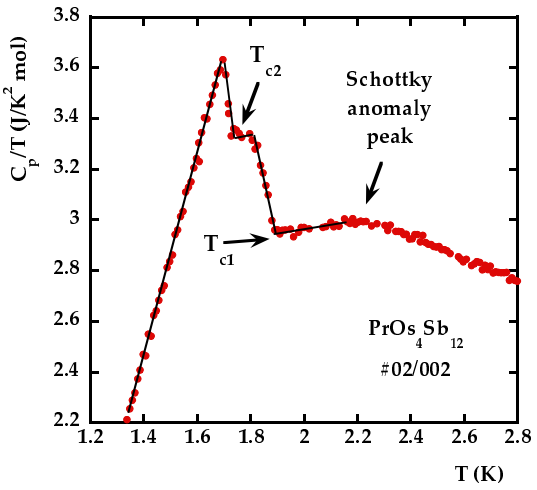

Figure 2.6. Low temperature specific heat on $PrOs_4Sb_{12}$ at zero field. The sharp double superconducting transition is superposed on a broad SCHOTTKY anomaly peak. The measurements were carried out on the sample used to determine the $H-T$ phase diagram in [130] (see also fig. 2.7).

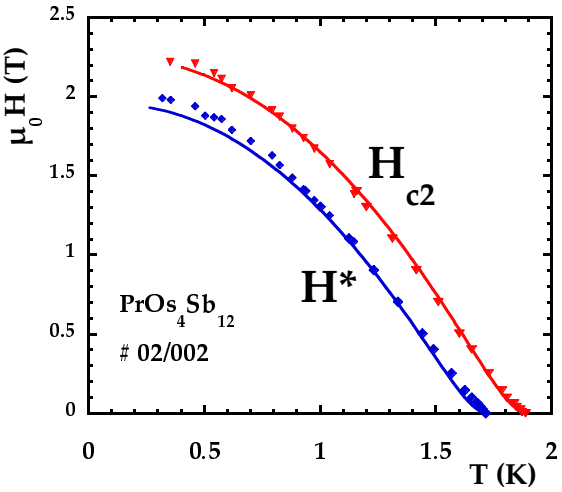

Figure 2.7. $H-T$ phase diagram of $PrOs_4Sb_{12}$ obtained by following the double superconducting transition in the specific heat (see fig. 2.6) under magnetic fields. $H^*(T)$ corresponds to T_{c2} in fig. 2.6, and the solid lines correspond to fits within a two-band model [130]. Obviously, both transitions behave similarly under magnetic fields.

The speculations on unconventional superconductivity are amplified by further, intriguing experimental observations:

- Muon spin relaxation measurements [10] indicate a small internal magnetic moment within the superconduction phase of $PrOs_4Sb_{12}$, suggesting time-reversal symmetry breaking.

- Whereas the first paper [19] reports a broad superconducting anomaly in the specific heat (see fig. 2.5), the subsequent articles [210, 125] evoke the possibility of a double superconducting transition, reminding the well-known case of the *unconventional* superconductor

UPt_3 [68] with its multiple phases within the $(H-T)$ plane. Since then, the superconducting anomaly in specific heat has been intensively studied (see [129] for a detailed discussion) and confirmed by several groups (see fig. 2.6), and also by thermal expansion measurements[8] [146]. Nevertheless, taking into account the similar behavior of both transitions under field [130] (see fig. 2.7) and pressure [129], and regarding the corresponding resistivity and susceptibility measurements[9], which show that superconductivity is always inhomogeneous between T_{c2} and T_{c1}, an extrinsic origin of this double transition is not excluded, as indicated by recent measurements on tiny samples [131], and as will be shown at the beginning of chapter III.

- A strong distortion from the ideal hexagonal flux-line lattice was reported from small-angle neutron scattering experiments [81], and explained by point nodes of the gap. However, a more conventional explanation involving the tetrahedral T_h point group was suggested by Dao et al. [49], and recent new measurements [163] would not confirm the interpretation given in [81].

- The angular dependence of thermal conductivity in a rotated magnetic field [92] suggests an anisotropic superconducting gap with point nodes. In the corresponding $(H-T)$-plane, Izawa et al. propose two distinct superconducting phases with a change from four- to two-fold symmetry for the order parameter when passing from phase A to phase B (see fig. 2.8). Other experiments also report an unusual behavior within the superconducting phase: the absence of a coherence peak in Sb NQR measurements [101] or the temperature dependence of the London penetration depth [40] point to gap nodes.

From this experimental puzzle, it is not surprising that $PrOs_4Sb_{12}$ has become a promising candidate for unconventional (in all senses) superconductivity. Note, however, that several experiments report a rather conventional scenario within the superconducting state (finite gap in tunneling spectroscopy by STM [192], exponential decrease of $1/T_1(T)$ in Sb-NQR studies [101], relevance of paramagnetic limitation in the upper critical field (supporting even parity pairing) [130] and ordinary temperature dependence of the London penetration depth as seen by μSR [120]). Altogether, there is no straightforward conclusion available, that could account for all these different observations. Especially, the question of unconventional superconductivity and of the gap topology in $PrOs_4Sb_{12}$ remains open. In this thesis, we bring another, formerly neglected aspect into play: multiband effects. Their relevance for the superconducting state is uncovered from the very strong sensitivity of thermal transport to small magnetic fields. This feature probably stands in close relation with the electronic band structure of the compound, as we will explain later on. Eventually, considering a multiband superconductivity scenario in the case of other experimental results might help to overcome the present contradictory interpretations. Moreover, we will give evidence, from the temperature dependence of thermal conductivity, for fully open gaps on the whole Fermi surface (excluding gap nodes). A detailed comparison of our results with other experiments on the superconducting phase will follow at the end of chapter III.

[8] However, both jumps of the thermal expansion coefficient β at the higher and lower T_c behave similarly (same sign for $\Delta\beta$), so that they cannot help to distinguish the nature of the two transitions.

[9] Resistivity only becomes zero at the lower T_c, and instead of showing perfect diamagnetism just below the upper T_c, ac susceptibility is also non-zero down to the lower one [130, 129].

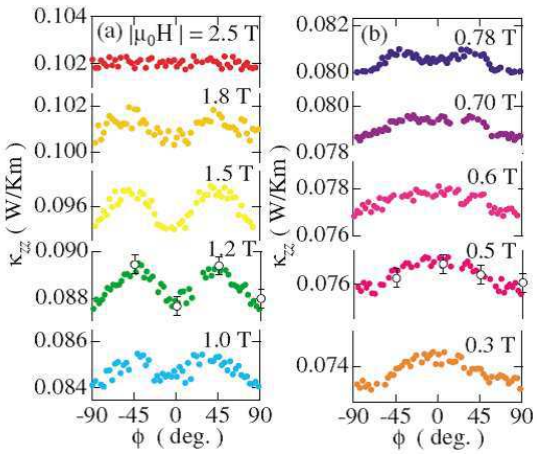

(a) Experimental results: angular variation of κ_{zz} in a magnetic field rotating within the ab-plane at 520 mK.

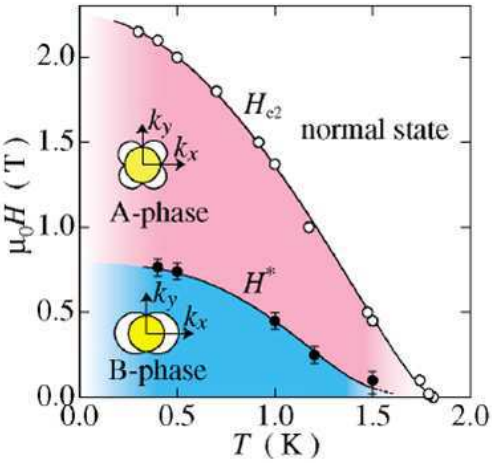

(b) Resulting phase diagram. At the field $H^*(T)$ a transition from fourfold to twofold symmetry of the superconducting order parameter takes place.

Figure 2.8. Angle-resolved measurement of thermal conductivity in a rotated magnetic field as reported in [92] with its resulting phase diagram for $PrOs_4Sb_{12}$. **Remark**: Note that the field $H^*(T)$ does not correspond to the lower transition observed by specific heat in figures 2.6 and 2.7.

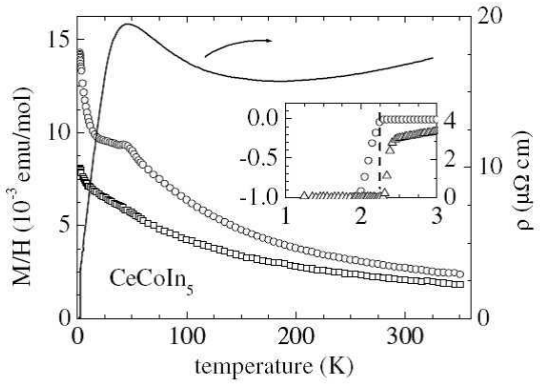

(a) Electric resistivity and magnetic susceptibility (measured in a 100 mT applied field parallel (circles) and perpendicular (squares) to the c-axis. The inset shows zero-field-cooled magnetic susceptibility (circles) and resistivity (triangles) in vicinity of the superconducting transition.

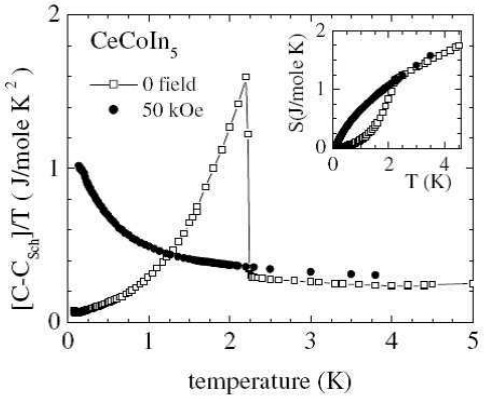

(b) Specific heat $C_p/T(T)$. A nuclear SCHOTTKY-contribution, due to the large nuclear quadrupole moment of In has been subtracted. The inset shows the entropy $S(T)$ in the superconducting (open squares) and field-induced normal (solid circles) states.

Figure 2.9. First report of record-T_c heavy fermion superconductor $CeCoIn_5$ [154].

$CeCoIn_5$

$CeCoIn_5$ is a layered superconductor with the highest known ambient-pressure transition temperature $T_c \simeq 2.3$ K in the class of heavy fermion materials [154] (see fig. 2.9). The specific heat coefficient just above T_c yields $\gamma \sim 300$ mJ mol^{-1}K^{-2}, indicating substantial mass renormaliza-

tion. Compared to BCS-theory, the specific heat jump at T_c is quite large and may point to strong-coupling behavior, but another scenario involving coupling between the superconducting order parameter and fluctuating magnetic moments was also suggested [100]. There is a factor of ~ 2 in the anisotropy of the upper critical field H_{c2} with respect to field orientation, yielding $H_{c2}(T \to 0) \approx 5$ T for $H \parallel c$ and $H_{c2}(T \to 0) \approx 11.5$ T for $H \parallel a$ [202], see fig. 2.10. The most striking characteristic of $H_{c2}(T)$ is the presence of a *first order* transition below ~ 1 K for both field orientations, as observed in magnetization [202, 138], specific heat, thermal expansion, magnetostriction [26, 200] and thermal conductivity measurements [94]. Estimates of the orbital limiting field for each orientation, as obtained from the initial slope of $H_{c2}(T)$ are much greater than the observed values, indicating that the orbital limit is strongly suppressed in $CeCoIn_5$ by Pauli paramagnetism. Indeed, a first-order transition is predicted to occur in this case, but it could also be linked to the possible presence of a Fulde–Ferrel–Larkin–Ovichinnikov (FFLO) phase [202, 138, 25, 158, 96]. The long-range magnetic order that appears in $CeRhIn_5$ at ambient pressure can be continuously tuned away, either by alloying or pressure. Thus $CeCoIn_5$ seems to be on the verge of long-ranged order. As a function of temperature, $\chi(T)$ yields an anisotropy depending on field orientation, showing a continuous increase for $H \perp [001]$ and a sign of saturation below $T \sim 50$ K for $H \parallel [001]$ (the latter being somewhat typical of a heavy fermion metal) [154]. Above this shoulder, $\chi(T)$ is well-described by the effects of crystalline electric fields based on a $4f$-level scheme (Ce^{3+} ion with $[Xe]5s^2 5p^6 4f^1$ in tetragonal symmetry site) [182, 202], and the shoulder itself may be due to the onset of coherence of the Kondo lattice (analogous feature in resistivity) [154]. But the continual increase below ~ 25 K finds no explanation from either of these phenomena - it has largely been classified as a Non-Fermi-liquid effect arising from the proximity of a Quantum Critical Point (QCP).

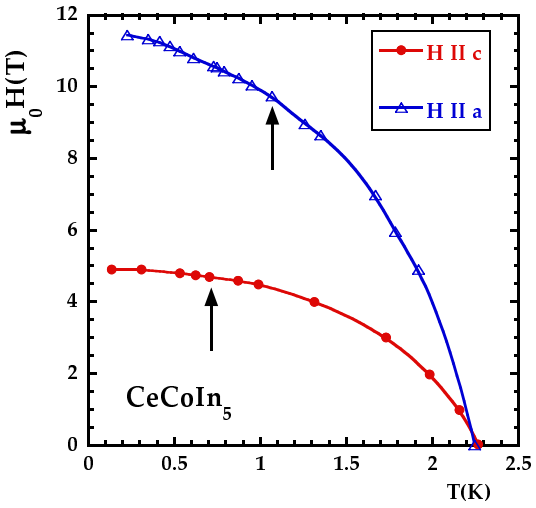

Figure 2.10. Temperature dependence of the upper critical field $H_{c2}(T)$ in $CeCoIn_5$ for both $H \parallel a$ and $H \parallel c$, data taken from [25] and obtained from specific heat measurements. The arrows indicate the temperature below which the transition becomes first order.

As mentioned earlier, there is a class of heavy fermion materials for which, in a certain range of pressure and temperature, Landau's Fermi-liquid picture fails to explain the physical properties. A promising way to understand this type of behavior comes from the concept of a zero-temperature or *quantum* phase transition: in the proximity of such a transition, Non-Fermi-liquid behavior (such as non-quadratic temperature dependence of electric transport, non-Curie-like susceptibility and non-saturating electronic specific heat) can be expected. Indeed, quantum critical fluctuations are present down to $T \to 0$, and can strongly alter the physical properties, preventing the Fermi-liquid ground state to prevail. Experiments probe

the properties of a system at small but finite temperatures, not at $T = 0$. Nevertheless, in the vicinity of a quantum critical point ("quantum critical region"), the physics is still controlled by the QCP itself. In reality, quantum phase transitions are "tuned" by changing (external) parameters – such as pressure, chemical composition, magnetic field, etc. – that couple directly to the dynamics of the system. Among the most well-studied heavy fermion materials to exhibit quantum critical behavior are $CeCu_{6-x}Au_x$ [173] and $Ce_{1-x}La_xRu_2Si_2$ [117, 56, 69]. The ground state of this material can be tuned by substituting Au for Cu or La for Ce, from paramagnetic (heavy fermion) at $x = 0$ to antiferromagnetic at $x > x_c$. Hence, a QCP associated with the suppression of T_N to $T = 0$ occurs at the critical Au concentration of $x_c = 0.1$ or La concentration of $x_c = 0.075$. Interestingly, in addition to chemical tuning, the critical behavior can also be influenced with applied pressures or magnetic fields [116].

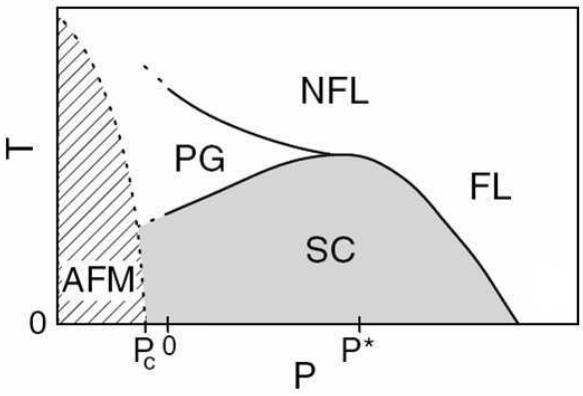

Figure 2.11. Schematic temperature-pressure phase diagram for $CeCoIn_5$, taken from [184]. AFM: Néel state, PG: preudogap state, SC: unconventional superconducting state, FL: Fermi-liquid, NFL: Non-Fermi-liquid.

For $CeCoIn_5$, several experiments and comparison with $CeRhIn_5$ suggest that ambient-pressure $CeCoIn_5$ lies in vicinity of an antiferromagnetic QCP at a slightly negative (inaccessible) pressure p_c [184, 98], see fig. 2.11. More recent measurements also point to a field-tuned quantum critical point close to $H_{c2}(T \to 0)$ [149, 148, 18, 164]. In any case, these observations highlight the strong interplay between antiferromagnetic order and superconductivity in $CeCoIn_5$. So let us have a closer look to the superconducting phase. Here the situation seems less ambiguous than in the case of $PrOs_4Sb_{12}$, and unconventional superconductivity is experimentally established from a converging body of experimental facts:

- The temperature dependence of specific heat below T_c is non-exponential [154], and a power law suggesting line nodes of the superconducting gap is observed [136]. Angle-resolved specific heat measurements in a magnetic field rotating in the basal *ab*-plane show a fourfold symmetry in $C(H, \theta)$, implying nodes along the [100] and [010] directions (d_{xy} type symmetry) [8].

- Park et al. [151] report a temperature dependence of the conductance of Au-$CeCoIn_5$ point contacts which is consistent with a *d*-wave order parameter symmetry. Point-contact spectroscopy on Pt-$CeCoIn_5$ junctions also gives strong support for an unconventional pairing state [62].

- $1/T_1(T)$ (T_1: nuclear spin-lattice relaxation rate) in In NQR measurements [98] exhibits no coherence peak below T_c and shows a power-law dependence (close to T^3) at very low temperatures, hence also pointing to line of nodes in the gap. NMR KNIGHT-shift experiments [98, 46] have revealed even-parity pairing in the superconducting state.
- Different measurements of the penetration depth $\lambda(T)$ [39, 147, 145] also indicate power law behavior, but eventually not corresponding to a standard "d-wave" superconductor.
- The first thermal conductivity measurements show a power law behavior of $\kappa(T)$ [136], and a fourfold symmetry for $\kappa(H, \theta)$ in the basal plane [94], indicating that the order parameter symmetry is of $d_{x^2-y^2}$ type (see fig. 2.12).
- Analysis of the flux line lattice by small-angle neutron scattering [55] seems compatible with "d-wave" order parameter symmetry.

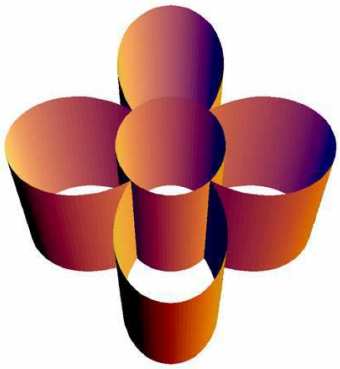

Figure 2.12. Nodal structure of a $d_{x^2-y^2}$ type order parameter (tetragonal symmetry is broken, irreducible representation B_{1g}, $\Delta_k = \Delta_0(k_x^2 - k_y^2)$), as it is suggested in the high-T_c cuprates and $CeCoIn_5$.

As usual no unique scenario for the superconducting state (order parameter symmetry, pairing interaction) of $CeCoIn_5$ emerges from these measurements, which all point to unconventional, non-s-wave superconductivity. Of course, the questions of the pairing mechanism and of the high transition temperature cannot be answered directly, but the relevance of antiferromagnetic fluctuations in the 115 family [46, 14, 89] eventually gives some hints to further understanding [154, 134]. For magnetically mediated superconductivity on the border of antiferromagnetism, the pairing interaction is long ranged and oscillatory in space. In some regions of k-space it is attractive, but in others it is repulsive, and therefore tends to cancel on average. Although this might, at first sight, rule out the possibility of transition temperatures resulting from such an interaction, it is possible to construct a COOPER-pair wavefunction that only has a significant probability in regions where the oscillatory potential is attractive (the repulsive regions of the potential being neutralized). Calculations for quasi-2D or orthorhombic crystal structures with nearly commensurate antiferromagnetic correlations show that magnetic pairing can be strong enough to explain high transition temperatures (even for the cuprate case). The choice of a COOPER-pair wavefunction with nodes along the diagonals $x = \pm y$ and opposite phase along the $x-$ and $y-$directions almost perfectly matches the oscillations of the pairing potential. For 3D cubic crystal structures, the situation is much more complicated, and lower values of T_c are expected. As a result, magnetically mediated superconductivity is favored in quasi-2D over 3D systems, which could explain the much higher transition temperatures in $CeMIn_5$ compared to $CeIn_3$. Indeed, the structural layering in $CeMIn_5$ should produce electronic and magnetic states that are less 3D than in cubic $CeIn_3$. This seems to be confirmed by DE

Haas–van Alphen measurements [177], by NMR and NQR studies [46, 89] which suggest that AFM fluctuations are 2D in nature, and by EXAFS measurements on Sn substituted $CeCoIn_5$ [48]. To summarize, *d*-wave superconductivity mediated by spin fluctuations seems a very likely scenario in $CeCoIn_5$. Together with the quasi-two-dimensionality and the appearance of superconductivity in the vicinity of an antiferromagnetic state, this underlines the parallels to the case of high-T_c cuprates, and explains why the heavy-fermion superconductor $CeCoIn_5$ has attracted so considerable attention.

Nevertheless, this is not the end of the story. The discrepancy between the interpretations of angle-dependent specific heat [8] and thermal conductivity measurements [94], the non-usual power law found in $\lambda(T)$ [147] and the saturation of the spin-relaxation rate below 0.3 K [89, 98] remain unexplained in the above picture. A recent thermal conductivity study [201], point-contact spectroscopy[10] [166] measurements and angular-dependent torque experiments [216] emphasize the possibility of multiband superconductivity in $CeCoIn_5$. So in our heat transport measurements, we concentrate on the superconducting phase and the impact of magnetic field, revealing a strong enhancement of thermal transport already for $H \sim H_{c2}/500$ at very low temperatures.

2.2.3. $PrOs_4Sb_{12}$ and $CeCoIn_5$ – electronic structure

Electronic band structure properties are essential for the understanding of both the heavy fermion behavior and the superconducting state. Besides, precious information on the eventual relevance of multiband effects might be inferred, as we will show in the next section.

Due to the cubic crystal structure in $PrOs_4Sb_{12}$, one can a priori expect a relatively simple Fermi surface. Band structure calculations were carried out by Harima et al. [67], the corresponding Fermi surface sheets (two closed, nearly spherical and one multi-connected) are shown in figure 2.13. From the investigations of the superconducting state (specific heat coefficient and slope of the upper critical field near T_c), one expects the presence of strongly correlated electrons, i.e. *heavy* quasiparticles with an effective mass estimated up to $m^* \sim 50m_0$ (as indicated earlier). However, in de Haas–van Alphen measurements [194, 195], quasiparticles with cyclotron effective masses ranging from $m_c^* \sim 2.4m_0$ to $7.6m_0$ were detected. Moreover, these measurements have revealed that the topology of the Fermi surface is close to the reference compound $LaOs_4Sb_{12}$. Since La has no *f* electrons, this resemblance evidences the well localized nature of the *f* electrons in $PrOs_4Sb_{12}$, in contrast with other *heavy fermion* superconductors like UPt_3 [91] or $CeCoIn_5$, where an itinerant *f* electron model seems more appropriate. This localization has been accounted for theoretically with a LDA+U method [67], and the agreement with the angular dependence of the de Haas–van Alphen measurements is quite good. The only weak point is that the density of states at the Fermi level contains a rather small amount (some few %) of *f* components in that calculations, which is difficult to reconcile with the large observed mass enhancement in $PrOs_4Sb_{12}$. By reducing the U value [67], it is possible to increase the *f* component at the Fermi level (leading to a rather itinerant picture), but the topology of the Fermi surface would change, and the angular dependence of the de Haas–van Alphen measurements could no longer be explained. As to the discrepancy on the experimental level mentioned above (dHvA versus specific heat), even the highest measured cyclotron effective masses cannot completely account for the measured γ coefficient [194, 195] – a simple estimation of γ from the dHvA frequencies and cyclotron effective masses, assuming spherical

[10] In recent comments Sheet et al. [180] and Park et al. [152] partly disagree with the interpretations of the PCS-measurements.

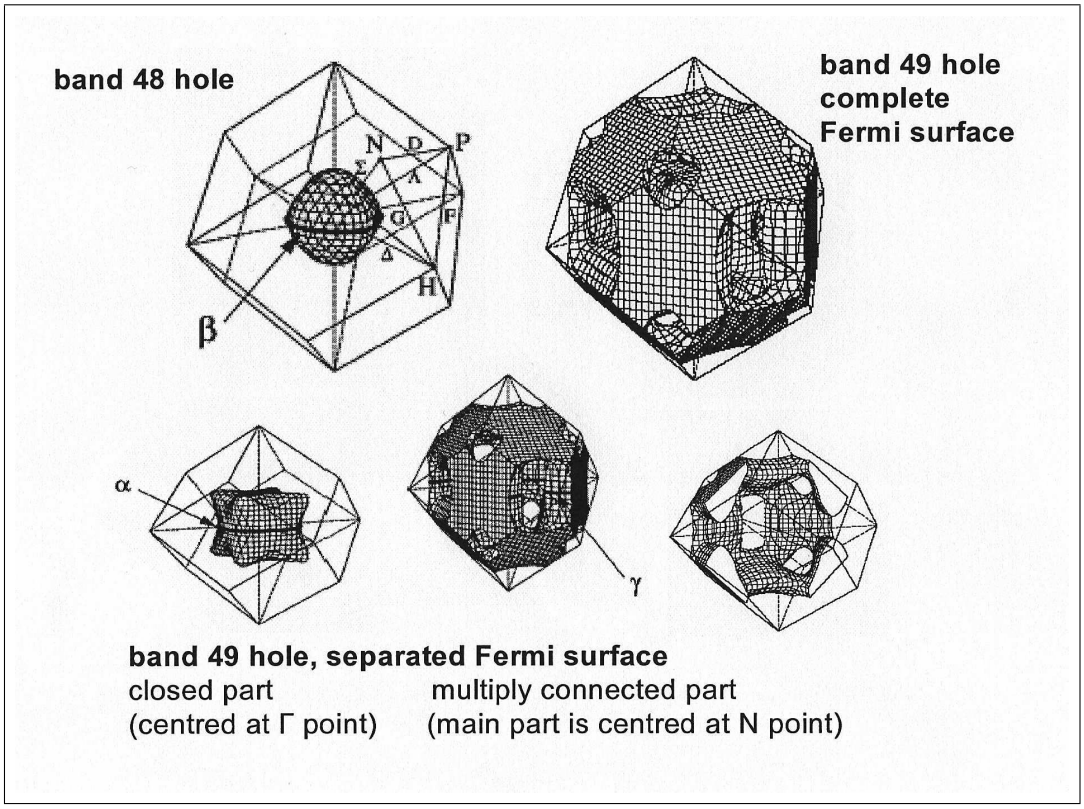

Figure 2.13. Calculated 48th and 49th Fermi surfaces (upper part) [67] in $PrOs_4Sb_{12}$. Below are shown separately the closed and the multiply connected part of the 49th Fermi surface in order to see the lack of fourfold symmetry, associated with the T_h space group.

FERMI surfaces, roughly yields only $\gamma^{el} \sim 20 - 150$ mJ mol^{-1}K^{-2} [19, 194]. At present, it is not clear if this mismatch comes from the different experimental conditions (magnetic field and temperature) or from the fact that the heavier quasiparticles could simply not be detected in the DE HAAS–VAN ALPHEN experiment. Despite these uncertainties, the key result is that different types of electron quasiparticles, *light* and *heavy* ones, seem to coexist at low temperature in $PrOs_4Sb_{12}$ (see fig. 2.14).

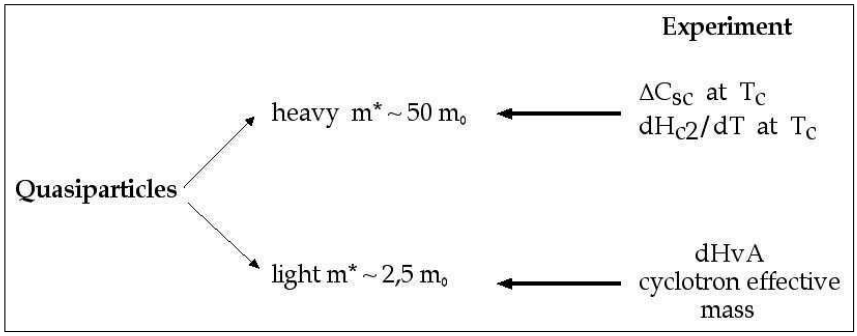

Figure 2.14. Schematic representation of the experimentally observed spread of effective masses in $PrOs_4Sb_{12}$.

What does this multiband electronic structure imply for the superconducting state ? In [130] we refer to the cases of MgB_2 [114, 128] and the borocarbides YNi_2B_2C and $LuNi_2B_2C$ [183], and propose the possibility of different gap amplitudes for the different corresponding sheets of the FERMI surface, a scenario which is made quantitative by a "two-band model", presented in the next section. This two-band superconductivity has, among other features[11], theoretical impacts on the upper critical field $H_{c2}(T)$ which are very well reproduced by the experimental data, namely in the $H_{c2}(T)$ curve at very low fields [130]. Here I only want to stress that this model has nothing to do with the specific heat double transition discussed above, which anyway clearly involves *heavy* electron quasiparticles both at T_{c1} and T_{c2}, according to the size of the two specific heat jumps (besides, no double transition has ever been observed in MgB_2 or in the specified borocarbides).

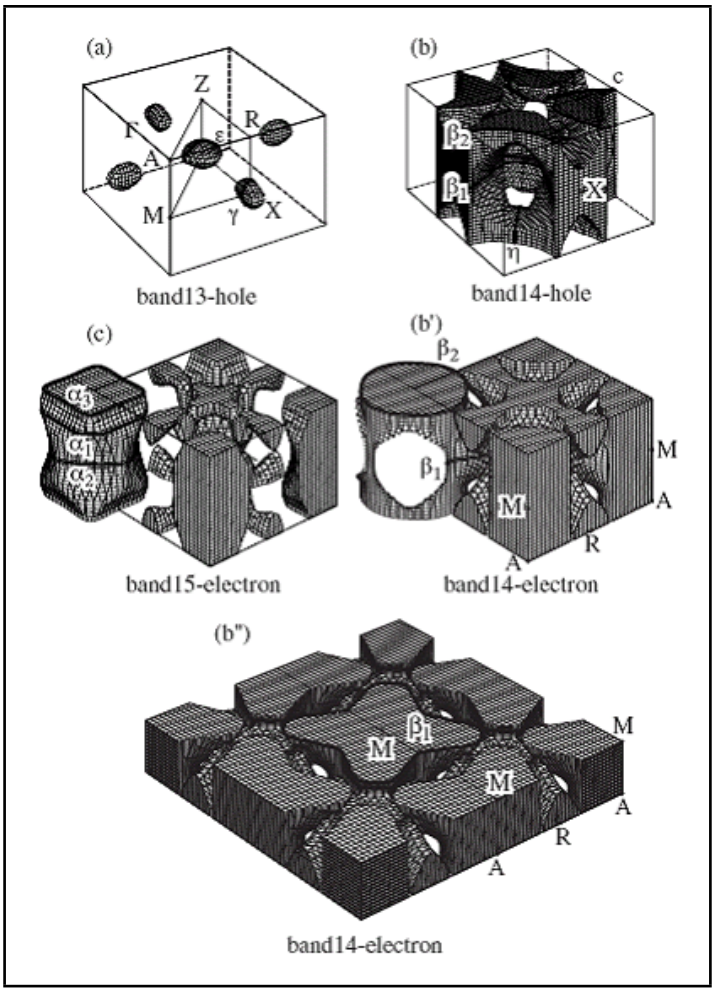

Figure 2.15. Theoretical FERMI surfaces in $CeCoIn_5$ (taken from [182]). The α branches have a nearly cylindrical character.

In $CeCoIn_5$, the question of how the structural dimensionality translates to the electronic properties is particularly important, and was addressed by both band structure calculations

[11] Eventually, the proposed two-band superconductivity can in return explain why the heavy quasiparticles are not observed in dHvA measurements, see [35] for more details.

and experimental studies of the FERMI surface (DE HASS–VAN ALPHEN effect). From their comparison, it is generally accepted that the FERMI surface consists of multiple quasi-2D and 3D sheets associated with four to five bands crossing the FERMI level [177, 121]. More precisely, nearly cylindrical, and small ellipsoidal FERMI surfaces are detected experimentally [177, 182]. The angular dependence of the dHvA frequency is well explained by the FERMI surfaces shown in fig. 2.15, calculated on the basis of the *itinerant* $4f$ band model [52, 121]. The cyclotron effective mass determined from the temperature dependence of the dHvA signal amplitude is expected to be quite large. Experimentally, there is a wide spread of $m^* \sim 4 - 87m_0$ (the heavier masses corresponding to the rather 2D α and β branches, and the lighter ones to the 3D pockets (ε branch)). Comparing the ratio between the measured cyclotron masses and the calculated band masses on the one hand, to the ratio between the experimental and theoretical γ coefficients on the other, probably reveals some missing heavy masses in the dHvA measurements [177]. However, the cyclotron mass is found to be field dependent: it decreases with increasing field, and much higher m^* (over $100m_0$) are expected at lower fields. At this stage, the main outcome is the large dispersion of m^* established in $CeCoIn_5$.

Note that a wide spread of effective masses is generally associated with a wide range of FERMI velocities.

2.3. Some aspects of Multiband Superconductivity

This section is intended to recall the main properties of a multiband superconductor, essentially from an experimentalist's point of view.

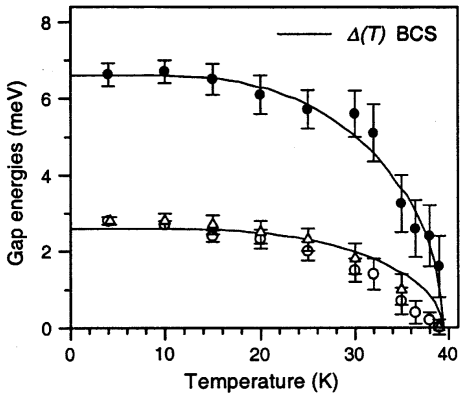

Figure 2.16. Temperature dependence of both energy gaps in the multiband superconductor MgB_2, figure 2 in [198]. The data was obtained from ANDREEV reflection (tunneling) spectra on Cu-MgB_2 junctions fitted by a generalized BTK-model [27] for two gaps.

Multiband superconductivity was evoked for the first time in 1959 [196], shortly after the theoretical description of superconductivity by BARDEEN, COOPER and SCHRIEFFER [16]. Experimentally, its first "textbook" host was discovered only in 2001 [139]: the electron-phonon superconductor MgB_2 with $T_c \approx 40$ K. The main physical ingredient is to suppose the existence of several order parameters of amplitude $\Delta_i(\vec{k})$, corresponding to the different sheets i of the FERMI surface (see fig. 2.20), and originating from different inter- and intra-band coupling strengths [128]. In general, because of strong interband coupling, all gaps have the same (upper) transition temperature (see fig. 2 of [196] and fig. 2.16) (there is only *one* phase transition). On a more formal level, this means that the "coupling constant" λ has to be replaced by a matrix $(\Lambda)_{ij}$ $(i,j=1,2)$ with elements λ_{ij} where i and j are the indexes of the initial and final bands in the (phonon) scattering process, respectively. A priori, there is no reason for this matrix to be symmetric. The λ_{ij} characterize the interactions between the bands i and j, and in general, one separates them into two main contributions: the interaction matrix element ("interaction potential") V_{ij} and the density of states N_j of the final band j

$$\lambda_{ij} = V_{ij} N_j \ . \tag{2.1}$$

The matrix $(V)_{ij}$ is of course *hermitean*, but the density of states of band i and j need not to be equal. In MgB_2, it is claimed that the various λ_{ij} originate from different electron-phonon coupling V_{ij}, which might be larger in the σ band than in and between the other (π) bands. In $PrOs_4Sb_{12}$, as we know little about the pairing mechanism, a starting point can be with inter- and intra-band coupling of the same "strength": $V_{ij} = V_0 \equiv const$, so that the relative weight of the coupling constants λ_{ij} only depends on the density of states of the final band j (and hence on the effective mass of the quasiparticles in that band). The self-consistent equations [128]

$$\Delta_i = \sum_j \lambda_{ij} \Delta_j F(\Delta_j, T), \text{ where } F = \int_0^{\hbar\omega_D} dE \tanh\left(\frac{\sqrt{E^2+\Delta^2}}{2k_B T}\right) \frac{1}{\sqrt{E^2+\Delta^2}} \tag{2.2}$$

implicitly define the dependence on temperature of the superconducting gaps Δ_i belonging to the different bands i. ω_D is the maximum phonon frequency. In order to find the critical

temperature T_c, one sets $\Delta(T = T_c) = 0$ in the function F and finally obtains in the *weak* coupling approach involving several electronic bands:

$$k_B T_c \approx \hbar\Omega \exp\left(\frac{-1}{\lambda_{\text{eff}}}\right), \tag{2.3}$$

where λ_{eff} is the largest eigenvalue of the matrix $(\Lambda)_{ij}$ and Ω a mean energy of the phonon spectrum (simple EINSTEIN model). Of course, this can be expanded to the strong-coupling regime, including mass renormalization. In any case, due to the variational character of BCS-theory, one should retain the general feature that a bigger energy gain and a higher transition temperature can be achieved if more variational freedom is provided, i.e. by allowing different order parameters in the different bands ($\bar{\lambda} \leq \lambda_{\text{eff}}$ where $\bar{\lambda} = \sum_i N_i \Lambda_{ij}/N_{tot}$ describes the isotropic limit with equal order parameters).

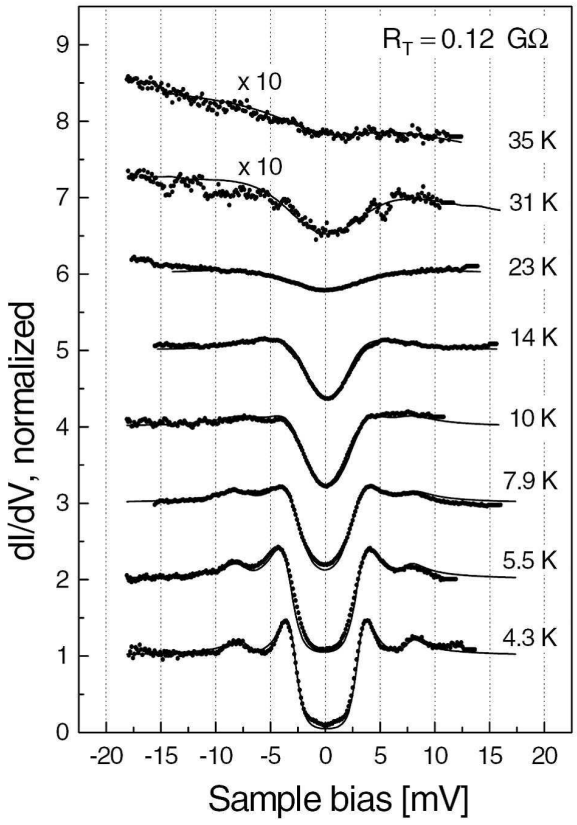

Figure 2.17. Temperature dependence of tunneling conductance spectra in the simple binary compound MgB_2 between 4.3 and 35 K (taken from [59]). In fact, in the STM experiment, MgB_2 is used as a tip and the "sample" is a 2H-$NbSe_2$ single crystal. All experimental curves (black dots) are fitted by a sum of two weighted BCS-shape densities of states (solid lines). The spectra are shifted by unity for clarity.

How does multiband superconductivity translate to the experiment? First of all, two different energy scales are clearly observed in STM measurements [59, 126, 82] (see fig. 2.17). At low temperatures, the tunneling conductance spectra show a gap at the FERMI energy, followed by two well-pronounced conductance peaks on each side, and their shape can be modeled with a sum of two weighted BCS-shape densities of states. Further evidence for the "two-band superconductor" scenario comes from high-resolution angle-resolved photoemission spectroscopy (ARPES) [207] and ANDREEV reflection (tunneling) spectroscopy [198] (the corresponding gap functions $\Delta_i(T)$ are shown in fig. 2.16), and from numerous other experiments. Let us look at experiments using a more macroscopic probe: the (electronic) specific heat [32, 50] – its temperature dependence at several fields is plotted in fig. 2.18. In zero field, it rises at lower

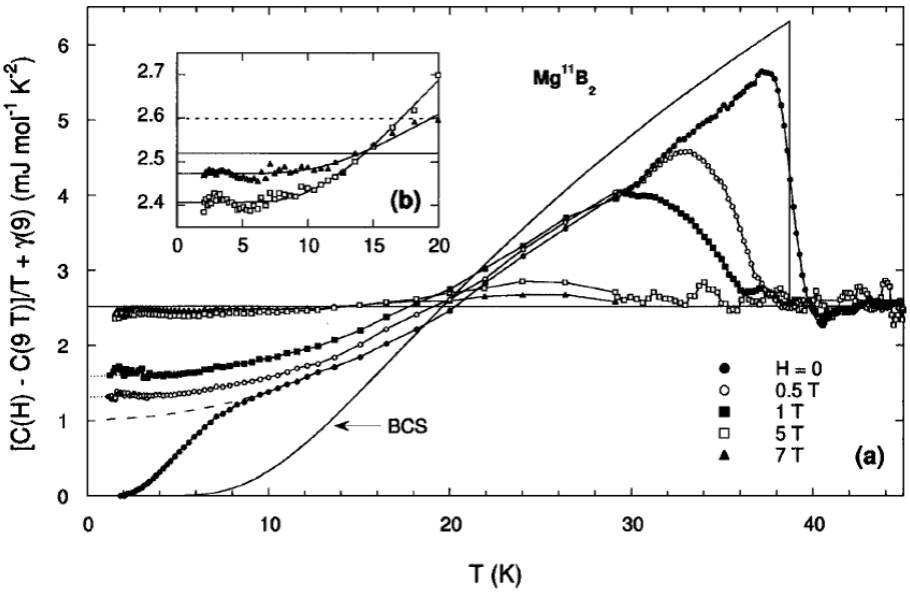

Figure 2.18. Temperature dependence of specific heat at different magnetic fields in MgB_2, taken from [32]. The low field low temperature data clearly reveal the existence of a second energy gap.

temperatures than predicted by BCS (single-gap) theory (Δ_{BCS} corresponding to $T_c \sim 40$ K), and exhibits a sort of shoulder after the first step increase. This low temperature behavior is the clear signature of a second energy scale smaller than Δ_{BCS} in MgB_2. Multiple gaps also lead to different coherence lengths $\xi_{0i} \approx \hbar v_{Fi}/\Delta_i$, and different *effective* upper critical fields $H^i_{c2} \approx \Phi_0(2\pi\xi^2_{0i})^{-1}$, even if the latter term might be misleading, since generally interband coupling will prevent a real suppression of the smallest Δ_S at the corresponding field H^S_{c2} [205]. More correctly, $H^S_{c2}(T)$ is a cross-over field above which the vortex cores of radius $\xi_S(T)$ overlap, driving normal the majority of the electrons of the corresponding band. Note that the large coherence length of the smallest gap band is observed experimentally through the determination of the vortex profile by scanning tunneling spectroscopy [54]. Evidence for different characteristic field scales in MgB_2 also comes from specific heat: it is strongly increased under low fields at low temperatures (see fig. 2.18), meaning that $H \geq H^S_{c2}$. Another characteristic feature of multiband superconductors is revealed in in the $H_{c2}(T)$ curve (see fig. 2.19) at low fields, near $T_c(H \to 0)$. For sufficiently low fields, the slope of the upper critical field[12] will be influenced by the large coherence length ξ_S of the smallest gap band, and hence the total slope will be lower than in the region for high fields with $H \geq H^S_{c2}$. As a result, we observe a positive curvature in $H_{c2}(T)$. Note that in the case where quasiparticle of quite different effective masses are associated to the several bands (like in $PrOs_4Sb_{12}$ or $CeCoIn_5$), it is convenient to replace the ξ_i by the Fermi velocities v_{Fi} in the above reasoning, since the latter may vary a lot among the different bands ($\xi_0 = 2\hbar v_F/(\pi\Delta_0)$).

Several years after its discovery, there exists already a precise understanding and a universal

[12] For the initial slope, one gets the following relation in a BCS superconductor

$$\left|\left(\frac{dH_{c2}}{dT}\right)_{T=T_c}\right| = \frac{\Phi_0}{2\pi T_c\,(0.74\xi_0)^2} = \frac{\Phi_0}{2\pi T_c\left(0.74\cdot 0.18\frac{\hbar v_F}{k_B T_c}\right)^2} \propto \frac{1}{v_F^2}$$

.

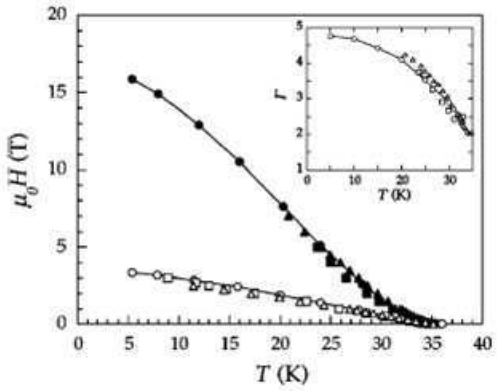

Figure 2.19. Temperature dependence of the upper critical field $H_{c2}(T)$ in MgB_2, taken from [119]. Data obtained from transport (circles), ac-susceptibility (squares) and specific heat (triangles) measurements (filled symbols for $H \parallel ab$). A positive curvature, signature of multiband effects, is observed for low fields. The inset shows the evolution with temperature of the anisotropy.

consensus about the physics of superconducting MgB_2. This is mainly due to the fact that in this compound (in contrast to most heavy fermions), detailed first-principle calculations of electron and phonon spectra, and of the electron-phonon interaction are possible, and lead to excellent agreement with experiments [128]. The origin for the peculiar properties of MgB_2 resides in its particular electronic structure, i.e. the charge carriers fall into two distinctive groups (see the FERMI surface in fig. 2.20): π-electrons, similar to those in graphite (here the π-bands form planar honeycomb tubular networks), and σ-electrons (on quasi-cylindrical FERMI surfaces) which represent the unusual case of covalent bands crossing the FERMI level. Only the latter group exhibits an anomalous strong interaction, and only with the phonons of sufficiently small wave vectors [128, 114]. This leads to several uncommon features, especially to a superconducting state characterized by two different order parameters (the large one being associated with the σ-band, the smaller with the π-band, as indicated in fig. 2.20). Current research on MgB_2 concerns the property changes (regarding H_{c2} and T_c) with Al and C doping [215, 7, 50].

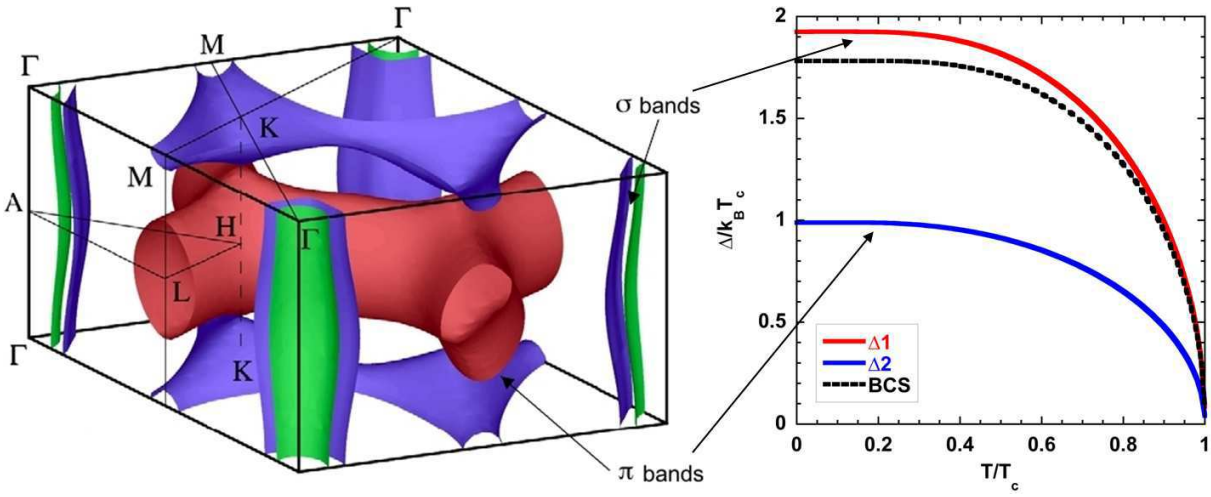

Figure 2.20. FERMI surface of MgB_2 [128]. The temperature dependence of the order parameter corresponding to the σ- and π-bands are plotted on the righthand side. For comparison, we also plot a BCS-type gap function for $T_c = 39$ K.

Multiband superconductivity is also experimentally established in other compounds, especially in the borocarbides [28, 183, 193, 137] and $NbSe_2$ [29]. In this thesis, we will show its relevance

for two heavy fermion compounds.

2.4. Aims of this work – Motivation

As already mentioned, the aim of our work was to have a closer look at the *superconducting* properties of two heavy fermion compounds, namely $PrOs_4Sb_{12}$ and $CeCoIn_5$.

$PrOs_4Sb_{12}$

In this compound – as we have just seen – the situation is rather complex according to various intriguing experimental results and their different corresponding interpretations. To be more precise, we were particularly interested in the *superconducting gap topology*, i.e. we wanted to check whether the gap has a nodal structure (whether $PrOs_4Sb_{12}$ is an *unconventional* superconductor), and if so, the aim is to determine the type of the nodes (point and/or line nodes) and the corresponding irreducible representation the order parameter symmetry belongs to. This is a quite ambitious objective, but it would definitely conclude one of the main controversies as to the superconducting phase of $PrOs_4Sb_{12}$, and eventually allow some further speculations on the pairing mechanism. At the beginning of this thesis, strong support for unconventional superconductivity came essentially from the specific heat double transition (but with hesitations on its *intrinsic* character!) and from angle-resolved thermal conductivity measurements under a rotated magnetic field down to about 350 mK [92]. In Grenoble, there is good experience in measuring thermal transport properties at very low temperatures ($T < 100$ mK) – the "reference-experiment" being the characterization of the different superconducting phases of the heavy fermion superconductor UPt_3 by thermal conductivity measurements ([189], [190] and [191]) - we decided to try to repeat this type of characterization on $PrOs_4Sb_{12}$. Indeed, the thermal conductivity constitutes an excellent probe of low energy excitations (quasiparticles) and of the superconducting gap: In the superconducting phase, as the Cooper pairs do not carry any entropy, the only contribution to the heat transport comes from phonons (often negligible at very low temperatures) and from thermally excited quasiparticles. Evidently, the presence of these excitations and therefore the thermal conductivity strongly depend on the superconducting gap. So, for conventional superconductors, thermal conductivity decreases exponentially when lowering temperature, reflecting a typical behavior of *thermal activation* because of the existing energy gap. In contrast, for unconventional superconductors with gap nodes on the Fermi surface, the thermodynamical properties completely change. In particular, a gap node allows very low energy excitations and, in general, the exponential behavior of the thermal conductivity is replaced by a power law behavior (its concrete parameters depend on the node type, line or point node). Specific heat measurements are also possible, but they are sensitive to all the excitations of the considered system (electronic, magnetic, local like CEF excitations, etc.), which makes the interpretation of the experiments much more complicated. In addition, another advantage of thermal transport is to be a *directional* probe, which can be very useful for the investigation of the anisotropy of the gap. The "weak" point of thermal conductivity is that its interpretation requires in addition the understanding of the scattering processes, for example between the electron quasiparticles and the impurities.

In practice, we had carried out successful preliminary thermal conductivity measurements on a bar shaped sample (same as used in ref. [92]) with three major outcomes:

- The fully characterized contacts for the thermometer thermalization on the sample can

eventually be improved.

- Sample quality did not allow any sophisticated conclusions on the gap topology from the very low temperature dependence of thermal transport in zero field.
- The low temperature field dependence of thermal conductivity is reminiscent of the case of MgB_2 [186], possibly confirming a multiband superconductivity scenario, suggested previously to explain the slight positive curvature in the low field region of $H_{c2}(T)$ [130].

So the aim for the thesis period was rapidly fixed: make a new thermal conductivity study on $PrOs_4Sb_{12}$ with

- a sample of better crystal quality (additional question: consequences on specific heat double transition?),
- improved thermalization contacts (including their complete characterization),

in order to

- confirm the low temperature field dependence (two-band superconductivity), and
- determine the gap topology from the temperature dependence of thermal transport for $T \ll T_c$.

Let me add that (heat) transport has another "advantage" compared to thermodynamic probes like specific heat measurements for studying multi-band superconductivity that is associated to electronic bands of different effective masses (as we will suppose in the heavy fermion case): thermal conductivity might have equal sensitivity to the different types of heat carriers[13], whereas specific heat will be dominated by the bands of heavier effective mass.

$CeCoIn_5$

The idea of measuring thermal transport properties in superconducting $CeCoIn_5$ is a direct consequence of our results on $PrOs_4Sb_{12}$. Due to the large spread of effective masses in $CeCoIn_5$ as described above (eventually similar to that in $PrOs_4Sb_{12}$), the possibility of important multi-band effects arises (and was already reported [149, 166]), so that we wanted to probe the sensitivity of low temperature thermal conductivity on small magnetic fields (compared to the field scale of H_{c2}), an investigation which had, to our knowledge, not been carried out before. Besides, recent reports on thermal transport in $CeCoIn_5$ [201, 94] are quite controversy, so that we wanted to perform our own measurements on the previously optimized and well-characterized experimental setup. Eventually, such kind of study could contribute to elucidate the still open questions and experimental discrepancies on the superconducting phase of $CeCoIn_5$ mentioned in a previous section.

The plan of the following chapters is as follows: First, I will explain the essential of our experimental techniques, emphasizing the characterization of contact resistances, before exposing our main thermal transport results on $PrOs_4Sb_{12}$ and $CeCoIn_5$, concluded by some critical remarks and perspectives.

[13] In a simple picture, the effect of high masses will be compensated by low FERMI velocities and vice versa.

3. Experimental Techniques

In this chapter, I will give a brief description of the different methods and techniques we developed and used during the PhD period. From low temperatures as a starting point, focus will be set on the procedures of reliable transport property measurements (thermal and electric conductivity), including the characterization of the thermometer thermalization contact resistances. This last point represents an original part of this work, since the quantitative *thermal* characterization of contact resistances has been rarely addressed till now.

3.1. Experimental environment: low temperatures and cryogenics

All the measurements presented in this thesis were performed on a standard ^{3}He/^{4}He dilution refrigerator[1]. Its effective, experimentally exploitable temperature range spans from about 7 mK up to 6 K, the integrated (superconducting) magnet being able to generate magnetic fields up to about 8 T. Due to the *continuous* cooling power (yielding a very high temperature stability), even sophisticated and time-consuming very low temperature thermal conductivity measurements were possible: down to 10 mK without field, and down to about 50 mK under a magnetic field up to 7 T.

When working in vicinity of the absolute zero, measuring temperature becomes an important, non-trivial issue. Skipping further details (see [189]), I only want to mention that we used a standard germanium thermometer (doped semiconductor resistance thermometer which exhibits very reproducible calibrations with thermal cycling) placed in the zero field compensated region of the magnet, against which we could calibrate all the other thermometers at every magnetic field and in the most common temperature range, i.e. from 100 mK to 6 K. For temperature measurements below 100 mK, we used a standard *Matshushita* carbon resistance thermometer (also placed in the zero field compensated region) calibrated at each run in zero field against a paramagnetic CMN salt and the Ge thermometer.

3.2. Experimental methods: principles, setup realization and measurement procedures

Preliminary remark on the different investigated setups/samples

After several preliminary, more or less successful tests we finally realized a reliable thermal conductivity setup, suitable for measurements at very low temperatures. This setup design was used during the whole PhD period, with some minor modifications according to each investigated sample (changes on the contact sample-fridge, field orientation, etc.). At the beginning of the corresponding chapters, the samples will be presented in more detail – at this stage, I only want to mention the following points in order to avoid any confusion: on the $PrOs_4Sb_{12}$ compound,

[1] see for exemple [53], chapter 11 or [156], chapter 7 for some more details on dilution refrigerators

we analyzed two samples of different batches, the first one of Prof. Sugawara's group (labeled A or #02.03.11), and the second one from G. Lapertot (labeled B2 or LAP#0262pl). Concerning $CeCoIn_5$, the analyzed sample also comes from G. Lapertot's group, namely from D. Aoki (labeled C2 or #LAPplaqbar2).

3.2.1. Thermal conductivity

Principles

Basically, the setup for measuring thermal and electric conductivity, κ and σ, corresponds to the standard two-thermometers-one-heater setup for steady-state measurements ([79, 189, 28]): one creates a well-defined heat-flow through a sample of given geometry and then measures the resulting temperature gradient between two points. κ is extracted from:

$$\kappa = \frac{l}{S}\frac{P}{\Delta T} \ , \tag{3.1}$$

where l is the distance between two points on the sample between which the temperature gradient ΔT is measured, and P the applied heating power (or heat flux $\dot{q}$) flowing through the sample's section S (supposed to be constant over l). In practice, at very low temperatures, a large variety of problems, especially those related to deficient thermal contacts on the setup (as will be detailed further on), may arise requiring some caution.

Setup realization and optimization

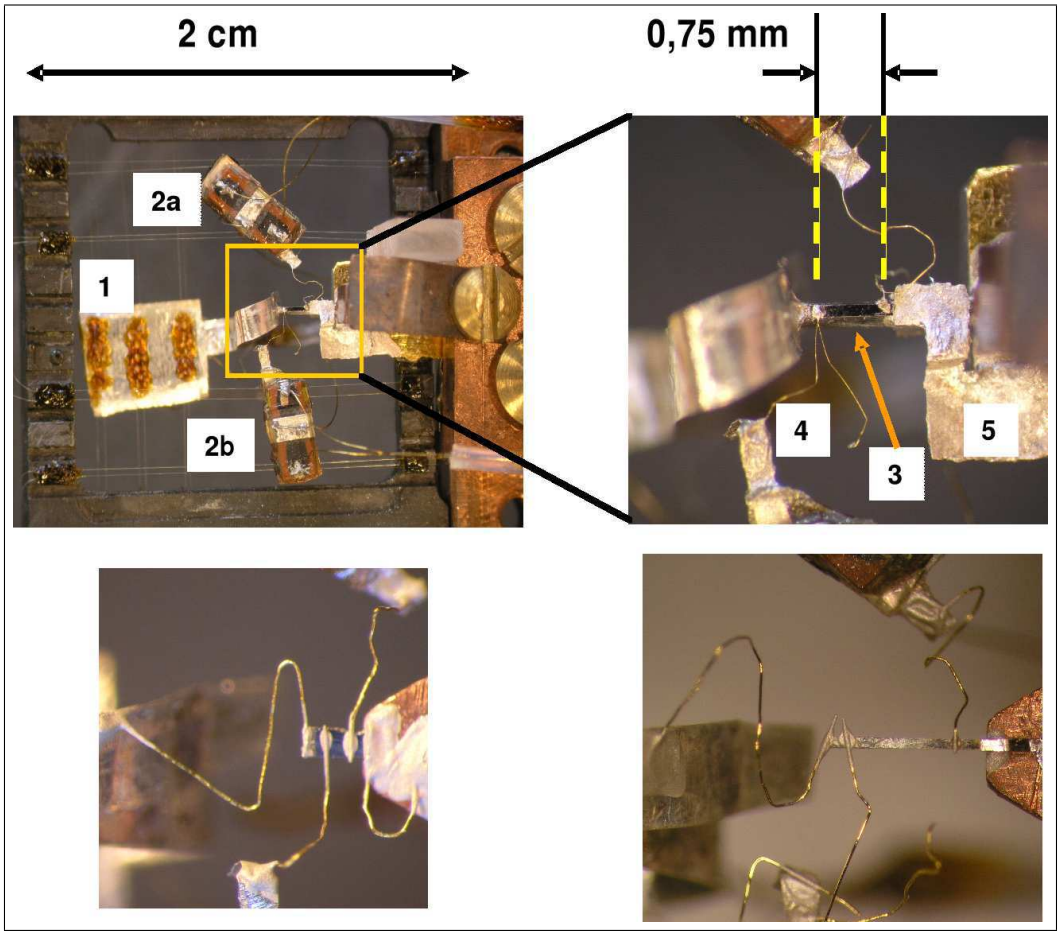

Figure 3.1. Pictures of the experimental setup. **(a)** top left: general overview 1: heater, 2a: cold thermometer, 2b: warm thermometer. In addition, one can see the 17 µm kevlar fibers, glued on the vespel frame and holding the thermometers and the heater. **(b)** top right: zoom on the first $PrOs_4Sb_{12}$ sample (3), labeled A. 4: 17 µm (diameter) gold wire connecting the sample to the warm thermometer, 5: Ag film acting as thermal short-circuit of R_{sc}^{th}. **(c)** bottom left: zoom on the second $PrOs_4Sb_{12}$ sample, labeled B2. **(d)** bottom right: zoom on the $CeCoIn_5$ sample C2. In the two latter cases, the samples are connected to the Ag film of the heater by an intermediate gold wire (diameter 38 µm), like the thermometers. In addition, the contact to the fridge is realized by a supplementary Cu platelet.

Figure 3.1 contains a picture of our experimental setup. At one end, the (generally) bar shaped sample is fixed to the cryostat, while at the other, it is related to the heater (a PtW alloy strain gauge heater, whose resistance R_{heater} is constant at low temperatures). On each side of the sample, there is one thermometer, connected to the sample by a gold wire (diameter 17 or 38 µm). The thermometers are standard *Matshushita* carbon resistance thermometers[2]. Further, we used NbTi superconducting wires ($T_c \approx 9$ K, in a CuNi matrix, diameter 70 µm) for

[2] These thermometers exhibit a good sensitivity over the whole investigated temperature range. However, the pay off of this sensitivity are important changes of calibration under magnetic field and thermal cycling [156].

the electric connections of the heater and the thermometers in order to limit the heat losses[3]. Our setup makes it possible to measure also the electric resistivity of the sample with a standard 4 point technique, exactly with the same geometric factor as the thermal conductivity (the current contacts are situated on the heater and the fridge, the voltage contacts on the thermometers). The two thermometers and the heater are hold by very tiny kevlar fibers (diameter 17 µm) glued on the vespel frame.

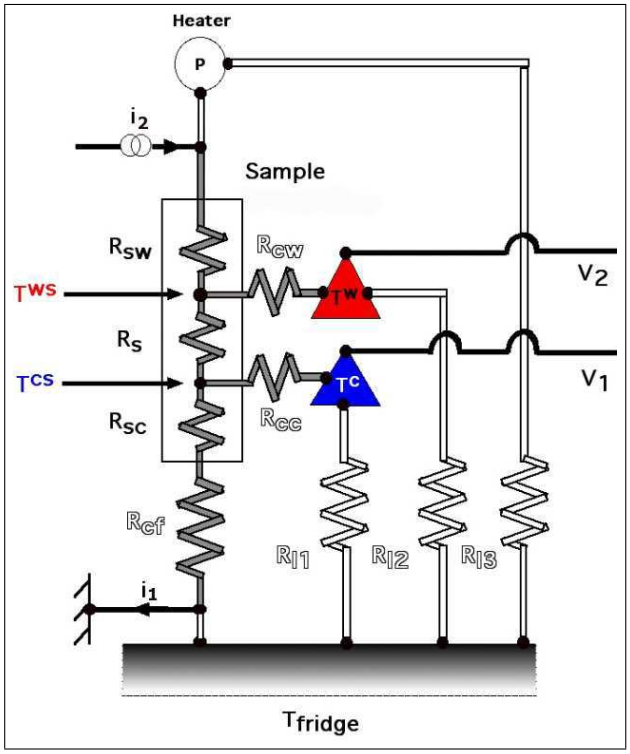

Figure 3.2. Schematic view of the setup (see the text for the explanation of the used symbols). The thermal circuit is not colored (white), the electric circuit is black - the part which is common to both circuits is colored in grey.

Now let's take a more schematic view of our setup, as shown in fig. 3.2. All the relevant resistances are listed below:

- R_{cf} : contact resistance sample-fridge
- R_{sc} : resistance representing the cold part of the sample
- R_s : resistance representing the part of the sample we are really interested in
- R_{sw} : resistance representing the warm part of the sample
- the contact resistance sample-heater is not as crucial as the others on our thermal circuit, that's why I omitted it on figure 3.2.

[3] More details on the thermal conductivity of NbTi at low temperatures can be found for exemple in [144] or [172].

- R_{cc} : contact resistance sample-gold wire, connecting the cold thermometer
- R_{cw} : contact resistance sample-gold wire, connecting the warm thermometer
- R_{l1}, R_{l2} and R_{l3}: resistances (heat leaks) cold/warm thermometer-fridge and heater-fridge respectively
- T^c, T^w : temperatures measured by the cold and warm thermometer respectively
- T^{cs}, T^{ws} : sample temperatures as indicated

In order to achieve reliable thermal conductivity measurements at very low temperatures, the thermal circuit with all its components has to be optimized, which means:

1. **Maximizing the heat leak resistances**

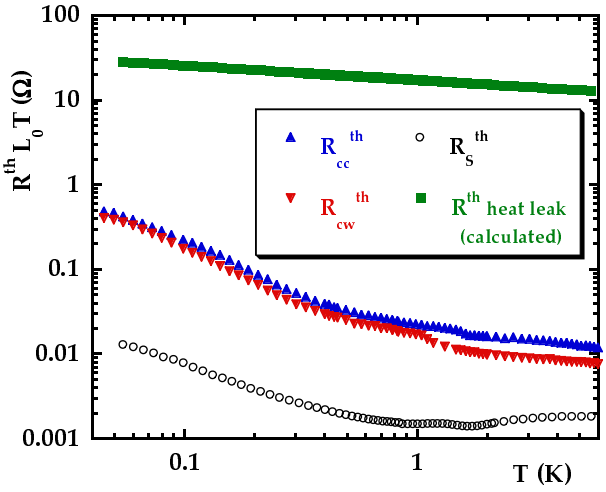

Figure 3.3. Comparison of the thermal resistance (converted in ohms via the Wiedemann–Franz law) of the kevlar fibers (calculated according to [161]) and the resistance of the first $PrOs_4Sb_{12}$ sample (data from our experiments). In addition, we plotted the thermal resistances of the thermometer contacts, R^{th}_{cc} and R^{th}_{cw}. Both the contact resistances and the thermal resistance of the sample are much smaller than the thermal resistance of the kevlar fibers.

As there is no way to measure a heat current in a direct manner, we assume in (3.1) that the whole power P generated by the heater ($P = R_{\text{heater}} \cdot i^2$, where i is the current passing through the heater resistance R_{heater}) will pass through the sample. If we want this to be a good approximation, we must minimize the leak heat currents and thus have

$$R_{l1}, R_{l2}, R_{l3} \gg R_{sw} + R_s + R_{sc} + R_{cf}{}^4. \tag{3.2}$$

The heat leaks are coming from the suspension of the thermometers and the heater, and from the NbTi wires. As in the electric case, the thermal resistance R^{th} of any (well-defined) object is obtained from its thermal conductivity κ via

$$R^{th} = \frac{1}{\kappa}\frac{l}{S} \tag{3.3}$$

(l/S is the geometric factor, as introduced in equation 3.1). Hence, it is obvious that one needs a suspension material with a low thermal conductivity and a small section. Both

[4] To be correct, one has to add the contact resistance between the heater and the sample, not explicitely mentioned on fig. 3.2, otherwise the heat flow might directly pass through R_{l3} and not through the sample.

conditions are fulfilled by the kevlar fibers we used (best ratio mechanical rigidity to low thermal conductivity). Figure 3.3 shows the measured thermal resistance of the sample R_S^{th} in comparison with the heat leak resistances R_{l1} and R_{l2} (calculated[5] thermal resistance of the kevlar fibers supporting the thermometers - the glue contacts and the vespel frame can be neglected). We see that condition (3.2) is certainly valid (at least for R_s and the other two parts of the sample R_{sc} and R_{sw}, which are smaller than the middle part), the ratio of both resistances being of several orders of magnitude over the whole temperature range (most of all, it is the small section of the fibers which leads to such high values for R_{l1} and R_{l2}).

2. **Minimizing the thermal resistance between the sample and the fridge**
There are three reasons for doing this:

   (i) **Reducing the heat leak**
   As already mentioned above, the heat leak currents through R_{l1}, R_{l2} and R_{l3} have to be as small as possible, yielding condition (3.2). This implies to make R_{sc} and R_{cf} as small as possible, so that the heat current will pass through the sample and not through the heat leak resistances.

   (ii) **Reducing the limitation in temperature**
   As we have seen above, a heat current through a thermal resistance always implies a temperature gradient. Thus, when the applied heat current passes R_{sw}, R_s, R_{sc} and R_{cf}, inevitably, the mean sample temperature will be higher than that of the fridge, i.e.

$$T^{cs} > T_{fridge}. \tag{3.4}$$

   At very low temperatures, equation (3.4) still holds even when there is no heating power applied because of the permanent presence of a parasite heating power, as small as it may be. In practice, this means that the measurements at lowest temperatures are not only limited in temperature by the temperature minimum of the mixing chamber, but also by the temperature elevation due to heat currents passing through R_{sc} and R_{cf} (for our first $PrOs_4Sb_{12}$ sample, at low temperatures, a parasite heating power of 32 pW is enough to raise its temperature from 7 mK to 25 mK). Thus one needs to control the resistances R_{sc} and R_{cf} in order to reach the lowest temperatures. This is not only true for parasite heating powers. R_{sc} and R_{cf} also determine the temperature minimum in the κ measurements due to the heating power P applied to create a temperature gradient on the sample: P also implies a temperature elevation of T^c (compared to T_{fridge}) of the order of $P \cdot (R_{sc} + R_{cf})$. If $R_{sc} + R_{cf} \gg R_s$, this becomes dominant, and a choice will have to be made between the minimum temperature for the κ measurements and the precision of the data points (size of the thermal gradient).

   (iii) **Simplifying the temperature regulation**
   This argument concerns the regulation of temperature. In general, there is no difficulty to regulate temperature on the mixing chamber of a dilution refrigerator. For thermal conductivity measurements it turns out (for reasons that I will explain

[5] Ref. [161] contains analytical expressions of the thermal conductivity at very low temperatures of different polymers (kevlar, vespel, etc.).

later) to be necessary to regulate temperature on the cold thermometer. In this configuration, regulation becomes much more difficult, again especially at very low temperatures, because of the strongly increasing (diverging) time constants. In the case of a big difference between T_{fridge} and T^c (i.e. R_{sc} and R_{cf} not minimized), temperature regulation becomes nearly impossible, at least if the measuring student does not dispose of an infinite time interval for doing his job...

3. **Minimizing the contact resistances between the sample and the gold wires connecting the thermometers**

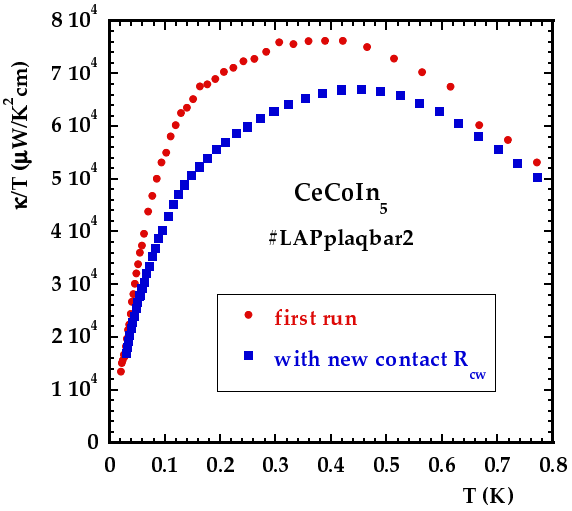

Figure 3.4. Comparison of two κ scans of the same $CeCoIn_5$ sample. During the first scan, a bad thermalization contact (high R_{cw}) led to an overestimation of κ (underestimated ΔT in the region of extremely high κ.

Besides the power P, the temperature gradient on the sample ΔT is the main ingredient of equation (3.1). In practice, what is measured are T^c and T^w, the temperatures of the thermometers. If the thermal resistance of the heat leaks (R_{l1} and R_{l2}) is not large enough, a heat current will flow through the contact resistance of the thermometers (R_{cc} and R_{cw}), leading to sample temperatures T^{cs} and T^{ws} different from (larger than) T^c and T^w. So, if we want $\Delta T = T^c - T^w$ to be a good approximation, we have to minimize the temperature gradient related to R_{cc} and R_{cw} (in analogy to the voltage gradient upon a resistance in an electric circuit). This means via $\Delta T = R^{th}\dot{q}$ minimizing the contact resistances R_{cc} and R_{cw}, and maximizing R_{l1} and R_{l2}, as described above (analogy to a voltage divider). This point will be addressed in more detail in the section about contact resistances. At this stage, I only want to give a qualitative example illustrating the importance of a good thermometer thermalization and its influence on κ measurements. Figure 3.4 compares two scans of the thermal conductivity of a $CeCoIn_5$ sample. The only modification between the two scans concerns the contact R_{cw}, which has been improved (renewed) for the second scan. In the temperature range from 0.1 to 0.5 K, the discrepancy in κ/T is rather striking, and can not be explained for example by different geometric factors. In fact, in this temperature range, $CeCoIn_5$ is a very good *thermal* conductor, so that a considerable heating power (250 nW) is needed to create a detectable temperature gradient between T^c and T^w, yielding a large temperature gradient between T^c and the fridge, essentially due to the contact resistance between the sample and the fridge, R_{cf} (as detailed in the paragraph above), where $R_{cf} \gg R_s$. Typically, when the setup thermometers differ of several mK at 400 mK, the fridge temperature is of about 250 mK only. This situation

favors inevitably heat leak currents through the thermometers towards for example the vespel frame via the kevlar fibers. In this case, if the contact resistance R_{cw}^{th} has not been correctly minimized, the thermometer will measure a lower temperature, i.e. $T^w < T^{ws}$, and the resulting κ value will be enhanced compared to the true value. This is very likely the case for the first scan in figure 3.4. Even if the test conditions may seem particularly severe in the considered example (note that in the temperature ranges with lower κ/T both setups yield equivalent results), it illustrates in an impressive manner the importance of a good thermometer thermalization, and hence the need for its characterization (following in the next section).

4. **Maximizing the geometric factor $\frac{l}{S}$**
For high-κ samples (small R_s^{th}), a considerable heating power P is necessary to obtain the appropriate[6] temperature gradient ΔT. As shown above, elevated heating powers can have undesired effects such as the increase of the achievable low temperature limit. Hence, from equation 3.3, it is obvious that $\frac{l}{S}$ has to be as big as possible in order to obtain a high R_s^{th} (compared to the contact resistance R_{cf}) and hence a high ΔT (for a given P). In practice, this means to prefer long bar shaped samples with a small section S.

Experimental procedure

Having optimized as much as we could the components of our setup, I will now sketch the main steps of the procedure of measuring thermal conductivity. Again, we start from equation (3.1). The precision of κ measurements depends essentially on the precision of the temperature gradient[7] ΔT. This represents a great experimental challenge as it is not possible to measure the temperature gradient ΔT directly, but only the difference of two absolute temperatures T^c and T^w. That is the reason why some precautions have to be taken:

(a) **Calibration errors**
In order to avoid calibration errors (of the order of 0.1%, see also the "Experimental Techniques" chapter of [189]) of the thermometers, we measure them for each point of κ *with* and *without*[8] applied heating power P. Equation (3.1) then becomes

$$\kappa = \frac{l}{S} \frac{P}{(T^w - T^c)_{P\neq 0} - (T^w - T^c)_{P=0}}. \tag{3.5}$$

Furthermore, one has to take into account that the calibration errors are strongly temperature dependant, which can make equation (3.5) meaningless in the case where $R_{sc}, R_{cf} > R_s$ (the mean temperature of the sample with applied heating power would be higher than without applied heating power where $T^c, T^w \approx T_{fridge}$). Now, the key point is not to regulate temperature on the fridge, but on one of the two thermometers, let us say the cold one, T^c. That way, we have $T^c(P = 0) = T^c(P \neq 0)$ and - that is the inevitable

[6] At low temperatures, measuring small temperature gradients with high accuracy is complex; to keep the level of precision satisfactory, the applied $\frac{\Delta T}{T}$ should not be less than a few percent – but not more, otherwise the linear approximation for calculating κ from $\frac{P}{\Delta T}$ is no longer valid for samples with a strong T-dependent thermal conductivity.

[7] As to the heating power P, the heater resistance and the heating current can be determined more easily and with more accuracy than the ΔT.

[8] Note that the data taken without heating power are used for the posterior thermometer calibration.

drawback - an enhanced measuring time because it is much more difficult to regulate on a thermometer which is not directly coupled to the mixing chamber (where the heating power for regulation is injected) and because conditions for temperature regulation change with and without applied heating power.

(b) **Drift errors**
Drift errors have to be avoided, too. In order to achieve this, the two thermometers are measured simultaneously by two independent boards on the same electronics (an automatic bridge, called TRMC2 and developed by the electronics department of the laboratory) without any interruption of the regulation process on T^c (the precision of the control temperature is of at least 0.03%). The time derivation of the temperature gradient ΔT is also measured over a period of 30 s (or of a few minutes at very low temperatures if necessary). Finally, a point of κ is validated only when its drift is less than 0.1% of the expected ΔT.

(c) **Large time constants**
Drifts mostly appear under magnetic field and at low temperatures (especially when coming from higher temperatures), due to creeping relaxation phenomena in the thermometers and the sample. A proper equilibrium state (i.e. correct temperature gradient ΔT) can then easily take several hours to establish. In addition, such large time constants make the normal process of temperature regulation extremely time-consuming, or simply impossible (one observes a sort of *decoupling* of the regulation thermometer from the mixing chamber on the fridge), so that the only way out is to regulate on the fridge thermometer (and not on the cold thermometer). Again to avoid calibration errors, the analyzed part of the sample has to be at the same temperature without and with heating power, which means readjusting the regulation (fridge) temperature between the two steps of each κ point. Nevertheless, reliable measurements can be achieved under such severe conditions by introducing a suitable *waiting period* before verifying the ΔT as described just above in 3.2.1. This waiting period is essential for a real steady-state measurement of the temperature gradient. Even in this operating mode, and under extreme conditions (near the temperature minimum and under strong fields), the very slow relaxation processes require so long stabilization periods that it becomes difficult to complete one single κ data point between two successive helium and nitrogen transfers (which inevitably disturb the temperature regulation[9]. Generally, one can state that strong relaxation phenomena inducing large time constants constitute one of the main limiting factors of our experimental technique.

The typical thermal history of a κ measurement is illustrated in figure 3.5. The temperature gradient ΔT is always measured twice , with and without heating power[10] P (as explained above to reduce the calibration errors). The data collected at $P = 0$ are also used for the a posteriori calibration of the setup thermometers. Typical order of magnitudes are 1.5 to 4% for the applied $\Delta T/T$ on the sample, 0.1% for the required precision of the ΔT and a few minutes to several hours for the waiting and stabilization periods, depending on the temperature and field range.

[9] About every 24 hours, the helium and nitrogen reservoirs of the dilution fridge have to be filled, leading to some vibrations and thus power dissipation on the setup, rising its temperature up to at least 100 mK. In order to improve this situation, we modified the filling mechanism for the liquid nitrogen reservoir (installation of supplementary absorber and vapor-liquid separator), so that the setup temperature reached only about 30 mK during the transfers, but even this is a quite high temperature level when measuring near the temperature minimum...

[10] the chronological order depends on the regulation method

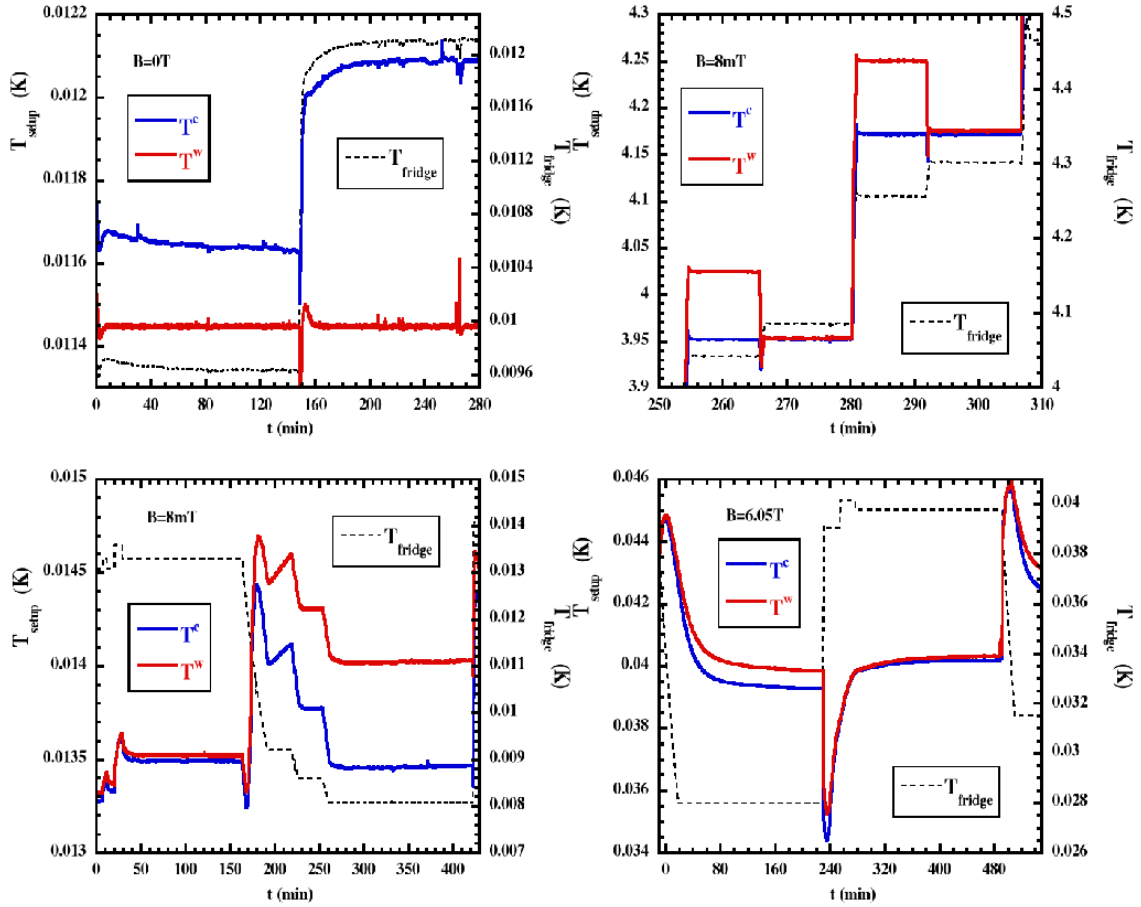

Figure 3.5. Monitoring of the two setup and the fridge thermometers (separated temperature axis) during a typical thermal conductivity measurement (stabilization period *with* and *without* heating power). The four "screenshots" illustrate the different techniques for temperature regulation : regulating on T^w(top, left), on T^c(top, right) and on the fridge thermometer with readjustment in order to keep T^c constant (bottom). Note the different temperature, time and field scales.

Altogether, computer control plays a key role in the experiment, and is of great support to the experimentalist when applying a magnetic field for measuring $\kappa(H)$, since the described method then rapidly becomes complicated and time consuming: because of the magnetoresistance of the carbon thermometers ($\Delta R(3\text{ T})/R(0\text{ T})$ at 100 mK is of about 3%, which roughly corresponds to a $\Delta T/T$ of 4%) preliminary calibrations have to be done. In order to determine κ at the wished fields H_i and the regulation temperature $T(=\text{const})$, the resistances of the two thermometers have to be measured without applied heating power at these fields H_i and at two different temperatures, T and $T + \Delta T$ (ΔT has to be estimated in order to correspond to the sample's temperature with applied heating power and in order to be sufficiently large to permit the calculation of the slope $\Delta R/\Delta T$ with sufficient precision - in general, we took $\Delta T/T \approx 10\%$). For these calibrations, we regulate on the thermometers in the zero field compensated region. Afterwards, we use them to determine the appropriate regulation temperature on T^c under magnetic field and to have a reliable calibration of the thermometers under magnetic field.

This procedure simplifies a lot when regulating on the fridge (first without and then with heating power and readjustment of the fridge temperature in order to get the same temperature on T^c than without P). That way, no preliminary calibration of the sample thermometers is necessary, only a simple calibration point at $T + \Delta T$ for each H_i, as described above. For our field scans $\kappa(H)$ on $CeCoIn_5$ we exclusively used this last method for its simplicity and because of the large relaxation rates under field and at low temperatures (see above).

Before closing this part, I want to mention that during the measurements on $CeCoIn_5$, we (experimentalists) were not only supported by the computer control of the whole measurement procedure, but also by the remote control software "Timbuktu Pro", which allowed us to check (and even modify!) what was going on the experimental setup from our home computers. Together with the (nearly) automatic nitrogen and helium transfers, it contributed to reduce and organize better the control missions to the lab on week-ends, etc.

3.2.2. Electric conductivity

In this paragraph, just a few words about the (simple) principle of *electric* conductivity measurement. As already mentioned, no modification for that is necessary on the setup itself. It constitutes a direct measurement of the sample's electric resistance (same geometrical factor in order to calculate the electric resistivity as for thermal conductivity). The principle is as follows: an alternative current (frequency range: 10 to 70 Hz) is injected in the sample, and the corresponding voltage drop is measured with a low-noise preamplifier and a standard lock-in technique. The only (minor) difficulty with highly conductive (metallic) samples (which means measuring a very small voltage drop) is to obtain a good signal to noise ratio without self-heating of the sample. In our case, typical injected currents at the lowest temperatures were about several μA for resistances of some μΩ, and we averaged the lock-in output signal for about half a minute. By computer control, the current was automatically adapted to the control temperature.

3.2.3. Electric and thermal contact resistance

Technique

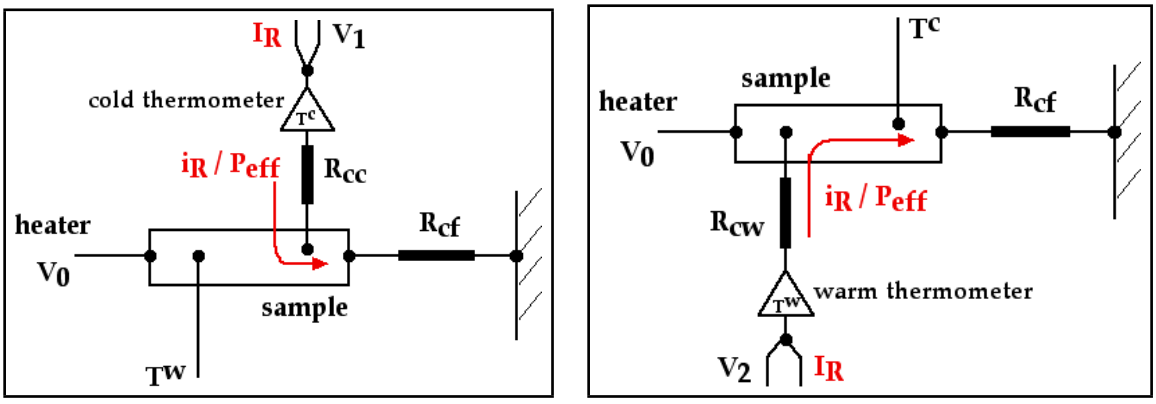

(a) Configuration for measuring R_{cc}. **(b)** Configuration for measuring R_{cw}.

Figure 3.6. Schematic view of the thermal conductivity setup in the configuration for contact resistance measurements. As indicated in the text, for the *electric* contact resistance experiment, the voltage and current connections are simply crosschanged compared to the resistivity measurement (see fig. 3.2): the current is injected with the lead labeled I_R on each figure (voltage leads for the resistivity measurement), and grounded by the fridge. The voltage drop is measured between the same lead V_1 (for R_{cc}) or V_2 (for R_{cw}) and the heater (label V_0, normally used for current injection). In the case of the *thermal* measurement, JOULE heating with an enhanced current i_R creates a heat flux P_{eff} in the contact resistance itself, which is evacuated by the sample and the fridge. The temperature gradient is measured as usual with both thermometers, see text.

Measurements with our experimental setup are not limited to the thermal and electric resistance of the sample. It also allows the quantitative characterization of the electric and thermal contact resistances between the sample and the setup thermometers, i.e. R_{cc} and R_{cw}, and of the thermal resistance towards the fridge[11], i.e. R^{th}_{cf}. As already mentioned, these resistances (especially R_{cc} and R_{cw}) play a key role in order to achieve reliable thermal conductivity measurements, which means they have to be controlled very carefully. Actually, this is rarely done in practice, especially as to the *thermal* contact resistances: to our knowledge, there is no publication treating that issue in detail and reporting *direct* measurements. For that purpose, we have added wires and connections which allow to send an electric current in one of the two superconducting voltage leads (and back through ground), while still measuring the voltage on that lead, and on the lead connected to the heater[12] (used as current lead to measure sample resistance), see also figures 3.6 and 3.2. The corresponding (measured) voltage drop is dominated by the contact resistance between the sample and the gold wire towards the thermometer (see fig. 3.12), as will be justified in the next section ("Examples and Details"). Finally, we succeeded to adapt our setup for measuring *in situ* the following resistances:

[11] More precisely, the experimentally accessible quantity includes the contribution of the "cold part" of the sample, R^{th}_{sc}, see fig. 3.2.

[12] Reminder: both thermometers and the heater are connected to the sample by gold wires, used for both electric and thermal contacts.

- **Thermometer – sample electric resistance** R^{el}_{cc} and R^{el}_{cw} by crosschanging the resistivity voltage and current connections for each contact, so that (with i_R the injected current for the measurement of the electric contact resistance, see fig. 3.6 vor the notations of the voltage connectors, same as in fig. 3.2)

$$R^{el}_{cc} = \frac{\mathrm{v}_1 - \mathrm{v}_0}{i_R},\ i_R \text{ injected in contact } \mathrm{v}_1 \tag{3.6}$$

$$R^{el}_{cw} = \frac{\mathrm{v}_2 - \mathrm{v}_0}{i_R},\ i_R \text{ injected in contact } \mathrm{v}_2 \tag{3.7}$$

  In all other respects, the same remarks as for the electric resistivity measurements apply, except that typical R^{el}_c values at low temperatures are 10 to 50 mΩ.

- **Thermometer – sample thermal resistance** R^{th}_{cc} and R^{th}_{cw} by measuring the temperature difference between the two setup thermometers[13] when R^{el}_{cc} / R^{el}_{cw} are measured with an enhanced current i_R, so that the JOULE heating and the corresponding temperature gradient upon R_{cc} / R_{cw} lead to a detectable temperature elevation in T^c / T^w. Up to now, we defined the thermal resistance as follows: $R^{th} = \frac{\Delta T}{P}$ with $P = R \cdot i^2$. This relation is exact for our thermal conductivity measurements, where the heat current is generated outside the sample (external electric circuit with $P = R_{ch} \cdot i^2_{ch}$ in the PtW resistance heater). In the case of the thermal contact resistances, this picture has to be (slightly) modified since the heat is now produced by JOULE heating of the contact itself. As a result [78], the *effective* (i.e. responsible for the temperature gradient ΔT) heat current (which varies inside the contact) equals

$$P_{\text{eff}} = \frac{1}{2} R^{el}_{cc \text{ or } cw} \cdot i^2_R\ , \tag{3.8}$$

  which means that our above definition for R^{th} underestimates by a factor 2 the thermal resistance value supposing a constant, homogeneous heat current. Instead, we have:

$$R^{th}_{cc} = \frac{(T^c - T^w)_{P\neq 0} - (T^c - T^w)_{P=0}}{P_{\text{eff}}} \tag{3.9}$$

$$R^{th}_{cw} \approx \frac{(T^w - T^c)_{P\neq 0} - (T^w - T^c)_{P=0}}{P_{\text{eff}}} \qquad (\text{for} \qquad R^{th}_{cw} \gg R^{th}_s) \tag{3.10}$$

  In the case of R^{th}_{cw}, $T^c - T^w$ measures not only the temperature gradient due to the contact, R^{th}_{cw}, but also that related to the sample, R^{th}_s, which has to be subtracted (known from κ measurements) if it is not negligible compared to R^{th}_{cw}.
  The practical procedure is similar to that of ordinary κ measurements (same computer control program, regulation method, etc.), the major difference being only the heat current source.

- **Sample-fridge thermal resistance** $R^{th}_{cf} + R^{th}_{sc}$ ("automatically" obtained by thermal conductivity measurements[14])

$$R^{th}_{cf} + R^{th}_{sc} \equiv \frac{T^{P=0}_{\text{fridge}} - T^{P\neq 0}_{\text{fridge}}}{P\left(= R_{ch} \cdot i^2_{ch}\right)} \text{ for } \left(T^{P=0}_{\text{fridge}} - T^{P\neq 0}_{\text{fridge}}\right) \ll T^{P=0}_{\text{fridge}}, T^{P\neq 0}_{\text{fridge}} \tag{3.11}$$

[13] In the same manner as for the thermal conductivity, one has to be aware of calibration errors. The easiest way to do so is again to subtract the temperature gradient without applied heating power, see equation (3.5).

[14] The following formula is precisely valid when regulating on T^c, for the other regulation modes, it has to be slightly modified.

In the case of simple geometries (bar shaped samples, platelets, etc.), the factor l/S of R_{sc} is easily known, so that R_{cf}^{th} can be separated in a precise manner from the measured quantity.
As already mentioned, all the necessary data are collected during the ordinary κ scans, so that in practice the determination of R_{cf}^{th} is only of a matter of data analysis.

Examples and Details

Now, all the relevant quantities of the setup being available experimentally, I will give an example of how the measurements helped us to improve the contacts between the sample and the thermometer thermalization. The broad utility of controlling contact resistances will become further evident in the next section where we will analyze how to validate the thermal conductivity setup.

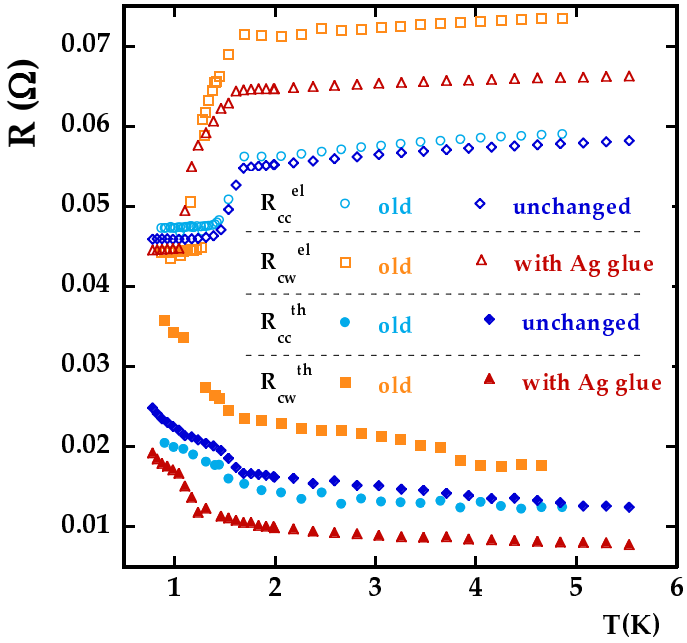

Figure 3.7. Illustration of the effect of adding some silver glue on the contact sample-warm thermometer R_{cw}. Plotted are the electric and thermal resistances (the values of the latter were converted via the WIEDEMANN-FRANZ law to facilitate the comparison) of both contacts, R_{cc} and R_{cw}. After the addition of silver glue on R_{cw}, one observes quite unchanged results on R_{cc}, proving the reproducibility of the experiment, and that the thermal resistance R_{cw}^{th} has been strongly reduced (by a factor > 2), whereas the electric resistance R_{cw}^{el} is hardly affected by the supplementary Ag glue (reduced by about 15%).

Both (*cold* and *warm*) thermometers are well thermalized on thin silver foils, on which the gold wires coming from the sample are fixed with silver glue, as already described at the beginning of this chapter. At first, the contacts between gold wires and sample were made by microarc-soldering only, exhibiting a relatively high thermal resistance. Later, as we became aware of the fact that the heat transfer was mainly controlled by the phonons and not by the electrons (see next section), we decided to reinforce the contacts and to add a tiny drop of silver

glue on them[15]. The effect is more than significant: Figure 3.7 shows the electric and thermal contact resistances R_{cc} and R_{cw} before and after we added Ag glue on the *warm* contact. As expected, the contact resistances R_{cc} did not change whereas the electric contact resistance R_{cw}^{el} was improved (reduced) by about 15% and the thermal contact resistance R_{cw}^{th} by nearly 50% (at least in the "high" temperature range). The thermometers now seem to be much better coupled to the sample. Hence, for further setups, we gave up the microarc-soldering: the sample surface was etched with an ion gun and a thin gold film ($\sim$ 5000 Å) was evaporated on each contact area. Then, the gold wire was glued with silver paste.
Hence, thanks to the detailed contact analysis, we introduced an improved thermalization method, which now yields very reliable thermal conductivity measurements, as we will see in the next section.

So far, I did not mention that the measurement of R_{cc}^{el} (R_{cw}^{el}) does not only include the "real" contact resistance sample - gold wire (as shown in fig. 3.12), but also the resistance of the gold wire itself, the silver glue contact between the gold wire and the silver foil on the *cold* (*warm*) thermometer and eventually supplementary contributions from other connections or connectors, etc. (all these elements contribute to the measured voltage drop because the same connector (on the *cold* or *warm* thermometer) is used as current *and* voltage contact in this configuration of the setup). We measured at least the order of magnitude of these in separate experiments: the lowest R_{cc}^{el} we measured was about 13.5 mΩ (below T_c in $PrOs_4Sb_{12}$). Silver glue contacts between gold wires and silver foils exhibit typical resistances of about or less than 1 mΩ at low temperatures; the gold wires have a residual resistivity ratio (between 300 K and 2 K) of about 120, yielding a resistance of about 1.5 mΩ per cm (for a diameter of 38 µm). On the setup, the length of the gold wires between the sample and the thermometer is smaller than 5 mm, so that their typical contribution to R_{cc}^{el} will be below 1 mΩ at low temperatures. The largest parasitic contribution ($\sim$ 5 mΩ) comes from the connectors of the dispatching electric circuits. So the contact resistance gold wire - sample will finally be of the order of 8 mΩ or slightly below (for $R_{cc}^{el} = 13.5$ mΩ). In this specific case, the corrections are quite important, but for higher R_{cc}^{el} values (like obtained on $CeCoIn_5$ or on the first $PrOs_4Sb_{12}$ sample), we are dealing with minor corrections only. To be consistent, one has to take into account these corrections also for the determination of the *thermal* contact resistance gold wire - sample: in formula 3.9, the heating power has to be calculated with the revised R_{cc}^{el}, subtracting the 5 mΩ connector resistance which is behind the superconducting wires.

Another example illustrates the utility of controlling quantitatively $R_{cf}^{th} + R_{sc}^{th}$. In section 3.2, we already stated the necessity to keep these resistances as low as possible. How to minimize them in practice? For R_{sc}, minimization means to make the distance between the "cold" thermometer and fridge contact as small as possible. On the setup, this is not always easy to realize because of the fact that the sample has to be fixed correctly (i.e. well thermalized) to the fridge. In our case (first $PrOs_4Sb_{12}$ sample) the cold part of the sample is slightly longer ($\sim$ 1 mm) than the measured part. In terms of thermal resistance, this is unsuitable because at very low temperatures the superconducting sample exhibits a low thermal conductivity and thus R_{sc}^{th} gets very high. That is why we decided to short-circuit thermally this part of the sample by placing in parallel a small piece of silver foil (see the picture of the sample, figure 3.1). As to R_{cf}, it is materialized as follows: a small vespel point (diameter 0.5 mm) presses the sample on a gold

[15] We did not do this from the beginning because we wanted the contact surface on the sample to be as small as possible (maintenance of a correct geometry, otherwise the thermometers measure the mean value of a temperature distribution). This is in practice easier to achieve by micro-soldering than with difficult to dose glue drops.

film (which is thermalized with the mixing chamber of the fridge). In order to improve this contact, we added some silver glue between the sample and the gold film. Figure 3.8 shows the thermal resistance $R_{sc}^{th} + R_{cf}^{th}$ without and with the added silver film in comparison to the sample's thermal resistance R_s^{th}. Above 1 K, the influence of the short-circuit is evident (R_{sc}^{th} reduced of about 30%, if we assume that $R_{sc}^{th} \gg R_{cf}^{th}$). Below 1 K, the contact resistance R_{cf}^{th} becomes non-negligible in relation to R_{sc}^{th} and the influence of the silver film is therefore less obvious.

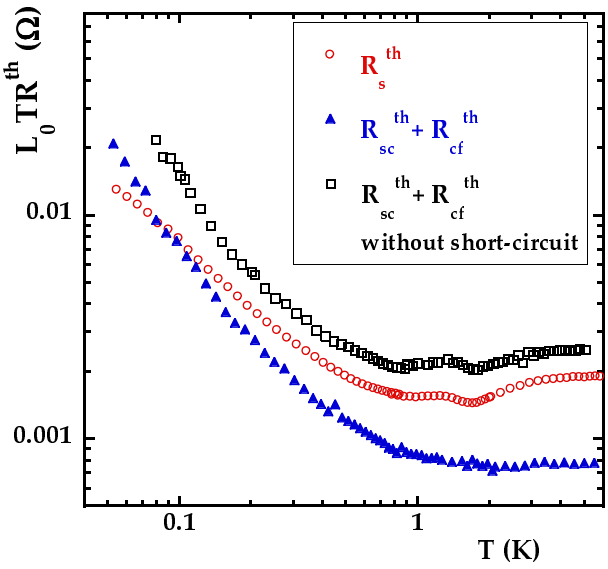

Figure 3.8. Temperature dependence at zero field of the thermal resistance of the cold part of the sample R_{sc}^{th} (first $PrOs_4Sb_{12}$ sample) before and after the addition of a silver film (acting as a sort of thermal short-circuit). Experimentally accessible is only the quantity $R_{sc}^{th} + R_{cf}^{th}$ (values converted via the WIEDEMANN - FRANZ law). In order to get an idea of the relevance of the thermal contact resistance R_{cf}^{th}, the thermal resistance of the sample R_s^{th} is also plotted. At "high" temperatures, the latter is the dominant contribution, and the resistance drop in R_{sc}^{th} due to the silver film is easy to observe. At lower temperatures the effect is less significant because of the increasing contribution of the contact itself.

Measuring the thermal contact resistances R_{cc}^{th} and R_{cw}^{th} was also very illuminating from another point of view: on our first experimental setups with $PrOs_4Sb_{12}$ the two thermometers saturated (without applied heating power) at relatively "high" temperatures of about 30 mK, whereas the fridge was at its minimum temperature. This is particularly intriguing because in previous experiments on UPt_3 samples in roughly the same setup configuration and on the same fridge (see [189], [190] and [191]), thermal conductivity measurements were possible down to 16 mK (and this limitation in temperature was due to the radioactivity of the samples and not to experimental problems). Another striking behavior of all our $PrOs_4Sb_{12}$ setups is that applying a small magnetic field ($B \ll B_{c2}$) is sufficient to reduce considerably the lower temperature limit. Again, this is particularly difficult to understand if one considers the thermal contacts sample-thermometers as being responsible for the limitation in temperature (thermal isolation of the thermometers at very low temperatures because of diverging contact resistances) since the contacts should exhibit a very small field dependence. To suggest that the limitation in temperature comes from a *parasite* heating power passing through R_{sc} and R_{cf}, as explained above, is another possible scenario. The field dependence could then be explained if the temperature gradient towards the fridge essentially comes from R_{sc} (strongly field dependent) and not from R_{cf} (supposed to be weakly field dependent). But the contrary seems to be the case, since the silver film we added on the cold part of the sample (see above) was not very efficient in reducing T_{limit}. Altogether, at this stage, there was no simple, conclusive explanation available for the "failure" of our experimental setup. Finally, it was the measurement of R_{cc}^{th} and R_{cw}^{th} without and under magnetic field that revealed new insights: the limitation in temperature of the setup

indeed comes from the thermal decoupling of the thermometers from the sample (diverging R_{cc}^{th} and R_{cw}^{th} in the low temperature limit), but under small magnetic fields, R_{cc}^{th} and R_{cw}^{th} remain nearly temperature independent at a much lower level, allowing reliable κ measurements near the temperature minimum (see figures of the next section). Of course, in a second step, the physical meaning of these unexpected experimental facts has to be addressed, which will be done in the next section and in the chapter on $PrOs_4Sb_{12}$, when analyzing the contact resistance data in more detail.

3.3. Validation of the experimental setup

In this section, I will explain how we checked the reliability of our thermal conductivity setup, and especially illustrate to which extend the joined analysis of electric and thermal contact resistance can contribute to accomplish this task.

3.3.1. Wiedemann–Franz law and thermal conductivity measurement

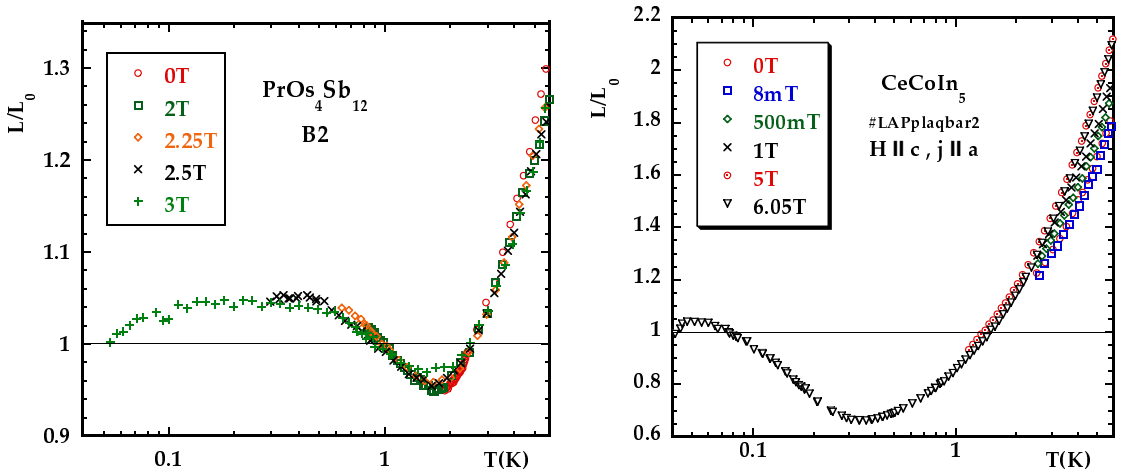

(a) $PrOs_4Sb_{12}$. **(b)** $CeCoIn_5$.

Figure 3.9. Lorenz ratio $L/L_0(T)$ at different magnetic fields in the normal phase. At very low temperatures (dominant elastic scattering, $B > B_{c2}(T)$), the Wiedemann–Franz law is verified.

A reliability check of every newly designed, or simply modified (change of the sample specimen, contacts, etc.) κ-setup should precede any sophisticated physical interpretation of the results. An easy way to find out whether an experimental setup measures the real physical quantity κ of a *metallic* sample or not, is to test whether it obeys the Wiedemann–Franz (WF) law [214], which states that electric conductivity and the electronic contribution to the thermal conductivity κ^{el} of metals are related by:

$$\frac{\kappa^{el}}{\sigma T} = L_0 \ , \tag{3.12}$$

where the Lorenz number L_0 is $L_0 \equiv \frac{1}{3}(\frac{\pi k_B}{e})^2 = 2.44 \times 10^{-8}$ W Ω K^{-2}. This stems from the fact that heat and charge transport in a metal involve essentially the same carriers, namely electrons. This law was first discovered empirically by Wiedemann and Franz [214], who showed

it to hold in a large range of metals at room temperature. Since then, numerous investigations have been undertaken, and nowadays, the WF law is expected to be valid for any system which supports heat and charge transport governed by mobile carriers of charge e and which experience strictly *elastic* scattering.

Back to the setup–validation, one simply has to check whether the experimentally determined quantities κ and σ verify condition (3.12). For this purpose, it is quite usual to plot the ratio $L/L_0(T,H)$ with $L = \frac{\kappa}{\sigma T}$ and to observe eventual deviations from unity. Evidently, recovering equation (3.12) can only be expected in its validity range, that is in the normal, non-superconducting phase and at lowest temperatures (where in general the electronic contribution κ^{el} largely dominates the phonon contribution κ^{ph} to κ and where κ and σ are mainly limited by elastic (impurity) scattering processes). This validity range is not always easy to access, especially for superconductors with a large upper critical field H_{c2}, where elaborate measurements both at low temperatures and under high magnetic fields are required. Otherwise, the test of the Wiedemann–Franz law can be accurate if the same contacts are used for the ρ and κ measurements: the problem of the precise determination of the geometrical factor is circumvented, so that it is possible to check the absolute value of the thermal measurement, considering the electric measurement much less susceptible to experimental errors.

We obtained a quite good agreement (within a few percent, see figure 3.9) with the Wiedemann–Franz law at very low temperatures and at magnetic fields $B > B_{c2}$ both for $CeCoIn_5$ and $PrOs_4Sb_{12}$. The figures are also shown in the corresponding chapters on $CeCoIn_5$ and $PrOs_4Sb_{12}$ and will be discussed in detail there. But roughly speaking, the "high" temperature excess thermal conductivity can be explained by the phonon contribution to κ, and at intermediate temperatures *inelastic* scattering leads to a L/L_0 ratio smaller than unity. The main outcome is that we recover the WF law in the low temperature limit, supporting a reliable thermal conductivity setup.

3.3.2. Wiedemann–Franz law and contact resistance measurement

Experimentally, a recovery of the WF law is not always achieved: for example, we had to give up some previous experimental setups with $PrOs_4Sb_{12}$ because we observed a notable violation of relation (3.12), probably due to serious contact and heat leak problems (see figure 3.10).

On more exotic systems, like the high-T_c superconductors (HTSC), the interpretation of an experimental violation of the Wiedemann–Franz law is less straightforward, since in such strongly correlated systems theory does not exclude deviations from the ordinary metal case, especially a possible excess heat conductivity is evoked [175]. Hill et al. [74] observed in optimally doped PCCO a strong downturn of κ below 0.3 K (at 13 T in the field-induced normal phase), and thus a substantial deviation from the Wiedemann–Franz law[16] – this behavior was attributed to a breakdown of the *Fermi* liquid regime... A similar downturn was reported on LSCO [140], but there the phenomenon appeared to be sample dependent, pointing to an extrinsic origin. More recent publications [22, 23] do not report such a low-temperature κ-downturn (at least in optimally doped BSCO), and it is widely believed that contact problems distorted the first measurements. On the same footing, analogous downturns on low temperature κ of $CeCoIn_5$ samples are reported in ref. [149], and ascribed to electron–phonon decoupling [185] in the thermalization contacts.

These *experimentally* observed violations of the *Wiedemann–Franz* law and their possible

[16] just to be complete: above 0.3 K, an excess heat conductivity ($L \simeq 2L_0$) was measured [74, 22]

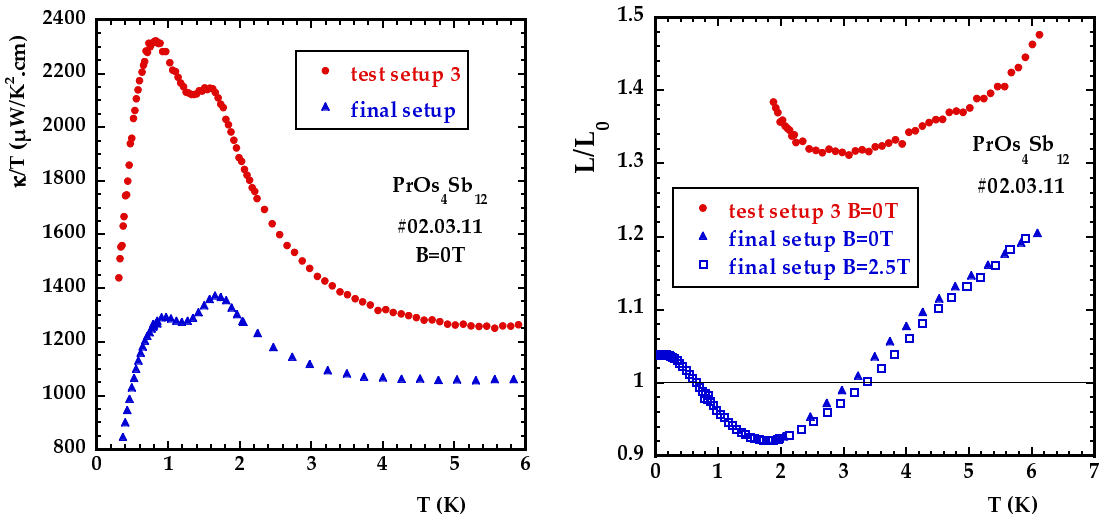

(a) Temperature scans of κ/T.

(b) LORENZ ratio $L/L_0(T)$ on both setups.

Figure 3.10. Comparison of thermal conductivity measurements at zero field on the experimental setup in its trial stage (test setup 3) and in its final version (with sample A). There is a significant difference in the shape of the $\kappa(T)/T$ curve and in the magnitude of thermal conductivity. The final setup verifies the WIEDEMANN–FRANZ law at very low temperatures (see also figure 3.9a), and therefore it allows reliable thermal conductivity measurements. This is not the case for the setup in the trial stage: because of important deviations already at "high" temperatures we skipped the test at low temperatures and gave up this setup.

origins reveal the necessity of a proper setup-characterization, including a comparison of the relevant electric *and* thermal contact resistances. In this context, it is worthy to note that in all the experiments cited above, no details on the considered *thermal* contacts are provided in the corresponding literature, if at all, the *electric* contact resistances were evaluated. In what follows, we will give the results from our experimental approach to the contact resistance problem.

In figure 3.11 we plot the "cold" thermometer contact resistance ($L_0 T R_{cc}^{th}$ and R_{cc}^{el}) for $PrOs_4Sb_{12}$ (sample B2, in zero field and under 20 mT) and for $CeCoIn_5$ in zero field. For the contact resistance gold–$CeCoIn_5$, the two main results are the following: at higher temperatures, the (converted) thermal resistance is smaller than the electric one, revealing a large phonon contribution to the heat transport, as already mentioned earlier. Towards lower temperatures, $L_0 T R_{cc}^{th}$ increases and finally "saturates" in agreement with the WIEDEMANN–FRANZ law for the value of R_{cc}^{el}. This signs the good quality of our thermalization contacts, and rules out electron–phonon decoupling in the contacts [185]. Even more, the R_{cc}^{th} data can be understood quantitatively within a simple model which will be presented in the next section. Together with the validity of the WF law for the κ measurements in the normal phase, the "ordinary" behavior of the thermalization contacts in zero field is a strong support for the reliability of our experimental setup with its silver glue contacts on evaporated gold stripes on the sample. Compared to other methods for contacting the thermometers to the sample, our technique seems to be a good choice, especially in zero magnetic field, where other procedures like contacts by indium solder might suffer from a very low thermal conductivity when getting *superconducting*. Of course, under magnetic field, this argument does not hold any longer, as indium solder contacts

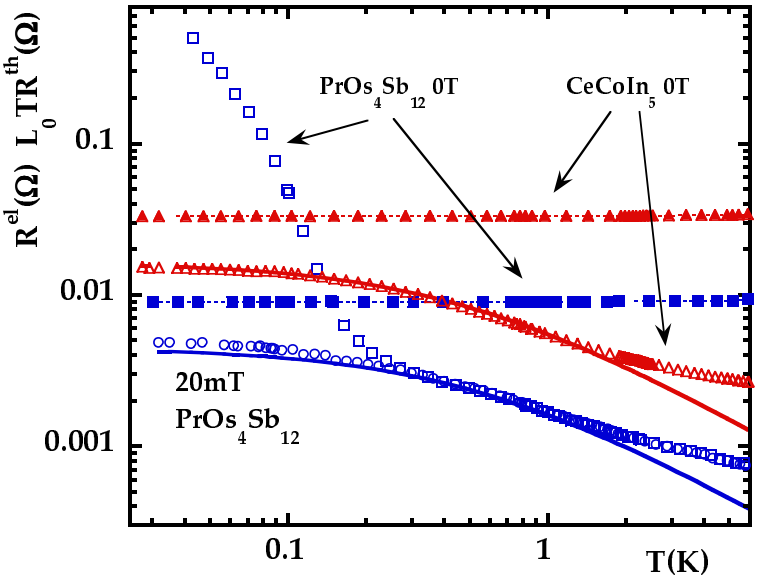

Figure 3.11. Electric $R_{cc}^{el}(T)$ (full symbols) and thermal $R_{cc}^{th}(T)L_0T$ (open symbols) resistance of the Au-$PrOs_4Sb_{12}$ or Au-$CeCoIn_5$ contacts towards the "cold" thermometer. At low temperatures, the WIEDEMANN–FRANZ law is recovered, in zero field for $CeCoIn_5$, and under 20 mT in $PrOs_4Sb_{12}$. Reminder: for all plots with R^{th} we use the initial definition $R^{th} = \Delta T/P$ with $P = R^{el}i^2$. Hence, to recover the WF law, the $R_{cc}^{th}(T)L_0T$ data have to be multiplied by a factor 2. The "divergence" of $R_{cc}^{th}(T \to 0)L_0T$ in zero field for $PrOs_4Sb_{12}$ will be addressed at the end of the next chapter. Full lines: fits of $R_{cc}^{th}(T)$, see next section for details.

can be much less resistive than those by silver glue (on $CeCoIn_5$ indium solder contacts of only 5 mΩ are reported [201], whereas we obtained R_{cc}^{el} values of about 30 mΩ).

In principle, the situation is similar for the case of $PrOs_4Sb_{12}$ samples, at least under small fields of about 20 mT $\ll H_{c2}$: the WF law in the contacts is satisfied in the low temperature limit, and it was possible to achieve lower values for R_{cc}^{el} (about 10 mΩ) than on $CeCoIn_5$. Nevertheless, in zero field, the situation is completely different; for the thermal channel, we observe a nearly diverging R_{cc}^{th} at lowest temperatures. In fact, this behavior reflects an intrinsic physical property of the gold–$PrOs_4Sb_{12}$ interface, related to the opening of a low energy scale gap on the whole FERMI surface in the thermal excitation spectrum at very low temperatures and without field (this is not the case in $CeCoIn_5$ because the superconducting gap is believed to exhibit nodes). In the chapter on $PrOs_4Sb_{12}$, we will give a detailed analysis of the R_{cc}^{th} data.

In summary, the recovery of the WF law for the sample *and* the thermalization contacts make us feel confident that the thermal conductivity setup is reliable, and the detailed contact resistance analysis will reveal as a complementary probe to the ordinary thermal conductivity measurement.

3.4. More detailed discussion of contact resistance measurements – $R_c(T, H)$ scans

In this part, I will expose and discuss in more detail our electric and thermal contact resistance measurements, concentrating on the contact between the sample and the gold wire acting as thermalization of the "cold" thermometer, namely R_{cc} (see fig. 3.12). The experimental

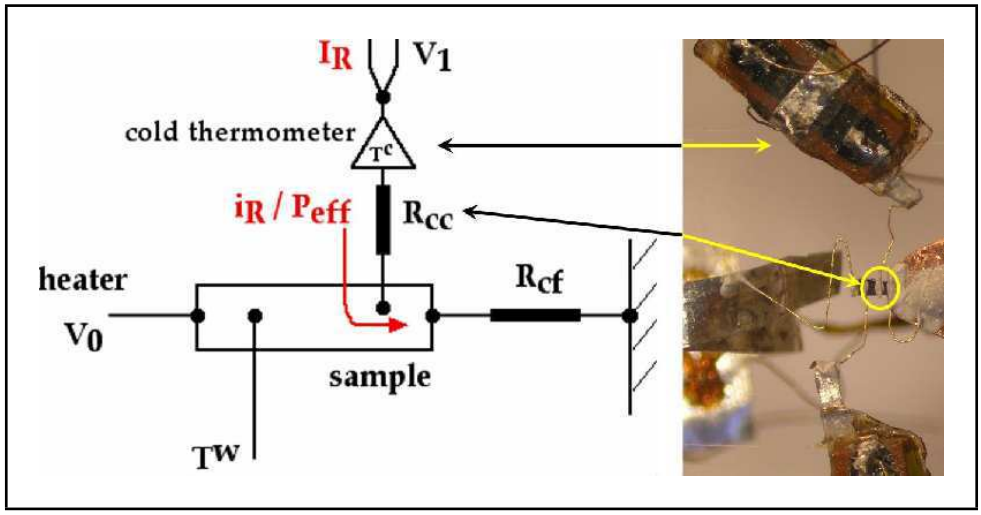

Figure 3.12. Just a reminder: correspondence between the "real" contact R_{cc} on the setup (here on sample B2) and its schematic representation (see also fig. 3.6).

technique was already presented previously, so that we can straightaway focus on the resulting experimental data and their interpretation. Nevertheless, as the subject of (thermal) contact resistances might be less common, I will only insist on the basic ideas – further details can be found in the appendix and in the corresponding literature. An expanded discussion of the thermal contact resistance in the scope of the multiband superconductivity scenario in $PrOs_4Sb_{12}$ will be given at the end of this chapter.

Understanding the electric and thermal contact resistance

In general, our analysis concerns the setup with sample B2, where it was possible to characterize the contact resistances quantitatively within a basic model. On sample A, the contacts "suffered" from their preparation method (arc-soldering), limiting the analysis to qualitative aspects. Nevertheless, the first contacts largely contributed to our general understanding of contacts resistances, benefitting to sample B2, on which the contact resistances were considerably improved.

a) Electric contact resistance

Figure 3.13 shows the temperature dependence of the electric contact resistance R_{cc}^{el} at zero magnetic field and under a field of 20 mT – in fact, R_{cc}^{el} does not change significantly under such low fields. The data were obtained as indicated in chapter 2, including the correction for the parasitic contribution of about 5 mΩ coming from the connectors of the dispatching electric circuits. At first sight, in the considered temperature range, $R_{cc}^{el}(T)$ seems quite constant. However, when zooming, a tiny jump at T_c appears, and above T_c, $R_{cc}^{el}(T)$ rises slowly (see fig. 3.14).

We suggest the following scenario: the contact resistance R_{cc}^{el} might consist of two *additional* parts, namely

- the usual Maxwell contribution R_M^{el} (coming from the concentration of current and field lines in the small contact area: constriction resistance), and

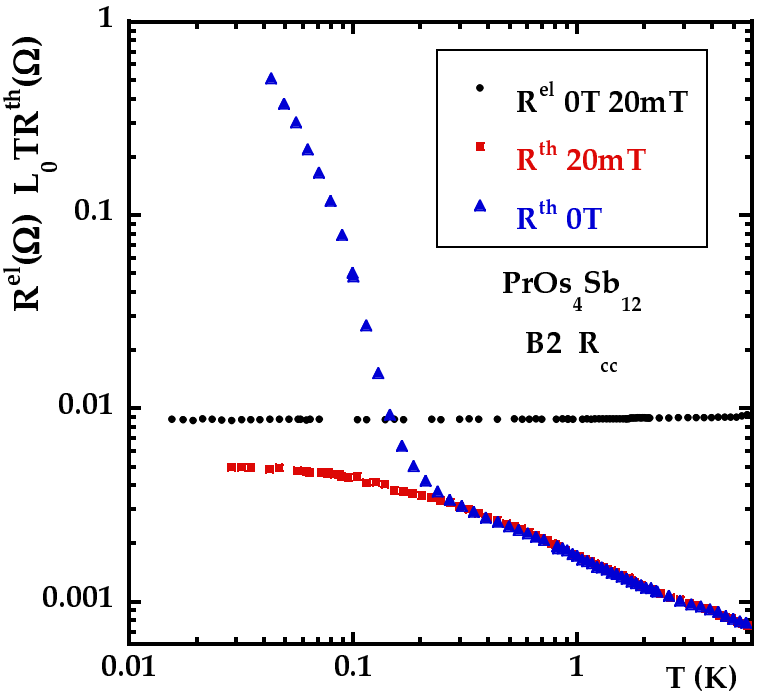

Figure 3.13. Overview on the temperature behavior of the electric and (converted) thermal contact resistance R_{cc} in zero field and under 20 mT. The electric resistance remains unchanged, whereas the thermal resistance is much lower under field in the low temperature range. Here we will first concentrate on the behavior under field.

- a constant (ohmic) contribution, R^{el}_{const}. Its origin has not been clearly identified yet, eventually it involves scattering at the Au-$PrOs_4Sb_{12}$ interface.

Generally, for contacts in the *diffusive* (thermal) regime (contact dimension $\gg$ mean free path) with a clean interface, the MAXWELL resistance yields $R^{el}_M = \rho/2a$ (with a: radius in the case of a circular orifice and ρ: bulk resistivity of the contact material). In our case ($\rho_{\text{Au}} \ll \rho_{PrOs_4Sb_{12}}$) we can neglect the contribution coming from the gold wire and hence $\rho \approx \frac{\rho_{PrOs_4Sb_{12}}}{2}$. Using d as a characteristic dimension of the contact area, $R^{el}_{cc}(T)$ can be described as follows:

$$R^{el}_{cc}(T) = \begin{cases} R^{el}_{\text{const}} + \rho_{PrOs_4Sb_{12}}(T)/2d & \text{for} \quad T \geq T_c \\ R^{el}_{\text{const}} & \text{for} \quad T < T_c \end{cases} \tag{3.13}$$

According to this equation, the electric contact resistance should be controlled by $\rho_{PrOs_4Sb_{12}}(T)$ above T_c, and the height of the resistance drop ΔR at $T = T_c$ should be inversely proportional to the typical contact dimension, i.e. $\Delta R \propto 1/d$. So an estimate of the size of the contact can either be derived from $\Delta R|_{T_c}$, from $R^{el}_{cc}(T)$ above T_c or more precisely, from the temperature derivatives [60], i.e. $d = (\mathrm{d}\rho_{PrOs_4Sb_{12}}/\mathrm{d}T)/2(\mathrm{d}R^{el}_{cc}/\mathrm{d}T)|_{T_c^+}$.[17]

When we apply this model to our experimental data, the agreement of the temperature dependence $R^{el}_{cc}(T)$ with that of $\rho_{PrOs_4Sb_{12}}(T)/2d$ is quite satisfactory (see fig. 3.14), and we get $d \approx 550$ µm as an order of magnitude. This is quite large, but corresponds approximately to

[17] The last method avoids relying on the absolute value of $\rho_{PrOs_4Sb_{12}}$ near the contact, which may deviate from the bulk value.

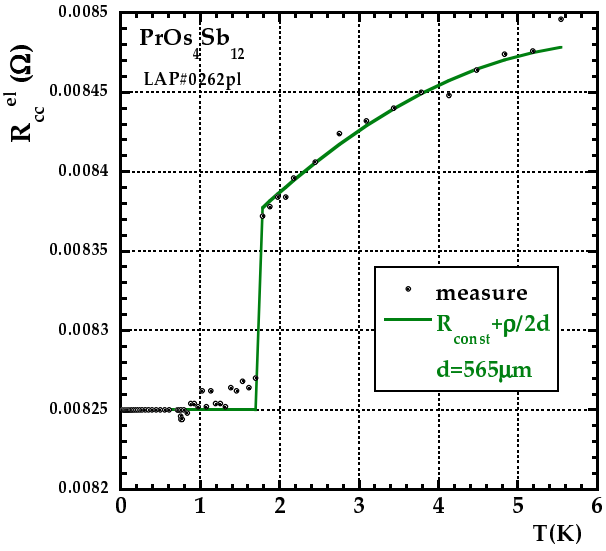

Figure 3.14. Zoom on the temperature dependence of the electric contact resistance $R_{cc}^{el}(T)$ in zero magnetic field. It exhibits a tiny jump at T_c, and can be modeled over the whole temperature range by equation (3.13), yielding $d \approx 565$ µm.

the dimension of the Ag paint drops on the gold stripes. Nevertheless, it becomes questionable whether the description of the contact in terms of a constriction resistance remains valid for such large d values. Further, one could object that equation (3.13) resembles a phenomenological description rather than a well-founded "theory", but its application to the *thermal* contact resistance (under magnetic field) will reveal its capacity to account for the experimental data again to a very satisfactory extend.

b) Thermal contact resistance

Figure 3.13 compares the $R_{cc}^{th}(T)$ data with the electric data. First a reminder to the convention on our notations (see previous sections): the measured R_{cc}^{th} is defined as $\Delta T/P$ with $P = R_{cc}^{el} i^2$ so that the "real" contact resistance values correspond to $2 \cdot R_{cc}^{th}$. For easier comparison with the electric measurements, we always convert the thermal resistances in Ω, which means we plot $L_0 T R_{cc}^{th}$ rather than R_{cc}^{th} in K/W. At this stage, we will only analyze the results under magnetic field, in order to avoid supplementary effects, not included in this model. For $T > T_c$, in the normal phase, the thermal contact resistance lies well below the electric one, reflecting the phonon contribution to the heat transport. However, in the low temperature limit, the Wiedemann–Franz law is recovered. It is possible to reproduce the data quantitatively after transposing equation (3.13) in terms of thermal transport, still containing two contributions:

$$R_{cc}^{th}(T) = R_{\text{const}}^{th}(T) + R_M^{th}(T) \tag{3.14}$$

The "thermal" Maxwell contribution yields, in analogy to the electric problem ($\rho^{-1} \to \kappa$): $R_M^{th}(T) = 1/(2d\kappa_{PrOs_4Sb_{12}}(T))$. The first term in equation (3.14) comes from the temperature gradient related to the constant, ohmic contribution to the electric contact resistance, where we assume

- a *linear* increase of the heating power P, i.e. $P(x) = (R_{\text{const}}^{el} \cdot x/l) i^2$ with x a coordinate along the contact and l its total length (with constant cross-section S). Hence the total power available for self-heating is $\frac{1}{2} R_{\text{const}}^{el} i^2$), so that the temperature gradient ΔT upon this part of the contact is (κ_c: thermal conductivity of the contact):

$$\Delta T = \frac{1}{2} R_{\text{const}}^{el} i^2 \cdot l/(S\kappa_c)\,, \tag{3.15}$$

- a thermal conduction following the WIEDEMANN–FRANZ law for the electronic contribution, which means $l/(S\kappa_c) = R^{el}_{\text{const}}/(L_0 T)$ (L_0: LORENZ number), and
- a usual $\alpha T^{n=2}$ law for the parallel phonon contribution (where α has the same value for all fields, and strictly speaking αT^2 corresponds to a thermal conductance ($(R^{th})^{-1}$).

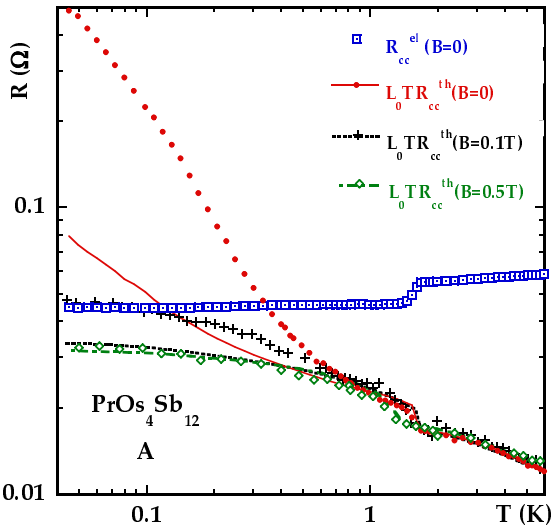

Figure 3.15. Electric and thermal contact resistance R_{cc} on $PrOs_4Sb_{12}$, sample A (figure 4 in [178]). Here, we do not want to go into detail as to sample A, but just illustrate that equation (3.17) reproduces well the jump in R^{th}_{cc} at T_c and the complete temperature dependence $R^{th}_{cc}(T)$ under a magnetic field of 500 mT.

Altogether, dividing equation (3.15) by $P = R^{el}_{cc} i^2$ (above convention), we get

$$R^{th}_{\text{const}}(T) = \frac{1}{2\left(L_0 T/R^{el}_{\text{const}} + \alpha T^2\right)}. \tag{3.16}$$

In order to include the complete temperature dependence of $R^{th}_{cc}(T)$, we have to consider that the electric contact resistance changes at T_c, due to the breakdown of the superconduction state within the constriction, and hence the distribution of the heating power. In particular, the MAXWELL contribution then has a *uniform* heating power ($R^{el}_{\text{const}} i^2$) plus a non uniform heating power generated by R^{el}_M itself (non zero only above T_c) [213]. Altogether,

$$R^{th}_{cc}(T) = \frac{R^{el}_{\text{const}}}{2R^{el}_{cc}} \frac{1}{L_0 T/R^{el}_{\text{const}} + \alpha T^2} + \frac{1}{4d\kappa_{PrOs_4Sb_{12}}}\left(1 + \frac{R^{el}_{\text{const}}}{R^{el}_{cc}}\right) \tag{3.17}$$

Note that in the case of a negligible MAXWELL contribution (depending on the contact size and its thermal conductivity), the thermal contact resistance reduces to equation (3.16), and that there is no a priori necessity to fix the exponent n in the thermal conductivity of the phonon channel, it could also figure as fit parameter. However, $n = 2$ is certainly a reasonable and common approximation at low temperatures, hence limiting the free parameters to the sole α coefficient.

On sample A, we verified equation (3.17) as the small d (~ 30 µm) of the contact areas yielded a sizable jump of R^{el}_{cc} and R^{th}_{cc}, and an evolution of R^{th}_{cc} under field matching that of $\kappa_{PrOs_4Sb_{12}}$ [178] (see fig. 3.15). On sample B2, we improved the set-up to increase d, and reduce this MAXWELL contribution.

In fig. 3.16 we compare the different contributions to the thermal contact resistance (according to equation (3.17)) with the experimental data $R^{th}_{cc}(T)$ for the contact towards the cold thermometer on $PrOs_4Sb_{12}$ in 20 mT. This comparison implies several remarks:

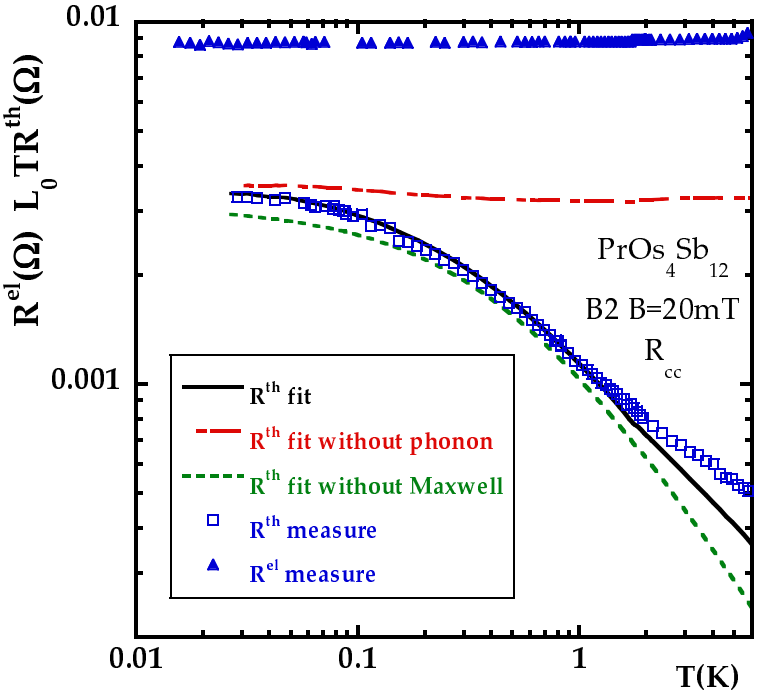

Figure 3.16. Electric and thermal contact resistance R_{cc} on $PrOs_4Sb_{12}$ in 20 mT. The different fits refer to equation (3.17), see text. At low temperatures, the WIEDEMANN–FRANZ law is recovered (factor of two on the thermal resistances). Fit parameter $\alpha \approx 5 \cdot 10^{-6}$ WK^{-3}.

- The calculation of $R_{cc}^{th}(T)$ including all contributions of equation (3.16) (solid line in fig. 3.16) reproduces to a large extend the experimental curve. Small deviations are only observed at higher temperatures where the phonon conductivity might no longer obey a αT^2-behavior. Nevertheless, the dominant contribution to the temperature dependence comes of course from the phonon channel of the ohmic resistance R_{const} (the calculation with $\alpha = 0$ leads to a high, quasi constant contact resistance value).

- The MAXWELL contribution to the thermal resistance is only significant at lower temperatures (where the thermal conductivity of the sample is low), and at higher temperatures (where it becomes comparable to the phonon channel of R_{const}). This observation is consistent with the large contact dimension, yielding a tiny jump of $R_{cc}^{el}(T)$ at T_c, and no detectable anomaly in the thermal analogue. Therefore, as a rough estimation, equation (3.16) already gives a sufficiently good agreement with the data points (dashed-line in fig. 3.16).

- Once again, by multiplying the thermal data by a factor of two, the electric contact resistance values are recovered in the low temperature limit, meaning a negligible phonon contribution and a normal metallic behavior within the contacts.

The good agreement between calculation and experimental data supports the description of the contact resistance in terms of an ohmic and a constriction resistance. Nevertheless, this scenario is consistent only when applying a magnetic field. To get further insight, we applied a similar analysis to the same contact resistance (R_{cc}) on our $CeCoIn_5$ sample, as detailed in fig. 5.12. Since the contact elaboration for sample C2 obeyed the same procedure than in the case of

$PrOs_4Sb_{12}$ (sample B2), we can expect similar results.

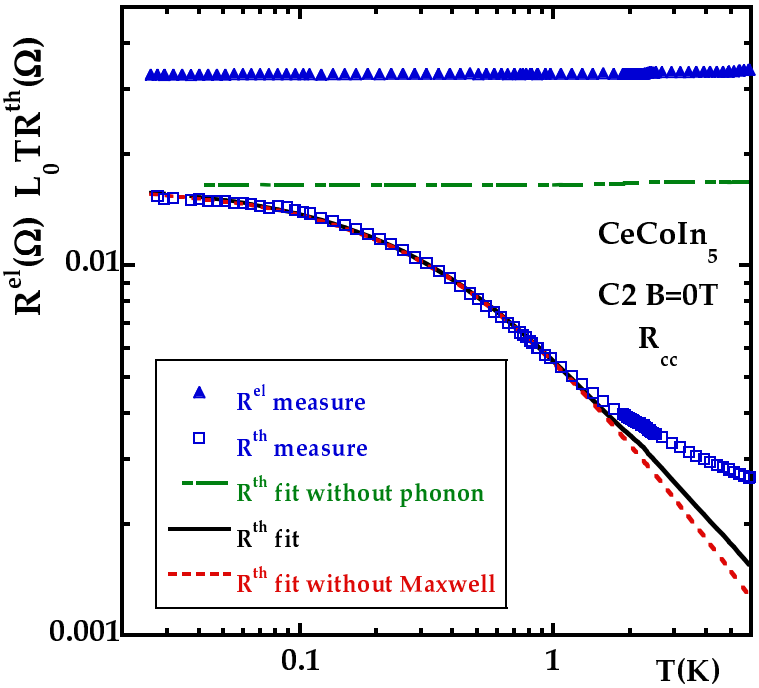

Figure 3.17. Electric and thermal contact resistance R_{cc} on $CeCoIn_5$ in zero field. The different fits refer to equation (3.17), see text. At low temperatures, the WIEDEMANN–FRANZ law is recovered (factor of two on the thermal resistances). Fit parameter $\alpha \approx 1.5 \cdot 10^{-6}$ WK^{-3}.

Indeed, fig. 3.17 resembles, at least qualitatively, the case of $PrOs_4Sb_{12}$. However, there are two major differences: fig. 3.17 corresponds to the case of zero magnetic field, and the absolute values of the contact resistances are increased by a factor of about 3. As already mentioned, the question of magnetic field is postponed to a later section and should not matter here. As to the magnitude of the contact resistance, regarding R_{cc}^{el}, we observe an enhanced ohmic contribution, indicating that the contact quality on $CeCoIn_5$ is not the same than on $PrOs_4Sb_{12}$. Nevertheless, on zooming, $R_{cc}^{el}(T)$ also exhibits a small jump at T_c, and the overall temperature dependence matches well with the $CeCoIn_5$ analogue of equation (3.13), yielding $d \approx 100$ µm. This results seem reasonable owing to the smaller contact areas on sample C2 compared to sample B2. As to the thermal contact resistance, the same remarks as above apply, except that the relevance of the MAXWELL contribution is even less than before, despite the reduced contact area, due to the extremely high thermal conductivity of $CeCoIn_5$ in the superconducting phase.

Interestingly, the fit of the thermal contact resistance on $PrOs_4Sb_{12}$ and $CeCoIn_5$ is possible with the same "phonon exponent" $n = 2$ and, more surprising, with the same relative weight of electric and phononic contributions ($\alpha \cdot R_{\mathrm{const}}^{el} = \mathrm{const}$). So it might characterize the silver paint thermal conductivity which was used for the contacts both on $PrOs_4Sb_{12}$ and $CeCoIn_5$.

Altogether, we could minimize on the contact resistance, the constriction contribution (increasing the contact area), and we have a simple description of this thermal contact resistance in agreement with the WIEDEMANN–FRANZ law. The zero field case in $PrOs_4Sb_{12}$ will be addressed in the last part of the next chapter, as it shows spectacular deviations from this behavior.

Changes on the contacts

As a sort of conclusion, let me a posteriori sum up how we modified the contacts when preparing the setup for sample B2 (benefitting from the first contact resistance analysis on sample A), in order to improve the thermometer thermalization. Even though some points have already been mentioned earlier, here a list of the main changes:

- **Surface treatment** Soldering by arc-melting eventually leads to the formation of some new material at the interface between both contact members, which happened on sample A. Similarly, the contact resistance might be enhanced by other additional "material" on the surface such as oxide layers, etc. Sample A had only been rinsed by acetone and ethanol. In order to get the gold-sample interface as clean and large as possible, and hence to avoid any supplementary ohmic contribution to the contact resistance, we etched the sample surface with an ion gun and evaporated gold on the contact areas before putting back to air.

- **Contact size** Another shortcoming of the arc-melting method is that the contact area will always be of the order of the diameter of the gold wire. This might give a non-negligible Maxwell contribution to the contact resistance (see sample A, fig. 3.15).

- **Contact medium** On the one hand, our first contact analysis (3.7) had revealed that silver paint reinforces the thermal contact when added on the junction of two arc-melted objects, on the other hand, the electric contact resistance of a silver paint junction, for example between two gold wires, exhibits only very low values. So to take advantage of the large areas of the gold pads on the sample, we glued to wires with silver paint, avoiding superconducting solders (like In) despite their better electrical contacts: they would have forced us to apply fields ~ 0.05 T for good thermal contacts.

When comparing the $R_{cc}^{el}(T)$ curves with the former ones (sample A, fig. 3.15), the apparent modifications are a significant lower magnitude of R_{cc}^{el} over the whole temperature range (decrease by at least a factor of $3 \sim 4$) and the quasi-absence of a jump at T_c. This reflects indeed a significant reduction of both the constant (ohmic) part of the contact resistance and of the Maxwell contribution.

4. Low temperature thermal conductivity of $PrOs_4Sb_{12}$

This chapter summarizes the main outcomes of the PhD period. It is exclusively devoted to the measurements on $PrOs_4Sb_{12}$. First I will present the samples and their characterization by additional specific heat measurements, before switching to the core work with the thermal conductivity and contact resistance data. The last part contains our conclusions drawn from these results on the superconducting state of $PrOs_4Sb_{12}$.

4.1. Samples

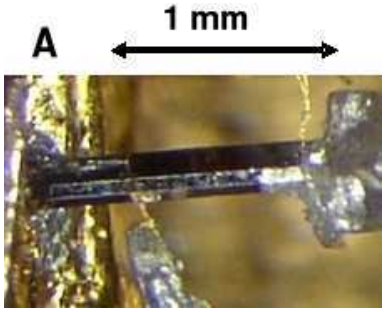

Figure 4.1 Bar shaped $PrOs_4Sb_{12}$ sample of the Sugawara batch, labeled A or #02.03.11, used for the first scan of thermal conductivity in $PrOs_4Sb_{12}$. Here on this picture it is seen included in a previous test setup with some wires contacting the thermometers.

As a general feature, $PrOs_4Sb_{12}$ single crystals have either a bar or a cubic shape [129]. For our experiment, we first studied a quite large bar-shaped ($\sim 0.4 \times 0.4 \times 2$ mm^3) sample (see fig. 4.1) from the Sugawara batch (labeled A or #02.03.11), grown by the Sb-flux method [92]. We determined its residual resistivity ratio (RRR between 300 K and T_c) to be of about 15. The gold wires (thermometer thermalization) were contacted by microarc-melting and additional silver glue, but no gold had previously been evaporated on the contact areas.

In this thesis, we will not focus too much on the results obtained on that sample, but it will be important to compare them with what we measured on the second, much smaller ($\sim 760 \times 340 \times 45$ µm^3) sample (label B2 or LAP#0262pl), belonging to the Lapertot batch. It has the shape of a tiny platelet, and was extracted from a small ($\sim 1 \times 0.75 \times 0.6$ mm^3) $PrOs_4Sb_{12}$ cubic single crystal (see fig. 4.2, label B1) by sawing and grinding with a diamond saw. We determined its RRR to be of about 30, and evaporated some gold on the contact areas after ion gun etching its surface.
For both $PrOs_4Sb_{12}$ samples, the applied magnetic field was parallel to the heat current.

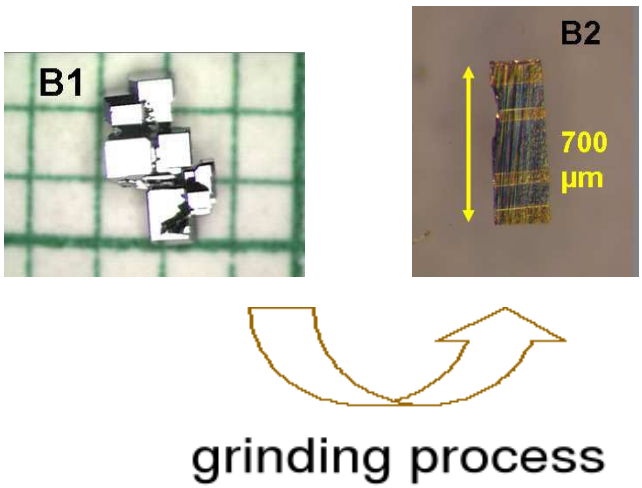

Figure 4.2. Left: Conglomerate of cubic $PrOs_4Sb_{12}$ single crystals, from Lapertot batch (label B1). The biggest cube was ground in order to extract a very thin platelet (45 µm), labeled B2 or LAP#0262pl (on the right), used for the second scan of thermal conductivity in $PrOs_4Sb_{12}$. Here the platelet is already shown with its gold stripes evaporated on the future contact areas after ion gun etching its surface.

4.2. Experimental results

In this section, all relevant experimental results obtained on $PrOs_4Sb_{12}$ will be exposed, postponing their global, physical discussion to the next section. As already mentioned, emphasis will be put on the second $PrOs_4Sb_{12}$ sample (label B2 or LAP#0262pl), but results on the former one (label A or #02.03.11) will also be presented, in order to show their evolution with sample quality.

4.2.1. Sample characterization by specific heat – sample quality and double transition mystery

We have characterized our samples by specific heat measurements (carried out by ourselves at CRTBT/CNRS lab and by Marie-Aude Méasson at SPSMS lab of CEA Grenoble). In the introductory chapter, I already mentioned that the great interest in the skutterudite compound $PrOs_4Sb_{12}$ was partly due to the observation of a *double* superconducting transition in the specific heat, like in the historical case of UPt_3 [68]. When reviewing the literature on $PrOs_4Sb_{12}$ and low temperature specific heat measurements, the development of the superconducting anomaly is as follows: first studies [19] revealed a very broad transition peak, progressing towards *two* more or less sharp specific heat jumps in the next papers [125, 210, 130, 66]. Recently, *single*, sharp transition peaks were reported on very tiny single crystals [131, 129]. What about our samples ? In figure 4.3a is shown the superconducting transition as probed by specific heat of the first, bar-shaped $PrOs_4Sb_{12}$ sample (label A or #02.03.11). It exhibits a very broad transition peak, compared to the double transition of another sample (labeled #02/002) from Prof. Sugawara's group[1], available just after starting the thermal conductivity measurements.

[1] This sample was used to determine the $H-T$ phase diagram published in [130]. It consists of an aggregate of small single crystals with well developed cubic faces, similar to sample B1.

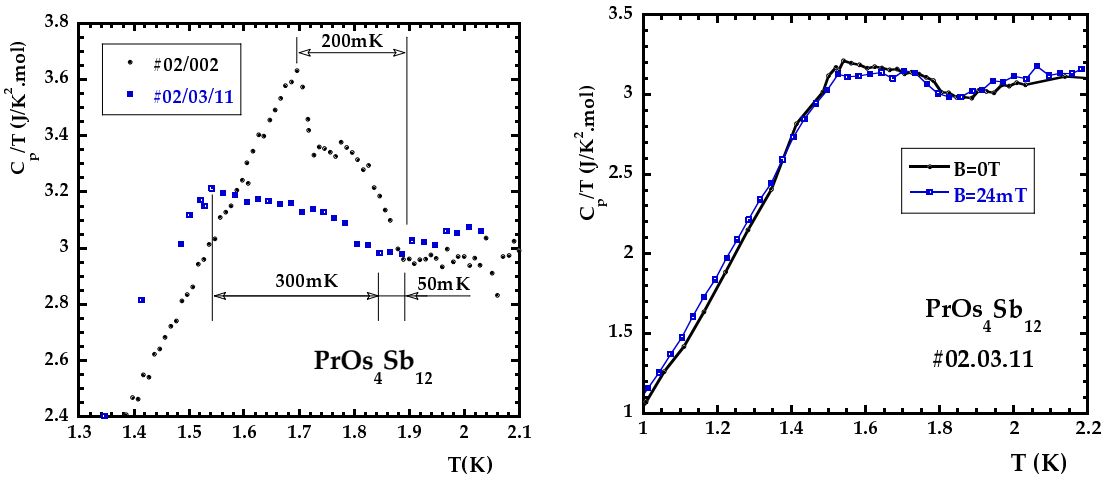

(a) Comparison of the superconducting transition in the specific heat of sample #02.03.11 (bar shape) and of sample #02.002 (aggregate of small cubes). The experimental method used is in both cases a semi-adiabatic technique.

(b) Influence of a small magnetic field on the specific heat in vicinity of the superconducting transition of sample #02.03.11. Obviously, there is no significant change in its density of states.

Figure 4.3. Sample characterization by specific heat measurements.

Generally, a broadened jump at T_c in specific heat (bulk probe!) signs a distribution of T_c, related to some sample inhomogeneities. This is confirmed by the fact that the change of slope in the thermal conductivity $\kappa/T(T)$ (local maximum at about 1.7 K, see fig. 4.5b) is very broad and does not appear at exactly the same temperature than the onset of superconductivity as seen by specific heat and resistivity (see the following results on sample B1).

After the characterization of several samples of different shapes and batches, it seems to be a general fact that the bar shaped samples always exhibit a broadened transition in C_p compared to small, cubic ones [129].

Let me add some further information on our sample #02.03.11. As the behavior and changes of thermal conductivity under small (compared to H_{c2}) magnetic fields will play an important role later on, it might be instructive to compare the sample's specific heat without and with a small applied magnetic field (24 mT), which has been done in figure 4.3b, where no significant change of the specific heat under field can be observed in vicinity of the transition temperature T_c [2]. The main result we should keep in mind is that a small magnetic field does not affect the density of states and hence changes in the thermal conductivity in that temperature range are *exclusively* due to transport phenomena (quasiparticle scattering, etc.).

Figure 4.4 displays the specific heat $C_p(T)/T$ (blue open circles) in vicinity of the transition temperature of sample B1 (non-modified aggregate of small crystals with cubic faces). It exhibits two sharp jumps at about 1.9 K and 1.75 K, comparable to what is found on other samples (with cubic or rectangular shape). As already mentioned in the introduction, the origin of the double transition has not been clarified yet, although great experimental efforts (sample growth and

[2] Note that $C_p(T)$ exhibits a pronounced upturn at low temperatures (below 0.5 K [210]), probably involving nuclear contributions, so that it becomes difficult to extract the electronic specific heat and its changes with magnetic field.

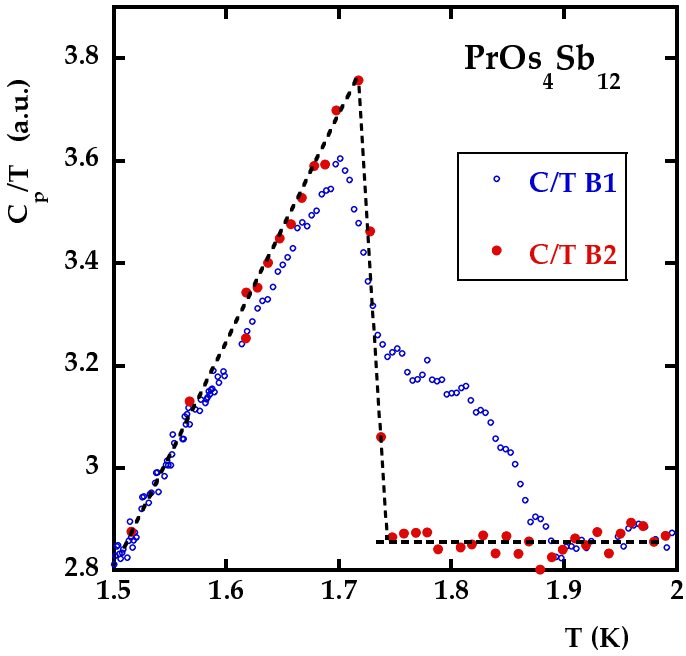

Figure 4.4. Specific heat $C_p/T(T)$ in vicinity of T_c of sample B1 (small cubes) and of sample B2 (platelet, after grinding process), documenting the collapse of the double transition.

characterization) have been undertaken for several years now (a good summary of the state of the art can be found in [129]). The fact that both transitions behave quite similarly under magnetic field and pressure, and that the upper one always appears inhomogeneous (for example in ac-susceptibility or resistivity measurements [130, 129]), have cast doubt on the intrinsic nature of this phenomenon. In fig. 4.4, we plot for comparison the $C_p(T)/T$ curve of our small platelet B2, extracted by sawing and grinding from crystal B1. The remarkable result is now that the double transition collapses to a single, sharp jump of C_p (at the lowest T_c and of about the same overall height) just by reducing the crystal dimensions (sample B1 $\rightarrow$ B2). Obviously, areas with a single and a double transition coexist within the same sample. It suggests that, like in URu_2Si_2 [159], the observed double superconducting transition in $PrOs_4Sb_{12}$ is related to sample inhomogeneity. On the same footing, the resistivity data of sample B2 (see fig. 4.5a) still shows a small deep at the upper T_c, but full drop to zero clearly appears only below the lower transition temperature. A hint for extracting samples with a single transition comes from the preparation stage: in order to remove all small cavities appearing during the sawing process of B1, we had to reduce the thickness of B2 down to only about 50 µm. Similarly, such tiny dimensions were reported for other samples exhibiting a single, sharp C_p jump [131, 129]. Further systematic (structural) investigations seem necessary to determine the nature of defects which might be at the origin of the sharp double transition in $PrOs_4Sb_{12}$. At this stage, I will not go into more detail as to the double transition issue – the main point for the following is that with sample B2, we are examining a crystal with a single, sharp specific heat jump, and hence a very *homogeneous* sample. Its excellent homogeneity is furthermore documented by the fact that the bulk superconducting transition appears at exactly the same temperature on C_p/T, κ/T and ρ (see fig. 4.4 and 4.5a), which was not the case on former sample A (see fig. 4.5b). Another criterion regarding crystal purity is the residual value of κ/T in the $T \rightarrow 0$ limit. For platelet B2, it is smaller than 1.6 $\mu W/K^2\,cm^{-1}$, which corresponds to 0.07% of

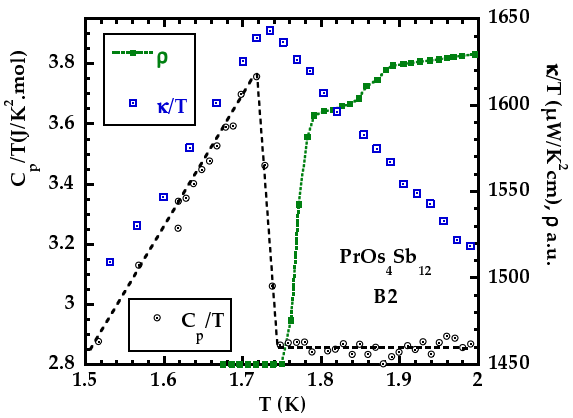

(a) Specific heat $C_p/T(T)$, resistivity $\rho(T)$ and thermal conductivity $\kappa/T(T)$ of sample B2 in zero magnetic field at the superconducting transition. The respective signatures of T_c appear at the same temperature, revealing the high homogeneity of sample B2.

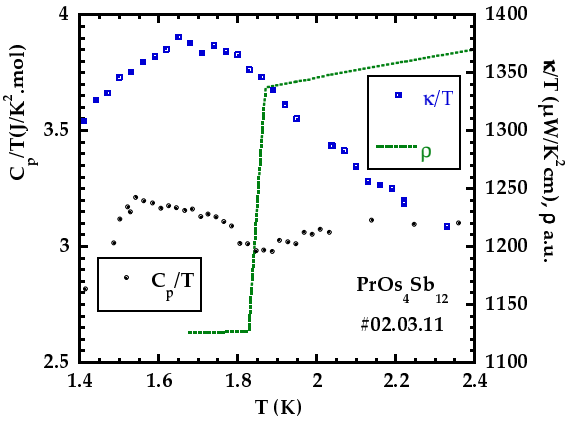

(b) Specific heat $C_p/T(T)$, resistivity $\rho(T)$ and thermal conductivity $\kappa/T(T)$ of sample A in zero magnetic field at the superconducting transition. Remarkably, the anomaly in $\kappa/T(T)$ appears at lower temperatures than that seen by $C_p/T(T)$ and $\rho(T)$, hence documenting some lack of homogeneity in sample A.

Figure 4.5. Comparison of the homogeneity of $PrOs_4Sb_{12}$ samples A and B2.

$\kappa/T(T \to 0,\ \mu_0 H = 2.5\ \mathrm{T} > H_{c2})$ and is significantly lower than in former sample A (see fig. 4.6). These signatures of high sample quality allow us to use thermal transport at very low temperatures as a sensitive probe of the low lying energy excitations in $PrOs_4Sb_{12}$.

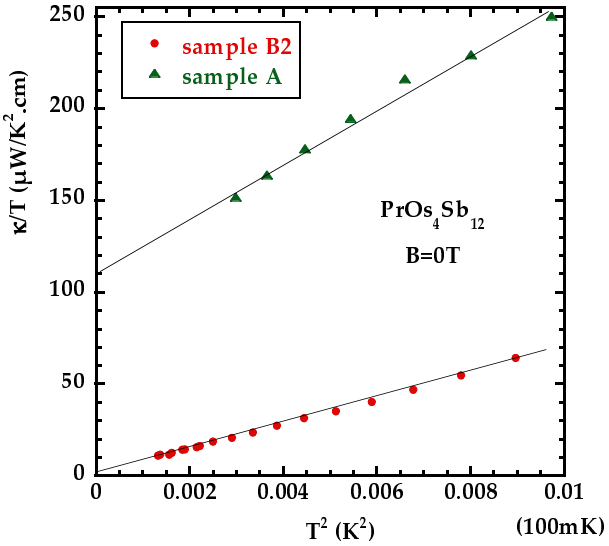

Figure 4.6. Comparison of $\kappa/T(T)$ as a function of T^2 at very low temperatures ($T < 100$ mK) in zero magnetic field ($PrOs_4Sb_{12}$ samples A and B2). The residual term (extrapolation for $T \to 0$) is considerably lower in sample B2, as a signature of improved sample quality.

4.2.2. Reliability of thermal conductivity measurement and Wiedemann–Franz law

As already mentioned in the experimental chapter, the Wiedemann–Franz law represents a severe examination of the experimental setup and of the thermometer calibrations. This law

establishes a simple relation between the thermal and the charge transport in the case where these two phenomena are mediated by the same particles (electrons) and when the effective mean free paths for both quantities are equivalent (at very low temperatures). Hence a first check consists of measuring in the *normal* phase the thermal and electric resistivity of the sample. A good estimate for the upper critical field of each sample is obtained from electric resistivity temperature and field scans (even though one has to keep in mind that resistivity is neither a thermodynamic nor a and bulk probe): for sample #02.03.11, we get $B_{c2}(T \to 0) \approx 2.2$ T, and for sample B2 (with the same criterion) a similar order of magnitude (see fig. 4.7). For the sake of completeness, I should mention that below 100 mK, $B_{c2}(T)$ as seen by electric resistivity, begins to decrease again (see fig. 4.7b), but since $\rho(T, H)$ was our only probe in this temperature and field range, we will not detail these observations here. To do so, supplementary studies (for example magnetization measurements) would be necessary in order to get more reliable data about this reentrance-like behavior...

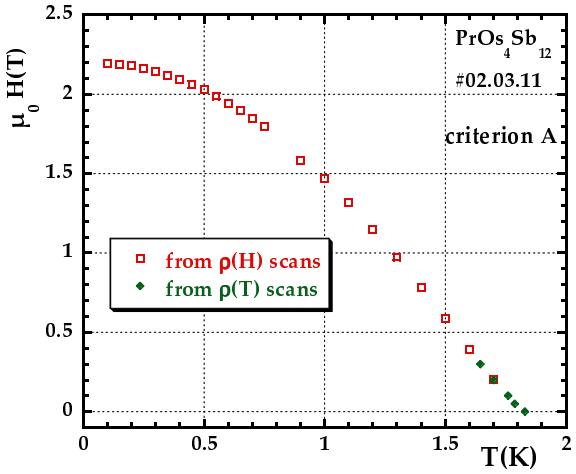

(a) H–T phase diagram of sample A as obtained with criterion A.

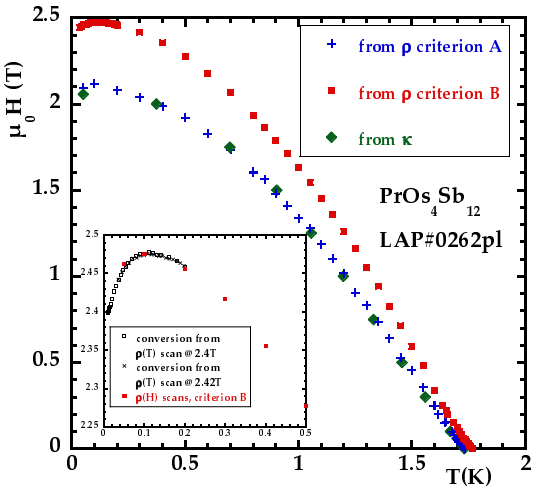

(b) H–T phase diagram of sample B2 obtained with different criteria. The insert is a zoom on the low temperature region and the data determined with criterion B.

Figure 4.7. Comparison of the H–T phase diagram as obtained by resistivity on samples A and B2. The used criteria are explained in fig. 4.8.

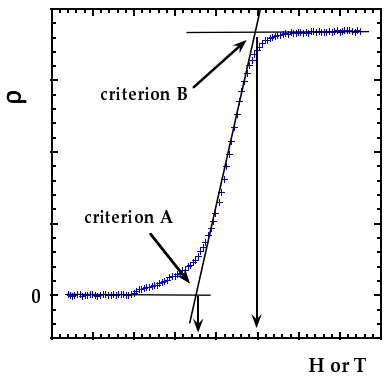

Figure 4.8. Schematic representation of the criteria A and B used to determine the H–T phase diagrams by resistivity measurements in fig. 4.7.

Concerning the verification of the WIEDEMANN–FRANZ law, we have to apply a magnetic field that is high enough to avoid any traces of superconductivity in the electric resistivity, i.e. $B \geq 2.5$ T. More strictly, for sample B2, the $L/L_0(T)$ curve at 3 T (rather than that at 2.5 T as for sample #02.03.11) will figure as "reference curve" in the normal state. Indeed, the resistivity curve at 2.5 T on that sample exhibits a slight downturn below 300 mK, which might be related to some residual superconducting phases...

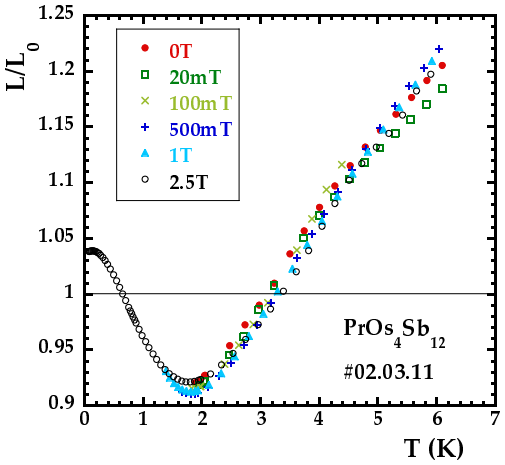

(a) $L/L_0(T)$ on sample A.

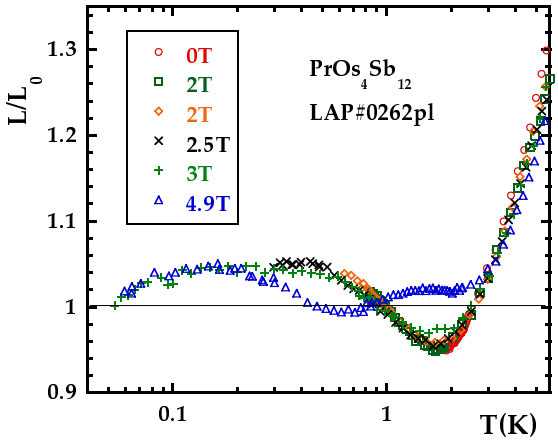

(b) $L/L_0(T)$ on sample B2. The data at 4.9 T show a different behavior, probably due to the vicinity of the field-induced ordered phase observed in $PrOs_4Sb_{12}$.

Figure 4.9. Comparison of the calculated LORENZ-ratio $L/L_0(T)$ on samples A and B2: The overall behavior is quite similar. $L/L_0(T)$ is plotted in the whole temperature range for 2.5 T $\geq B_{c2}$ and at lower fields for $T > T_c(B)$, where $L = \frac{\kappa\rho}{T}$ (from experimental data) and $L_0 = 2.44 \cdot 10^{-8}$ W Ω K^{-2} (universal LORENZ number). The agreement with the WIEDEMANN–FRANZ law is quite good at low temperatures, hence validating our experimental setup. At higher temperatures, the phonon contribution becomes non-negligible.

Finally, we calculated the ratio L/L_0 (where $L = \frac{\kappa\rho}{T}$) for each couple of κ and ρ data, in the whole temperature range above B_{c2}, and at lower fields just above $T_c(B)$. The resulting curves are plotted in fig. 4.9. Qualitatively, the overall shape of the curves is quite similar for both samples, so that I will not make any specific distinction in the following analysis:

- At very low temperatures, in the $T \to 0$ K limit, one finds $L \to L_0$. This is the result one expects when the phonons do not contribute to the thermal conductivity and when there is only *elastic* (impurity) scattering having the same impact on charge and thermal transport. It is even remarkable that the WIEDEMANN–FRANZ law is so well verified (deviations of only a few percent), a fact that is certainly due to the compound's particularly simple and nearly isotropic FERMI surface (see figure 2.13). In any case, it constitutes an excellent validation of our experimental setup.

- For temperatures around and just above 1 K we observe some deviations of the WIEDEMANN–FRANZ law: the ratio L/L_0 decreases. A possible explanation could be that inelastic collisions (due to the electron-phonon interaction or to the magnetism of the Pr^{3+} ion) appear. In general, the thermal transport is more affected (reduced) by

this inelastic scattering than the electric conductivity (this is particularly obvious in the case of electron-phonon scattering: as we are still in a relatively low temperature range, only low-$\overrightarrow{q}$ phonon modes are thermally activated which mainly allow *vertical* processes, affecting essentially the heat transport but which are less effective in reducing the electric current).

- When $T \geq 3$ K, the ratio L/L_0 increases significantly which is a clear evidence that the phonons begin to participate to the heat transport. This result is obtained for each applied field in the normal phase above T_c – the phonon contribution is roughly estimated to be about $20 - 25\%$ at 6 K.

4.2.3. Thermal conductivity measurements I – $\kappa(T)$ scans

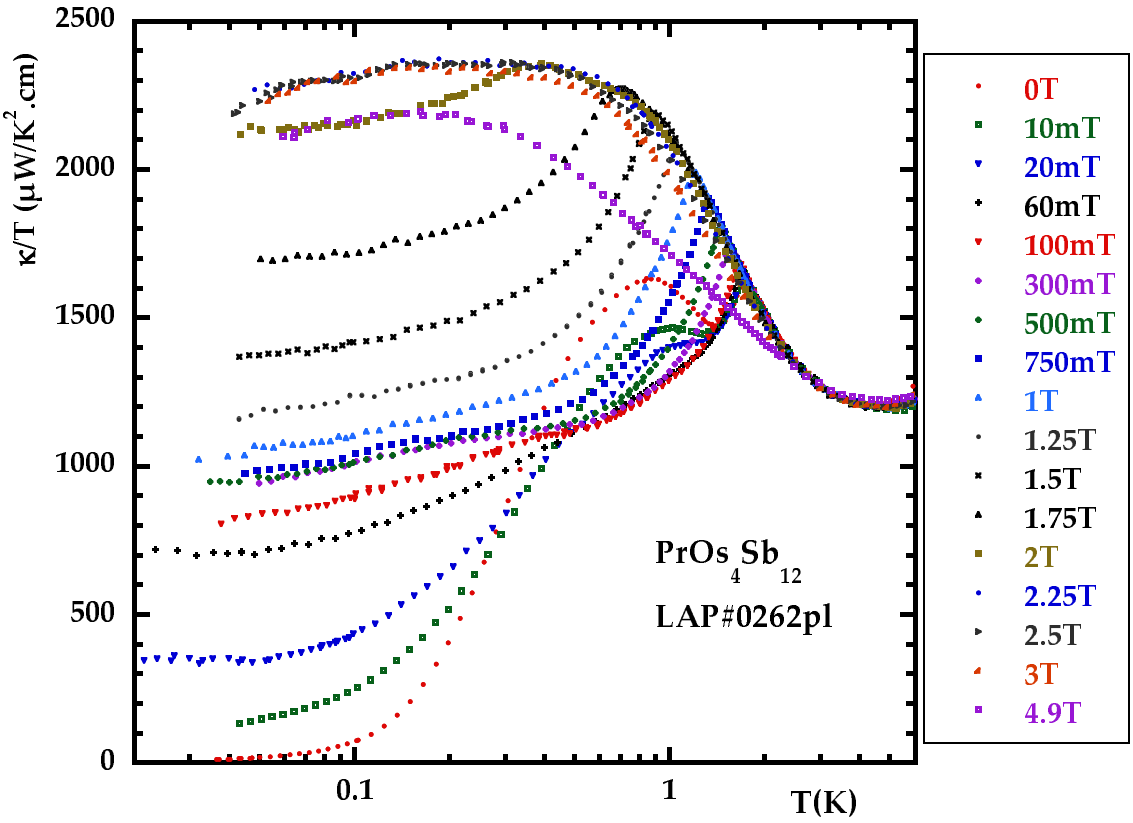

Figure 4.10. Overview: thermal conductivity $\kappa/T(T)$ at various magnetic fields of sample B2 (all available temperature scans). The effect of magnetic field on thermal transport at very low temperatures is very strong. For more clarity, see the next figure (4.11) which depicts only the curves at some selected magnetic fields.

Now being convinced that our experimental setup gives reliable measurements in the normal phase at low temperatures, we can discuss our results for $\kappa(T)$ (more precisely: $\kappa(T)/T$) at different magnetic fields, which are illustrated in figures 4.10, 4.11 and 4.13. Emphasis will be put on sample B2, and when necessary, we will compare the results with those of sample #02.03.11 (fig. 4.13).

Let us first remain in the *normal*, non-superconducting phase and take the curves at 2.5 and 3 T. When coming from "high" temperatures, the thermal conductivity decreases, due to the decrease of the phonon contribution, as already seen above. At about 4.5 K, it exhibits a minimum, and then it increases again and reaches a nearly constant value for $T \lesssim 300$ mK. This behavior reflects, by the means of the WIEDEMANN–FRANZ law, the temperature dependence of the electric resistivity, that decreases when lowering temperature in metals and strongly correlated electron systems. The overall shape of the corresponding κ/T curves is very similar for both examined samples, even if it seems that on sample B2, κ/T decreases slightly at very low temperatures (feature that is also reflected in the $L(T)/L_0$ data, see fig. 4.9). This was not observed on sample #02.03.11, but measurements stopped at ≈ 75 mK, whereas on sample B2 we tried to go down to ≈ 45 mK.

Next we will analyze what happens when entering the superconducting phase, coming from higher temperatures (without applied magnetic field). The WIEDEMANN–FRANZ law is no longer valid below the transition temperature since the charge transport is managed by the COOPER pair condensate whereas the heat transport is mediated by the electron quasiparticles (simple picture within the two fluid model). At T_c, BCS theory does not predict any anomaly in the electronic thermal conductivity at zero field[3]. From the characterization section, we already know that the situation is different in the case of $PrOs_4Sb_{12}$, where the $\kappa(T)/T$ curve exhibits a local maximum at T_c. In sample B2, the change of slope is quite abrupt (sharp peak) and the position of the κ/T maximum corresponds exactly to the onset of superconductivity as seen by C_p, whereas in sample #02.03.11 a detectable change of behavior in $\kappa/T(T)$ only takes place slightly below T_c (broad maximum at about 1.65 K). As discussed above, this difference is probably due to questions of sample quality. As to the origin of the local maximum at T_c and thus the deviations from standard BCS theory, we will give some possible explanations later on.

For the moment, I will also skip the analysis of the intermediate region between T_c and 0.5 K with the thermal conductivity enhancement just below 1 K (which disappears when applying a small magnetic field of only 20 mT, see fig. 4.11a). This second local maximum can be found on both samples, but is more pronounced on sample B2. In this temperature range, conclusions are in general not straightforward, so that we will treat the possible origins separately.

At lower temperatures ($T \ll T_c$) one expects a very small thermal conductivity because of the continuously decreasing number of excited quasiparticles. In the limit $T \to 0$ K, one has to distinguish between conventional and unconventional superconductors. In the first case, given the finite energy gap, the thermal conductivity yields a thermal activation behavior. This *exponential* drop of the "electronic" thermal conductivity often leads again to the apparition of the *phonon* contribution at very low temperatures. In contrast, in *unconventional* superconductors, the gap nodes are responsible for a larger quasiparticle contribution to the heat transport and the thermal conductivity exhibits a power law behavior as function of temperature, depending on the type and structure of the nodes. In the case where the phonons are negligible at T_c (like in UPt_3), it is possible to determine the structure of a non-isotropic gap or the type and the position of the gap nodes by measuring the thermal conductivity (i.e. the low energy excitations) following different crystallographic orientations. The behavior under applied magnetic field is also a good probe [189]. Of course, this type of measurement requires very pure crystal samples, otherwise additional effects like impurity scattering could influence and disturb the physics one

[3] In a simplified picture this can be explained as follows: the jump (divergence) in the specific heat C^{el} at T_c is "compensated" by a FERMI velocity tending to zero since within a simple calculation $v_F \sim \frac{dE_k}{dk}|_{k_F} \sim \frac{4E_F^2}{\Delta}\frac{(k-k_F)}{k_F^2} \overset{k\to k_F}{\to} 0$.

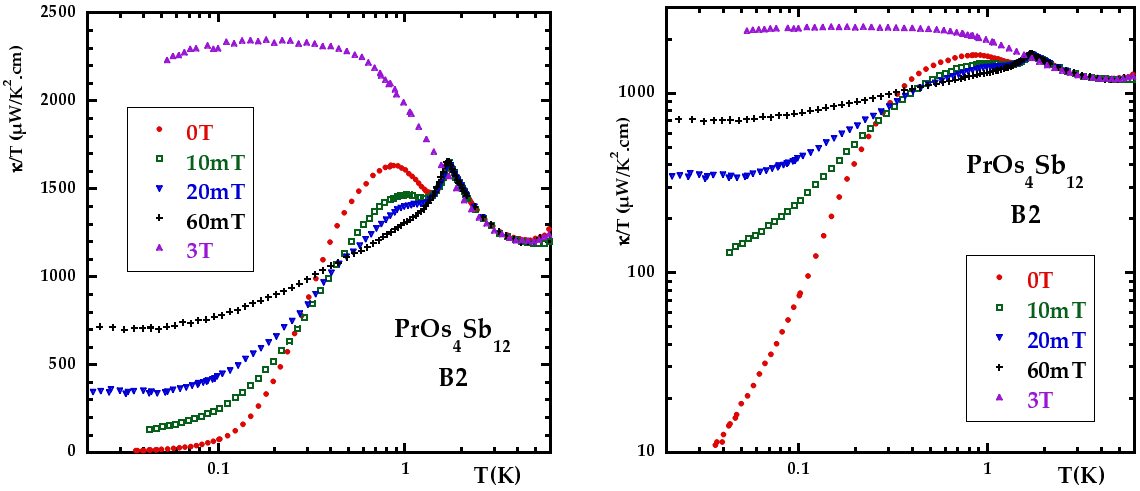

(a) Linear κ/T and logarithmic T scale. **(b)** Logarithmic scales for κ/T and T.

Figure 4.11. Thermal conductivity $\kappa/T(T)$ of sample B2 in zero field, low fields and in the normal phase. The linear scale plot (left) shows the effect of small fields at intermediate temperatures, and the logarithmic scale plot reveals the huge impact of small fields down to 20 mK.

intends to observe.

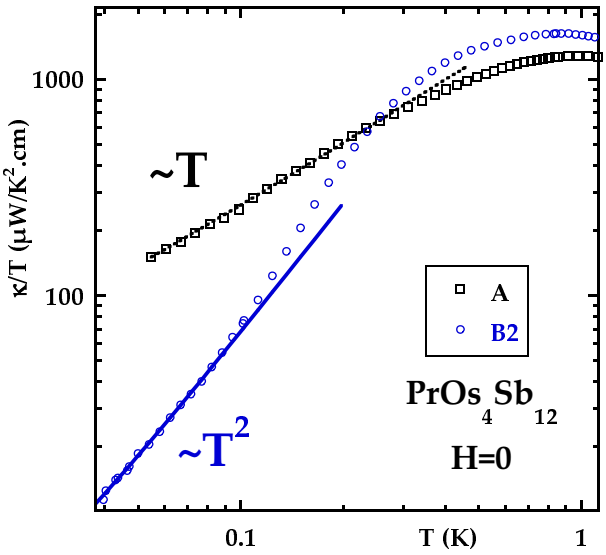

Figure 4.12. Comparison of the zero field thermal conductivity $\kappa/T(T)$ at lowest temperatures of sample A ($\kappa \propto T^2$) and B2 ($\kappa \propto T^3$, see also fig. 4.6).

This remark on the sample quality brings us back to our own experimental results. At very low temperatures (below 0.1 K), the $\kappa(T)/T$ curve exhibits a T^2-behavior, which corresponds to $\kappa \propto T^3$ (figures 4.12 and 4.6), with $\kappa/T(T \to 0) \sim 1.6$ μW/K^2 cm^{-1}, as already mentioned earlier when discussing sample quality. In principle, one can imagine two possible origins for the low temperature T^3 behavior: a dominant phonon contribution to heat transport or the signature of gap nodes in the electronic contribution (unconventional superconductivity). During the overall discussion (next chapters) of our results on $PrOs_4Sb_{12}$, we will develop a global scenario favoring the phonon origin.

In sample A, the situation is quite different (fig. 4.12 and 4.13): the low temperature behav-

ior of κ/T is probably dominated by inhomogeneities, resulting in a sort of cross-over regime with $\kappa/T \sim T$. This interpretation is compatible with the lower RRR value, the much higher $\kappa/T(T \to 0)$ value (see fig. 4.6) and the homogeneity problems (broad superconducting transition!) found on this sample. Hence we will not include this part of our measurements in the physical discussion, as they probably do not represent the intrinsic behavior of the compound.

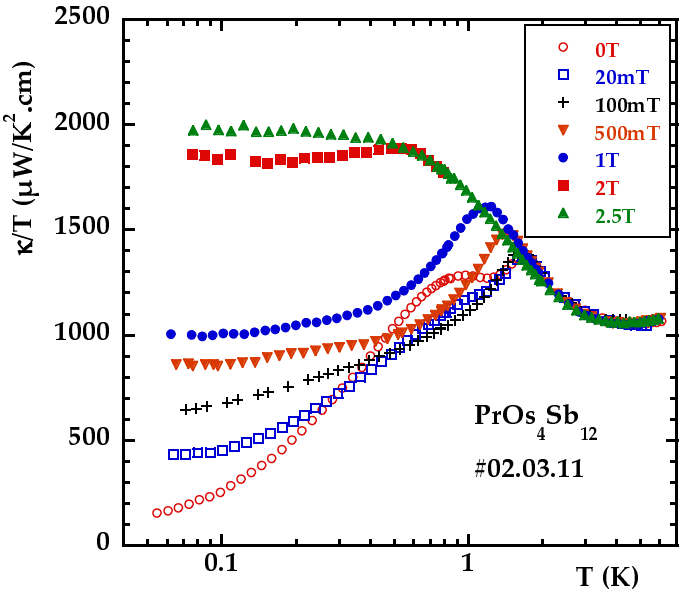

Figure 4.13. For comparison: $\kappa/T(T)$ scans at various magnetic fields on sample A. Qualitatively, we recover a similar behavior than on sample B2 (fig. 4.10): at very low temperatures, the magnetic field leads to a strongly enhanced thermal conductivity, at intermediate temperatures the opposite field effect is observed: κ decreases.

However, the most intriguing (and sample *independent*) feature is the huge increase of thermal conductivity at lowest temperatures when applying small magnetic fields $H \ll H_{c2}(0)$, as seen for example in fig. 4.11b. Such a behavior is quite uncommon, at least for conventional superconductors, and will play a key role for further exploring the experimental results. So let us first look at the field scans of thermal conductivity, $\kappa(H)$, especially at low temperatures.

4.2.4. Thermal conductivity measurements II – $\kappa(H)$ scans

Figure 4.14 displays our $\kappa(H)/T$ curves obtained on sample #02.03.11. As already mentioned in chapter 2, from an experimental point of view, $\kappa(H)$ scans are particular difficult to obtain:

- Preliminary thermometer calibration measurements are necessary if regulating on the setup thermometers, and at very low temperatures, one has to add extremely large time constants under magnetic field (this corresponds to long waiting periods for the experimentalist, which can attain several hours for one data point under the most unfavorable conditions!).

- Another, minor difficulty comes from the fact that our setup was not equipped with an independent magnetic field probe during the $PrOs_4Sb_{12}$ campaign; the field magnitude is deduced from the value of the current in the magnet. Under usual conditions, the precision of this method is sufficient, but in the case of $PrOs_4Sb_{12}$, the thermal conductivity field dependence at low fields is very strong, so that for example a small residual field of a few G can have a large effect on thermal conductivity. This might explain some minor mismatch between the starting point ($H = 0$) of our low temperature $\kappa(H)$ scans and the $\kappa(T)$ data in zero field, but the results are consistent when introducing error bars due to

the uncertainty in the determination of the magnetic field[4].

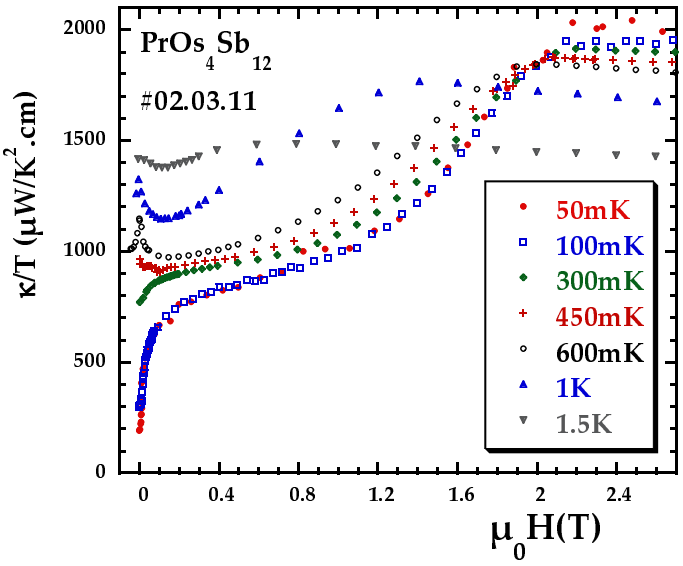

Figure 4.14. $\kappa(H)$ scans at different temperatures on sample A. The thermal conductivity increases strongly with magnetic field at very low temperatures, whereas it first decreases at intermediate temperatures.

As to the physical interpretation of the $\kappa(H)/T$ curves, this is also a quite subtle task. For fields $H > H_{c2}$, in the normal phase, the thermal conductivity follows the behavior of the electrical resistivity, according to the Wiedemann–Franz law, at least for low temperatures where we can neglect the phonon contribution. In the superconducting phase however, things are more complicated: essentially, the introduction of vortices into the sample strongly modifies its physical properties. The main changes concerning thermal transport are:

- quasiparticle scattering by the vortex lattice
- the contribution of the normal state electrons in the vortex cores
- in the case of *unconventional* superconductors, the modification of the excitation spectrum by the screening supercurrents around the vortices (the so-called Doppler shift).

To these effects one has to add the implications of the varying (with field and temperature) mean free paths of the other scattering mechanisms (quasiparticle-quasiparticle, quasiparticle-phonons, impurities, etc.). This last point (the influence of scattering) will be discussed in the analysis of the $\kappa(T)$ scans (at intermediate temperatures). Besides, one has to keep in mind that a magnetic field might also influence the phonon contribution κ^{ph} due to the induced vortices (additional scattering centers in the vortex cores). Altogether, to reduce the influence of these various effects, we will concentrate on the $\kappa(H)$ curves at lowest temperatures ($T \ll T_c$), where *elastic* scattering is predominant, and hence density of states effects constitute the main dependency of heat transport. At higher temperatures ($T \leq T_c$), the correct interpretation of $\kappa(H)$ curves would become rather sophisticated, at least without the knowledge/measurement of other independent physical properties of the sample. For similar reasons, on sample B2, we performed only one $\kappa(H)$ scan, namely at 50 mK (as a "compensation", over 15 much less time-consuming $\kappa(T)$ scans at different magnetic fields and over the whole temperature range were carried out, as shown previously on fig. 4.10).

[4] For the $\kappa(T)$ scan at zero field there is no uncertainty as to the magnetic field because these measurements were carried out *before* the $\kappa(H)$ scans, i.e. when the superconducting magnet was in its virgin, initial state.

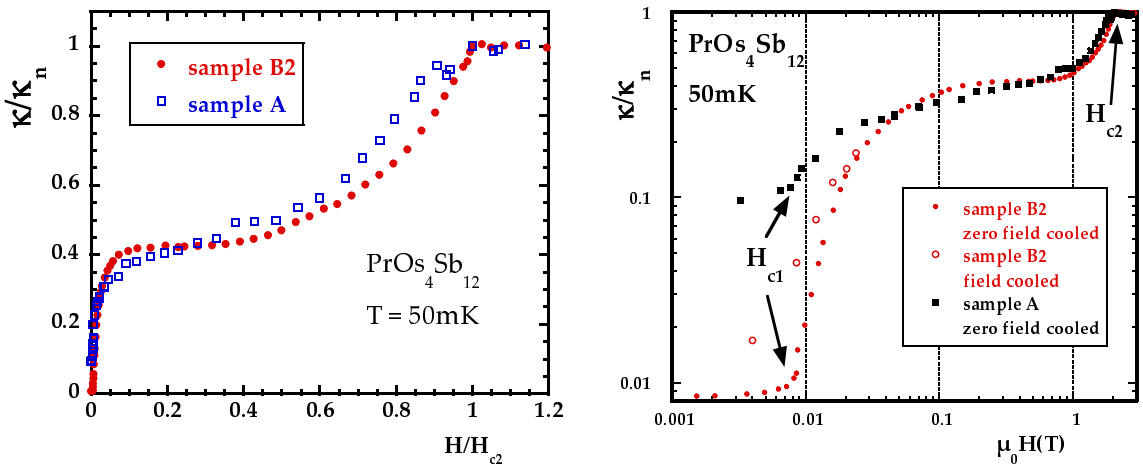

(a) Comparison of $\kappa/T(H)$ of samples A and B2 with linearly scaled axes.

(b) Comparison with logarithmic axis scaling. The arrows indicate the lower (H_{c1}) and upper (H_{c2}) critical fields. The data in the "field cooled" mode reveal residual flux pinning below 50 mT and a sensitivity to κ to fields as low as 5 mT.

Figure 4.15. Comparison of the thermal conductivity field scans ($\kappa/T(H)$ normalized to its value in the normal state, κ_n) at 50 mK on samples A and B2 with linear and logarithmic scales. The overall behavior on both samples is quite similar. The first steep in the thermal conductivity rise takes place at very low fields.

In fig. 4.15, we compare the $\kappa(H)$ scans at 50 mK of both samples, A and B2. The qualitative, and even quantitative agreement between the two curves is striking. $\kappa(H)$ increases almost stepwise, the first steep occurring at a very low field scale H_{c2}^S (compared to the upper critical field H_{c2}). This is consistent with the temperature scans at different (low) fields shown previously in fig. 4.11b. The difference between the two samples is of course that for sample B2, κ begins to increase from a much lower value, as already inferred from the comparison of the low temperature regime of the zero field $\kappa(T)$ scans (fig. 4.12). But the overall, characteristic shape seems to be a robust feature, at least much less sample sensitive than the $\kappa(T \to 0, H = 0)$ behavior. For sample B2, we also measured some data points in the "field cooled" mode, revealing residual flux pinning below 50 mT and a sensitivity of κ to fields as low as 5 mT. These low temperature $\kappa(H)$ scans form the basis for the multiband superconductivity (MBSC) scenario in $PrOs_4Sb_{12}$.

4.3. Discussion of $\kappa(T,H)$ and $R_c(T,H)$

This section is devoted to the physical discussion of our experimental results on $PrOs_4Sb_{12}$. First we will analyze the low temperature field dependence of thermal conductivity, $\kappa(H, T \to 0)$, which is consistent with a multiband superconductivity (MBSC) scenario in this compound. The next step consists of a detailed examination of the temperature dependence of thermal conductivity, $\kappa(T, H = 0)$. Especially, we will comment on its behavior

- at T_c, probably revealing strong coupling effects,
- at intermediate temperatures, partly related to the phonon contribution, and
- at very low temperatures, in order to extract some information about the superconducting gap topology and structure.

This last point leads to different conclusions than those of *Izawa* et al. [92], who claimed that $PrOs_4Sb_{12}$ is an unconventional superconductor with two distinct phases in the $H-T$ diagram, each one having point node gap singularities (derived from the anisotropy of the thermal conductivity when a magnetic field is rotated relative to the crystal axes, see fig. 2.8).

Finally, we will illustrate to which extend the thermal contact resistance data support the conclusions on the superconducting phase of $PrOs_4Sb_{12}$ obtained by thermal conductivity, and discuss our results in the light of the interpretations of other experiments.

4.3.1. Low temperature field dependence of κ and the two-band model

As regards the bare temperature dependence of the thermal conductivity below 0.2 K on the first sample A ($\kappa \propto T^2$), it does neither correspond to any simple case expected for nodes of the gap (for example $\kappa \propto T^5$ for point nodes [15, 64]), nor to a phonon contribution, and it is probably still a crossover regime. As shown before, a completely different behavior is observed on sample B2. Nevertheless, let us for the moment concentrate on the very low temperature field dependence of the thermal conductivity: $\kappa(H, T \to 0)$. It shows a striking feature, namely a strong increase of $\kappa(H, T \to 0)$ within a field scale $H^S \ll H_{c2}$ (see figures 4.11b and 4.15), followed by a plateau between 0.1 and $0.4H_{c2}$ (see fig. 4.15). Since this behavior seems quite robust, i.e. nearly sample independent, its analysis should be a good starting point.

As a first step, let us remind that through $\kappa(H)$ at $T \ll T_c$, we really probe electronic density of states effects. Indeed, from resistivity data above H_{c2}, it is clear that the electron mean free path is governed by impurities already below 0.3 K (see also the nearly temperature independent behavior of L/L_0 at 2.5 or 3 T below ~ 0.3 K in fig. 4.9). This will be even more true in the superconducting state. So the thermal conductivity is certainly controlled by *elastic* scattering below 300 mK. As to the phonon contribution to heat transport for temperatures low compared to T_c, phonon scattering is governed by static defects rather than by electronic quasiparticles. At very low temperatures, the phonon mean free path is large and often limited by the sample size. Hence, the phonon contribution should be field independent (at least, it cannot be increased by field), and it may only contribute to the temperature dependence of κ.

Starting from thermal conductivity values at $T \ll T_c$ and $B = 0$ T, let us switch on a small magnetic field (for example successively 10, 20, 60 and 100 mT) and look at the changes in the thermal conductivity: by contrast to higher, intermediate temperatures where κ decreases with field (fig. 4.11a), we observe a drastic increase in thermal conductivity, which is clearly seen when comparing the very low temperature range of the different $\kappa(T)$ scans (fig. 4.11b

for sample B2), or directly from the beginning (low field range) of the $\kappa(H)$ scans at 50 and 100 mK (see figures 4.14 and 4.15). This pronounced and rapid increase with field of the thermal conductivity is remarkable and cannot be explained within the framework of a simple one-band BCS superconductor theory. Usually, small magnetic fields hardly affect the low temperature thermal conductivity: for conventional superconductors in the clean limit (neglecting the heat transport by the vortex cores with localized quasiparticles) vortex scattering reduces thermal conductivity (but this is in general a small effect at low temperatures).

Doppler shift?

A first idea to explain this unusual, pronounced enhancement in thermal conductivity at very low temperatures and low fields is to think of *unconventional* superconductivity. Excitations in an unconventional superconductor in the mixed state experience a Doppler shift due to the existence of the supercurrents building the vortex lattice. So the density of states for such a superconductor changes substantially at low energies under magnetic fields above H_{c1}. In particular, if the gap has a line of nodes in the plane perpendicular to the field, the Fermi surface density of states differs from zero, and after averaging over the vortex lattice, found proportional to $\sqrt{H}$. In that case, under the same conditions, κ is a linear function of the magnetic field [123]. Calculations for the thermal conductivity in the case of unconventional superconductors with point nodes of the gap [123] yield a smaller field dependence of κ: in the "superclean" limit ($\hbar\Gamma$ is a characteristic energy related to the quasiparticle scattering rate Γ in the unitary limit)

$$\kappa \sim H^{3/2} \ln\left(\frac{\Delta}{v_F\sqrt{eH}}\right) \text{ for } \hbar\Gamma \ll k_B T \ll \Delta \text{ and } \frac{\hbar\Gamma}{\Delta} \ll H/H_{c2}. \tag{4.1}$$

Here, our purpose is not to look at the detail of the formulas and their validity range; the important point is to get an idea of the possible κ variation as a function of the magnetic field in superconductors with nodes in $\Delta(\overrightarrow{k})$ at very low temperatures and low fields.

These results for unconventional superconductors have to be compared to our experimental data and to the $\kappa(H)$ behavior of other classes of superconductors. Figure 4.16 contains several lowest temperature $\kappa(H)$ scans[5] in reduced units, namely of a simple BCS superconductor (exemplified by Nb), the *heavy fermion* UPt_3 (unconventional superconductor with gap nodes) and of the multiband superconductor MgB_2, the whole amended by our own $\kappa(H)$ data at 50 mK on sample B2 of $PrOs_4Sb_{12}$.

It is clear from this plot that:

- For Nb, the typical field dependence of a clean and isotropic *s*-wave superconductor is observed, in particular the thermal conductivity is completely field independent for $H < 0.4H_{c2}$.
- A much faster increase in κ is observed for UPt_3: It is almost linear in H and corresponds to the predictions in the case of line nodes (a similar H variation has been observed for $LuNi_2B_2C$ where a strong anisotropy of the energy gap is claimed, $\Delta_{max}/\Delta_{min} > 10$ [28]). But this increase is still much slower than what is measured in $PrOs_4Sb_{12}$, whereas the Doppler shift for point nodes in this compound should be much less effective in $\kappa(H)$.

[5] Reminder: here, at lowest temperatures, we only analyze the electronic contribution to κ.

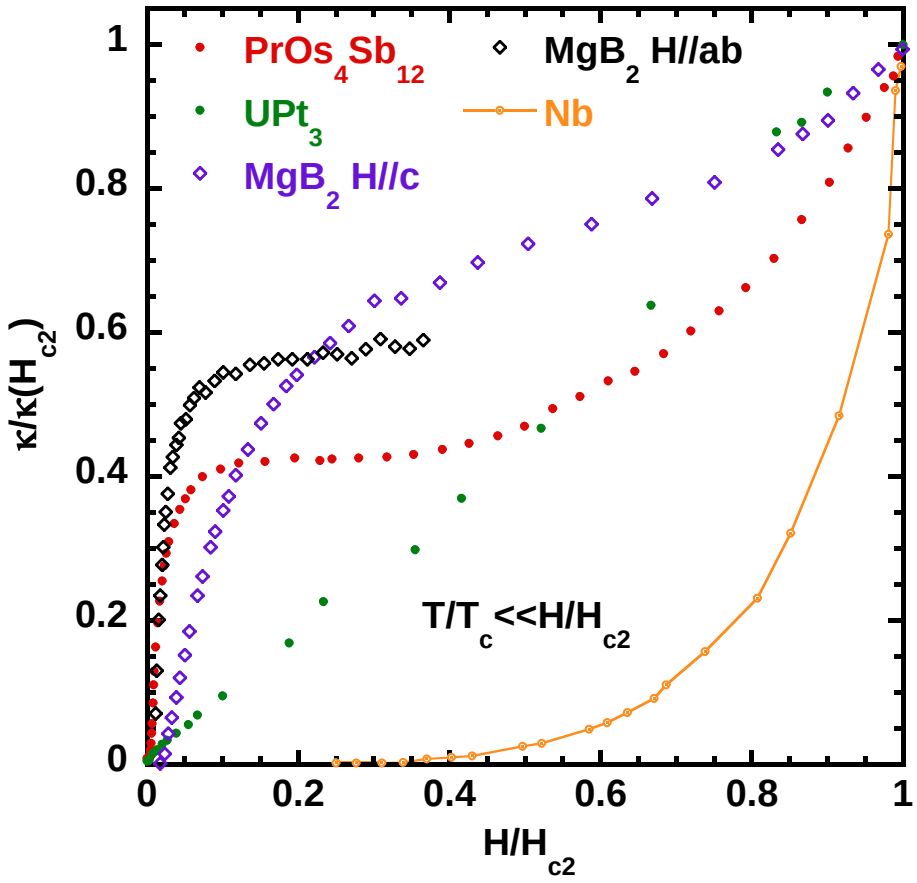

Figure 4.16. Comparison of the normalized, very low temperature (electronic) thermal conductivity of several superconductors (Nb, UPt_3, MgB_2 and $PrOs_4Sb_{12}$) as a function of H/H_{c2}. This plot originates from [186] – we just superposed our own $PrOs_4Sb_{12}$ data at 50 mK of sample B2. The comparison between MgB_2 and $PrOs_4Sb_{12}$ is striking, and hence supports MBSC in $PrOs_4Sb_{12}$.

MgB_2 and multiband superconductivity (MBSC) scenario

The last superconductor represented in fig. 4.16 is MgB_2 (in two different field orientations), which has obviously a field dependence of κ very similar to that of $PrOs_4Sb_{12}$. This compound is now considered as the archetype of a two-band superconductor with fully opened gaps: it is experimentally well established that two superconducting gaps of different amplitudes open at the same bulk transition temperature of about 40 K on the σ and π sheets of the FERMI surface, revealing the strong *interband* pairing interaction in this compound. Several of the experiments reporting MBSC in MgB_2 are: high-resolution angle-resolved photoemission spectroscopy (ARPES) [207], thermal conductivity measurements [186], specific heat measurements [32], "ANDREEV reflection" (tunneling) spectroscopy [198] and scanning tunneling microscope measurements (STM) [59]. The strong field sensitivity of the smallest gap on the minor band has been demonstrated by several of these experiments [32, 59, 186].

The possibility of multiband superconductivity in $PrOs_4Sb_{12}$ was for the first time derived from our low field $H_{c2}(T)$ data [130]. Indeed, in $PrOs_4Sb_{12}$, there are several electronic bands which can contribute to the formation of COOPER pairs. From the comparison of DEHAAS-VANALPHEN and specific heat measurements, we know that some of them contain quasiparticles

with large effective masses and the other light quasiparticles (see figure 2.14 in the introductory chapter). This can be modeled by two bands with different density of states. In this configuration, *inter-* **and** *intra*band interactions can now exist. On the formal level ([128], see also introductory chapter), this means that the coupling constant λ has to be replaced by a matrix $(\Lambda)_{ij}$ $(i,j=1,2)$ with elements λ_{ij} where i and j are the indexes of the initial and final band in the scattering process, respectively. The λ_{ij} characterize the interactions between the bands i and j, and in a weak coupling scheme, one separates them into two main contributions: the interaction matrix element ("interaction potential") V_{ij} and the density of states N_j of the final band j

$$\lambda_{ij} = V_{ij} N_j \ . \tag{4.2}$$

The matrix $(V)_{ij}$ is *hermitean*, but the contribution of the density of states naturally depends on the considered band interaction ([130]). As a result of the interband interactions, the transition temperature is slightly enhanced (compared to the case where there is only the band of heavy quasiparticles), and there now exist two superconducting gaps (corresponding to the different sheets on the FERMI surface) with the same transition temperature. Compared to MgB_2, the main difference in the λ_{ij} on the various sheets of the FERMI surface in $PrOs_4Sb_{12}$ might come already from the different density of states contributions N_j, not only from different pairing interactions (V_{ij}).

Theoretically, for κ (as well as for the specific heat) the field dependence of the smallest gap is controlled by a field scale named H_{c2}^S, corresponding to the overlap of the vortex cores[6] of the band with the smallest gap (Δ_S), having a coherence length of order $\frac{\hbar v_F}{\Delta_S}$ [205, 105]: above H_{c2}^S, the contribution to κ of the small gap band is close to that in the normal state, *only* when it is in the dirty limit (a condition easily satisfied owing to the large coherence length of that band). This remains true even if small inter-band coupling prevents a real suppression of Δ_S at H_{c2}^S [205]. In the case of $PrOs_4Sb_{12}$, the large ratio of H_{c2}/H_{c2}^S may originate both from the difference in the gap and from the difference in the FERMI velocity between the bands, where

$$H_{c2}/H_{c2}^S \sim \left(\frac{\Delta_\mathrm{l} \cdot \mathrm{v}_\mathrm{s}^F}{\Delta_\mathrm{s} \cdot \mathrm{v}_\mathrm{l}^F} \right)^2 . \tag{4.3}$$

.

In the framework of the superconducting two-band model, the explanation for $\kappa(H)$ becomes quite intuitive (see above): a small magnetic field of order H_{c2}^S already restores a large number of light mass thermal excitations in the small gap band (delocalized quasiparticles), providing an additional channel for heat transport. Hence the thermal conductivity is strongly enhanced at fields $H \sim H_{c2}^S$. The crossover to a plateau observed on $\kappa(H)$ between ~ 0.1 and ~ 1 K is governed by the field-independent contribution of this light band, until the contribution of all bands is restored closer to H_{c2} yielding a new increase of $\kappa(H)$. Further, it can be noticed (compare for example the beginning of the $\kappa(H)$ curves at 50, 100 and 300 mK in fig. 4.14 or the several $\kappa(T)$ curves at low temperatures in fig. 4.11b) that with increasing temperature, the low field "step" in κ is reduced. This behavior reflects the fact that with rising temperature more and more light quasiparticle excitations are present above the small energy gap, even at zero field, and hence the effect of a magnetic field (of "gap suppression") becomes less significant. At higher temperatures supplementary effects (to be discussed later on) come into play.

Back to $\kappa(H, T \to 0)$. Quantitatively, the increase at low field for MgB_2 and $PrOs_4Sb_{12}$ is much stronger than in any of the materials evoked before. More than half of the normal state

[6] Note that H_{c2}^S is only a cross-over field: it does not mark a real phase transition, which only happens at H_{c2}.

thermal conductivity is restored already at $H \approx 0.05 \cdot H_{c2}(0)$ for MgB_2 ($H \parallel ab$), and about 40% in the case of $PrOs_4Sb_{12}$. These figures reveal the existence of an additional field scale much below H_{c2}. Note that for DOPPLER shift effects in unconventional superconductors, H_{c2} remains the only field scale. To date, the only available explanation for the large κ increase at low fields in $PrOs_4Sb_{12}$ is the existence of gaps of different amplitudes on the different sheets of the FERMI surface, and the "suppression" by vortex overlap of the smallest energy gap in small fields.

Altogether, $\kappa(H, T \to 0)$ provides clear evidence that $PrOs_4Sb_{12}$ is also a host of multiband superconductivity, like MgB_2. But several questions remain open:

- It is possible to extract an order of magnitude for the small superconducting gap $\Delta_S(0)$? We only know from $\kappa(H, T \to 0)$ the existence of H_{c2}^S, but equation (4.3) shows that both v_F and Δ can yield a $H_{c2}^S \ll H_{c2}$.
- What is the topology of the gaps, especially of Δ_S? Are there any gap nodes ?
- Is it possible to observe a field effect on the electronic density of states by specific heat measurements at very low temperatures, like in the case of MgB_2 [32] ?

At this stage, here are some comments:

- **On the value of Δ_S** To directly evaluate the smallest gap value from equation (4.3), *theoretical* work combining band calculations (for the determination of the v_F) and a realistic fit of $\kappa(H)$ (to extract H_{c2}^S) would be needed. If instead we take the inflection point at low fields of $\kappa(H)$ at 50 mK as a "typical value", we get $H_{c2}^S \approx 15$ mT. With the ratio of the FERMI velocities of both bands extracted from $H_{c2}(T)$ [130], we then find a gap ratio of order 2-3: this rough estimate contrasts with the very large field effect. It is a consequence of the hypothesis that the two bands of the model have very different renormalized FERMI velocities. The mere fact that this is possible may be taken as indicative of weak interband scattering, justifying the possibility of MBSC. In what follows, we proceed the other way round: we try to estimate the small gap magnitude from other measurements (notably $\kappa(T \ll T_c, H = 0)$, and then a posteriori check the overall consistency with equation (4.3), owing to the $\kappa(H)$ data.
- **On the confirmation by specific heat** Up to now, we are not aware of such measurements. The most likely reason for this is related to the order of magnitudes: In MgB_2, it is sufficient to measure $C_p(H, T)$ in the K range, because of the relatively large gap magnitudes. In the $PrOs_4Sb_{12}$ case, temperatures down to 100 or 50 mK are probably necessary in order to be sensitive to the small gap excitations under field, but in this temperature range, the measured specific heat exhibits a large upturn, possibly due to *nuclear* contributions. Hence the precise determination of changes in the *electronic* contribution to the specific heat under small magnetic fields turns out to be a great experimental challenge... Moreover, if the bands are indeed associated to light and heavy masses, a negligible effect on C_p is expected.

4.3.2. Temperature dependence of κ in zero and low magnetic field

In the remaining part of this chapter, we try to refine the MBSC scenario in $PrOs_4Sb_{12}$ with respect to the gap topology and an estimation of the magnitude of the smallest gap. For this

purpose, we examine carefully the temperature dependence of thermal conductivity, notably in zero field. Here we will essentially take into account the results obtained on sample B2, circumventing sample A where the data might suffer from homogeneity problems.

Before concentrating on the very low temperature range, let us successively analyze $\kappa(T)$ at the superconducting transition and at intermediate temperatures.

Signature of the superconducting transition in thermal conductivity

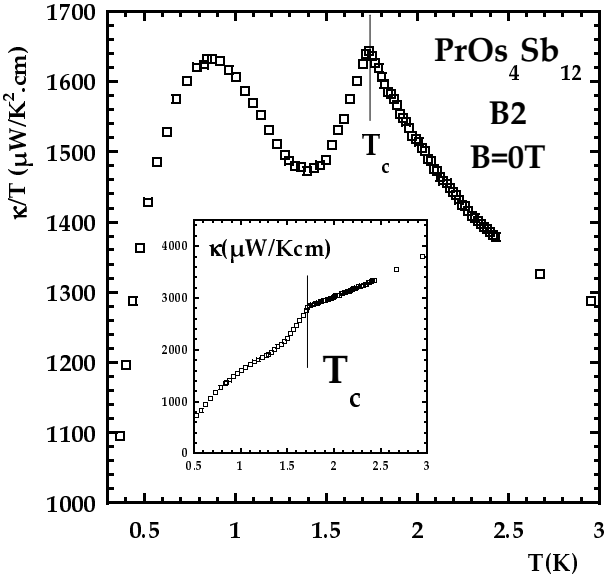

Figure 4.17. Zoom on the superconducting transition (local maximum) in the zero field thermal conductivity $\kappa/T(T)$. The inset shows the change of slope of $\kappa(T)$ at T_c.

At the beginning of this chapter, we already stressed the highly improved homogeneity of sample B2, deduced from the simultaneous appearance of a superconducting anomaly in specific heat, electric resistivity and thermal conductivity (see fig. 4.5a). Now we have to clarify the origin of the kink of $\kappa(T)/T$ at T_c (change of slope in $\kappa(T)$, see fig. 4.17), since it seems to be a characteristic feature of $PrOs_4Sb_{12}$, although it is not a universal behavior of κ in superconductors: in the case of UPt_3, there is no detectable signature of T_c in the thermal conductivity, at least in zero field [189]. The opposite behavior is known from heat transport in the superconducting phase of high-T_c cuprates, where $\kappa(T)$ exhibits a strong upturn below T_c due to the boosting of the quasiparticle–quasiparticle scattering lifetime [217]. A pronounced effect on thermal conductivity is also known from strong-coupling superconductors (for example Pb). There the predominant role of inelastic electron-phonon scattering mechanisms leads to a strong reduction of the electronic heat transport below T_c, and the slope $d(\kappa_S/\kappa_N)/d(T/T_c)$ at T_c^- is typically of the order of 5-10 [24, 2].

In $PrOs_4Sb_{12}$, just above T_c, $L/L_0 \lesssim 1$, which indicates a phonon thermal conductivity (κ^{ph}) negligible compared to the electronic heat transport (κ^{el}) in the neighborhood of T_c. The change of slope observed at T_c ($d(\kappa_S/\kappa_N)/d(T/T_c)$) is of order 1.4. In conventional superconductors, it is generally ascribed to the combined effects of the opening of the gap and the energy dependence of the electron-phonon scattering rate on κ^{el} [24, 2]. In the BCS weak-coupling limit, its maximum value is of order 1.4 when lattice scattering is the limiting mechanism for κ^{el} (see measurements on very pure In or Sn [87, 204, 95]). For $PrOs_4Sb_{12}$, electronic inelastic scattering may replace the effect of electron-lattice scattering. Nevertheless, taking into account the relative weight of elastic to inelastic scattering, as well as MBSC (negligible effect of gap opening in the small gap

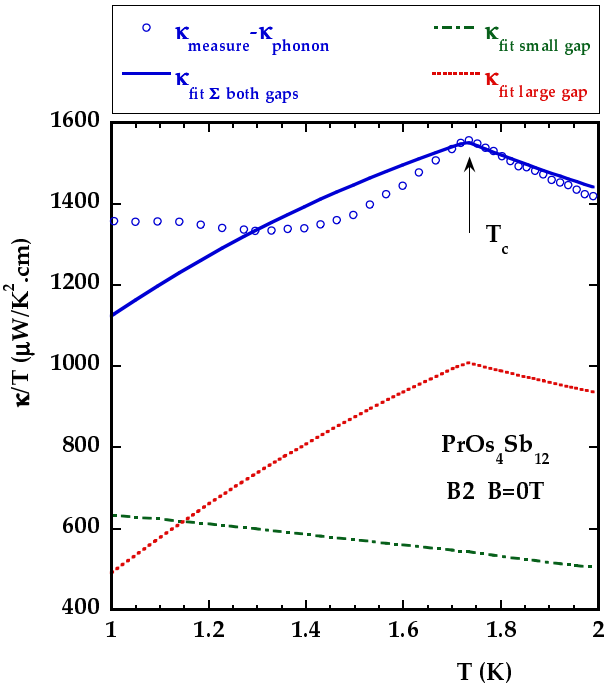

Figure 4.18. Analysis of the slope $d(\kappa^{el}/T)/dT$ at T_c^-. For the separation of electronic and phonon contribution, see fig. 4.23 and the next section. The data fit is based on a weak-coupling scheme and predominant phonon scattering [204] with $\rho(T_c)/\rho(T \to 0) \sim \rho_{\text{inelastic}}/\rho_{\text{elastic}} \sim 20$. It includes two parallel conduction channels associated to electronic bands with different gap amplitudes (see fig. 4.26), with a relative weight of the small gap band of 0.35. For the contribution of the large gap band, a clear change of slope occurs below T_c (but less pronounced than measured on $PrOs_4Sb_{12}$), whereas the thermal conduction channel related to the small gap band remains unaffected.

band, as seen in fig. 4.18), the value of $d(\kappa_S/\kappa_N)/d(T/T_c) \approx 1.4$ appears very large. Indeed, even if assuming predominant inelastic scattering at T_c (with $\rho_{\text{inelastic}}/\rho_{\text{elastic}} \sim 20$ like in very pure metals), calculations within a weak-coupling scheme [204] yield a smaller slope than measured in $PrOs_4Sb_{12}$ (see fig. 4.18). This is likely a signature of strong-coupling effects, as observed (and calculated) for example in lead ($d(\kappa_S/\kappa_N)/d(T/T_c) \approx 7$ [86, 24, 2, 104]). Indeed, Sb NQR [101] or heat capacity analysis [66] have already stressed strong-coupling effects in $PrOs_4Sb_{12}$.

Origin of the "1 K anomaly", very low temperature behavior and superconducting gap topology

Relevance of phonon contribution

Let us continue the analysis of $\kappa(T)$ towards lower temperatures. In the vicinity of about 1 K, $\kappa/T(T)$ exhibits a second local maximum ("1 K-anomaly", precisely at $\sim$ 875 mK, reaching approximately the same κ/T-value than at T_c, see fig. 4.17), which diminishes when applying small magnetic fields and has completely disappeared in the κ/T-curve at 60 mT (see fig. 4.19). Finally, below about 100 mK, we have $\kappa \propto T^3$.

A qualitatively similar κ-behavior is found in several compounds. Indeed, a maximum of κ/T below T_c followed by a T^3 behavior of κ at low temperature is well-documented from superconducting Pb, Ta and Nb [86, 143, 44], from the rare earth nickel borocarbides RNi_2B_2C (R=Lu, Y) [30, 176, 73], and also for other materials. The overall scenario is as follows: On cooling, the phonon mean free path l^{ph} increases from a law $l^{ph} \sim T^{-1}$ (when it is limited by electron-phonon interactions above T_c), up to a typical crystal dimension (boundary scattering) at the lowest temperatures, where then $\kappa^{ph} \propto T^3$ (as experimentally observed). Due to the reduction of scattering by electrons, an intermediate regime with a "boosted" phonon mean free path starts below T_c, described empirically by $l^{ph} \sim T^{-1}(T_c/T)^n$. Together with κ^{el} (depending on the

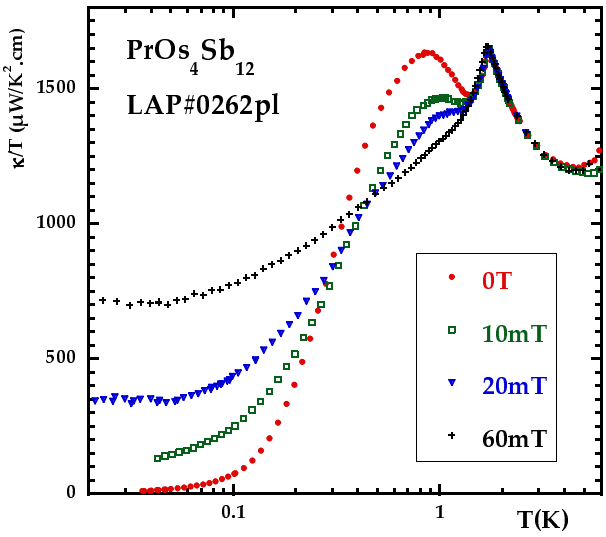

Figure 4.19. Temperature scans $\kappa/T(T)$ at small magnetic fields on sample B2, allowing to follow the successive decrease of the "1 K-anomaly".

different compounds), it is responsible for the κ/T enhancement at intermediate temperatures (see for example the detailed κ-analysis on superconducting Pb given in [86, 24], see also fig. 4.20). The vanishing of this anomaly under magnetic field is documented in the borocarbides [176], the other

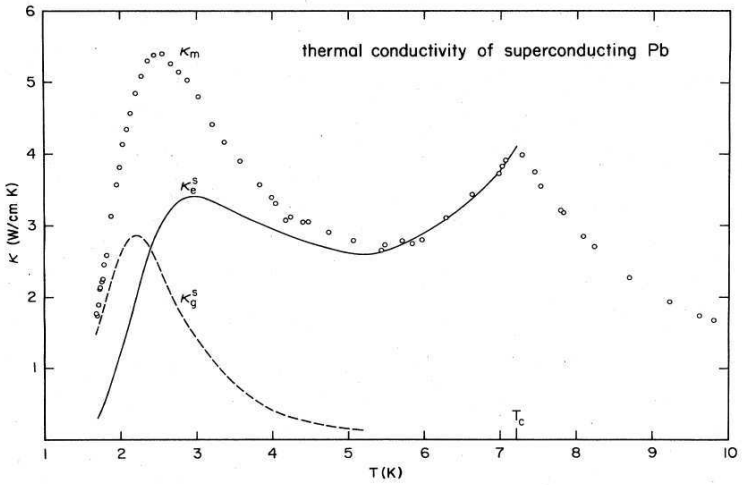

Figure 4.20. Low temperature thermal conductivity $\kappa(T)$ of Pb (open circles, κ_m), taken from [86]. κ_g^s and κ_e^s are the estimated phonon and electronic contribution to heat transport, respectively. In the Pb case, the local maximum of $\kappa(T)$ at intermediate temperatures within the superconducting phase is clearly comes from both an enhanced phonon and an enhanced electronic contribution, due to the reduction of electronic scattering centers within the superconducting phase.

Apart from the qualitative agreement, is it reasonable to apply this scenario to $PrOs_4Sb_{12}$?

In *ordinary* superconductors, κ^{el} drops exponentially in the $T \to 0$ limit, which often leads to the appearance of the phonon contribution to heat transport, even if it is negligible at T_c. Of course, a measured $\kappa \propto T^3$ behavior for $T \ll T_c$ is not necessarily due to κ^{ph}, it could also result from the electronic contribution in the case of line nodes of the gap in *unconventional* superconductors [15, 64], like the high-T_c cuprates [75, 115] or UPt3 [189]. However, in $PrOs_4Sb_{12}$, we

have no clear indication for gap nodes, in agreement with STM [192], Sb NQR [101] and μSR [120] measurements. Nevertheless, we recall that other experiments point to a gap with nodes [92, 40, 81].

At intermediate temperatures, the situation is rather complex, with no generic behavior. Most intuitively, the condensation of electronic scattering centers may act on two competing channels: diminution of the available thermal excitations on the one hand, and increase of the inelastic mean free path of both electrons and phonons on the other. We already mentioned the high-T_c cuprates where the κ-enhancement below T_c is essentially related to a boosted quasiparticle inelastic scattering lifetime [217, 102, 42]. In UPt_3, $\kappa/T \simeq \kappa^{el}/T$ increases below T_c in continuity of the behavior in the normal phase ($L/L_0 < 1$), before dropping at lower temperatures [189]. In less "exotic" superconductors like Nb or Pb, one finds the results given above that resemble the $PrOs_4Sb_{12}$ data and altogether reflect the increase of the phonon (and electron) inelastic scattering times.

On that basis, it seems worth to try a simple but quantitative analysis within a reinforced κ^{ph} scenario in $PrOs_4Sb_{12}$, similar to the observations on Pb, even if there the main electronic scattering mechanism above T_c is due to phonons ($\rho \propto T^5$), whereas it is dominated by electron-electron scattering in $PrOs_4Sb_{12}$. The extracted orders of magnitude, for example for the phonon mean free path l^{ph}, will then give further insight to the validity of this scenario.

Let me first remind the simple kinetic expression for κ^{ph} at low temperatures:

$$\kappa^{ph} = \frac{1}{3} C^{ph}\, c_s\, l^{ph} = \frac{1}{3} C^{ph}\, c_s^2 \tau \ , \quad \tau^{-1}(T) = \tau_{\text{ph-e}}^{-1}(T) + \tau_{\text{size}}^{-1}, \tag{4.4}$$

where c_s: sound velocity, $\tau_{\text{ph-e}}$: phonon-electron scattering lifetime and τ_{size}: boundary scattering lifetime and $C^{ph} = \beta \cdot T^3$: phonon specific heat ($\beta \sim 16.3$ μJK^{-4}cm^{-3} [125]). In the regime of dominant electron-phonon scattering (normal phase), one generally finds $\kappa^{ph} \propto T^2$, meaning $l^{ph}(T) \propto T^{-1}$.

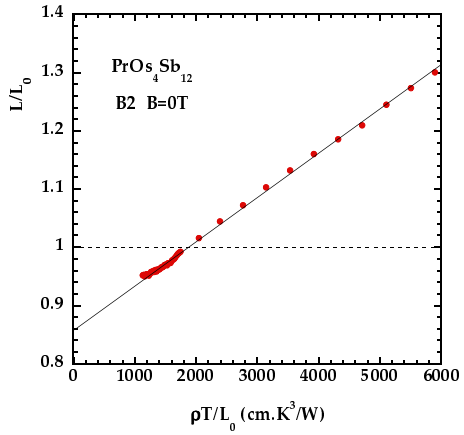

Figure 4.21. Determination of the phonon coefficient a according to equation (4.5), yielding $a \sim 75$ μWK^{-3}cm^{-1}, as obtained from a linear fit of the data. However, note that this simple picture implies a temperature independent $L^{el}/L_0 \sim 0.85$.

First, we estimate κ^{ph} in the normal phase, where phonons are evidenced through $L/L_0(T > 3\text{ K}) > 1$. Quantitatively, the phonon contribution can be obtained from the deviation of the Wiedemann–Franz law by fitting $\frac{L}{L_0}$ as a function of $\left(\frac{\rho T}{L_0}\right)$, given the following relation

$$\frac{L}{L_0} = \frac{L^{el}}{L_0} + a\frac{\rho T}{L_0} \ , \tag{4.5}$$

with $\kappa^{el}/(T\sigma) \equiv L^{el} = \text{const}$ and $\kappa^{ph} = aT^2$. As seen on fig. 4.21, the law is approximately valid (and one gets $a \sim 75$ μWK^{-3}cm^{-1}) except that it extrapolates for $T \to 0$ to $L/L_0 = L^{el}/L_0 \sim$

0.85 instead of 1. This is due to the fact that inelastic scattering is more efficient on the collision time of thermal transport than on electric transport. Empirically, one can write that

$$\text{if } \rho = \rho_0 + AT^2 \ , \tag{4.6}$$

$$\text{then } \frac{T}{\kappa^{el}} \sim \frac{\rho_0}{L_0} + f\frac{A}{L_0}T^2 \sim \frac{\rho_0}{L_0} + f\frac{(\rho(T)-\rho_0)}{L_0} \text{ with } f > 1. \tag{4.7}$$

For $f = 1$, one recovers the WIEDEMANN–FRANZ law. If for $T \to 0$ L is slightly different from L_0 ($L \to \overline{L_0}$), one can try to extract the phonon contribution by fitting the thermal conductivity data $\kappa = \kappa^{ph} + \kappa^{el}$ to:

$$\frac{\kappa(T)}{T} \sim aT + \frac{\overline{L_0}}{\rho_0 + f(\rho(T)-\rho_0)}. \tag{4.8}$$

a and f are free parameters, $\overline{L_0}$ is deduced from the field measurements of L at very low temperatures, $\rho(T)$ and ρ_0 are experimental data. Then we get $a \sim 80\ \mu\text{WK}^{-3}\text{cm}^{-1}$ and $f = 1.4$ (for the data in 3 T with $\overline{L_0} \sim 1.01$). Note that both methods yield only rough estimates of the phonon contribution, since the temperature dependence of L^{el}/L_0 or f (varying influence of inelastic scattering on the ratio κ^{el}/σ) is not known from the experiment[7] and are simply assumed to be constant. In the following calculations, we will use a conservative value of $a \sim 60\ \mu\text{WK}^{-3}\text{cm}^{-1}$ for $\kappa^{ph}(T > T_c)$, meaning that inelastic scattering does not lead to strong deviations from $L^{el}/L_0 \sim 1$. This is only an assumption, but the low temperature part of κ^{ph} will be determined independently from this estimation (see below), and for the link between both, agreement on the correct order of magnitude is sufficient.

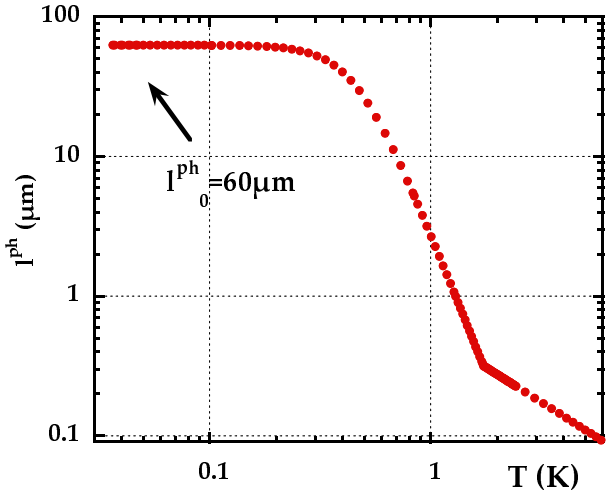

Figure 4.22. Plot of the phonon mean free path $l^{ph}(T)$ according to the model described by equation (4.9) with $n = 3$. In the normal phase, $l^{ph}(T) \propto T^{-1}$, then, when entering the superconducting phase, it is boosted due to the reduction of the number of electronic scattering centers, and at lowest temperatures $l^{ph}(T)$ saturates because of boundary scattering (l_0^{ph} of the order of the smallest sample dimension).

Now, we estimate the phonon contribution in the superconducting phase. As already indicated, we suppose that $\tau_{\text{ph-e}}$ is "boosted" below T_c, maintaining the general structure of equation (4.4):

$$\frac{1}{\kappa^{ph}_{sc}/T} = \frac{1}{\kappa^{ph}_{normal}/T}\left(\frac{T}{T_c}\right)^n + \frac{1}{bl_0^{ph}T^2}, \tag{4.9}$$

where $\kappa^{ph}_{normal} = aT^2$ with $a \sim 60\ \mu\text{WK}^{-3}\text{cm}^{-1}$ (see above). The second term on the right-hand side of equation (4.9) comes from the calculation of κ^{ph} according to equation (4.4) in the

[7] L^{el}/L_0 is typically close or slightly inferior to 1, but strong deviations with $L^{el}/L \sim 0.65$ (as observed in $CeCoIn_5$, see next chapter) are possible.

boundary scattering limit ($b = 1/3 \cdot \beta \cdot c_s$). For $T < 100$ mK, bl_0^{ph} is fixed by κ/T, yielding $l_0^{ph} \sim$ 60 µm, i.e. of the order of the smallest sample dimension ($b = 10.9 \times 10^3$ WK^{-4}m^{-2}, DEBYE temperature $\theta_D \approx 200$ K [125], sound velocity $c_s \approx 2000$ ms^{-1}). The adjustable parameter is mainly the power law (n) for the boosted temperature dependence of l^{ph} : it proved impossible (adjusting n) to account for the local maximum in κ/T only by the phonon contribution. In fig. 4.23, we plot the most "reasonable" case $n = 3$. The easiest way to catch the main point of this analysis is to follow first the temperature dependence of the phonon mean free path $l^{ph}(T)$, plotted in figure 4.22.

Indeed, $l^{ph}(T)$ is boosted within the superconducting phase and saturates at a length scale of the order of the sample dimension, supporting the boundary scattering regime. The corresponding transport property $\kappa^{ph}(T)$ is also boosted at the onset of superconductivity, follows the T^2 behavior of the measured $\kappa/T(T)$ at lowest temperatures, and exhibits a maximum below that of $\kappa/T(T)$ (at ~ 450 mK). So it is evident that κ^{el} also contributes to the "1 K-anomaly", as seen from the $\kappa^{el}/T = \kappa/T - \kappa^{ph}/T$ data points. Finally, a situation similar to that of Pb [86] or the high-T$_c$ cuprates [42, 102, 217] is recovered, where κ^{el} also benefits from the increased electron inelastic scattering time.

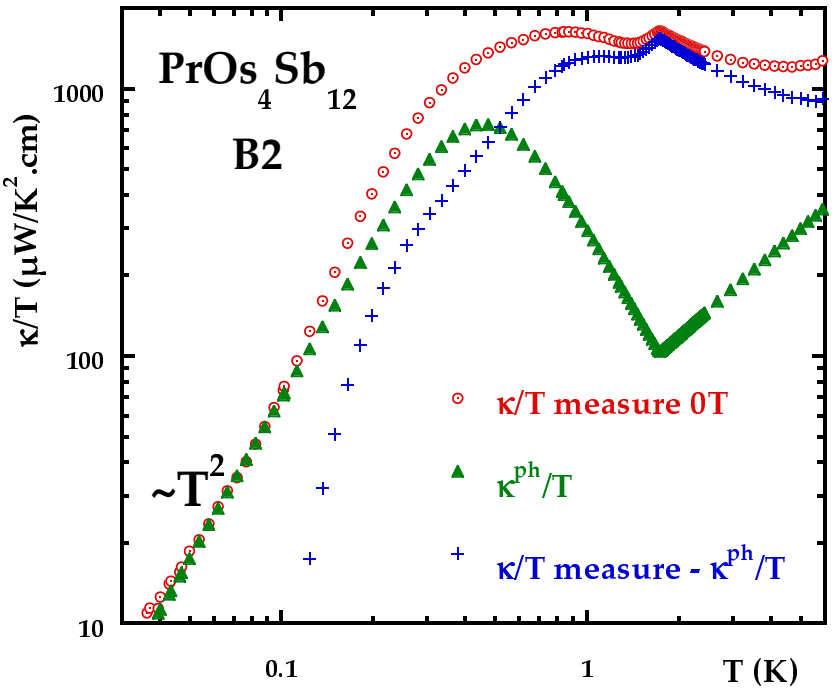

Figure 4.23. Estimation of the phonon contribution κ^{ph}/T to heat transport according to equation (4.9). It is fixed by the low temperature behavior ($\kappa \propto T^3$) and the deviations from the WIEDEMANN–FRANZ law in the normal phase. At intermediate temperatures, it gets boosted (reduced electronic scattering). The electronic contribution then corresponds to $\kappa^{el}/T = \kappa/T - \kappa^{ph}/T$. The local maximum in the measured thermal conductivity just below 1 K clearly has a phonon and an electronic contribution. Used parameter: $n = 3$ with the following constants: $a \sim 60$ µWK^{-3}cm^{-1}, $l_0^{ph} \sim 60$ µm, $b = 10.9 \times 10^3$ WK^{-4}m^{-2}.

In any case, this simple analysis of the zero field temperature dependence of κ clearly supports our hypothesis on the important contribution of phonons to heat transport, which was based initially only on phenomenological analogy. In particular, the results reveal

- that the T^3 behavior of κ for $T \to 0$ should come from the phonons (given the reasonable value extracted for l_0^{ph}), and
- that the "1 K-anomaly" in κ/T of $PrOs_4Sb_{12}$ probably involves both κ^{el} and κ^{ph}, even if it will be difficult to go into more detail on the basis of our simple estimation of κ^{ph} at intermediate temperatures, which was mainly intended to check qualitatively the validity of this scenario.

On sample A, we had carried out a similar analysis, of course limited to the "1 K-anomaly", the low temperature $\kappa/T \propto T$ behavior excluding any further interpretations. The result favored a phonon origin of the "1 K-anomaly", but an electronic contribution could not be ruled out. Now, if one compares both crystals, the local maximum seems more pronounced on sample B2 (it reaches nearly the magnitude of $\kappa(T_c)/T$, see fig. 4.24), and its RRR is twice of that found on sample A. As a higher RRR value generally means an increased (relative) relevance of inelastic compared to elastic scattering, one could imagine that the effect of electron condensation within the superconducting phase becomes more obvious on κ^{el}, whereas the overall, relative contribution of the phonons to κ should diminish, compared to the electronic one. Once again, our estimations do not provide the necessary accuracy to verify this idea and a possible gain of the electronic contribution. In any case, on Nb and YNi_2B_2C, where the κ-enhancement is essentially ascribed to the phonons, it seems to diminish when sample quality is increased [44, 176, 93].

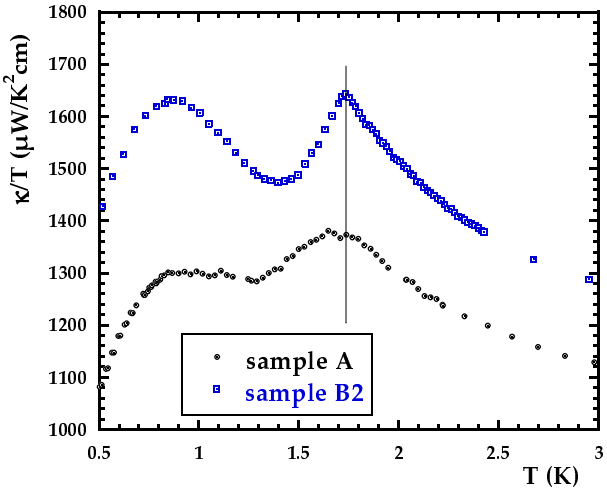

Figure 4.24. Comparison of the $\kappa/T(T)$ behavior at intermediate temperatures between sample A and B2. The "1 K-anomaly" as well as the peak at T_c are clearly more pronounced on sample B2.

As regards now the field dependence of the anomaly, one finds from our $\kappa(H)$ curves at intermediate temperatures (in accordance with the $\kappa(T)$ data at low fields, see figures 4.14 and 4.19) that with increasing magnetic fields, the thermal conductivity initially decreases (before an upturn at higher values). From specific heat measurements (see fig. 4.3b) we already inferred that changes in thermal conductivity under low fields at intermediate temperatures should essentially be related to effects on the scattering times, and not on the density of states. So the observed κ-drop can be explained as follows: the (zero field) enhancement of the phonon thermal conductivity is largely suppressed by vortices introduced at $H > H_{c1}$, because of a decreasing phonon mean free path due to the scattering with supplementary quasiparticles and excitations in the vortex cores. Similar arguments might be valid for electron-electron scattering and κ^{el}. The phenomenon of a decreasing thermal conductivity at low fields is also observed in the two-band

superconductor MgB_2 [186] and in the compound $NbSe_2$ [29], another candidate for multiband superconductivity.

Discussion of the electronic contribution κ^{el}

Let us now focus on the low temperature electronic contribution $\kappa^{el}(T)$ to heat transport in the superconducting state of $PrOs_4Sb_{12}$, reminding the still open question on the gap topology in this compound. We already mentioned that κ^{el} gets enhanced at intermediate temperatures due to an increasing inelastic scattering time, as seen on fig. 4.23. Of course, $\kappa^{el}/T = \kappa/T - \kappa^{ph}/T$ is only a rough estimate in that temperature region. But at low temperatures, it is seen that the phonon contribution $\kappa^{ph}(T)$ should follow a T^3-behavior up to about 0.3 K, giving between 0.1 and 0.3 K a *robust* estimate of κ^{el}/T. Even more, we will try in the following to understand κ^{el}/T quantitatively up to $T \leq 0.6$ K, i.e. in the region with dominant *elastic* impurity scattering.

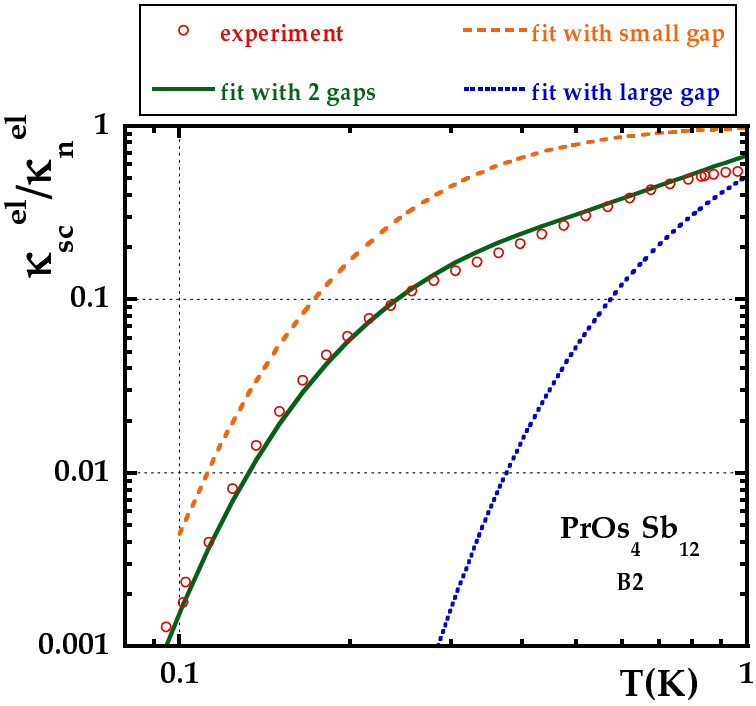

Figure 4.25. Zoom on the very low temperature behavior of the electronic thermal conductivity at zero field in the superconducting state, κ^{el}_{sc}, normalized to its value in the normal phase κ^{el}_{normal}. κ^{el}_{sc} corresponds to the difference between the measured thermal conductivity and the estimated phonon contribution, as shown in fig. 4.23. The lines correspond to different fits using equation (4.10)– dotted line (blue): one gap with $\Delta(0)/k_B \sim 3$ K, dashed-line (orange): $\Delta(0)/k_B \sim 1$ K and green line: two gaps with $\Delta_l/\Delta_s(T \to 0) \sim 3$, $\Delta_s(T \to 0) \sim 1$ K and a "weight" for the small gap band $n_s \sim 0.35$. Obviously, the experimental data start to rise at much lower temperatures than predicted in the case of a single BCS-like gap.

The most striking feature about κ^{el} in figures 4.23 and 4.25 is its *exponential* downturn for $T \to 0$, which clearly points to *node-less*, fully opened gaps on the whole Fermi surface. More quantitatively, let us fit the *normalized* electronic contribution $\kappa^{el}/\kappa^{el}_{2.5\,\mathrm{T}}$ in the elastic scattering

limit with BCS-theory, according to equation [160, 17]:

$$\frac{\kappa_{sc}^{el}}{\kappa_{normal}^{el}}(T) = \frac{\int_{\Delta(T)}^{+\infty} \mathrm{d}E\, E^2 \frac{\partial f}{\partial E}(T)}{\int_{0}^{+\infty} \mathrm{d}E\, E^2 \frac{\partial f}{\partial E}(T)}\,, \tag{4.10}$$

where E is the quasiparticle energy, f their equilibrium distribution function and $\Delta(T)$ a BCS type gap function with $\Delta(0) = 1.76 \cdot k_B T_c$. The ratio $\kappa_{sc}^{el}/\kappa_{normal}^{el}$ gives a universal function of reduced temperature T/T_c.

Interestingly, it turns out to be impossible to fit the data with a BCS (fully opened) gap corresponding to $T_c = 1.729$ K (see blue curve "large gap" in fig. 4.25): the measured κ^{el}/T starts to rise at much lower temperatures than expected, requiring a smaller gap value. This cannot be compensated by strong-coupling effects (which only make it worse, increasing the ratio Δ/T_c), nor by another estimation of the phonon contribution ($\kappa^{ph}(T)$ cannot be larger than $bl_0^{ph}T^3$, constrained by the measurements below 0.1 K).

Instead, the normalized κ^{el}/T data can be quantitatively reproduced within a MBSC scenario, i.e. when we include in equation (4.10) a small $\Delta_\mathrm{s}(T)$ and a large $\Delta_\mathrm{l}(T)$ gap function with the same T_c, and two associated conduction channels:

$$\kappa^{el}/T = n_s \cdot \kappa_{\Delta_s}^{el}/T + (1-n_s)\cdot \kappa_{\Delta_l}^{el}/T\,. \tag{4.11}$$

The best fit is then obtained for a zero temperature gap ratio of about $\Delta_\mathrm{l}/\Delta_\mathrm{s}(T\to 0) \sim 3$ with $\Delta_\mathrm{s}(T\to 0) \sim 1$ K, and a "weight" for the small gap band $n_s \sim 0.35$ (see figures 4.25 and 4.26). This value is close to the 40% deduced from the "plateau" of $\kappa(H, T\to 0)$ (fig. 4.15).

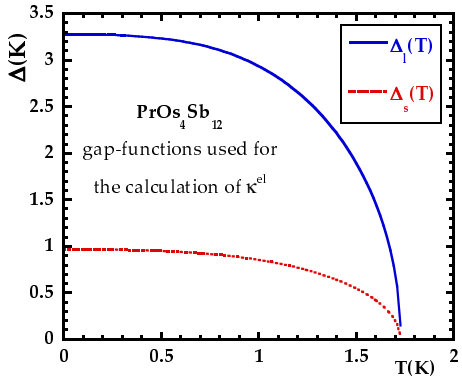

Figure 4.26. Gap functions Δ_l and Δ_s as used for the calculation of the electronic contribution to thermal conductivity according to equations (4.10) and (4.11).

As already evoked, the characteristic field scale H_{c2}^S for the vortex core overlap of the small band gap can now be estimated from

$$H_{c2}/H_{c2}^S \sim \left(\frac{\Delta_\mathrm{l}\cdot \mathrm{v_{F,s}}}{\Delta_\mathrm{s}\cdot \mathrm{v_{F,l}}}\right)^2\,, \tag{4.12}$$

where $v_{\mathrm{F,i}}$ is the average FERMI velocity of band i. If one assumes that the small gap band is also a light carrier band, with $\mathrm{v_{F,s}}/\mathrm{v_{F,l}} \sim 5$ (see introduction and [130]), we get $H_{c2}^S \sim 10$ mT, which is of the order of H_{c1} and seems reasonable owing to the $\kappa(H)$ data.

So the main outcome of this analysis is the existence of an additional, small but *finite* gap $\Delta_\mathrm{s}(T)$ in $PrOs_4Sb_{12}$, quantitatively consistent with the MBSC scenario deduced from $\kappa(H)$. Concerning the question of gap topology, our data clearly favor fully open gaps on the whole FERMI surface.

4.3.3. Interpretation of $R_c^{th}(T, H)$

Before comparing our overall thermal conductivity results on superconducting $PrOs_4Sb_{12}$ with other experiments, I will explain how the measurement of the *thermal* contact resistance of the thermometer thermalization (in this case of the "cold" thermometer, $R_{cc}^{th}(T, H)$) can contribute not only to the verification of the setup reliability (see previous chapter), but also to the physical discussion on the nature of the superconducting phase in $PrOs_4Sb_{12}$.

In section 4.2, we already compared the electric and thermal contact resistance data on $PrOs_4Sb_{12}$ and $CeCoIn_5$. Let me remind the main conclusions:

- The *electric* contact resistance is nearly constant below the superconducting transition, exhibits a tiny jump at T_c and remains quite unaffected under magnetic field. It is well understood and can be modeled by the sum of an ohmic (constant) and a constriction contribution.

- The same model applies to the *thermal* contact resistance in $PrOs_4Sb_{12}$ under magnetic field (and to $CeCoIn_5$ in zero field) when including a parallel phonon channel to the constant part of the electric measurements. It allows to reproduce the temperature dependence of the measured thermal contact resistance over a large range of temperatures, and in particular the recovery of the WIEDEMANN–FRANZ law for $T \to 0$.

Now let us try to understand the behavior of the thermal contact resistance on $PrOs_4Sb_{12}$ in zero field and in the light of the MBSC scenario.

Figure 4.27 again shows the enormous increase of $R_{cc}^{th}(T, H = 0)$ in the low temperature limit, and that it cannot be accounted for by the MAXWELL contribution, even if the latter raises due to the strongly reduced thermal conductivity of $PrOs_4Sb_{12}$. Considering the contact resistance results on $CeCoIn_5$ and the discussion on the multiband superconductivity in $PrOs_4Sb_{12}$, one could imagine the following (intuitive) scenario: when the thermal energy k_BT gets smaller than the energy scale related to the small gap $\Delta_S(T)$, the superconducting gaps act as strong barrier for thermal excitations, hence leading to a collapse of the heat current (whereas the electric current benefits from ANDREEV [4] processes). A total breakdown of thermal transport might only be prevented by a parallel phonon channel. Nevertheless, the situation clearly leads to a thermal decoupling (huge relaxation times of several days) of the thermometers from the sample, explaining why they remained stuck at about 25 mK and did not allow any thermal conductivity measurement on $PrOs_4Sb_{12}$ below that temperature.

Apparently (see the low temperature field dependence $R_{cc}^{th}(T = 50\,\mathrm{mK}, H)$ in fig. 4.28), this thermal barrier is rapidly suppressed under magnetic fields, confirming the low field scale H_{c2}^S (recovery of the "normal phase" related to the small gap band) in $PrOs_4Sb_{12}$. Indeed, at 20 mT we encountered no difficulty in measuring the thermal conductivity of $PrOs_4Sb_{12}$ down to about 12 mK. Altogether, the temperature *and* field dependence of the thermal contact resistance agree, at least qualitatively, with the existence of a low energy and field scale in superconducting $PrOs_4Sb_{12}$. The latter is quantitatively consistent with the suggested MBSC scenario. By contrast, in $CeCoIn_5$, the formation of a thermal barrier in zero magnetic field might be prevented by gap nodes (observed by several experiments [136]), which allow the thermal excitations to pass the interface even at lowest temperatures. In any case, the fact that the thermal resistance of the thermalization contacts behaves in a completely different manner (for $T \ll T_c$) on $PrOs_4Sb_{12}$ and $CeCoIn_5$, whereas the contacts followed the same elaboration process, certainly reveals some intrinsic property. As the change in behavior concerns not the

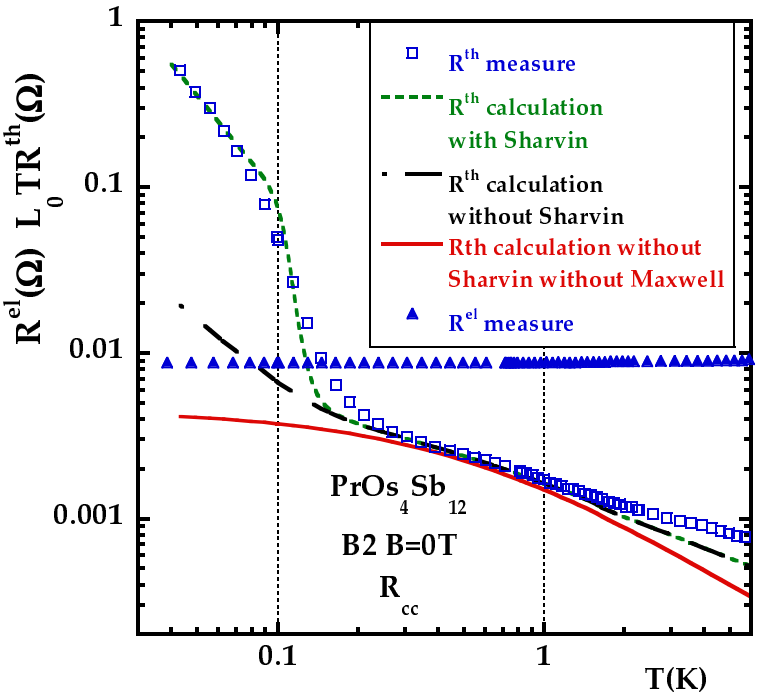

Figure 4.27. Electric and (converted) thermal contact resistance of the cold thermometer thermalization (setup with sample B2). The strong increase of the thermal contact resistance at low temperatures cannot be reproduced with our simple contact resistance model from chapter 2 and equation (3.17), even if the MAXWELL contribution is enhanced compared to the case with a small applied magnetic field, as shown in fig. 3.16. However, the fit curve including the additional thermal SHARVIN resistance (see text and appendix A.2.2) with a parallel phonon channel and two gap-functions gives a fair account of the experimental data even at very low temperatures. The procedure for the fits without the SHARVIN contribution is similar as in the 20 mT case, see fig. 3.16 with $\alpha \approx 5 \cdot 10^{-6}$ WK^{-3}. For the calculation of the thermal SHARVIN resistance, we used the gap-functions plotted in fig. 4.29 with a gap ratio of 0.4, similar to the calculation of κ^{el}, $d = 560$ µm (even if too large to respect the ballistic limit) and $b = 3 \cdot 10^{-5}$ WK^{-4}, see equation (4.13).

electric but the thermal contact resistance, sensitive to the low energy thermal excitations, it seems reasonable to think of some influence of the gap structure.

In fact, the zero field increase of $R_{cc}^{th}(T)$ for $T \ll T_c$ on $PrOs_4Sb_{12}$ might be understood in terms of the SHARVIN contact resistance (see appendix A.2.2), well-known from the *ballistic* description of electric point contacts [179]. Between two normal metals, the SHARVIN contribution to the electric contact resistance primarily results from the mismatch of the FERMI momenta, and can be enhanced (reduced) by supplementary interface barriers (ANDREEV reflection [4]). In general, it becomes non-negligible only for very small contact areas, since $R_{\text{Sharvin}}^{el} \propto a^{-2}$ (a: radius of point contact) [179]. A complete calculation of the effects of a finite voltage on a metal(N)–superconductor(S) junction limited by the SHARVIN resistance (ballistic limit) was carried out by BLONDER, TINKHAM and KLAPWIJK ("BTK–model", [27]) in a simple 1D model.

So we adapted the "BTK–model" to thermal transport and tried to adjust the thermal contact resistance data (in zero field) with equation (3.17), now also including the thermal SHARVIN resistance R_S^{th} with a parallel phonon channel (free parameter b). More precisely, in equation

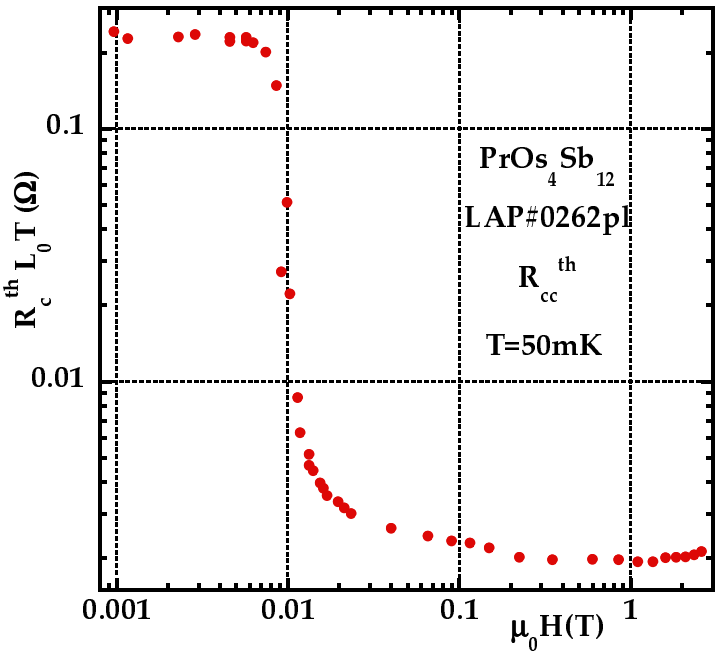

Figure 4.28. Magnetic field dependence of the thermal contact resistance R_{cc}^{th} at 50 mK. The drop observed at about 10 mT seems to reflect the low field scale $H_{c2}^{S}(T)$ in $PrOs_4Sb_{12}$: the recovery of the normal phase within the small gap band suppresses the thermal barrier at the Au-$PrOs_4Sb_{12}$ interface.

(3.17) $R_{cc}^{th}(T)$ now has an additional term:

$$R_S^{th}(T) = \frac{1}{\kappa_{\text{Sharvin}}(T) + bT^3}\,, \tag{4.13}$$

where κ_{Sharvin} represents the electronic thermal conductance of the Au-$PrOs_4Sb_{12}$ interface (in the ballistic limit) which is calculated with the thermal 'BTK–model", as shown in appendix A.2.2.

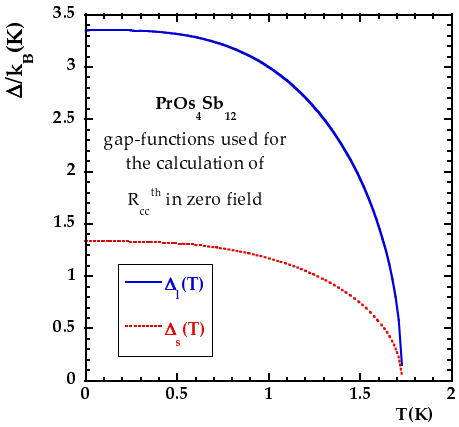

Figure 4.29. Gap functions Δ_l and Δ_s as used for the calculation of the thermal Sharvin resistance for fig. 4.27.

The result can be summarized as follows (see the fit including the thermal Sharvin resistance in fig. 4.27): it is possible to account for the strong upturn in $R_{cc}^{th}(T)$ using two superconducting gaps (with amplitude and weight ratios similar to those of the $\kappa(T)$ analysis, see fig. 4.29),

leading to an enhanced, dominating SHARVIN resistance at temperatures below the small characteristic energy scale ($T < 300$ mK). However, our contacts are clearly too large to respect the ballistic limit, so that this analysis can, if at all, only give some indications about the relevance of our ideas, but no reliable quantitative results. For a more detailed analysis within the SHARVIN contact resistance, much smaller contact dimensions would be necessary.

To summarize, the thermal contact resistance measurements are consistent, at least qualitatively, with a MBSC scenario in $PrOs_4Sb_{12}$. In particular, they confirm the relevance of a low field scale $H \sim 10$ mT $\ll H_{c2}$, and a low energy gap.

4.3.4. Comparison with other experiments on $PrOs_4Sb_{12}$

In this section, we will review the outcome of our thermal conductivity measurements on $PrOs_4Sb_{12}$ in the light of other experimental results, focussing on the superconducting gap structure. Indeed, various measurements on the superconducting state of $PrOs_4Sb_{12}$ have been interpreted either as pointing to gap nodes, or to fully open gaps.

Let me recall the starting point. The first measurements suggesting a non-ordinary superconducting phase in $PrOs_4Sb_{12}$ were the angle-dependent thermal conductivity study under magnetic field, $\kappa(H,\theta)$ [92], indicating point nodes of the gap and leading to a H–T phase diagram with two distinct phases of different symmetry, separated by the proposed $H^*(T)$ line (see introduction). Then came the double transition in the specific heat [210], resembling to that on UPt_3.

The specific heat anomaly at the superconducting transition proved to be only a single jump on the homogeneous sample B2. Even if the origin of the sharp double transition observed on other samples is not clearly identified yet, it is quite certain that the C_p-jump at lower temperatures is neither related to a change of the symmetry of the superconducting order parameter (like in UPt_3) nor to the $H^*(T)$ line observed with thermal conductivity. Concerning this $H^*(T)$ line , our $\kappa(H, T \to 0)$ curve has no anomaly as signature of a phase transition at $H^*(T \to 0) \approx 0.8$ T, whereas the $B \to C$ transition in UPt_3 was clearly seen in $\kappa(H)$ [190]. H^* rather corresponds to the plateau observed in $\kappa(H)$, possibly there is an anisotropy change when the normal phase in the small gap band is restored.

Gap nodes were also deduced from the temperature dependence of the LONDON penetration depth in $PrOs_4Sb_{12}$ [40]. Similar remarks for the thermal conductivity study apply: the conclusions of these measurements might be reviewed in the light of the existence of two superconducting gaps with different amplitude. Altogether, owing to the still mysterious homogeneity problems and the strong field sensitivity, all analysis require a close look at the experimental conditions such as sample quality, field and temperature range, etc. This may have induced the diverging interpretations on different measurements.

A particular remark can be made on the analysis of the distortion of the vortex lattice reported in [81], again pointing to gap nodes. A recent calculation carried out by Dao et al. [**?**, **?**] on the effects of the T_h symmetry on the anisotropy of the FERMI surface provides another possible explanation for the deviations from the hexagonal vortex lattice in $PrOs_4Sb_{12}$. Further neutron diffraction measurements are necessary (and actually undertaken) to check the different hypotheses.

Next let us comment on the experiments indicating fully open gaps and compare the extracted gap values. The Sb nuclear quadrupole resonance (NQR) [101] as well as the muon spin relaxation (μSR) [120] studies propose large ratios of $2\Delta/k_BT_c$, respectively ~ 5.2 and ~ 4.2, supporting strong-coupling effects but not the presence of a small gap. Nevertheless, the NQR

data show a large residual relaxation rate ($1/T_1$) below 0.5 K, which may point, as for our sample A, to crystal inhomogeneities which prevent observation of the smallest gap. Moreover, like specific heat, the nuclear relaxation rate should be rather sensitive to bands with large density of states. So, if our interpretation of the small gap band as being also a "light mass" band is correct, it may have indeed little contribution to $1/T_1$. The muon relaxation rate (σ_s) measured by μSR is controlled by the field distribution which may not put more weight on the heavy than on the light bands. But the measurements were performed in a residual field of 20 mT, already larger than H_{c2}^S, so that again $\sigma_s(T)$ is probably governed by the high energy excitations. But the "unusual" non-linear field dependence of $\sigma_s(T = 0.1\ \mathrm{K})$ compares well with $\kappa(H)$: the MBSC scenario, with the small gap band associated to light carriers can even "explain" the increase of σ_s at low fields as $\sigma_s \propto 1/m^*$. STM measurements [192] proposed a gap distribution, which may extend from 120 µV to 325 µV ($2\Delta/k_BT_c \sim 1.5 - 4.1$), not so far from our analysis of $\kappa(T)$ ($2\Delta_S/k_BT_c \sim 1.15$, $2\Delta_L/k_BT_c \sim 3.5$). Further support for a node-less gap in $PrOs_4Sb_{12}$ comes from recent angle-resolved specific heat $C(H,\varphi)$ measurements [47]. Contrary to $\kappa(H,\phi)$, $C(H,\varphi)$ does not point to a transition from four- (A-phase) to two-fold (B-phase) symmetry of the superconducting gap within the H–T diagram. In the B-phase, $C(H,\varphi)$ rather maintains a clear four-fold oscillation (in the basal planes). Along the [100] directions, 6 minima are observed in $C(H,\varphi)$, but for $H \to 0$, the oscillation amplitude vanishes, suggesting deep minima in the superconducting gap, not nodes.

In conclusion on the topology of the superconducting gap in $PrOs_4Sb_{12}$, we believe that our thermal conductivity measurements provide new, compelling arguments in favor of a gap structure without any nodes. $\kappa(T,H)$ measurements were performed on a highly homogeneous single crystal exhibiting a *single* jump on C_p at T_c. The reproducible field dependence $\kappa(H)$ at $T \ll T_c$ confirms a MBSC scenario, i.e. the existence of 2 (or more) superconducting gaps sharing the same T_c (like in MgB_2). Further support comes from the low temperature $\kappa(T)$ and thermal contact resistance $R_c^{th}(T,H)$ data which both point to isotropic, *fully opened* gap functions with $\Delta_l/\Delta_s(T \to 0) \sim 3$, in comparison with other measurements (NQR, μSR, STM, $C(H,\varphi)$. Remaining discrepancies with the interpretations of other experiments (in particular those pointing to gap nodes) might be related to issues such as sample quality and the strong field sensitivity.

4.3.5. Outlook

In any case, the mystery of the superconducting state in the heavy fermion $PrOs_4Sb_{12}$ is far from being uncovered, and many details are still not understood. In particular, concerning the MBSC scenario, we can only speculate on the microscopic origin of the different coupling strength among the various bands. In MgB_2, numerous theoretical and experimental investigations boosted the understanding of many of the compound's features, especially the spread of the coupling constants can be deduced from precise band structure calculations and the well-known phonon spectra. In $PrOs_4Sb_{12}$, we expect that the heavy bands with f character are strongly coupled. However, whether this is due to density of state effects, or to a pairing mechanism involving f electrons, remains an open question. In this context, a complete understanding of the heavy fermion behavior in the normal state, and of the field-induced ordered phase might be helpful. Another intriguing question on the nature of the superconducting state and the corresponding pairing interaction arises from the time-reversal symmetry-breaking, as concluded from a zero-field μSR study. So, even with fully opened gaps, superconducting $PrOs_4Sb_{12}$ might still be "unconventional" in some sense.

5. Low temperature thermal conductivity of $CeCoIn_5$

In this chapter, we will analyze the thermal transport in the superconducting phase of the heavy fermion compound $CeCoIn_5$, focussing on its behavior at low temperatures and low fields. As already mentioned in the introduction, several thermal conductivity studies are reported in the literature [94, 136, 37, 201], but the results are quite controversial, and no special attention has been paid to the low temperature-low field region (at least below ^{3}He-fridge temperatures), most promising to uncover possible multiband effects. However, our own $CeCoIn_5$ study began only during the last year of my PhD period and was confronted to severe experimental difficulties, so that the results remain naturally incomplete, especially as anisotropy is concerned, since we performed measurements in the only $H \parallel \vec{c}$ configuration (other field orientations had to be left for further studies). Besides, the sample has not been entirely characterized, in particular regarding the complete upper critical field curve $H_{c2}(T)$. Nevertheless, the first outcomes revealed some rather unexpected features, and hence merit to be presented in a separate chapter of this thesis. So let us go *in medias res*.

5.1. The sample

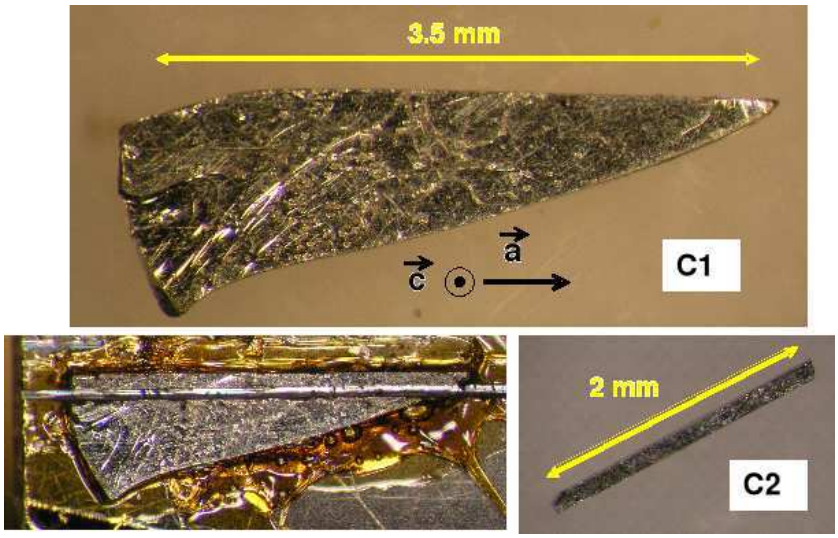

Figure 5.1. Bar shaped $CeCoIn_5$ sample used for our thermal conductivity scans (label C2 or #LAP-plaqbar2). It was obtained from the single crystal labeled C1 (Aoki batch). The picture on the left shows the result at the last step of the sawing process. The $\vec{c}$-axis is always perpendicular to the sheet plane.

Our $CeCoIn_5$ sample, labeled C2 or #LAPplaqbar2, is bar-shaped (dimensions:

$2.1 \times 0.13 \times 0.14$ mm^3, with an effective length between the cold and warm contact of 1.2 mm, yielding a geometric factor $l/S \sim 660$ cm^{-1}), and was extracted from a platelet-type single crystal, labeled C1, by sawing carefully with a diamond saw (see fig. 5.1). It has been synthesized by D. Aoki in the group of G. Lapertot, during his post-doc at the SPSMS/CEA Grenoble with J. Flouquet. We determined its residual resistivity ratio (RRR between 300 K and T_c) to be of about 6. Like in the case of the $PrOs_4Sb_{12}$ platelet, gold stripes were evaporated after ion gun etching the sample surface. The crystal orientation was checked by simple X-ray analysis, and the experimental setup was modified to allow the heat flow (in our case parallel to the $\vec{a}$-axis) being perpendicular to the applied magnetic field (parallel to the $\vec{c}$-axis). Note that this configuration is opposite to the previous measurements on $PrOs_4Sb_{12}$, where magnetic field and heat flow were parallel.

5.2. Experimental results

Before exposing our first thermal conductivity results on $CeCoIn_5$, I will summarize the sample characterizations we performed, and confirm the reliability of our heat transport measurements via the verification of the Wiedemann–Franz law.

5.2.1. Sample characterization

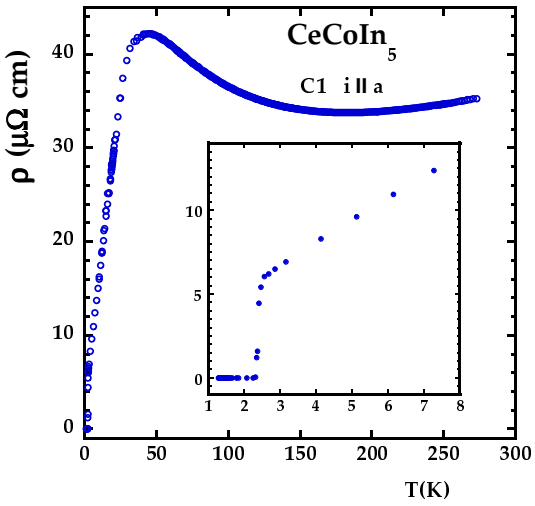

Figure 5.2. Electric resistivity $\rho(T)$ in zero field of $CeCoIn_5$ (sample C1) with zoom on the superconducting transition. The shape of the curve with its local maximum below 50 K is quite characteristic.

Generally, the easiest way for sample characterization is electric resistivity. Figure 5.2 displays the entire resistivity curve $\rho(T)$ from room temperature downwards. Its characteristic shape with a local maximum just below 50 K corresponds well to previous reports [154]. The significant drop of $\rho(T)$ at lower temperatures, combined with the corresponding "plateau" in susceptibility $\chi(T)$ (see fig. 2.9a), possibly signs the onset of the formation of a coherent state, a somehow generic feature in heavy fermion compounds. As to the magnitudes, we find $\rho(T_c) \approx 6.3$ μΩcm. In the literature, one remarks a considerable spread of $\rho(T_c)$-values, ranging from about 3 [154] to ~ 6.5 μΩcm [141], probably due to uncertainties in the determination of the geometric factor, in addition to effects of crystal purity. So it is more convenient to compare the residual resistivity ratio (RRR between 300 K and T_c). In our sample, as mentioned above, it is of the order of 6, which is low in comparison with ordinary metals like gold or copper, but not uncommon for

heavy fermions. It fits well to other reports: RRR$\sim$ 6 in [154, 124], about 8.5 in [141] and 9.4 in [37]. From that point of view, our sample C2 seems quite similar to those synthesized by other groups. Let us note that within the Aoki batch, we also measured a bar shaped sample with a high RRR of about 75, but its $\rho(T)$ curve did not show the characteristic local maximum, instead $\rho(T)$ is continuously decreasing from room temperature downwards. This underlines once more the necessity of careful sample characterization.

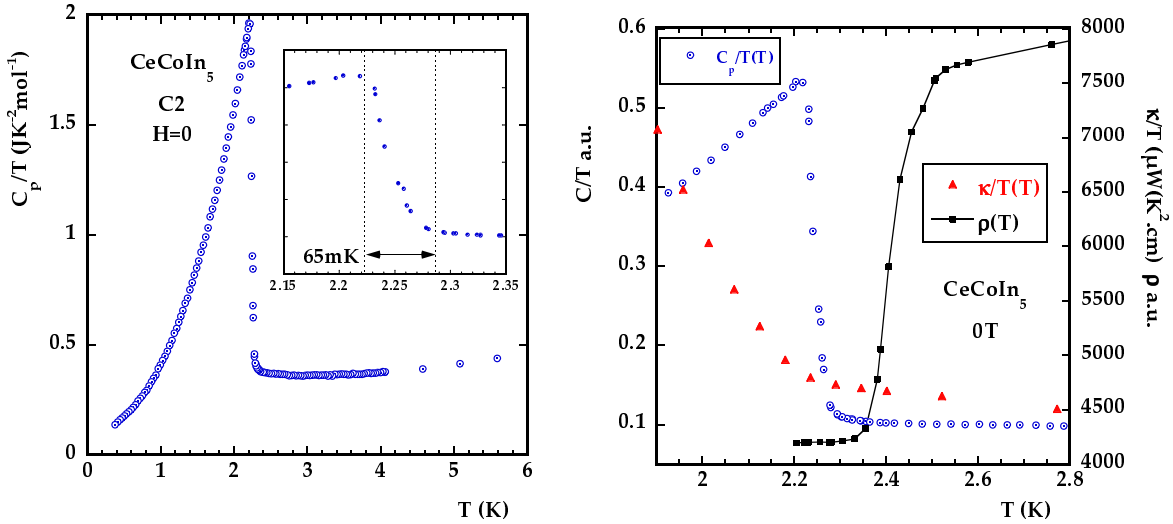

(a) Specific heat $C_p/T(T)$ of sample C2 with its characteristic high jump at T_c. The transition width is of about 65 mK as shown in the inset.

(b) The simultaneous occurrence of anomalies in specific heat (jump), thermal conductivity (upturn) and electric resistivity (vanishing) demonstrates *bulk* superconductivity and the good homogeneity of the sample.

Figure 5.3. Sample characterization by comparison of the superconducting transition as seen by $C_p/T(T)$, $\kappa/T(T)$ and $\rho(T)$ in zero magnetic field.

Supplementary information on sample quality is gained from specific heat measurements, because it probes bulk properties. Figure 5.3a shows the specific heat of sample C2 in zero field (more precisely another part of the small bar sawed from sample C1, see fig. 5.2), measured with a PPMS device by G. Knebel (CEA Grenoble). It matches very well the large jump at the superconducting transition ($T_c \sim 2.3$ K), found in previous reports [154, 90]. Here we concentrate on crystal quality and homogeneity, testified by the narrow transition width of about 65 mK (corresponding to what is published in the literature). Further support comes from the comparison of the superconducting transition as seen by specific heat and thermal conductivity as plotted in fig. 5.3b: the specific heat jump coincides well with the κ-upturn. From this point of view, we are sure to examine a high quality single crystal of $CeCoIn_5$. As regards resistivity, it vanishes at the temperature of the onset of the specific heat jump. But if we compare the mid-transition, it is 8% higher. This is common in the 115 family, where much larger discrepancies are observed in $CeIrIn_5$ [90] or $CeRhIn_5$ [70] under pressure. It might be due to residual strain in the sample, given the large sensitivity of T_c to pressure or stress ($dT_c/dp > 0$ in $CeCoIn_5$ [141, 132]), together with the sensitivity of resistivity to very small volume fraction of superconducting material (a "superconducting path" is enough for a resistivity drop). Such an inhomogeneous origin for the higher T_c given by resistivity is also supported by the width of the

resistive transition (> 0.2 K), which significantly exceeds that of the bulk transition (65 mK).

5.2.2. Reliability of thermal conductivity measurement and Wiedemann–Franz law

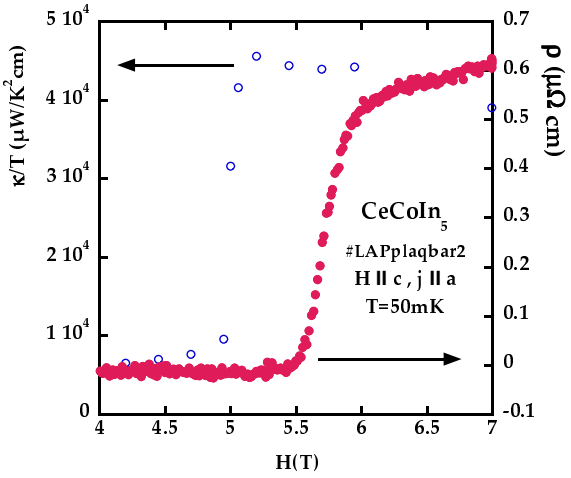

Figure 5.4. Comparison of the superconducting transition under magnetic field at 50 mK as seen by electric resistivity and thermal conductivity. The field shift between both transitions is of about 20%. A similar picture is obtained at 500 mK with a field shift of about 15% (not shown).

Next, we have to verify the reliability of the experimental setup. As usual, a good method is to check the validity of the Wiedemann–Franz law in the normal phase for $T \to 0$. In the literature, one finds for the upper critical field in our configuration ($j \parallel a$ and $H \parallel c$): $H_{c2}(T \to 0) \sim 5$ T, as determined by bulk probes like the specific heat (see fig. 2.10). However, in a simultaneous low temperature field scan of κ and ρ (as shown in fig. 5.4), we observed a substantial discrepancy: the onset of superconductivity as seen by electric resistivity is enhanced by roughly 15%, compared to thermal transport. The same phenomenon was already reported elsewhere [149], even so it occurred in a less pronounced manner than on our sample C2. The origin is probably the same as in zero field (compare again the transition width in fig. 5.4), amplified because $H_{c2}(0)$ scales in between T_c (for paramagnetic limitation) and T_c^2 (for orbital limitation). In any case, this means that we have to determine the relevant $L/L_0(T)$[1] curve at magnetic fields $H > 6$ T, in order to dispose of unaffected ρ data (above the superconducting transition). Figure 5.5 displays the the corresponding result. Qualitatively, the shape of $L/L_0(T, H = 6.05\ \text{T})$ differs not so much from that in $PrOs_4Sb_{12}$ for $B = 3$ T. In the $T \to 0$ limit, the Wiedemann–Franz law is recovered, for higher temperatures, the phonons contribute to the heat transport and in an intermediate regime $L/L_0(T) < 1$, indicating the dominance of *inelastic* scattering. Discrepancies are only visible on a more quantitative level:

- The role of inelastic scattering is strongly enhanced in $CeCoIn_5$, since $L/L_0(T)$ gets as low as 0.65 (0.95 in $PrOs_4Sb_{12}$).
- The recovery of the Wiedemann–Franz law ($L/L_0 \to 1$, *elastic* scattering regime) takes place at lower temperatures: below 100 mK for $CeCoIn_5$, in $PrOs_4Sb_{12}$ already for $T \lesssim 700$ mK. This is again a consequence of the large difference in the inelastic to elastic ratio of the contributions to the scattering rate at T_c in both systems.
- At higher temperatures, the phonon contribution seems more important, since $L/L_0(T_c, H = 0) \approx 1.2$ (and for $T > T_c$ L/L_0 is rising rapidly with increasing temperature), whereas in $PrOs_4Sb_{12}$ the phononic heat transport was smaller at T_c.

[1] Reminder: $L = \rho\kappa/T$.

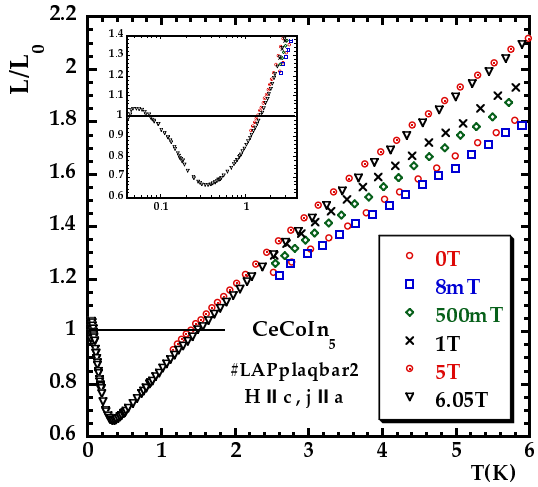

Figure 5.5. Temperature dependence of the LORENZ-ratio L/L_0 at different magnetic fields in the normal phase of $CeCoIn_5$. The inset shows the low temperature data on a logarithmic scale.

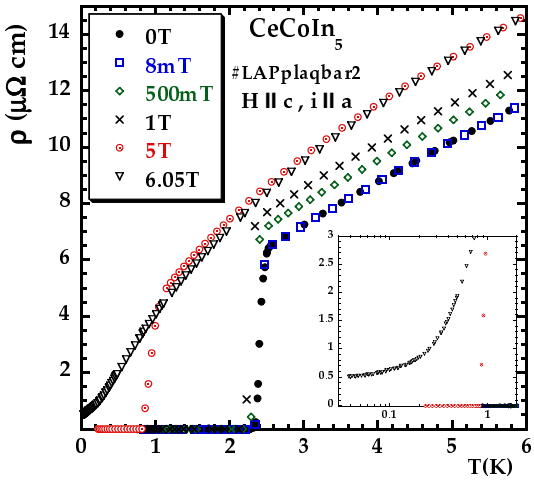

Figure 5.6. Temperature scans of the electric resistivity of $CeCoIn_5$ at various magnetic fields. The inset shows the low temperature data on a logarithmic scale. Above T_c and in the considered field range, the magnetoresistance is positive.

The increase with magnetic field of the ratio L/L_0 for $T > T_c$, as seen in fig. 5.5, is explained by the positive magneto-resistance[2], which can be inferred from fig. 5.6. Note that the comparison of $\rho(T_c, H = 0)$ and $\rho(T \to 0, B = 6.05\ \mathrm{T})$ evidences the predominant role of *inelastic* scattering at T_c, qualitatively consistent with the pronounced drop of L/L_0 at intermediate temperatures $T < T_c$. A simple estimation based on fig. 5.6 yields about 5% as an order of magnitude for the contribution of *elastic* scattering to the resistivity at T_c (for comparison, in $PrOs_4Sb_{12}$ a similar reasoning leads to a contribution of *elastic* scattering of roughly 70%).

At this stage, the main result is the recovery of the WIEDEMANN–FRANZ law at lowest temperatures in the normal phase, validating our experimental setup. The data scatter in L/L_0 for temperatures around 50 mK (near the experimental limit) at 6.05 T (seen on the inset of fig. 5.5) reflects the scatter on the thermal conductivity measurement, for which such conditions are particularly unfavorable (long relaxation times under magnetic field).

5.2.3. Thermal conductivity measurements – $\kappa(T, H)$ scans

Figure 5.7 displays the totality of our temperature scans of thermal conductivity on sample C2. Again, they were obtained for the configuration where the heat current is along $\vec{a}$ and the magnetic field along $\vec{c}$. A detailed discussion including complementary measurements (magnetic field scans) will follow in the next section. Here let us just remark the most prominent features:

- In zero field, there is an enormous increase of the thermal conductivity when entering the superconducting phase, reminiscent of what is observed in the high-T_c cuprates [42, 102, 217]. In $\kappa/T(T)$, the local maximum is reached at about 450 mK. In the $T \to 0$-limit,

[2] As we will see in the next section, this effect is only slightly compensated by a decreasing $\kappa(H)/T$ in that temperature region.

even so we pushed measurements down to 10 mK (corresponding to $T/T_c \sim 0.004$), κ/T is still about a factor of 2 higher than at T_c !

- The effect of magnetic field is not less spectacular: at lowest temperatures, a field of 8 mT ($H/H_{c2} \approx 0.0015$) is sufficient to enhance considerably thermal transport, and to restore a metallic-like behavior ($\kappa/T(T) \sim$ const.). At higher temperatures, magnetic field leads to the suppression of the strong κ/T-enhancement below T_c.

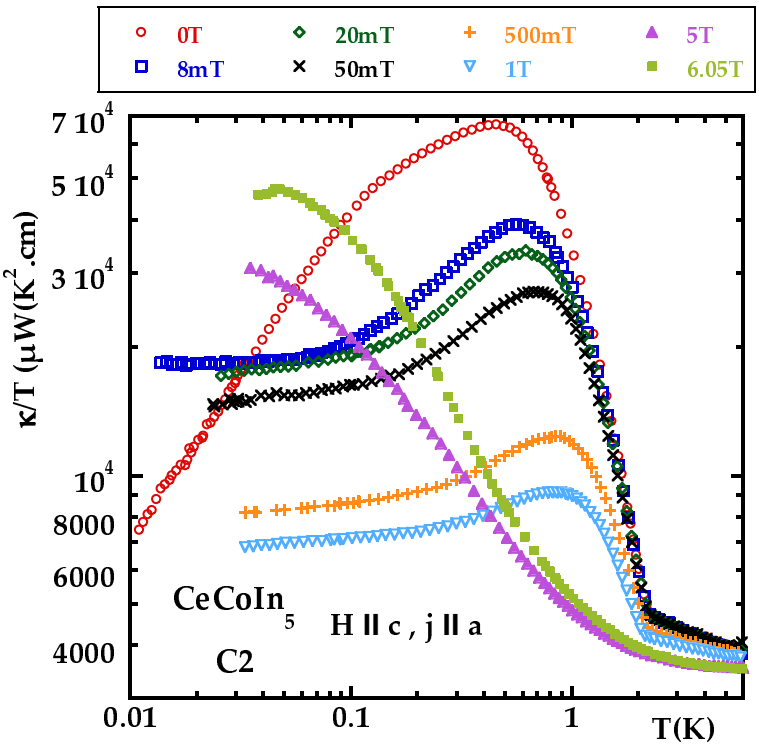

Figure 5.7. Temperature scans of thermal conductivity $\kappa/T(T)$ on $CeCoIn_5$ at various magnetic fields. Most striking features are the strong κ/T-upturn for $H = 0$ below T_c, the high value of κ/T(10 mK) (compared to that at T_c) and the strong κ/T-enhancement observed at $T \ll T_c$ for $H \ll H_{c2}$.

5.3. Discussion of $\kappa(T, H)$

Now we will discuss our thermal transport results on $CeCoIn_5$, first generally in the light of previous reports in the literature, and then concentrating successively on the behavior at the superconducting transition, in the $T \to 0$ limit and under magnetic field.

5.3.1. Comparison with other experiments

As already mentioned before, there is a significant discrepancy among the low temperature thermal conductivity reports on $CeCoIn_5$, as illustrated in fig. 5.8. The disagreement concerns both the κ/T-increase just below T_c and the behavior for $T \to 0$. At this stage, the following remarks on possible origins can be made:

- As we have already seen on $PrOs_4Sb_{12}$, crystal quality is a major aspect for heat transport measurements, so that the diverging results might be simply related to the different samples. There is no complete characterization available for all of them, but basically they seem quite similar. First of all, no significant spread of the transition temperature is observed. The superconducting transition jump in specific heat appears slightly broader for the sample of Movshovich et al., compared to that from Tanatar et al., but nevertheless it remains rather narrow (of the order of 100 mK). Concerning the residual resistivity ratio, Izawa et al. report RRR ≈ 18, Capan et al. ≈ 9.4 and ours is of the order of 6[3].

- Even small magnetic fields (such as remanent fields of magnets or some pinned flux) may have a profound impact on the properties of superconducting $CeCoIn_5$, so special experimental care is necessary to meet the zero field condition.

- In the second chapter, we already mentioned that measuring heat transport in superconducting $CeCoIn_5$ represents a particular challenge for the experimental setup because of the extremely high thermal conductance of the sample, and we explained how the resulting data might suffer from non-appropriate (thermal) contacts (see fig. 3.4). From that point of view, a *precise* determination of the local maximum in κ/T will be particularly delicate. More generally, under severe conditions such as high κ samples or very low temperatures, each irregularity on the setup (especially concerning the thermal contacts) will be "uncovered" and impair the measurement (even if these irregularities remain undetected under usual conditions). On the same footing, Tanatar et al. [201] pointed out that the discrepancy with the data of Movshovich et al. [136] at lowest temperatures is due to the use of different contacts for the thermometer thermalization (other (probably silver paint) than In solder as used in [201]). In particular, Tanatar et al. claim that the (even so not clearly specified) contacts used by Movshovich et al. would lead to a violation of the Wiedemann–Franz law at lowest temperatures in the normal phase. In return, no comment is given on the unfavorable properties of In solder in zero field (when In remains superconducting and hence a thermal insulator).

Altogether, the experimental situation is quite complex, and critical judgement necessary, but difficult. However, our own data are not so different from those of Tanatar et al. [201], and

[3] Note that our "definition" of the RRR involves $\rho(300\ \mathrm{K})/\rho(T_c)$, whereas Capan et al. use $\rho(4.2\ \mathrm{K})$ as reference, and Izawa et al. probably $\rho(300\ \mathrm{K})/\rho(T \to 0)$. We remind that in our $CeCoIn_5$ batch we also measured one sample with high RRR, but which did not exhibit the typical local maximum in $\rho(T)$.

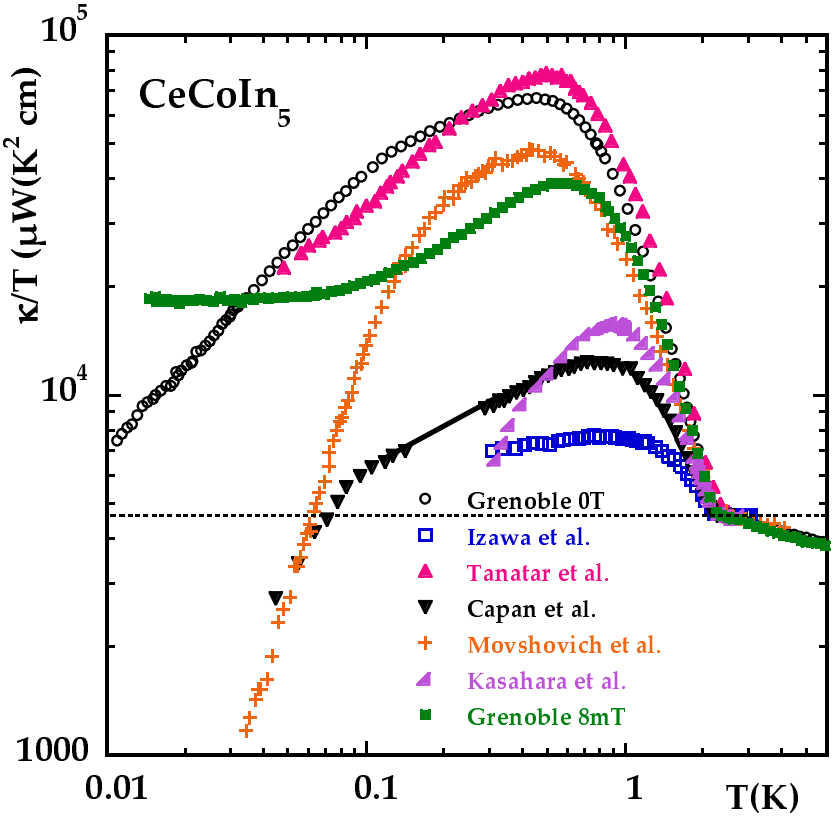

Figure 5.8. Comparison of our thermal conductivity measurements $\kappa/T(T)$ on $CeCoIn_5$ (sample C2) in zero field and in 8 mT with zero field data taken from Izawa et al. [94], Tanatar et al. [201], Capan et al. [37], Movshovich et al. [136] and Kasahara et al. [88]. All data were normalized to the value at T_c: $\kappa/T(T_c) \approx 4670\ \mu WK^{-2}cm^{-1}$ (dashed line). The solid line within the data of Capan et al. is a guide to the eyes since it was not possible to digitize the data properly in that temperature range. There is a considerable discrepancy between the different experimental results.

the recovery of the Wiedemann–Franz law (see fig. 5.5) for $T \to 0$ in the normal phase (from the other experiments solely reported by Tanatar et al. (see [149] for details)) is a good point, even so it does not check the difficult regime where κ/T is maximum (see also fig. 3.4). As regards the low temperature regime, the measurements under 8 mT where we observe a clear metallic (constant) behavior for $\kappa/T(T)$ down to 14 mK is in favor of a reliable thermometry and a good check that the thermal contacts are "good enough". Further support comes from the measurement of the thermal contact resistances on the sample, as described in the experimental chapter (see for example fig. 3.17). The observed recovery of the Wiedemann–Franz law within the thermometer contacts should indicate that the thermal conductivity data is not inhibited by contact resistance problems (thermometer decoupling, etc.). Of course, compared to the data of Movshovich et al. [136], it is quite uncommon to find a low temperature thermal conductivity higher than that measured at T_c, but let us now look at the different regimes in more detail, in order to get a some more insight...

5.3.2. κ/T-upturn for $T \lesssim T_c$

Despite the obvious discrepancies listed above, all measurements (see fig. 5.8) "agree" on a strong κ/T-upturn below the superconducting transition temperature. According to our zero field data, κ/T rises by a factor of about 14 between T_c and the local maximum around 450 mK, which is eventually more pronounced than in the high-T_c cuprates [217] (see fig. 5.9).

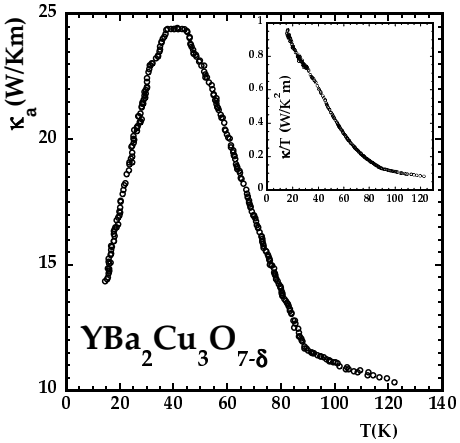

Figure 5.9. Thermal conductivity $\kappa(T)$ (in zero field and in the $\vec{a}$-direction) of $YBa_2Cu_3O_{7-\delta}$, data taken from [217]. The inset shows the same data plotted as $\kappa/T(T)$ for a better comparison with $CeCoIn_5$ of the strong upturn below $T_c \sim 90.5$ K.

Even if a clear separation of phonon and electron contribution to heat transport seems rather complicated in $YBa_2Cu_3O_{7-\delta}$ [217, 42], YU et al. [217] favor an *electronic* origin for the κ-enhancement, i.e. a strong suppression of the quasiparticle *inelastic* scattering rate for $T < T_c$. No anomaly is visible in $\kappa/T(T = T_c, H = 0)$ in UPt_3, a pronounced kink only develops under magnetic field [189]. In the case of $PrOs_4Sb_{12}$, we observed a downturn of κ/T for $T \leq T_c$ (see fig. 4.17), reminiscent of what is known from weak-coupling In or strong-coupling Pb, and probably due to the gap opening in conjunction with the energy dependence of electron scattering. An enhancement of κ/T can only be observed at lower temperatures (≈ 1 K) and is attributed to both electrons and phonons (see fig. 4.23). In $CeCoIn_5$, the upturn sets in much closer to T_c (see fig. 5.12), and is extremely strong. Two facts point to a predominant electronic origin:

- According to the analysis of $L/L_0(T)$, the phonon contribution to heat transport at T_c yields only $\approx 20\%$. So the increase of the phonon mean free path in the superconducting state might become "visible" only at temperatures well below T_c, similar to the case of $PrOs_4Sb_{12}$.
- From the comparison of the resistivity data at T_c and for $T \to 0$ (normal phase) in fig. 5.6, we already inferred the clear-cut predominance of *inelastic* (most likely quasiparticle-quasiparticle or quasiparticle-magnetic fluctuations) scattering at T_c (very short *inelastic* scattering life time compared to the *elastic* one). So it is likely that the loss of thermal excitations for thermal transport (due to the condensation process below T_c) is largely "overcompensated" by the fast increase of the quasiparticle mean free path. As a result, thermal conductivity is boosted, up to a point (≈ 450 mK) below which the density of states effect dominates (or the *elastic* mean free path is reached). Of course, this scenario can be complicated by the phonon contribution, which might also be enhanced at intermediate temperatures, as in $PrOs_4Sb_{12}$.

More concretely, MOVSHOVICH et al. [136] relate the κ-upturn to the suppression of magnetic

fluctuations (which scatter electrons) when entering the superconducting state. The presence of magnetic fluctuations above T_c is deduced from the large $\gamma(T \to 0) = 1.1$ J mol^{-1}K^{-2} in the normal state specific heat at 5 T. In any case, if thermal conductivity is dominated by effects of inelastic scattering, a microscopic description will be rather complicated, and probably limited to empirical models as in the case of the high-T_c cuprates or UPt_3 [64, 142].

By surface impedance measurements Ormeno et al. [145] determined the temperature dependence of the quasiparticle relaxation rate in $CeCoIn_5$, and found it to vary as T^4 close to T_c in the superconducting state, which is very similar to observations on YBCO [31]. Below 0.8 K, the temperature dependence weakens and is almost linear. Such a strong variation of the scattering rate is expected when inelastic scattering originates from interactions that become gapped below T_c. A model based on quasiparticle lifetimes limited by spin-fluctuation scattering has been proposed [157], although the predicted temperature dependence does not exactly correspond to the observations, neither on YBCO, nor in $CeCoIn_5$. A strong increase of the quasiparticle mean free path below T_c is also reported from thermal Hall angle measurements [88].

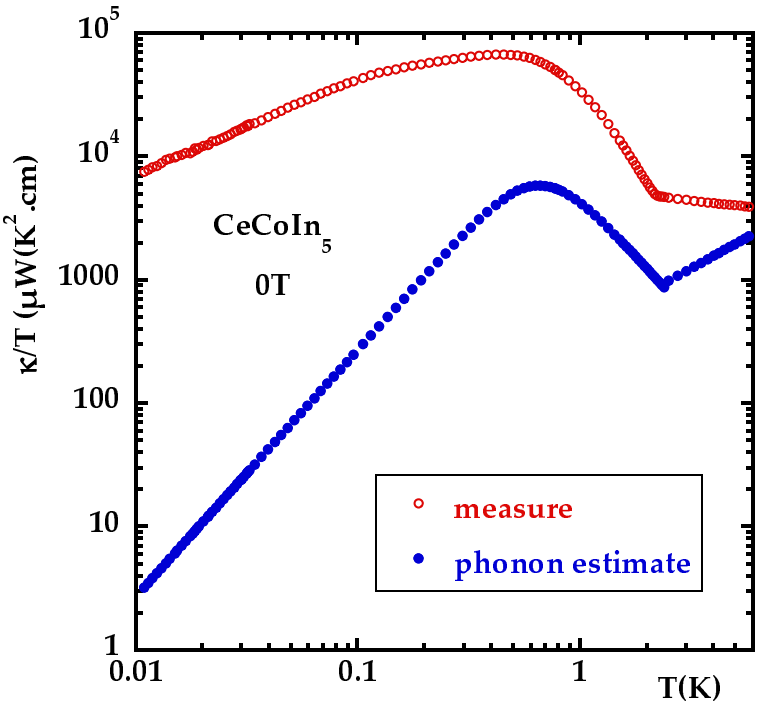

Figure 5.10. Comparison of the measured $\kappa/T(T)$ with a simple estimation for the phonon contribution, according to the analysis on $PrOs_4Sb_{12}$ with $\frac{1}{\kappa^{ph}_{sc}/T} = \frac{1}{\kappa^{ph}_{normal}/T}\left(\frac{T}{T_c}\right)^{n=3} + \frac{1}{bl_0^{ph}T^2}$ where $\kappa^{ph}_{normal} = aT^2$. We used the following constants: $a = 386$ μWK^{-3}cm^{-1} (obtained with equation (4.5)), $\beta = 20$ μJK^{-4}cm^{-3} (value measured for $CeIrIn_5$ [90]), $c_s = 2000$ m/s and $l_0^{ph} = 200$ μm. At low temperatures, the phonon contribution to heat transport seems completely negligible.

In order to verify the eventual impact of the phonon contribution to the measured thermal conductivity in the superconducting state of $CeCoIn_5$, we tried a similar analysis as in $PrOs_4Sb_{12}$ (see fig. 4.23 and equation (4.9)). Even if the assumptions of this simple model seem to apply in a minor extend to $CeCoIn_5$ (notably concerning the temperature dependence $\kappa^{ph} = aT^2$ above T_c which is not realized), it allows us a rough estimation of the corresponding orders

of magnitude. In fig. 5.10, we assumed a boosted phonon mean free path below T_c (like in $PrOs_4Sb_{12}$), and the very low temperature region was calculated on the basis of the data in the literature (for specific heat) [90] as well as our crystal dimensions. What can be inferred is that, whatever the corrections to the simple estimate for κ^{ph}, the electronic contribution clearly dominates over the phonon heat transport, at least in the investigated temperature range.

5.3.3. κ/T-behavior for $T \to 0$

Let us now turn to the lowest temperatures ($T \to 0$) (still in zero magnetic field). Here the divergence between the different thermal conductivity reports is quite amazing, and displayed in fig. 5.11.

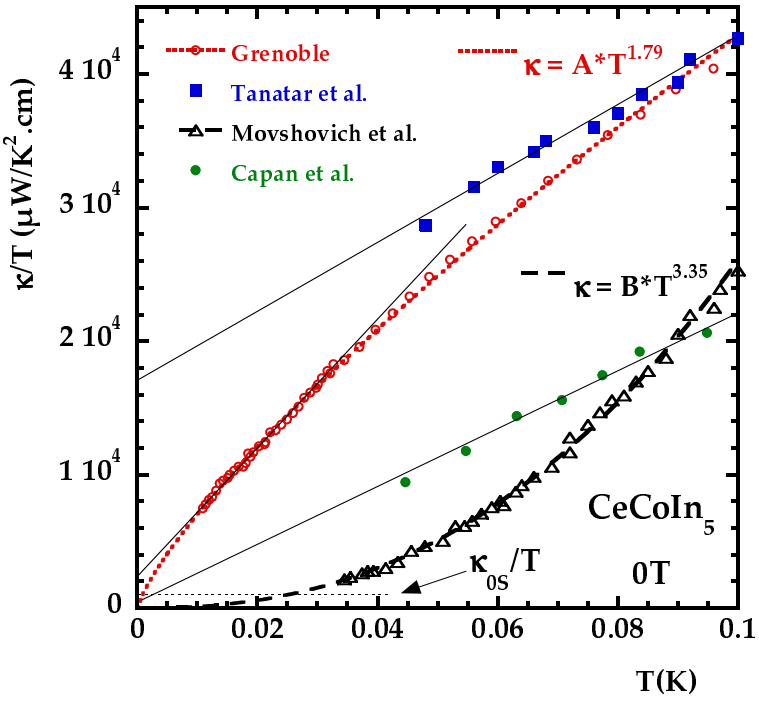

Figure 5.11. Comparison of our thermal conductivity measurements $\kappa/T(T)$ on $CeCoIn_5$ (sample C2) at very low temperatures with that reported from TANATAR et al. [201], CAPAN et al. [37] and MOVSHOVICH et al. [136] (*not* normalized, "original" data). The solid lines and power law fits just indicate possible (not necessarily physical) extrapolations towards $T \to 0$. Of course, such extrapolations strongly depend on the chosen temperature range. The black dotted line at the bottom of the view-graph indicates an estimate of the *universal* limit $\kappa/T(T \to 0) \equiv \kappa_{0S}/T$ according to [136].

As already discussed in the introductory chapter, several experiments point to *unconventional* superconductivity with line nodes of the gap in $CeCoIn_5$: temperature (power law) dependence and angle-resolved measurements of specific heat, power law behavior of $1/T_1(T)$ in NQR measurements and absence of coherence peak, flux-line lattice analysis, temperature dependence of LONDON penetration depth and angle-resolved thermal conductivity measurements. In the case of unconventional superconductivity, a specific κ-behavior in the $T \to 0$ limit is expected, which can be explained qualitatively as follows (application of kinetic theory to residual normal fluid of nodal quasiparticles): $\kappa/T(T \to 0) \equiv \kappa_{0S}/T \propto \gamma_{0S} \cdot v_F^2 \cdot \tau$ with $\tau \propto 1/\rho_0$ (scattering

lifetime inversely proportional to the impurity concentration x or the residual resistivity). If the superconducting state has a density of states which varies linearly with energy, then one expects $\gamma_{0S} \propto x$ (as is experimentally observed in La- (impurity-) doped $Ce_{1-x}La_xCoIn_5$ [201]). Finally, the dependencies on the impurity concentration of τ and γ_{0S} cancel out, leaving κ_{0S}/T *universal* (independent of x). A complete theoretical treatment confirms this simple analysis [64]. In [136], MOVSHOVICH et al. give a rough estimate of the universal limit in $CeCoIn_5$ in the case of a d-wave gap function, yielding $\kappa_{0S}/T \approx 1000\ \mu WK^{-2}cm^{-1}$. This value is marked in fig. 5.11. Regarding our low temperature measurements down to 10 mK, it is difficult to draw any conclusions on that topic. The extrapolation of the data for $T \to 0$ strongly depends on the chosen temperature range, and several scenarios seem possible, as shown in fig. 5.11. However, it is quite certain that our $T \to 0$ limit will lie much lower than that deduced by TANATAR et al. [201] – an extrapolation to very low values close to the *universal* limit cannot be excluded, and hence the existence of "unpaired electrons" [201] is *not* confirmed. Eventually, we recover a sort of cross-over regime, differing from more common behaviors established under well defined conditions ($T \ll T_c$), because of the existence of a very low energy scale in $CeCoIn_5$, so that in the considered temperature range the intrinsic $T \to 0$ behavior has not clearly emerged. In this context, it might be worth to recall that already in the normal phase, the WIEDEMANN–FRANZ regime is recovered at much lower temperatures (see fig. 5.5) than for example in $PrOs_4Sb_{12}$. For the moment, straightforward conclusions on the recovery of the universal limit and the gap topology seem not possible from the available data, and require complementary experiments, for example on other samples. In any case, our measured κ/T values at 10 mK are curiously high compared to $\kappa/T(T_c)$ (and compared to the universal limit), which might be related to the enormous κ-upturn below T_c and the strong relevance of inelastic scattering in $CeCoIn_5$ (with an eventually huge quasiparticle mean free path l^{mfp} at lowest temperatures, since $l^{\mathrm{mfp}}_{\mathrm{elast}} \gg l^{\mathrm{mfp}}_{\mathrm{inelast}}$).

5.3.4. κ/T-behavior at very low fields and temperatures

To gain further insight, we will consider the effect of (small, compared to $H_{c2}(T)$) magnetic fields on thermal transport in superconducting $CeCoIn_5$, first at the lowest temperatures. As already observed when discussing fig. 5.7, at 8 mT (i.e. $H/H_{c2} \sim 0.0015$) $\kappa/T(T \to 0)$ exhibits a metallic (constant) behavior (measurements were carried out down to 14 mK, i.e. $T/T_c \sim 0.006$). Remind that the extrapolation of $\kappa/T(H = 0)$ down to $T \to 0$ (fig. 5.11) is at maximum of order 4% of the normal phase value (from $B = 6.05$ T). This means, a magnetic field of only $0.0015H_{c2}$ is sufficient to restore nearly 40% of the normal state heat transport. This huge effect is quite spectacular and unprecedented. In $PrOs_4Sb_{12}$, at the equivalent field magnitude, κ/T is still only of the order of some percent of the normal state value (see first data point at 4 mT of the field scan in the "field cooled" mode at 50 mK in fig. 4.15b).

In order to determine its origin, this peculiar behavior has to be examined very carefully, especially in the light of other experiments placing $CeCoIn_5$ among the candidates for *unconventional* superconductivity with a d-wave order parameter symmetry, similar to the high-T_c cuprates. $CeCoIn_5$ most likely is a *clean* superconductor ($l^{\mathrm{mfp}} \gg \xi_0$) [136]. In conventional and clean type-II superconductors like Nb, for $T \ll T_c$ small magnetic fields $H \gtrsim H_{c1}$ only lead to a slightly decreasing κ^{el} probably due to quasiparticle scattering off the vortices [118] (not represented on the scale of fig. 4.16). Clearly, in $CeCoIn_5$, a phonon contribution to the κ-increase can be ruled out because of its negligible magnitude (see fig. 5.10, in addition, as we already pointed out, κ^{ph} should only diminish, and *not* increase with magnetic field). According to the resistivity data in this temperature range (see fig. 5.6), the *elastic* scattering regime is

already reached (in 6 T, so all the more in the superconducting state), so that the quasiparticle mean free path is already at its maximum.

An increasing κ^{el} hence can only come from either the recovery of part of the normal phase density of states (as in the case of multiband superconductors like $PrOs_4Sb_{12}$ and MgB_2 for $H \sim H_{c2}^S$) or, in *unconventional* superconductors, from the so-called VOLOVIK-effect or DOPPLER-shift [211] which increases the quasiparticle density of states as a function of magnetic field (in the case of line nodes and a *d*-wave order parameter symmetry as $\propto \sqrt{H}$). KÜBERT and HIRSCHFELD [103] essentially derived the same field dependence (neglecting vortex scattering) for thermal transport, i.e. $\kappa^{el}(H) \propto \sqrt{H}$ ($T \ll T_c$, $H \ll H_{c2}$, clean limit, heat current $j \perp H$, *d*-wave gap). Today, high-T_c cuprates are probably the most studied realization of a "*d*-wave superconductor". The VOLOVIK effect was first observed by specific heat studies [133], followed from several heat transport experiments investigating the corresponding work of KÜBERT and HIRSCHFELD. As a general result (without considering "high-T_c"-specific complications related to different doping concentrations, etc.), their theory fits very well (even quantitatively [41]) to the experimental data, at least at lowest temperatures [41, 197, 13], i.e. in the sub-K-range. What can be inferred for the case of $CeCoIn_5$? First of all, we have to compare the corresponding field scales. In the theory, the only relevant field scale is H_{c2}, which seems to be respected in the experiments: considerable variations of κ/T occur only within a field range up to several T (even if the upper critical field is not exactly known and experimentally inaccessible, we can assume that 10 T roughly correspond to $0.05 - 0.15 H_{c2}$). A more quantitative comparison with our measurements on $CeCoIn_5$ would require the knowledge of $H_{c2}(T \to 0)$ and of the corresponding κ/T values in the normal state of high-T_c cuprates. In UPt_3, another *unconventional* superconductor with E_{2u}-type pairing, the normalized $\kappa/T(T \to 0)$ rises linearly with magnetic field, as predicted by BARASH et al. [15], and as already discussed in the previous chapter. Again, like for the high-T_c cuprates, the corresponding field scale for the κ-increase is $H_{c2}(T)$ (see fig. 4.16, and for more details [189], page 98).

Back to $CeCoIn_5$. In fig. 5.12a, we plot a field scan $\kappa/T(H)$ for low fields $H \ll H_{c2}$ at 25 mK, and in fig. 5.12b for the whole field range up to H_{c2}, but at 50 mK. Indeed, as in $PrOs_4Sb_{12}$, very low temperature measurements under field are extremely time consuming due to the long relaxation times. In order to get a picture of the effects for $T \to 0$, we made the lowest field scan at 25 mK, and jumped to 50 mK above 50 mT: in any case, $\kappa/T(T)$ is close to a constant already at 8 mT (see fig. 5.7). In figure 5.12a, one observes a significant increment of κ/T (of about 30%) above 10 mT, the maximum being reached at about 20 mT. For further increasing fields, thermal conductivity decreases, as can be better inferred from fig. 5.12b with the complete field scan. The transition towards the normal state is quite abrupt (steep step in κ/T), signature of a *first order* transition. Let us still concentrate on the low field region at 25 mK. In addition to the "zero field cooled" (ZFC) data of the H-scan, we also plot the data of the T-scans taken in the "field cooled" (FC) mode in fig. 5.12a. A slight deviation between both data sets is revealed, probably due to flux pinning. Figure 5.13 shows up and down field sweeps at 50 mK, revealing the same pinning effects. Owing to the strong field dependence of κ, the field magnitude has to be determined very carefully (possible due to the newly installed HALL field probe close to the sample). In particular, this applies to the "zero field position" of the magnet in order to restore the initial, virgin state of the sample by heating above T_c. The *initial* plateau for ZFC data up to $H' \sim 10$ mT corresponds to the magnetization data of MAJUMDAR et al. [122], who estimate a lower critical field $H_{c1}(T \to 0)$ of roughly 15 mT. So it is quite natural to identify the field range where κ/T starts to increase with the beginning of field penetration, i.e. $H' \sim H_{c1}$. Clearly, the field scale of the κ-enhancement is of the order or

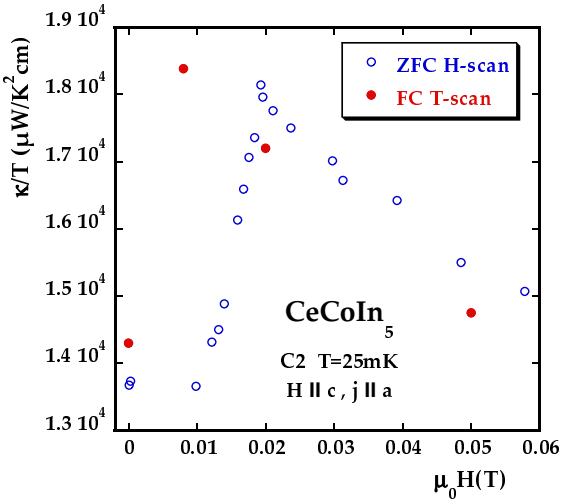

(a) Low field scan. With field penetration, above $H_{c1} \sim 15$ mT, a strong κ/T-increase of thermal conductivity is observed (within a MBSC scenario, $H_{c2}^S \sim H_{c1}$). For higher fields, the κ-increase is suppressed.

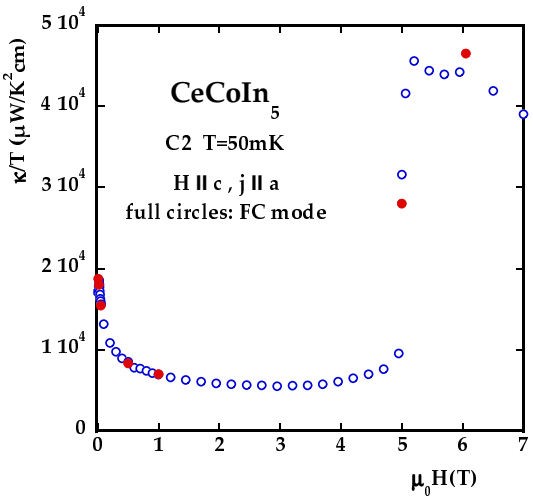

(b) Field scan up to H_{c2}, showing an initial κ/T-decrease, followed by a "plateau" and a steep upturn before H_{c2} (first order transition).

Figure 5.12. Field scan of thermal conductivity at very low temperatures. The low field part was realized at 25 mK (where a κ-increase is expected from the temperature scans (see fig. 5.7)). For experimental reasons, at higher fields, we switched to 50 mK. The corresponding data of the temperature scans (field cooled mode) are also plotted for comparison.

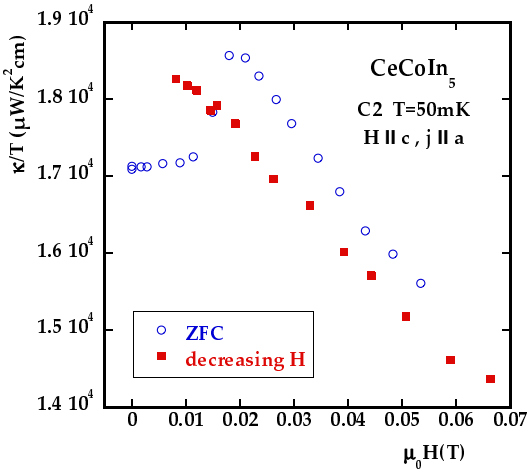

Figure 5.13. Comparison of thermal conductivity scans with increasing and decreasing field at 50 mK – the discrepancy is likely due to flux pinning. Note that the ZFC data at $H = 0$ do not match the virgin curve (see fig. 5.7): this is probably due to the large relaxation times after the field history preceding the measurements.

even lower than H_{c1}. Since field screening up to H_{c1} impairs the field scans in the ZFC mode, we tried to perform supplementary measurements at several fields between 0 and 20 mT and at 25 mK in the FC mode, in order to determine the field position of the κ/T-maximum. But creeping relaxation processes after heating the sample above T_c at each field require enormous waiting periods (of several days, if at all) to obtain reliable data. Nevertheless, measurements (not shown) carried out after reasonable waiting periods of only some hours might indicate that the maximum is situated slightly below 10 mT. What is the origin of the κ-enhancement at

such low magnetic fields in $CeCoIn_5$?

Even if several experiments point to *unconventional* superconductivity with a *d*-wave order parameter symmetry in $CeCoIn_5$, it is evident from the above discussion that a DOPPLER-shifted quasiparticle excitation spectrum alone is *not* sufficient to explain the field-induced increase in thermal conductivity for $T \ll T_c$, because of the very low field scale for which occurs. The most likely scenario to resolve this low field scale is to assume multiband superconductivity, like in the case of $PrOs_4Sb_{12}$, with a characteristic cross-over field $H_{c2}^S \lesssim H_{c1}$, above which the overlap of the vortex cores restores the normal phase of the small gap band. Such a scenario matches with the *constant* (normal state like) $\kappa/T(T)$ at 8 mT and lowest temperatures. In addition, this viewpoint is consistent with the characteristics of the electronic structure in $CeCoIn_5$ exposed in the introductory chapter (in analogy to $PrOs_4Sb_{12}$): DE HAAS–VAN ALPHEN measurements indicate a wide spread of effective masses, and the FERMI surface consists of more or less quasi-2D and 3D sheets, the former associated to the heavier, the latter to the lighter masses. Once again, such a MBSC scenario is essential to account for the low magnetic field scale of the experimentally observed κ-increase.

Of course, the DOPPLER-shift of the quasiparticles related to the small gap band (if the latter exhibits nodes of the gap) could also contribute to this initial κ-increase. However, it seems questionable whether the VOLOVIK effect would lead to a detectable change in the density of states, since above $H_{c1} \sim H_{c2}^S$, a major part of the normal phase is already recovered (vortex overlap), whereas the DOPPLER-shift has most impact when rising the density of states up from (nearly) zero. So the VOLOVIK-effect probably only gives a small contribution to the κ-increase.

In any case, as for $PrOs_4Sb_{12}$, the question of gap nodes has to be addressed by the temperature dependence of thermal transport (at $T \ll T_c$), not by its field dependence. However, in the case of $CeCoIn_5$, $\kappa(T)$ is strongly influenced by inelastic scattering, and no clear intrinsic behavior for $T \to 0$ can be extracted from the available experimental data. Hence, this topic is left for further investigations.

At this stage, we can only refer to our thermal contact resistance measurements on $CeCoIn_5$ (see figures 3.11 and 3.17), which do not show any upturn at low temperatures in zero field, in contrast to observations on $PrOs_4Sb_{12}$, where the low temperature increase of $R_{cc}^{th}(T)$ can be attributed to the opening of the small gap on the whole FERMI surface, in agreement with the exponential decrease of $\kappa^{el}/T(T \to 0)$. So, in $CeCoIn_5$, the absence of any anomaly in the thermal contact resistance may indicate either a very low energy scale of the gap, or, most likely, the presence of gap nodes, preventing the breakdown of thermal transfer at the contact interface.

5.3.5. $\kappa(H)$ at intermediate field range

Let us now analyze the κ-decrease for increasing magnetic fields. Indeed, above 20 mT, $\kappa/T(H)$ diminishes, as can be seen on fig. 5.12a (and fig. 5.12b). The same is true at 500 mK, but starting at $H = 0$ (see fig. 5.14). At 500 mK, the drop is considerable, and takes place again within a field scale much lower than H_{c2}. For higher fields, $\kappa(H)$ crosses a sort of "plateau", before a sudden upturn at $H_{c2}(T)$, due to the first order transition which appears below ~ 0.7 K.

For a more quantitative discussion of the κ-drop with field, we will concentrate on the H-scan at 500 mK, where most data points are available. Once again, the remarkable feature is the drop of thermal conductivity within a field scale much lower than H_{c2}. We already mentioned that a reduced thermal conductivity in the mixed state is well-known from clean, conventional type II superconductors like Nb [118], and ascribed to quasiparticle scattering off the vortices. Of

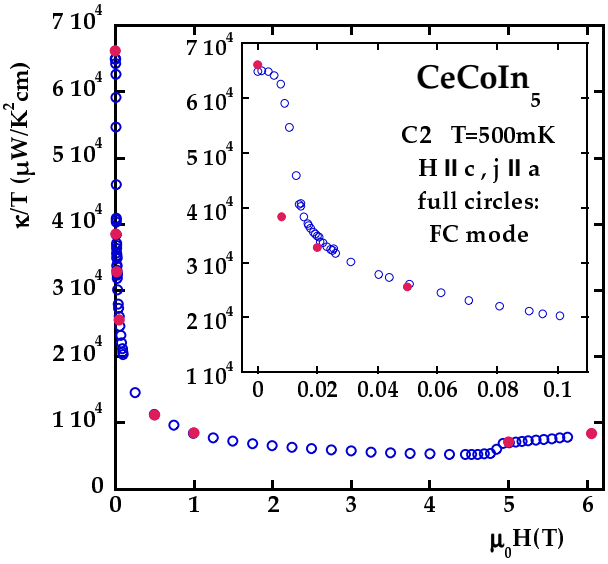

Figure 5.14. $\kappa/T(H)$ at 500 mK. The drop of thermal conductivity towards its normal state value is concentrated on a very low field scale (compared to H_{c2}). The ZFC and FC data correspond well, except for fields lower than H_{c1} (see inset).

course, the field-induced quasiparticles also represent supplementary scattering centers for the phonons, so that their contribution generally reduces with field. But in $CeCoIn_5$, such changes in κ^{ph} are negligible compared to the electronic contribution (see fig. 5.10). In a simple picture, the field dependence of κ^{el} can be derived as follows: the magnetic flux through the sample is $\phi_s = N \cdot \phi_0 = S \cdot B$ with N the number of vortices and A the sample area. Defining a_0 as the average intervortex distance, N becomes $N = A/a_0^2$ and

$$a_0^2 = \phi_0/B \propto 1/B, \qquad \text{or} \qquad (a_0/\xi_0)^2 \sim H_{c2}/H. \tag{5.1}$$

Considering a_0 as proportional to the corresponding mean free path against vortex scattering $l_{\text{vortex}} \propto a_0$, one obtains for the thermal conductivity

$$1/\kappa^{el} \sim \frac{3}{C_p v_F^2} \times (1/\tau_{\text{elast}} + 1/\tau_{\text{inelast}} + 1/\tau_{\text{vortex}}) \tag{5.2}$$

with $1/\kappa^{el} \propto 1/\tau_{\text{vortex}} \propto \sqrt{H/H_{c2}}$ [57, 218], if the other two scattering mechanisms and specific heat are supposed field-independent. Applied to the $\kappa/T(H)$ data at 500 mK, we find indeed $T/\kappa \propto \sqrt{B}$ (see fig. 5.15) for fields up to about 600 mT (of course apart from the field region $H < H_{c1}$ in the ZFC mode); for higher fields, the increase is slower than $\propto \sqrt{H}$.

In UPt_3, at intermediate temperatures, κ/T also decreases with low fields [189], and similar observations are reported for the high-T_c cuprates [6, 197]. In unconventional superconductors, another origin of the κ-decrease, without invoking vortex scattering of quasiparticles, is theoretically suggested by several authors [103, 15, 209]: at finite temperatures, the Doppler-shift of excitations leads to a decrease in the impurity scattering relaxation time at low fields, which can exceed the parallel rise in the quasiparticle density of states, and hence disrupt the monotonic increase of thermal conductivity (with a minimum in $\kappa(H)$ predicted at $H/H_{c2} \simeq (k_B T/a\Delta_0)^2$ with $a \sim 1$). However, comparing the magnitude of the κ-drop in high-T_c cuprates ($\kappa(H_{\min}/\kappa(H=0) \sim 0.8 - 0.95$) and $CeCoIn_5$ ($\kappa(H_{\min}/\kappa(H=0) \sim 0.1$ at 500 mK), it is clear that the effect is considerably stronger in $CeCoIn_5$. On the other hand, in order to explain the rapid decrease with field of the mean free path as probed by the Hall angle experiment, Kasahara et al. [88] suggest unusual vortex-quasiparticle scattering due to the

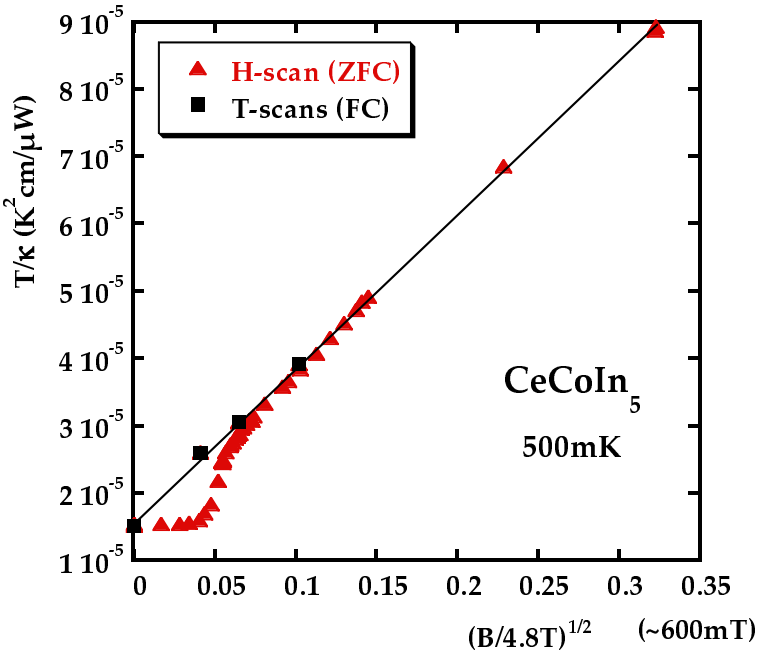

Figure 5.15. Evolution of $1/\kappa(\sqrt{H/H_{c2}})$ at 500 mK and in low fields. Apart from the data in the ZFC mode at $H < H_{c1}$, $\kappa \propto H^{-1/2}$ is verified, according to equation (5.2) and $l_{\text{vortex}} \propto \sqrt{H_{c2}/H}$. The average intervortex distance a_0 in 20 and 600 mT roughly corresponds to 0.32 μm and 60 nm, respectively, according to $a_0 = \sqrt{\phi_0/B}$, equation (5.1).

possible existence of antiferromagnetism in the vortex cores, or to the particulary high energy scale of the quasiparticle spectrum of the vortex core as a result of the low FERMI energy of about only 15 K [88].

Avoiding too sophisticated interpretations at this premature stage of the study, we just retain the experimental fact that the field-induced κ-decrease in $CeCoIn_5$ occurs on an unusually small field scale H_{c2}^S. In the picture of vortex scattering, this means that the limiting scattering length (related to the coherence length) is already approached on that field scale. Alternatively, one can argue as follows: Owing to the strong suppression of the inelastic scattering rate below T_c (in zero field), the recovery of quasiparticles with magnetic field possibly leads to a "comeback" of inelastic scattering, impeding thermal transport. This seems consistent with the experimental fact that at intermediate temperatures, heat transport appears to be much lower in the normal phase (at least when comparing with the data in 6.05 T). Indeed, the suppression of the sub-T_c κ-enhancement with field resembles the observations on $PrOs_4Sb_{12}$, with the differences that in $PrOs_4Sb_{12}$ the κ-increase appeared at temperatures well below T_c, was less marked, and somehow also involved the phonon contribution (see fig. 4.23). On $CeCoIn_5$, the suppression is realized on a very small field scale, consistent with a MBSC scenario (meaning that a large number of quasiparticles is already recovered for $H \sim H_{c2}^S$). However, note that at 500 mK a considerable fraction of the small gap band might already be in the "normal state", without any field. Nevertheless, a field of the order of H_{c2}^S creates supplementary (light) quasiparticles, leading to a decreasing κ, in the same manner as their "condensation" in zero field increases κ.

From these points of view, the high field sensitivity of the κ-increase for $T < T_c$ supports MBSC in $CeCoIn_5$, or at least the existence of a low field scale H_{c2}^S. As to its approximate magnitude, at 500 mK and only 20 mT, κ/T has dropped from 6.5×10^4 to about 3×10^4 $\mu WK^{-2}cm^{-1}$,

with $\kappa(500\,\mathrm{mK}, 6.05\,\mathrm{T}) \sim 1 \times 10^4\ \mu\mathrm{WK}^{-2}\mathrm{cm}^{-1}$. Note that in the high-$T_c$ cuprates, the κ-increase (see fig. 5.9) probably disappears on a (relatively) higher field scale $\sim H_{c2}$ [150] than in $CeCoIn_5$.

Two further remarks might be added: the first one concerns the orientation (angle) between the magnetic field and the heat flux (in $CeCoIn_5$: $j \perp H$, in $PrOs_4Sb_{12}$: $j \parallel H$). Intuitively, vortex scattering might be very effective in $CeCoIn_5$ because of the perpendicular position of the vortices compared to the heat flow. Indeed, measurements on Nb of the anisotropy of heat transport in the mixed state [118] indicate that thermal conductivity parallel to the magnetic field $\kappa_\parallel$ is higher than $\kappa_\perp$ for $T < T_c$. In any case, it would be interesting to measure $\kappa_\parallel$ in $CeCoIn_5$ and to compare the results with the existing $\kappa_\perp$ data.

Second, at very low temperatures, we already discussed the initial κ-increase with field within a MBSC scenario. In fact, the density of states induced by the magnetic field has to be balanced by the effects of vortex scattering. As a general feature, vortex scattering is thought to be less effective at lowest temperatures and low fields because of either the perfect ordering of the vortex array (in which case the Bloch theorem "prevents" quasiparticles from being scattered by vortices [103]), or due to the fact that vortices become "transparent" at low energies [57]. Nevertheless, we clearly observe a considerable κ-decrease even at 25 mK, as soon as $H \gtrsim 20$ mT and after the initial increase. Up to fields of the order of H_{c2}^S the density of states effect dominates (κ rises), but beyond, once the small gap has been suppressed (vortex overlap), increasing H will increase the number of vortices of the "large gap" band, which can only lower κ. Again, this effect is reinforced by the geometry $j \perp H$.

5.4. Conclusion

Our thermal transport study on $CeCoIn_5$, though uncomplete, reveals several intriguing features about this heavy fermion superconductor:

- We confirm the previously reported strong κ-increase below T_c in zero field and the large κ-value at low temperatures ($\kappa/T(10\,\mathrm{mK}) \sim 2\kappa/T(T_c)$), probably due to suppression of inelastic scattering.

- At lowest accessible temperatures, there is a striking discrepancy between the reported thermal transport results. In our measurements, the magnitude of $\kappa/T(T)$ is still higher than at T_c (but strongly decreasing), and a reliable extrapolation for $T \to 0$ seems difficult, so that no information on the gap topology can be deduced (nevertheless, thermal contact resistance measurements may indicate the existence of gap nodes). However, we can exclude the presence of "unpaired" electrons as proposed in [201].

- In only 8 mT $\ll H_{c2}$ a constant $\kappa/T(T \to 0) \sim 0.4\kappa/T(T \to 0, B = 6\,\mathrm{T})$ is recovered. This strong enhancement can not be attributed solely to a Doppler-shifted quasiparticle excitation spectrum because of the small field scale for which it occurs. It points again to a MBSC scenario like in MgB_2 or $PrOs_4Sb_{12}$ with a particular field scale ($\leq H_{c1}$).

After these "preliminary" results, further examination is necessary, notably to clarify the competing effects of small magnetic fields on heat transport at various temperatures and to determine the behavior in the $T \to 0$ limit in zero field. These studies should include measurements in the field configuration $H \parallel j$, and a complete characterization of the $H - T$ plane.

6. Conclusion

This thesis is devoted to the study by thermal transport of the superconducting phase of two heavy fermion compounds, $PrOs_4Sb_{12}$ and $CeCoIn_5$.

$PrOs_4Sb_{12}$

The starting point were reports on the angular dependence of thermal conductivity in a rotated magnetic field, and on the double transition in specific heat, both pointing to unconventional superconductivity in $PrOs_4Sb_{12}$. So we performed heat transport measurements down to 30 mK and up to magnetic fields of 5 T to analyze the gap topology and low lying energy excitations. For that purpose, we extracted a thin (45 µm) platelet from on a small cubic $PrOs_4Sb_{12}$ single crystal. Sample characterization by specific heat documents the collapse of a double superconducting transition to a single C_p jump within the same crystal, just by reducing its size. Coinciding signatures of the superconducting transition in C_p, ρ and κ further testify the homogeneity of the small $PrOs_4Sb_{12}$ platelet. On the experimental setup, particular attention was paid to the control and optimization of the thermal contacts, in order to achieve reliable κ-measurements even at very low temperatures and under field. As an original part of this thesis, we developed a method to fully characterize (quantitatively) the electric *and* thermal contact resistances, which allowed a better understanding and the improvement of the contacting method compared to previous setups.

First, we confirm measurements on a previous sample: the low temperature field dependence of the (electronic) thermal conductivity exhibits a striking increase ($\sim 0.4\kappa_n$) within fields $H \sim 0.05H_{c2}$. This small field scale (named H_{c2}^S) can only be accounted for in a MBSC scenario, i.e. assuming different gaps (with their corresponding characteristic fields) on the different sheets of the Fermi surface. This might be consistent with the wide spread of effective masses observed experimentally in $PrOs_4Sb_{12}$, explaining the eventually varying coupling strength among the bands from the differing density of states. Since the "limiting" magnetic field involves both the Fermi velocity and the gap amplitude, the field dependence of thermal conductivity alone is not sufficient to deduce the gap ratio or the small energy scale. Similarly, no information on the gap topology can be inferred.

Contrary to experiments on the previous sample, the zero field temperature dependence $\kappa(T) \sim T^3$ of our homogeneous $PrOs_4Sb_{12}$ platelet exhibits the intrinsic behavior at very low temperatures, which is ascribed to the phonon contribution. The remaining electronic contribution vanishes exponentially for $T \to 0$, pointing to fully open gaps on the whole Fermi surface. However, seen the other way round, it rises at temperatures much lower than predicted for a BCS gap corresponding to $T_c \sim 1.75$ K. This discrepancy can be resolved by assuming two parallel conduction channels (bands) with a gap ratio $\Delta_l/\Delta_S(T \to 0) \sim 3$, where $\Delta_S(T \to 0) \sim 1$ K (the relative weight of each channel corresponds to what is deduced from $\kappa(T \to 0, H)$). Altogether, temperature and field dependence of κ dress a "conventional" MBSC scenario in $PrOs_4Sb_{12}$ with fully open gaps on the whole Fermi surface. Support comes from the thermal contact resistance

measurements, exhibiting a strong upturn at very low temperatures (small gap opening acts as barrier for thermal excitations), which is rapidly suppressed under field.

Remaining questions concern discrepancies with the interpretations of other experiments, pointing to gap nodes. Eventually, they can be resolved by reconsidering these results in the light of the high field sensitivity of superconducting $PrOs_4Sb_{12}$, or they may be related to problems of sample quality. In this context, it is still not clear what kind of inhomogeneities might be responsible for the sharp double transition in specific heat. Finally, on a more fundamental level, the nature of the pairing interaction and of the heavy fermion behavior are still not identified.

$CeCoIn_5$

The measurements on $CeCoIn_5$ were motivated by the possibility of MBSC in this compound (among others deduced from the wide spread of effective masses), and essentially aimed to probe the dependence of thermal transport on low fields at very low temperatures, similar to $PrOs_4Sb_{12}$. However, contrary to the latter, the phonon contribution to heat transport in $CeCoIn_5$ is negligible at low temperatures, and the literature agrees on unconventional superconductivity with gap nodes. Here we present only first results of our κ-study. The characteristic feature of thermal conductivity in the superconducting state is an unprecedentedly strong increase below T_c, probably due to the suppression of inelastic scattering. A high thermal conductivity means a particular experimental challenge, and quantitatively, the difference between the existing κ-reports is remarkable. Our setup recovers the Wiedemann–Franz law on the sample for $T \to 0$ (in the normal phase), as well as in the contacts towards the thermometers. For the first time, we measured κ/T down to 10 mK, where it is still higher than at T_c. However, $\kappa/T(T)$ does not recover any simple behavior in that temperature region, but is probably still in a cross-over regime. So, a reliable extrapolation to $T = 0$ and conclusions on the gap topology are not possible. Instead, we uncover a field sensitivity of thermal transport which seems even stronger than on $PrOs_4Sb_{12}$: in 8 mT ($0.0015H_{c2}$), $\kappa/T(T \to 0)$ is constant and of the order of $0.4\kappa_n$ (with $\kappa/T(T \to 0, H = 0) < 0.03\kappa_n$). Within these low fields, such a κ-increase can not be explained by the Doppler shift alone (in the case of gap nodes), but rather reveals an intrinsic very small field scale (of the order of H_{c1}), reminiscent of MBSC. At higher temperatures, one observes a rapid suppression with field of the initial κ-enhancement, and again the characteristic field scale is much lower than H_{c2}. At this stage of the study, our data clearly point to a MBSC scenario in $CeCoIn_5$, but do neither allow any conclusion on the corresponding energy scales nor the gap topology. However, support for gap nodes comes from the measurements of the thermal contact resistance $R_{cc}^{th}(T \to 0, H = 0)$ which does not exhibit any upturn like in $PrOs_4Sb_{12}$. As a next step, κ-measurements in the configuration $H \parallel j$ should be carried out, in particular to lower the diffusion by vortices and enhance the contribution of "density of states" effects.

General conclusion

This thermal transport study on superconducting $PrOs_4Sb_{12}$ and $CeCoIn_5$ reveals that MBSC (discovered on a compound other than heavy fermion) might be more common among the class of strongly correlated materials than initially thought. In any case, MBSC introduces both a supplementary, small, energy and field scale, so that the properties of the superconducting state (and hence the experimentally measured response to temperature, field or electric potential) may be completely different than expected for a one-band superconductor. Further work will be necessary to clarify the microscopic origin of MBSC in heavy fermions compared to well-studied MgB_2. In particular, the idea of MBSC in Ce- or Pr-based heavy fermions comes from the

presence of unrenormalized bands, with little or no f character: this implies both a smaller density of states, but possibly also a smaller pairing interaction if it involves the f-electron degrees of freedom. A success in the determination of the various coupling constants, or at least of their relative weight, might help to discriminate models for the pairing interaction...

We all agree that your theory is crazy. The question which divides us is whether it is crazy enough to have a chance of being correct. My own feeling is that it is not crazy enough.

Niels Bohr

A. Elements on the electric and thermal contact resistance

The purpose of this appendix is to remind the basic ideas of the theory of metallic point contacts. A detailed discussion can be found in the famous textbook of R. Holm [78], and in ref. [84, 213].

A.1. Electric contact resistance

In general, the electric resistance of a metallic junction in the normal state is described by Wexler's formula [213, 61]. Its approximate form splits up the contact resistance R into a ballistic (also called Sharvin resistance) and a resistive part (so-called Maxwell or constriction resistance):

$$R(T) \approx \frac{2R_K}{(ak_F)^2} + \frac{\rho(T)}{2a}\,, \tag{A.1}$$

where $R_K \equiv h/e^2 = 25.8\ \mathrm{k}\Omega$, a the radius of the circular orifice, ρ the resistivity of the contact material and k_F the corresponding Fermi wave number (for simplicity, equal Fermi wave numbers with spherical Fermi surfaces on both sides of the junction are assumed).

A.1.1. Maxwell constriction resistance

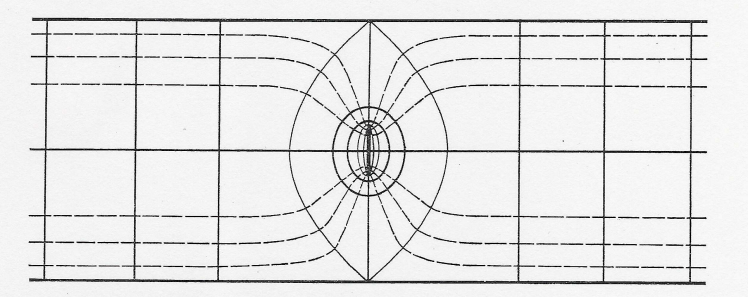

Figure A.1. Point contact in the Maxwell limit ($l < a$). Indicated are the electric field lines (broken curves) and the equipotential surfaces [78].

For large contacts with diameter d, radii $a \gg l$ (l: electronic mean free path), Maxwell's resistance $\rho(T)/2a$ dominates. Its physical origin is related to the fact that the current lines of flow are bent together through a narrow area (see fig. A.1), causing an increase of resistance compared with the case of a continuous material. This constriction resistance was first addressed by Maxwell in 1891: he solved Poisson's equation for the geometry of the orifice problem in oblate spherical coordinates, yielding

$$R_M = \rho(T)/2a = \rho(T)/d \tag{A.2}$$

for the resistance of the point contact. Here I will approach the real shape of the lines of flow with a much simpler calculation, just to demonstrate the main idea. Let's replace the contact surface by a sphere K of infinite conductivity of radius a. The lines of current flow start radially and are symmetrically distributed around K so as to arrange the equipotential surfaces as hemispheres concentric to K. Now, consider the constriction resistance in one contact member. The resistance $\mathrm{d}R$ between the hemispheres with the radii r and $r + \mathrm{d}r$ is

$$\mathrm{d}R = \frac{\rho \mathrm{d}r}{2\pi r^2} \,.$$

We integrate trough a hemisphere which passes through the point where the potential is tapped for measuring the contact voltage; its radius will large compared with a. As more distant parts add very little to the integral, we may choose infinity as the upper limit and then obtain for the total constriction resistance

$$R = 2 \cdot \frac{\rho}{2\pi} \int_a^{+\infty} \mathrm{d}r/r^2 = \frac{\rho}{\pi a} \,.$$

Equation (A.1.1) is approximate only, but differs from the result of detailed calculations (equation (A.2)) only by a numerical factor $(\pi/2)$. If the two materials on both sides are different,

$$R_M = \rho_1(T)/2d + \rho_2(T)/2d. \tag{A.3}$$

In our case, the resistivity of gold is negligible, compared to that of $PrOs_4Sb_{12}$, so that

$$R_M \sim \rho_{PrOs_4Sb_{12}}(T)/2d. \tag{A.4}$$

A.1.2. Sharvin resistance

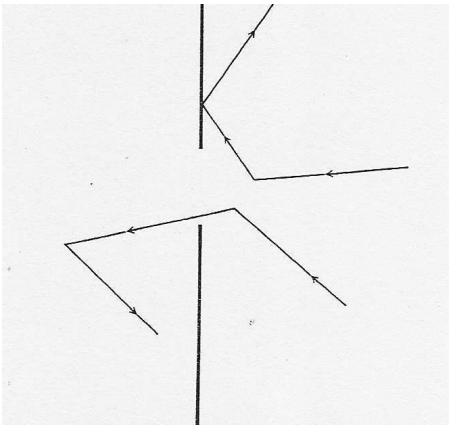

Figure A.2. Point contact in the Knudsen limit ($l > a$) leading to a *ballistic* transport of the electrons.

In the ballistic limit ($a \ll l$), the resistive part represents only a minor correction to the predominant Sharvin contact resistance, the first term of equation (A.1). The situation resembles the well known Knudsen problem in the kinetic gas theory (see fig. A.1.2): by pumping through a small hole in a gas container, the pressure of the gas will be lowered; however, at the moment where the mean free path of the molecules becomes comparable with the diameter of the hole, there is no longer a diffuse flow, and the molecules pass the orifice ballistically. The problem was first considered by Knudsen in 1934, and the different regimes are characterized

by the "KNUDSEN ratio" $K = l/a$. Electric contacts in the clean limit with large KNUDSEN ratios have a large gradient in the potential near the contact,, causing the electrons to be accelerated within the metal over a short distance. Crudely speaking, the electrons are injected with an excess energy from one metal to another. This type of contact with large KNUDSEN numbers was discussed for the first time by SHARVIN in 1965 [179]. The speed increment Δv for an electron which passes the orifice is proportional to the applied voltage V, $\Delta v = eV/p_F$, where p_F is the FERMI momentum. The speed increment results in a current I through the contact given by $I \simeq= \pi a^2 (N^e e^2/p_F)V$, where N^e is the electron density. Finally, the contact resistance is

$$R_S \simeq \frac{p_F}{\pi e^2 N^e a^2}\,. \tag{A.5}$$

Using the DRUDE formula for the resistivity, $\rho = p_F/(N^e e^2 l)$, one finds $R_S \simeq \rho l/\pi a^2$. A more detailed calculation gives an additional numerical factor of 4/3. Finally, the Sharvin resistance ($K \gg 1$) for a circular orifice yields ($p_F = \hbar k_F$ and $N^e = k_F^3/3\pi^2$)

$$R_S = \frac{4\rho l}{3\pi a^2} = \frac{2R_K}{(ak_F)^2}\,. \tag{A.6}$$

So in a simple picture, the main ingredient to the SHARVIN resistance is the FERMI velocity mismatch on both sides of the contact. Note that equation (A.5) is equivalent to the SHARVIN resistance calculated in the BTK-model [27] (see equation (A.17)). It depends on the density of states of the material (through k_F), but not on ρ (ballistic regime).

A.2. Thermal contact resistance

Already MAXWELL pointed out that temperature plays the same role in the theory of heat transport as does the electric potential in the theory of electric transport, and that thermal resistances may be expressed mathematically in the same manner as electric resistances, except that the electric conductivity is replaced by the thermal conductivity. Compared to the electric case, special attention must be paid to the fact that the heat transport is mediated by both electrons and phonons, which means that electric insulators also have a sizeable thermal conductivity.

A.2.1. Thermal Maxwell resistance

Let us return to the above situation and calculate the thermal resistance of the diffusive point contact of fig. A.1, first in the case of an external heat flux. In analogy to the electric case, changing voltage drop for temperature drop, we get a thermal resistance of

$$R^{th} = \frac{1}{2a\kappa}\,, \tag{A.7}$$

neglecting the dependence of electric and thermal conductivities upon temperature. The situation is different if the heat current is generated directly by JOULE heating of the contact resistance. First, for a homogeneous bar shaped metallic sample (section S and length l), with one end isolated (thermally) and the other connected to a heat sink, the heat power at position x is $(R\frac{x}{l})i^2$, and the temperature $T(x)$ is given by

$$-\kappa S[T(x) - T(0)] = \int_0^x \frac{Ri^2}{l} x' \mathrm{d}x' = \frac{1}{2}\frac{x^2}{l} Ri^2 \tag{A.8}$$

so that

$$\frac{\kappa S}{l}\Delta T = \frac{1}{2}Ri^2. \tag{A.9}$$

If R^{th} is defined by

$$R^{th} = \frac{\Delta T}{Ri^2}\,, \text{ then } R^{th} = \frac{1}{2}\frac{l}{\kappa S}, \tag{A.10}$$

which is half of the value compared to the case with an external heat current. So, substituting $\rho_{PrOs_4Sb_{12}}$ by $1/(2\kappa_{PrOs_4Sb_{12}})$ in equation (A.4) (if only one side of the contact matters), we get for the thermal resistance of an orifice-type contact in the case of direct JOULE heating:

$$R^{th} = \frac{1}{2d}\frac{1}{2\kappa} = \frac{1}{2}\frac{1}{4a\kappa}\,, \text{ or } \Delta T = \frac{1}{8a\kappa}\frac{U^2}{R} = \frac{1}{2}\frac{U^2}{L_0 T}\,. \tag{A.11}$$

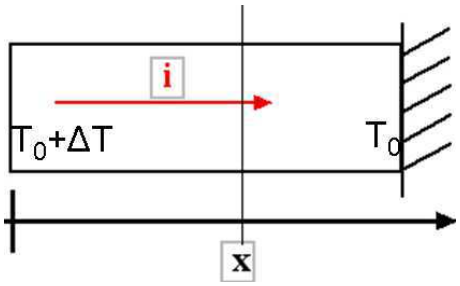

Figure A.3. Obtaining equation (A.9): schematic view of a metallic bar of electric resistance R and with circulating electric current i, leading to a heat current by JOULE heating. On the right-hand side, the bar is connected to a heat sink of temperature T_0.

A.2.2. Thermal Sharvin resistance

To go beyond the qualitative aspects, we tried to analyze quantitatively the thermal contact resistance, $R^{th}_{cc}(T)$ in $PrOs_4Sb_{12}$ and for $B = 0$ T. This section is intended to give the basis for a calculation of the thermal SHARVIN resistance R^{th}_S.

Previously, we already demonstrated that the temperature dependence of the thermal contact resistance can be described within contact theory in the case where no low temperature divergence occurs (zero field in $CeCoIn_5$ and under low field in $PrOs_4Sb_{12}$). Now we have to take into account the low temperature upturn in the calculations, i.e. on the basis of a "BTK–model" (from BLONDER, TINKHAM and KLAPWIJK [27]) adapted to thermal transport. In fact, we suppose here the ballistic limit to apply, even if from the contact dimension $d \approx 550$ µm it is clear that this is not the case. So our analysis, if at all, will give only some indication on the relevant orders of magnitude.

The "BTK–model" is the standard model to determine the effects of finite voltage on a metal(N)-superconductor(S) junction[1]. An applied voltage generates non-equilibrium quasiparticle populations, and in the case of a diffusive regime, solutions can only be obtained in the scope of a suitable BOLTZMANN equation. In contrast, the BTK model assumes *ballistic* acceleration of the particles without scattering (which is a good approximation in the case where the contact dimensions are small compared to the mean free path – supplementary scattering, typically due to oxide layers at the interface, can be accounted for by the Z-parameter, see below). The situation is then considerably simplified: one can assume that the distribution functions of all incoming particles are given by equilibrium FERMI functions, apart from the energy shift

[1] The model is easily adapted to the case of a multiband superconducting state, as the different bands act like parallel channels [34].

due to the acceleration potential. In particular, Blonder, Tinkham and Klapwijk calculate the resulting current I across the junction in a 1D model as follows:

$$I = A \cdot J = 2N(0)ev_F A \int_{-\infty}^{\infty} \mathrm{d}E \, [f_{\rightarrow}(E) - f_{\leftarrow}(E)] \ , \tag{A.12}$$

where A is an effective-neck cross-sectional area depending on the geometry (in the case of a point contact $A = \pi a^2/4$, a being the radius of the contact), J the current density, $N(0)$ the one-spin density of states at the Fermi level and $[f_{\rightarrow}(E) - f_{\leftarrow}(E)]$ the difference of the electron distribution functions for both particle directions ($f_{\rightarrow}(E)$ leaving the metal to cross the interface and to enter the superconductor, and $f_{\leftarrow}(E)$ leaving the "interface" to enter the metal). It is convenient to choose the chemical potential of the Cooper pairs in the superconductor as the reference level. With this convention, we have (f_0: equilibrium Fermi function):

$$f_{\rightarrow}(E) = f_0(E - eV) \, . \tag{A.13}$$

In the other direction (outcoming from the interface on the metal's side), we will get a sum of different contributions:

- As holes reflected quasiparticles (Andreev reflection, with branch crossing[2]): $A(E) \, [1 - f_{\rightarrow}(-E)]$,
- Normally reflected quasiparticles (without branch crossing): $B(E) f_{\rightarrow}(E)$,
- Transmitted quasiparticles (without branch crossing): $C(E) f_0(E)$,
- Transmitted quasiparticles (with branch crossing): $D(E) f_0(E)$, so that

$$f_{\leftarrow}(E) = A(E) \, [1 - f_{\rightarrow}(-E)] + B(E) f_{\rightarrow}(E) + [C(E) + D(E)] \, f_0(E) \tag{A.14}$$

The coefficients $A(E)$, $B(E)$, $C(E)$ and $D(E)$ give the probabilities (in terms of probability currents) of the corresponding processes to occur. Because of probability conservation, it is required that

$$A(E) + B(E) + C(E) + D(E) = 1 \ . \tag{A.15}$$

Finally, we get

$$I_{NS} = 2N(0)ev_F A \int_{-\infty}^{\infty} \mathrm{d}E \, [f_0(E - eV) - f_0(E)] \, [1 + A(E) - B(E)] \ . \tag{A.16}$$

If both sides of the interface are normal metals, we have $A = 0$ (no Andreev reflection) and $1 - B = C$. Knowing that the transmission coefficient in the normal state is simply $(1 + Z^2)^{-1}$, we get

$$I_{NN} = \frac{2N(0)ev_F A}{1 + Z^2} eV \equiv \frac{V}{R_N} \, . \tag{A.17}$$

R_N is here the normal state resistance (Sharvin resistance) which exists even when $Z = 0$ (see also equation (A.5)). Z characterizes the quality of the contact in terms of additional scattering, more precisely Z is the dimensionless barrier strength with $Z = H/\hbar v_F$, where the interfacial

[2] see fig. 4 of [27] for more details as to the branch crossing.

scattering is modeled by a repulsive potential $H\delta(x)$ located at the interface. In the case where $T \neq 0$ K, one has to use a thermally smeared version of the above "transmission coefficient".

In a *thermal* language, the voltage drop ΔV corresponds the temperature gradient ΔT, and in order to get the *heat* and not the charge current, we have to replace ev_F with $(E-\mu)v_F = Ev_F$. For the distribution function on the N side, we now have $f_0(E, k_B T_N)$ (instead of $f_0(E - eV)$), and $f_0(E, k_B T_S)$ (instead of $f_0(E)$) on the S side. The heat current I_Q becomes

$$I_Q = A \cdot J = 2N(0)ev_F A \int_{-\infty}^{\infty} \mathrm{d}E\, E\, [f_{\rightarrow}(E) - f_{\leftarrow}(E)] \ , \tag{A.18}$$

Similar reasoning as in the electric current case and relation

$$1 - f_0(-E, k_B T_N) = f_0(E, k_B T_N) \tag{A.19}$$

finally lead to

$$I_Q = 2N(0)ev_F A \int_{-\infty}^{\infty} \mathrm{d}E\, E\, [f_0(E, k_B T_N) - f_0(E, k_B T_S)]\, [1 - A(E) - B(E)] \ . \tag{A.20}$$

For a small δT:

$$R_S^{th}(T) = 2N(0)ev_F A \int_{-\infty}^{\infty} \mathrm{d}E\ [1 - A(E) - B(E)]\, \frac{E^2}{(k_B T)^2} \left(-\frac{\partial f_0}{\partial x}\right), \tag{A.21}$$

$$\left(-\frac{\partial f_0}{\partial x}\right) = \frac{\exp x}{(1+\exp x)^2} \qquad x = \frac{E}{k_B T}.$$

Again, in the simple case of $T > T_c$ ($\Delta = 0$), we can easily evaluate the integral:

$$R_S^{th}(T) = 2N(0)ev_F A k_B^2 T \frac{1}{1+Z^2} \pi^2/3 \tag{A.22}$$

With the Wiedemann–Franz law, we can convert this result into the electric Sharvin resistance, and find consistently the above R_N.

In the superconducting phase ($\Delta T \neq 0$), and for $E < \Delta$, the normal reflection probability $B = 1 - A$, so that

$$R_S^{th}/T = \frac{6}{\pi^2} L_0 \frac{1+Z^2}{R_N} \int_{\Delta/k_B T}^{\infty} \mathrm{d}x\, x^2 \left(-\frac{\partial f_0}{\partial x}\right) [1 - A(x k_B T) - B(x k_B T)]\,. \tag{A.23}$$

With equation (A.23), we have the main ingredient to calculate (numerically) the electronic thermal conductance $\kappa_{\mathrm{Sharvin}}(T)$ needed for formula (4.13).

Bibliography

[1] *Abrikosov* A.A. and Gorkov L.P., Contribution to the theory of superconducting alloys with paramgnetic impurities. *Soviet Physics JETP*, **12**, 1243 (1961)

[2] *Ambegaokar* V., Woo J., Calculation of the Thermal Conductivity of Pure Superconducting Lead. *Phys. Rev.*, **139**, A1818 (1965)

[3] *Anderson* P.W., Ground State of a Magnetic Impurity in a Metal. *Phys. Rev.*, **164**, 352 (1967)

[4] *Andreev* A.F., The thermal conductivity of the intermediate state in superconductors. *Soviet Physics JETP*, **19**, 1228 (1964)

[5] *Andres* K., Graebner J.E., Ott H.R., $4f$-Virtual-Bound-State Formation in $CeAl_3$ at Low Temperatures. *Phys. Rev. Lett.*, **35**, 1779 (1975)

[6] *Ando* Y., Takeya J., Abe Y., Sun X.F., Lavrov A.N., Novel Anisotropy in the Superconducting Gap Structure of $Bi_2Sr_2CaCu_2O_{8+\delta}$ Probed by Quasiparticle Heat Transport. *Phys. Rev. Lett.*, **88**, 147004 (2002)

[7] *Angst* M., Bud'ko S.L., Wilke R.H.T., Canfield P.C., Difference between Al and C doping in anisotropic upper critical field development in MgB_2. *Phys. Rev.* B, **71**, 144512 (2005)

[8] *Aoki* H., Sakakibara T., Shishido H., Settai R., Onuki Y., Miranovic P., Machida K., Field-angle dependence of the zero-energy density of states in the unconventional superconductor $CeCoIn_5$. *J. Phys.: Condens. Matter*, **16**, L13 (2004)

[9] *Aoki* Y., Namiki T., Ohsaki S., Saha S.R., Sugawara H., Sato H., Thermodynamical Study on the Heavy-Fermion Superconductor $PrOs_4Sb_{12}$: Evidence for Field-Induced Phase Transition. *J. Phys. Soc. Jpn.,* **71**, 2098 (2002)

[10] *Aoki* Y., Tsuchiya A., Kanayama T., Saha S.R., Sugawara H., Sato H., Higemoto W., Koda A., Ohishi K., Nishiyama K., Kadono R., Time-Reversal Symmetry-Breaking Superconductivity in Heavy-Fermion $PrOs_4Sb_{12}$ Detected by Muon-Spin Relaxation. *Phys. Rev. Lett.*, **91**, 067003 (2003)

[11] Ashcroft N.W., Mermin N.D., **Solid State Physics**, Harcourt, Orlando, 1976

[12] *Aswal* D.K., Sen S., Gadkari S.C., Singh Ajay, Gupta S.K., Gupta L.C., Bajapi A., Nigam A.K., Andreev reflections on a MgB_2 superconductor. *Phys. Rev.* B, **66**, 012513 (2002)

[13] *Aubin* H., Bahnia K., Ooi S., Tamegai T., Evidence for Field-Induced Excitations in Low Temperature Thermal Conductivity of $Bi_2Sr_2CaCu_2O_8$. *Phys. Rev. Lett.*, **82**, 624 (1999)

[14] *Bao* W., Aeppli G., Lynn J.W., Pagliuso P.G., Sarrao J.L., Hundley M.F., Thompson J.D., Fisk Z., Anisotropic three-dimensional magnetic fluctuations in heavy fermion $CeRhIn_5$. *Phys. Rev.* B, **65**, 100505(R) (2002)

[15] *Barash* Y.S., Svidzinsky A.A., Nonmonotonic magnetic-field dependence and scaling of the thermal conductivity for superconductors with nodes of the order parameter. *Phys. Rev.* B, **58**, 6476 (1998) and *Barash* Y.S., Svidzinsky A.A., Low-temperature properties and specific anisotropy of pure anisotropically paired superconductors. *Phys. Rev.* B, **53**, 15254 (1996)

[16] *Bardeen* J., Cooper L.N., Schrieffer J.R., Theory of Superconductivity. *Phys. Rev.* , **108**, 1175 (1957)

[17] *Bardeen* J., Rickayzen G., Tewordt L., Theory of the Thermal Conductivity of Superconductors. *Phys. Rev.* , **113**, 982 (1959)

[18] *Bauer* E.D., Capan C., Ronning F., Movshovich R., Thompson J.D., Sarrao J.L., Superconductivity in $CeCoIn_{5-x}Sn_x$: Veil over an Ordered State or Novel Quantum Critical Point? *Phys. Rev. Lett.*, **94**, 047001 (2005)

[19] *Bauer* E.D., Frederick N.A., Ho P.-C., Zapf V.S., Maple M.B., Superconductivity and heavy fermion behavior in $PrOs_4Sb_{12}$. *Phys. Rev.* B, **65**, 100506(R) (2002)

[20] *Bauer* E., Hilscher G., Michor H., Paul Ch., Scheidt E., Gribanov A., Seropegin Y., Noël H., Sigrist M., and Rogl P., Heavy Fermion Superconductivity and Magnetic Order in Noncentrosymmetric $CePt_3Si$. *Phys. Rev. Lett.*, **92**, 027003 (2004)

[21] *Bauer* E., Hauser R., Bühler-Paschen S., **Lecture on Highly correlated electron systems**, TU Vienna, 2003[1]

[22] *Bel* R., Behnia K., Proust C., v.d. Linden P., Maude D., Vedeneev S.I., Test of the Wiedemann-Franz Law in an Optimally Doped Cuprate. *Phys. Rev. Lett.*, **92**, 177003 (2004)

[23] *Bel* R., PhD thesis, ESPCI Paris, 2004

[24] *Beyer Nielsen* J., Smith H., Thermal Conductivity and Charge Relaxation in Strong-Coupling Superconductors. *Phys. Rev. Lett.*, **49**, 689 (1982)

[25] *Bianchi* A., Movshovich R., Capan C., Pagliuso P.G., Sarrao J.L., Possible Fulde-Ferrell-Larkin-Ovchinnikov Superconducting State in $CeCoIn_5$. *Phys. Rev. Lett.*, **91**, 187004 (2003)

[26] *Bianchi* A., Movshovich R., Oeschler N., Gegenwart P., Steglich F., Thompson J.D., Pagliuso P.G., Sarrao J.L., First-Order Superconducting Phase Transition in $CeCoIn_5$. *Phys. Rev. Lett.*, **89**, 137002 (2002)

[27] *Blonder* G.E., Tinkham M., Klapwijk T.M., Transition from metallic to tunneling regimes in superconducting microconstrictions: Excess current, charge imbalance, andsupercurrent conversion. *Phys. Rev.* B, **25**, 4515 (1982)

[28] *Boaknin* E., Hill R.W., Proust C., Lupien C., Taillefer L., Canfield P.C., Highly Anisotropic Gap Function in Borocarbide Superconductor $LuNi_2B_2C$. *Phys. Rev. Lett.*, **87**, 237001 (2001)

[29] *Boaknin* E., Tanatar M.A., Paglione J., Hawthorn D., Ronning F., Hill R.W., Sutherland M., Taillefer L., Sonier J., Hayden S.M., Brill J.W., Heat Conduction in the vortex state of $NbSe_2$: Evidence for Multiband Superconductivity. *Phys. Rev. Lett.*, **90**, 117003 (2003)

[30] *Boaknin* E., Hill R.W., Lupien C., Taillefer L., Canfield P.C., Heat conduction in the borocarbide superconductor $LuNi_2B_2C$. *Physica* C **341-348**, 1845 (2000)

[31] *Bonn* D.A., Kamal S., Zhang K., Liang R., Baar D.J., Klein E., Hardy W.N., Comparison of the influenece of Ni and Zn impurities on the electromagnetic properties of $YBa_2Cu_3O_{6.95}$. *Phys. Rev.* B, **50**, 4051 (1994)

[32] *Bouquet* F., Fisher R.A., Phillips N.E., Hinks D.G., Jorgensen J.D., Specific Heat of $Mg^{11}B_2$: Evidence for a Second Energy Gap. *Phys. Rev. Lett.*, **87**, 047001 (2001) and *Bouquet* F., Wang Y., Sheikin I., Plackowski T., Junod A., Lee S., Tajima S., Specific Heat of Single Crystal MgB_2: A Two-Band Superconductor with Two Different Anisotropies. *Phys. Rev. Lett.*, **89**, 257001 (2002)

[33] *Braun* D.J., Jeitschko W., Preparation and structural investigation of antimonides with the $LaFe_4P_{12}$ structure. *J. of the Less Common Metals*, **72**, 147 (1980)

[34] *Brinkman* A., Golubov A.A., Rogalla H., Dolgov O.V., Kortus J., Kong Y., Jepsen O., Andersen O.K., Multiband model for tunneling in MgB_2 junctions. *Phys. Rev.* B, **65**, 180517(R) (2002)

[35] *Burmistrov* S., Dubovskii L., De Haas–van Alphen Effect in a Type II Superconductor with the Two-Band Fermi surface. Poster-contribution to the International Conference on Strongly Correlated Electron Systems (SCES), Karlsruhe / Germany (2004)

[36] *Cao* D., Bridges F., Bushart S., Bauer E.D., Maple M.B., X-ray-absorption spectroscopy study of the heavy-fermion superconductor $PrOs_4Sb_{12}$. *Phys. Rev.* B, **67**, 180511 (2003)

[37] *Capan* C., Bianchi A., Movshovich R., Christianson A.D., Malinowski A., Hundley M.F., Lacerda A., Pagliuso P.G., Sarrao J.L., Anisotropy of thermal conductivity and possible signature of Fulde-Ferrel-Larkin-Ovchinnikov state in $CeCoIn_5$. *Phys. Rev.* B, **70**, 134513 (2004)

[38] *Champel* T. and Mineev, V., Theory of Equilibrium Flux Lattice in UPt_3 under Magnetic Field Parallel to Hexagonal Crystal Axis. *Phys. Rev. Lett.*, **86**, 4903 (2001)

[39] *Chia* E. E.M., van Harlingen D.J., Salamon M.B., Yanoff B.D., Bonalde I., Sarrao J.L., Nonlocality and strong coupling in the heavy fermion superconductor $CeCoIn_5$: A penetration depth study. *Phys. Rev.* B, **67**, 014527 (2003)

[40] *Chia* E. E.M., Salamon M.B., Sugawara H., Sato H., Probing the Superconducting Gap Symmetry of $PrOs_4Sb_{12}$: A Penetration Depth Study. *Phys. Rev. Lett.*, **91**, 247003 (2003)

[41] *Chiao* M., Hill R.W., Lupien C., Popic B., Gagnon R., Taillefer L., Quasiparticle Transport in the Vortex State of $YBa_2Cu_3O_{6.9}$. *Phys. Rev. Lett.*, **82**, 2943 (1999)

[42] *Cohn* J.L., Skelton E.F., Wolf S.A., Thermal conductivity in the ab plane of untwinned $YBa_2Cu_3O_{7-\delta}$. *Phys. Rev.* B, **45**, 13144 (1992)

[43] *Coleman* P., in Lectures on the Physics of Highly Correlated Electron Systems VI edited by Mancini F., p 79 - 160, American Institute of Physics, New York (2002), available as preprint on condmat/0206003

[44] *Connolly* A., Mendelssohn F.R.S., Thermal conductivity of tantalum and niobium below 1 K. *Proc. Roy. Soc.* (London) **A 266**, 429 (1962)

[45] *Cox* D.L., Quadrupolar Kondo effect in uranium heavy-electron materials? *Phys. Rev. Lett.*, **59**, 1240 (1987)

[46] *Curro* N.J., Simovic B., Hammel P.C., Pagliuso P.G., Sarrao J.L., Thompson J.D., Martins G.B., Anomalous NMR magnetic shifts in $CeCoIn_5$. *Phys. Rev.* B, **64**, 180514 (2001)

[47] *Custers* J., Yamada Y., Tayama T., Sakakibara T., Sugawara H., Aoki Y.,Sato H., Onuki Y., Machida K., to be published in JMMM (proceedings of ICM 2006, Kyoto)

[48] *Daniel* M., Bauer E.D., Han S.W., Booth C.H., Cornelius A.L., Pagliuso P.G., Sarrao J.L., Perturbing the Superconducting Planes in $CeCoIn_5$ by Sn Substitution. *Phys. Rev. Lett.*, **95**, 016406 (2005)

[49] *Dao* V.H., Zhitomirsky M.E., Distorted vortex lattice in a tetrahedral superconductor. *JETP Letters*, **83**, 167 (2006)

[50] *Dolgov* O.V., Kremer R.K., Kortus J., Golubov A.A., Shulga S.V., Thermodynamics of two-band superconductors: The case of MgB_2. *Phys. Rev.* B, **72**, 024504 (2005)

[51] *Doniach* J., The Kondo lattice and weak antiferromagnetism. *Physica* B, **91**, 231 (1977)

[52] *Elgazzar* S., Opahle I., Hayn R., Oppeneer P.M., Calculated de Haas-van Alphen quantities of $CeMIn_5$ (M = Co, Rh and Ir) compounds. *Phys. Rev.* B, **69**, 214510 (2004)

[53] Enss C., Hunklinger S., **Tieftemperaturphysik**, Springer, Berlin, 2000

[54] *Esklidsen* M.R., Kugler M., Tanaka S., Jun J., Kazakov S.M., Karpinski J., O. Fischwer, Vortex imaging in the π band of Magnesium Diboride. *Phys. Rev. Lett.*, **89**, 187003 (2002)

[55] *Esklidsen* M.R., Dewhurst C.D., Hoogenboom B.W., Petrovic C., Canfield P.C., Hexagonal and Square Flux Line Lattice in $CeCoIn_5$. *Phys. Rev. Lett.*, **90**, 187001 (2003)

[56] *Flouquet* J., **"On the heavy fermion road"**, in *Progress in Low Temperature Physics* edited by W. Halperin, **15**, (2005)

[57] *Franz* M., Mixed-State Quasiparticle Transport in High-T_c Cuprates. *Phys. Rev. Lett.*, **82**, 1760 (1999)

[58] *Fulde* P., Keller J., Zwicknagl G., **Theory of Heavy-Fermion Systems.** *Solid State Phys.*, **41**, 1 (1988)

[59] *Giubileo* F., Roditchev D., Sacks W., Lamy R., Thanh D.X., Klein J., Miraglia S., Fruchart D., Marcus J., Monod Ph., Two-Gap State Density in MgB_2: A True Bulk Property Or A Proximity Effect? *Phys. Rev. Lett.*, **87**, 177008 (2001)

[60] *Gloos* K., Kim J.S., Stewart G.R., Transition from Diffusive to Thermal Transport Through Metallic Point Contacts Between the Heavy-Fermion Superconductor UBe_{13} and Tungsten. *J. Low Temp. Phys.*, **102**, 325 (1996)

[61] *Gloos* K., Andreev Reflection at Point Contacts with Heavy-Fermion UBe_{13}? *Phys. Rev. Lett.*, **85**, 5257 (2000)

[62] *Goll* G., v. Löhneysen H., Zapf V.S., Bauer E.D., Maple M.B., Hints at Unconventional Superconductivity of zhe Heavy-Fermion Superconductor $CeCoIn_5$. *Acta Phys. Pol.* B, **34**, 575 (2003)

[63] *Goremychkin* E.A., Osborn R., Bauer E.D., Maple M.B., Frederick N.A., Yuhasz W.M., Woodward F.M., Lynn J.W., Crystal Field Potential of $PrOs_4Sb_{12}$: Consequences for Superconductivity. *Phys. Rev. Lett.*, **93**, 157003 (2004)

[64] *Graf* M.J., Yip S.K., Sauls J.A., Thermal conductivity of superconducting UPt_3 at low temperatures. *J. Low Temp. Phys.*, **102**, 367 (1996) and *Graf* M.J., Yip S.K., Sauls J.A., Rainer D., Electronic thermal conductivity and the Wiedemann-Franz law for unconventional superconductors. *Phys. Rev.* B, **53**, 15147 (1996)

[65] *Grin'* Yu.N., Yarmolyuk Ya.P., Gladyshevskii E.I., Crystal structures of R_2CoGa_8 (R=Sm, Gd, Tb, Dy, Er, Tm, Lu, Y) and $RCoGa_5$ compounds (R=Gd, Tb, Dy, Ho, Er, Tm, Lu, Y). *Sov. Phys. Crystallogr.*, **24**, 137 (1979)

[66] *Grube* K., Drobnik S., Pfleiderer C., v. Löhneysen H., Bauer E.D., Maple M.B., Specific heat and ac susceptibility studies of the superconducting phase diagram of $PrOs_4Sb_{12}$. *Phys. Rev.* B **73**, 104503 (2006)

[67] *Harima* H., Takegahara K., Fermi surfaces of $PrOs_4Sb_{12}$ based on a LDA+U method. *Physica* B, **359-361**, 920 (2005), and Harima H., private communication

[68] *Hasselbach* K., Taillefer L., Flouquet J., Critical point in the superconducting phase diagram of UPt_3. *Phys. Rev. Lett.*, **63**, 93 (1989)

[69] *Knafo* W., Raymond S., Flouquet J., Fak B., Adams M.A., Haen P., Lapierre F., Yates S., Lejay P., Anomalous scaling behavior of the dynamical spin susceptibility of $Ce_{0.925}La_{0.075}Ru_2Si_2$. *Phys. Rev.* B, **70**, 174401 (2004)

[70] *Knebel* G., Méasson M.A., Salce B., Aoki D., Braithwaite D., Brison J.P., Flouquet J., High-Pressure phase diagrams of $CeRhIn_5$ and $CeCoIn_5$ studied by ac calorimetry. *J. Phys.: Condens. Matter*, **16**, 8905 (2004)

[71] *Heffner* R.H. and Norman M.R., Heavy Fermion Superconductivity. *Comments Cond. Mat. Phys.*, **17**, 361 (1996)

[72] Heine V., **Group Theory in Quantum Mechanics**, Pergamon, New York, 1960

[73] *Hennings* B.D., Naugle G.D., Canfield P.C., Thermal transport of the single-crystal rare-earth nickel borocarbides RNi_2B_2C. *Phys. Rev.* B, **66**, 214512 (2002)

[74] *Hill* R.W., Proust C., Taillefer L., Fournier P., Greene R.L., Breakdown of Fermi-liquid theory in a copper-oxide superconductor. *Nature* (London), **414**, 711 (2001)

[75] *Hill* R.W., Lupien C., Boaknin E., Hawthorn D.G., Proust C., Ronning F., Taillefer L., Liang R., Bonn D.A., Hardy W.N., Transport in Ultraclean $YBa_2Cu_3O_7$: Neither Unitary nor Born Impurity Scattering. *Phys. Rev. Lett.*, **92**, 027001 (2004)

[76] *Hirschfeld* P.J., Wölfle P., Einzel D., Consequences of resonant impurity scattering in anisotropic superconductors: Thermal and spin relaxation properties. *Phys. Rev.* B, **37**, 83 (1988)

[77] *Ho* P.-C., Frederick N.A., Zapf V.S., Bauer E.D., Do T.D., Maple M.B., Christianson A.D., Lacerda A.H., High-field ordered and superconducting phases in the heavy-fermion compound $PrOs_4Sb_{12}$. *Phys. Rev.* B, **67**, 180508 (2003)

[78] R. Holm, **Electric Contacts Handbook**, Springer, Berlin, 1958[3]

[79] *Huxley* A.D., Suderow H., Brison J.P., Flouquet J., Thermal conductivity and symmetry of the superconductivity in UPt_3. *Physics Letters* A, **209**, 365 (1995)

[80] *Huxley* A., Rodière P., M^{c}K. Paul D., van Dijk N., Cubitt R., Flouquet J., Realignment of the flux-line lattice by a change in the symmetry of superconductivity in UPt_3. *Nature*, textbf406, 160 (July 13, 2000)

[81] *Huxley* A., Méasson M.A. , Izawa K, Dewhurst C.D., Cubitt R., Grenier B., Sugawara H., Flouquet J., Matsuda Y., Sato H., Flux-Line Lattice Distortion in $PrOs_4Sb_12$. *Phys. Rev. Lett.*, **93**, 187005 (2004)

[82] *Iavarone* M., Karapetrov G., Koshelev A.E., Kwok W.K., Crabtree G.W., Hinks D.G., Kang W.N., Choi E., Kim Hyun J., Kim Hyeong J., Lee S.I., Two-band superconductivity in MgB_2. *Phys. Rev. Lett.*, **89**, 187002 (2002)

[83] Ibach H., Lüth H., **Einführung in die Grundlagen der Festkörperphysik**, Springer, Berlin, 1999[5]

[84] *Jansen* A.G.M., van Gelder A.P., Wyder P., Point-contact spectroscopy in metals. *J. Phys. C: Solid St. Phys.,* **13**, 6073 (1980)

[85] *Jeitschko* W., Braun D., $LaFe_4P_{12}$ with filled $CoAs_3$-type structure and isotropic lanthanoid-transition metal polyphosphides. *Acta Cryst.*, **B 33**, 3401 (1977)

[86] *Jericho* M.H., Odoni W., Ott H.R., Evidence for strong-coupling effects in the thermal conductivity of superconducting lead. *Phys. Rev.* B, **31**, 3124 (1985)

[87] *Jones* R.E., Toxen A.M., Thermal Conductivity of Pure Indium. *Phys. Rev.*, **120**, 1167 (1960)

[88] *Kasahara* Y., Nakajima Y., Izawa K., Matsuda Y., Behnia K., Shishido H., Settai R., Onuki Y., Anomalous quasiparticle transport in the superconducting state of $CeCoIn_5$. *Phys. Rev.* B, **72**, 214515 (2005)

[89] *Kawasaki* Y., Kawasaki S., Yashima M., Mito T., Zheng G., Kitaoka Y., Shishido H., Settai R., Haga Y., Onuki Y., Anisotropic Spin Fluctuations in Heavy-Fermion Superconductor $CeCoIn_5$: In-NQR and Co-NMR Studies. *J. Phys. Soc. Jpn.,* **72**, 2308 (2003)

[90] *Kim* J.S., Alwood J., Stewart G.R., Sarrao J.L., Thompson J.D., Specific heat in high magnetic fields and non-Fermi-liquid behavior in $CeMIn_5$ (M=Ir;Co). *Phys. Rev.* B, **64**, 134524 (2001)

[91] *Kimura* N., Komatsubara T., Aoki D., Onuki Y., Haga Y., Yamamoto E., Aoki H., Harima H., Observation of a Main Fermi Surface in UPt_3. *J. Phys. Soc. Jpn.*, **67**, 2185 (1998)

[92] *Izawa* K., Nakajima Y., Goryo J., Matsuda Y., Osaki S., Sugawara H., Sato H., Thalmeier P., Maki K., Multiple Superconducting Phases in New Heavy Fermion Superconductor $PrOs_4Sb_{12}$. *Phys. Rev. Lett.*, **90**, 117001 (2003)

[93] *Izawa* K., Kamata K., Nakajima Y., Matsuda Y., Watanabe T., Nohara M., Takagi H., Thalmeier P., Maki K., Gap Function with Point Nodes in Borocarbide Superconductor YNi_2B_2C. *Phys. Rev. Lett.*, **89**, 137006 (2002)

[94] *Izawa* K., Yamaguchi H., Matsuda Y., Shishido H., Settai R., Onuki Y., Angular Position of Nodes in the Superconducting Gap of Quasi-2D Heavy-Fermion Superconductor $CeCoIn_5$. *Phys. Rev. Lett.*, **87**, 057002 (2001)

[95] *Kadanoff* L.P., Martin P.C., Theory of Many-Particle Systems. II. Superconductivity. *Phys. Rev.*, **124**, 670 (1961)

[96] *Kukuyanagi* K., Saitoh M., Kumagai K., Takashima S., Nohara M., Takagi H., Matsuda Y., Texture in the Superconducting Order Parameter of $CeCoIn_5$ revealed by Nuclear Magnetic Resonance. *Phys. Rev. Lett.*, **94**, 047602 (2005)

[97] *Koghi* M., Iwasa K., Nakajima M., Metoki N., Araki S., Bernhoeft N., Mignot J.-M., Gukasov A., Sato H., Aoki S., Sugawara H., Evidence for Magnetic-Field-Induced Quadrupolar Ordering in the Heavy-Fermion Superconductor $PrOs_4Sb_{12}$. *J. Phys. Soc. Jpn.*, **72**, 1002 (2003)

[98] *Kohori* Y., Yamato Y., Kohara T., Bauer E.D., Maple M.B., Sarrao J.L., NMR and NQR studies of the heavy fermion superconductors $CeTIn_5$ (T = Co and Ir). *Phys. Rev.* B, **64**, 134526 (2001)

[99] *Kondo* J., Resistance Minimum in Dilute Magnetic Alloys. *Progr. Theoret. Phys.*, **32**, 37 (1964)

[100] *Kos* S., Martin I., Varma C.M., Specific heat at the transition in a superconductor with fluctuating magnetic moments. *Phys. Rev.* B, **68**, 052507 (2003)

[101] *Kotegawa* H., Yogi M., Imamura Y., Kawasaki Y., Zheng G.Q., Kitaoka Y., Ohsaki S., Sugawara H., Aoki Y., Sato H., Evidence for Unconventional Strong-Coupling Superconductivity in $PrOs_4Sb_{12}$: An Sb Nuclear Quadrupole Resonance Study. *Phys. Rev. Lett.*, **90**, 027001 (2003)

[102] *Krishana* K., Harris J.M., Ong N.P., Quasiparticle Mean Free Path in $YBa_2Cu_3O_7$ Measured by the Thermal Hall Conductivity. *Phys. Rev. Lett.*, **75**, 3529 (1995)

[103] *Kübert* C., Hirschfeld P.J., Quasiparticle Transport Properties of d-Wave Superconductors in the Vortex State. *Phys. Rev. Lett.*, **80**, 4963 (1998)

[104] *Kus* F.W., The electronic thermal conductivity of lead and its dilute alloys in the normal and superconducting states. *J. Phys. F: Metal Phys.*, **11**, 1879 (1981)

[105] *Kusunose* H., Rice T.M., Sigrist M., Electronic thermal conductivity of multigap superconductors: Application to MgB_2. *Phys. Rev.* B, **66**, 214503 (2002)

[106] *Kuwahara* K., Iwasa K., Koghi M., Kaneko K., Araki S., Metoki N., Sugawara H., Aoki Y., Sato H., Magnetic Excitations in Heavy-Fermion Superconductor $PrOs_4Sb_{12}$. *J. Phys. Soc. Jpn.*, **73** 1438 (2004)

[107] *Kuwahara* K., Iwasa K., Koghi M., Kaneko K., Raymond S., Méasson M.-A., Flouquet J., Sugawara H., Aoki Y., Sato H., Magnetic Excitations in Heavy-Fermion Superconductor $PrOs_4Sb_{12}$. *Phys. Rev. Lett.*, **95** 107003 (2005)

[108] *Landau* L.D., The theory of a Fermi Lquid. *Soviet Physics JETP*, **3**, 920 (1957)

[109] *Lawrence* J.M. and Mills D.L., Recent Progress in Heavy Fermion/Valence Fluctuation Physics: Introduction. *Comments Cond. Mat. Phys.*, **15**, 163 (1991)

[110] *Lee* P.A., Rice T.M., Serene J.W., Sham L.J., Wilkins J.W., Theories of Heavy-Electron Systems. *Comments Cond. Mat. Phys.*, **12**, 99 (1986)

[111] *Leggett* A.J., A theoretical description of the new phases of liquid ^{3}He. *Reviews of Modern Physics*, **47**, 331 (1975)

[112] Lévy F., PhD Thesis: Etude de la coexistence de la supraconductivité et du ferromagnétisme dans le composé URhGe. Université Josep Fourier, Grenoble, 2006

[113] Lévy L.P., **Magnétisme et Supraconductivité**, CNRS Editions, Paris, 1997

[114] *Liu* A. Y., Mazin I.I., Kortus J., Beyond Eliashberg Superconductivity in MgB_2: Anharmonicity, Two-Phonon Scattering, and Multiple Gaps. *Phys. Rev. Lett.*, **87**, 087005 (2001)

[115] *Loefwander* T., Fogelstroem M., Low-Temperature Thermal Conductivity of Superconductors with Gap Nodes. *Phys. Rev. Lett.*, **95**, 107006 (2005)

[116] *v. Löhneysen* H., Pfleiderer C., Pietrus T., Stockert O., Will B., Pressure versus magnetic field tuning of a magnetic quantum phase transition. *Phys. Rev.* B, **63**, 134411 (2001)

[117] *v. Löhneysen* H., Rosch A., Vojta M., Wölfle P., Fermi-Liquid Instabilities at Magnetic Quantum Phase Transitions. Cond-mat/0606317 (2006), to be published in *Rev. Mod. Phys.*

[118] *Lowell*, J., Soussa J.B., Mixed-State Thermal Conductivity of type II Superconductors. *J. Low Temp. Phys.*, **3**, 65 (1970)

[119] *Lyard* L., Samuely P., Szabo P., Klein T., Marcenat C., Paulius L., Kim K.H.P., Jung C.U., Lee H.S., Kang B., Choi S., Lee S.I., Marcus J., Blanchard S., Jansen A.G.M., Welp U., Krarpetrov G., Kwok W.K., Anisotropy of the upper critical field and critical current in single crystal MgB_2. *Phys. Rev.* B, **66**, 180502 (2002)

[120] *MacLaughlin* D.E., Sonier J.E., Heffner R.H., Bernal O.O., Young B.-L., Rose M.S., Morris G.D., Bauer E.D., Do T.D., Maple M.B., Muon Spin Relaxation and Isotropic Pairing in Superconducting $PrOs_4Sb_{12}$. *Phys. Rev. Lett.*, **89**, 157001 (2002)

[121] *Maehira* T., Hotta T., Ueda K., Hasegawa A., Relativistic Band-Structure Calculations for $CeTIn_5$ (T = Ir and Co) and Analysis of the Energy Bands by Using Tight-Binding Method. *J. Phys. Soc. Jpn.*, **72**, 854 (2003)

[122] *Majumdar* S., Lees M.R., Balakrishnan G., McK. Paul D., Anisotropic low-field behavior and the observation of flux jumps in $CeCoIn_5$. *Phys. Rev.* B, **68**, 012504 (2003)

[123] *Maki* K., Thalmeier P., Won H., Anisotropic s-wave superconductivity in borocarbides $LuNi_2B_2C$ and YNi_2B_2C. *Phys. Rev.* B, **65**, 140502(R) (2002) and *Thalmeier* P., Maki K., *cond-mat*/0210364 (2002)

[124] *Malinowski* A., Hundley M.F., Capan C., Ronning F., Movshovich R., Moreno N.O., Sarrao J.L., Thompson J.D., *c*-axis magnetotransport in $CeCoIn_5$. *Phys. Rev.* B, **72**, 184506 (2005)

[125] *Maple* M.B., Ho P.-C., Zapf V.S., Frederick N.A., Bauer E.D., Yuhasz W.M., Woodward F.M., Lynn J.W., Heavy Fermion Superconductivity in the Filled Skutterudite Compound $PrOs_4Sb_{12}$. *J. Phys. Soc. Jpn.,* **71** Suppl., 23 (2002), and *Acta Phys. Pol.* B, **34**, 919 (2003)

[126] *Martinez-Samper* P., Rodrigo J.G., Rubio-Bollinger G, Suderow H., Vieira S., Lee S., Tajima S., Scanning tunneling spectroscopy in MgB_2. *Physica* C, **385**, 233 (2003)

[127] *Mathur* N.D., Grosche F.M., Julian S.R., Walker I.R., Freye D.M., Haselwimmer R.K.W., Lonzarich G.G., Magnetically mediated superconductivity in heavy fermion compounds. *Nature*, **394**, 39 (1998)

[128] *Mazin* I.I., Antropov V.P., Electronic structure, electron-phonon coupling, and multiband effects in MgB_2. *Physica* C, **385**, 49 (2003)

[129] *Méasson* M.A., La skutterudite $PrOs_4Sb_{12}$: supraconductivité et corrélations. PhD thesis, University of Grenoble (UJF) (2005)

[130] *Méasson* M.A., Braithwaite D., Flouquet J., Seyfarth G., Brison J.P., Lhôtel E., Paulsen C., Sugawara H., Sato H., Superconducting phase diagram of the filled skuterrudite $PrOs_4Sb_{12}$. *Phys. Rev.* B, **70**, 064516 (2004)

[131] *Méasson* M.A., Braithwaite D., Salce B., Flouquet J., Lapertot G., Pécaut J., Seyfarth G., Brison J.P., Sugawara H., Sato H., Nature of double superconducting transition in $PrOs_4Sb_{12}$. *Physica* B, **378-380**, 56 (2006)

[132] *Miclea* C.F., Nicklas M., Parker D., Maki K., Sarrao J.L., Thompson J.D., Sparn G., Steglich F., Pressure Dependence of the Fulde-Ferrel-Larkin-Ovchinnikov State in $CeCoIn_5$. *Phys. Rev. Lett.*, **96**, 117001 (2006)

[133] *Moler* K.A., Baar D.J., Urbach J.S., Liang R., Hardy W.N., Kapitulnik A., Magnetic Field Dependence of the Density of States of $YBa_2Cu_3O_{6.95}$ as Determined from the Specific Heat. *Phys. Rev. Lett.*, **73**, 2744 (1994)

[134] *Monthoux* P., Lonzarich G.G., Magnetically mediated superconductivity in quasi-two and three dimensions. *Phys. Rev.* B, **63**, 054529 (2001)

[135] *Movshovich* R., Graf T., Mandrus D., Hundley M.F., Thompson J.D., Fisher R.A., Phillips N.E., Smith J.L., Response of $CeRh_2Si_2$ to pressure. *Physica* B, **223&224**, 126 (1996)

[136] *Movshovich* R., Jaime M., Thompson J.D., Petrovic C., Fisk Z., Pagliuso P.G., Sarrao J.L., Unconventional Superconductivity in $CeIrIn_5$ and $CeCoIn_5$: Specific Heat and Thermal Conductivity Studies. *Phys. Rev. Lett.*, **86**, 5152 (2001) and *Movshovich* R., Bianchi A., Jaime M., Hundley M.F., Thompson J.D., Curro N., Hammel P.C., Fisk Z., Pagliuso P.G., Sarrao J.L., *Physica* B, **312-313**, 7 (2002)

[137] *Mukhopadhyay* S., Sheet G., Raychaudhuri P., Takeya H., Magnetic-field dependence of superconducting energy gaps in YNi_2B_2C: Evidence for multiband superconductivity. *Phys. Rev.* B, **72**, 014545 (2005)

[138] *Murphy* T.P., Hall D., Palm E.C., Tozer S.W., Petrovic C., Fisk Z., Goodrich R.G., Pagliuso P.G., Sarrao J.L., Thompson J.D., Anomalous superconductivity and field-induced magnetism in $CeCoIn_5$. *Phys. Rev.* B, **65**, 100514(R) (2002)

[139] *Nagamatsu* J., Nakagawa N., Muranaka T., Zenitani Y., Akimitsu J., Superconductivity at 39 K in magnesium diboride. *Nature*, **410**, 63 (2001)

[140] *Nakamae* S., Behnia K., Mangkorntong N., Nohara M., Takagi H., Yates S.J.C., Hussey N.E., Electronic ground state of heavily overdoped nonsuperconducting $La_{2-x}Sr_xCuO_4$. *Phys. Rev.* B, **68**, 100502(R) (2003)

[141] *Nicklas* M., Borth R., Lengyel E., Pagliuso P.G., Sarrao J.L., Sidorov V.A., Sparn G., Steglich F., Thompson J.D., Response of the heavy fermion Superconductor $CeCoIn_5$ to pressure: roles of dimensionality and proximity to a quantum-critical point. *J. Phys.: Condens. Matter*, **13**, L905 (2001)

[142] *Norman* M.R., Hirschfeld P.J., Heat transport and the nature of the order parameter in superconducting UPt_3. *Phys. Rev.* B, **53**, 5706 (1996)

[143] *Odoni* W., Fuchs P., Ott H.R., Size effect on the lattice thermal conductivity of lead single crystals. *Phys. Rev.* B, **28**, 1314 (1983)

[144] *Olson* J.R., Thermal conductivity of some common cryostat materials between 0.05 and 2 K. *Cryogenics*, **33**, 729 (1993)

[145] *Ormeno* R.J., Sibley A., Gough C.E., Sebastian S., Fisher I.R., Microwave Conductivity and Penetration Depth in the Heavy Fermion Superconductor $CeCoIn_5$. *Phys. Rev. Lett.*, **88**, 047005 (2002)

[146] *Oeschler* N., Gegenwart P., Steglich F., Frederick N.A., Bauer E.D., Maple M.B., Thermal Expansion of the Skutterudite Superconductor $PrOs_4Sb_{12}$. *Acta Physica Polonica B*, **34**, 959 (2003)

[147] *Özcan* S., Broun D.M., Morgan B., Haselwimmer R.K.W., Sarrao J.L., Kamal S., Bidinosti C.P., Turner P.J., Raudsepp M., Waldram J.R., London penetration depth measurements of the heavy fermion superconductor $CeCoIn_5$ near a magnetic quantum critical point. *Europhys. Lett.*, **62** (3), 412 (2003)

[148] *Paglione* JP., Tanatar M.A., Hawthorn D.G., Boaknin E., Hill R.W., Ronning F., Sutherland M., Taillefer L., Petrovic C., Canfield P.C., Field-Induced Quantum Critical Point in $CeCoIn_5$. *Phys. Rev. Lett.*, **91**, 246405 (2003)

[149] *Paglione* JP., Quantum Criticality in the Heavy-Fermion Superconductor $CeCoIn_5$. PhD thesis, University of Toronto, (2005)

[150] *Palstra* T.T.M., Batlogg B., Schneemeyer L.F., Waszczak J.V., Transport Entropy of Vortex Motion in $YBa_2Cu_3O_7$. *Phys. Rev. Lett.*, **64**, 3090 (1990)

[151] *Park* W.K., Greene L.H., Sarrao J.L., Thompson J.D., Andreev reflection at the normal-metal/heavy-fermion superconductor $CeCoIn_5$ interface. *Phys. Rev.* B, **72**, 052509 (2005)

[152] *Park* W.K., Greene L.H., Comment on "Spectroscopic evidence for Multiple Order Parameter Components in the heavy fermion superconductor $CeCoIn_5$". *Phys. Rev. Lett.*, **96**, 259702 (2006)

[153] *Petrovic* C., Movshovich R., Jaime M., Pagliuso P.G., Hundley M.F., Sarrao J.L., Fisk Z., Thompson J.D., A new heavy-fermion superconductor $CeIrIn_5$: A relative of the cuprates? *Europhysics Letters*, **53**, 354 (2001)

[154] *Petrovic* C., Pagliuso P.G., Hundley M.F., Movshovich R., GoremychkinSarrao J.L., Thompson J.D., Fisk Z., Monthoux P., Heavy-Fermion Superconductivity in $CeCoIn_5$ at 2.3 K. *Journal of Physics: Condensed Matter*, **13**, L337 (2001)

[155] Pines D., Nozières P., **The Theory of Quantum Liquids I**, Benjamin, New York, 1966

[156] Pobell F., **Matter and Methods at low temperatures**, Springer, Berlin, 1996[2]

[157] *Quinlan* S.M., Scalapino D.J., Bulut N., Superconducting quasiparticle lifetimes due to spin-fluctuation scattering. *Phys. Rev.* B, **49**, 1470 (1994)

[158] *Radovan* H.A., Fortune N.A., Murphy T.P., Hannahs S.T., Palm E.C., Tozer S.W., Hall D., Magnetic enhancement of superconductivity from electron spin domains. *Nature* (London), **425**, 51 (2003)

[159] *Ramirez* A.P., Siegrist T., Palstra T.T.M., Garrett J.D., Bruck E., Menovsky A.A., Mydosh J.A., Superconducting phases of URu_2Si_2. *Phys. Rev.* B, **44**, 5392 (1991)

[160] G. Rickayzen, in: "**Superconductivity**" by R.D. Parks (Ed.), M. Dekker, New York (1969)

[161] *Risegari* L., Barucci M., Olivieri E., Pasca E., Ventura G., Very low temperature thermal conductivity of polymeric supports for massive cryogenic detectors. Proceedings of 8th International Conference on Advanced Technology and Particle Physics, October 2003

[162] *Rodière* P., Supraconductivité et magnétisme dans le composé à électrons fortement corrélés UPt_3. PhD thesis, CEA Grenoble, 2001

[163] *Rodière* P., private communication (2006)

[164] *Ronning* F., Capan C., Bianchi A., Movshovich R., Lacerda A., Hundley M.F., Thompson J.D., Pagliuso P.G., Sarrao J.L., Field-tuned quantum critical point in $CeCoIn_5$ near the superconducting upper critical field. *Phys. Rev.* B, **71**, 104528 (2005)

[165] *Rotundu* C.R., Tsujii H., Takano Y., Andraka B., Sugawara H., Aoki Y., Sato H., High Magnetic Field Phase Diagram of $PrOs_4Sb_{12}$. *Phys. Rev. Lett.*, **92**, 037203 (2004)

[166] *Rourke* P.M.C., Tanatar M.A., Turel C.S., Berdeklis L., Petrovic C., Wei J.Y.T., Spectroscopic evidence for Multiple Order Parameter Components in the heavy fermion superconductor $CeCoIn_5$. *Phys. Rev. Lett.*, **94**, 107005 (2005), and Reply, *Phys. Rev. Lett.*, **96**, 259703 (2006)

[167] *Sakakibara* T., Tayama T., Onimaru T., Aoki D., Onuki Y., Sugawara H., Aoki Y., Sato H., *J. Phys.: Cond. Matter*, Quadrupole ordering and multipole interactions in Pr-based compounds. **15**, S2055 (2003)

[168] *Sales* B.C., Mandrus D., Williams R.K., Filled Skutterudite Antimonides: A New Class of Thermoelectric Materials. *Science*, **272**, 1325 (1996)

[169] *Sales* B.C., Handbook on the physics and chemistry of Rare Earths, edited by Gschneider, Bünzli and Pecharsky, **33**, chapter 211 1 (2003)

[170] *Sarachik* M., Corenzwit E., Longinotti L.D., Resistivity of Mo-Nb and Mo-Re Alloys Containing 1% Fe. *Phys. Rev.*, **135**, A1041 (1964)

[171] *Sarao* J.L., Morales L.A., Thompson J.D., Scott B.L., Stewart G.R., Wastin F., Rebizant J., Boulet P., Colineau E., Lander G.H., Plutonium-based superconductivity with a transition temperature above 18 K. *Nature*, **420**, 297 (2002)

[172] *Schmidt* C., Simple method to measure the thermal conductivity of technical superconductors, e.g. NbTi. *Rev. Sci. Instrum.*, **50**, 454 (1979)

[173] *Schroeder* A., Aeppli G., Coldea R., Adams M., Stockert O., v.Löhneysen H., Bucher E., Ramazashvili R., Coleman P., Onset of antiferromagnetism in heavy-fermion metals. *Phys. Rev.* B, **69**, 035111 (2004)

[174] *Seaman* C.L., Maple M.B., Lee B.W., Ghamaty S., Torikachvili M.S., Kang J.S., Liu L.Z., Allen J.W., Cox D.L., Evidence for non-Fermi liquid behavior in the Kondo alloy $Y_{1-x}U_xPd_3$. *Phys. Rev. Lett.*, **67**, 2882 (1991)

[175] *Senthill* T., Vojta M., Sachdey S., Weak magnetism and non-Fermi liquids near heavy-fermion critical points. *Phys. Rev.* B, **69**, 035111 (2004)

[176] *Sera* M., Kobayash S., Hiroi M., Kobayashi N., Takeya H., Kadowaki K., Thermal conductivity of RNi_2B_2C (R=Y,Ho) single crystals. *Phys. Rev.* B, **54**, 3062 (1996)

[177] *Settai* R., Shishido H., Ikeda S., Murakawa Y., Nakashima M., Aoki D., Haga Y., Harima H., Onuki Y., Quasi-two-dimensional Fermi surfaces and the de Haas-van Alphen oscillation in both the normal and superconducting mixed states of $CeCoIn_5$. *J. Phys.: Cond. Matter*, **13**, L627 (2001)

[178] *Seyfarth* G., Brison J.P., Méasson M.A., Flouquet J., Izawa K., Matsuda Y., Sugawara H., Sato H., Multiband Superconductivity in the Heavy Fermion Compound $PrOs_4Sb_{12}$. *Phys. Rev. Lett.*, **95**, 107004 (2005)

[179] *Sharvin* Yu.V., Possible method for studying Fermi surfaces. *Soviet Physics JETP*, **21**, 655 (1965)

[180] *Sheet* G., Raychaudhuri P., Comment on "Spectroscopic Evidence for Multiple Order Parameters in the Heavy Fermion Superconductor $CeCoIn_5$". *Phys. Rev. Lett.*, **96**, 259701 (2006)

[181] *Shiina* R., Matsumoto M., Koga M., Crystal-Field Excitations, Magnetic-Field-Induced Phase Transition and Neutron-Scattering Spectra in $PrOs_4Sb_{12}$. *J. Phys. Soc. Japan*, **73**, 3453 (2004)

[182] *Shishido* H., Settai R., Aoki D., Ikeda S., Nakawaki H., Nakamura N., Iizuka T., Sugiyama K., Takeuchi T., Kindo K., Kobayashi T.C., Haga Y., Harima H., Aoki Y., Namiki T., Sato H., Onuki Y., Fermi Surface, Magnetic and Superconducting Properties of $LaRhIn_5$ and $CeTIn_5$ (T: Co, Rh and Ir). *J. Phys. Soc. Jpn.*, **71**, 162 (2002)

[183] *Shulga* S.V., Drechsler S.L., Fuchs G., Müller K.H., Winzer K., Heinecke M., Krug K., Upper Critical Field Peculiarities of Superconducting YNi_2B_2C and $LuNi_2B_2C$. *Phys. Rev. Lett.*, **80**, 1730 (1998)

[184] *Sidorov* V.A., Nicklas M., Pagliuso P.G., Sarrao J.L., Bang Y., Balatsky A.V., Thompson J.D., Superconductivity and Quantum Criticality in $CeCoIn_5$. *Phys. Rev. Lett.*, **89**, 157004 (2002)

[185] *Smith* M.F., Paglione JP., Walker M.B., Taillefer L., Origin of anomalous low-temperature downturns in the thermal conductivity of cuprates. *Phys. Rev.* B, **71**, 014506 (2005)

[186] *Sologubenko* A.V., Jun J., Kazakov S.M., Karpinski J., Ott H.R., Thermal conductivity of single-crystalline MgB_2. *Phys. Rev.* B, **66**, 014504 (2002)

[187] *Steglich* F., Aarts J., Bredl C.D., Lieke W., Meschede D., Franz W., Schäfer H., Superconductivity in the Presence of Strong Pauli Paramagnetism: $CeCu_2Si_2$. *Phys. Rev. Lett.*, **43**, 1892 (1979)

[188] *Stewart* G.R., **Heavy-fermion systems.** *Rev. Mod. Phys.*, **56**, 755 (1984)

[189] *Suderow* H., Conduction thermique des phases supraconductrices de UPt_3. PhD thesis, CEA Grenoble, 1997

[190] *Suderow* H., Brison J.P., Huxley A.D., Flouquet J., Thermal conductivity and gap structure of the superconducting phases of UPt_3. *J. Low Temp. Phys.*, **108**, 11 (1997)

[191] *Suderow* H., Brison J.P., Huxley A.D., Flouquet J., Scaling and Thermal Conductivity in Unconventional Superconductors: The Case of UPt_3. *Phys. Rev. Lett.*, **80**, 165 (1998)

[192] *Suderow* H., Vieira S., Strand J.D., Bud'ko S., Canfield P.C., Very-low-temperature tunneling spectroscopy in the heavy-fermion superconductor $PrOs_4Sb_{12}$. *Phys. Rev.* B, **69**, 060504 (2004)

[193] *Suderow* H., Tissen V.G., Brison J.P., Martinez J.L., Vieira S., Lejay P., Lee S. Tajima S., Pressure dependence of the upper critical field of MgB_2 and of YNi_2B_2C. *Phys. Rev.* B, **70**, 134518 (2004)

[194] *Sugawara* H., Osaki S., Saha S.R., Aoki Y., Sato H., Inada Y., Shishido H., Settai R., Onuki Y., Harima H., Oikawa K., Fermi surface of the heavy-fermion superconductor $PrOs_4Sb_{12}$. *Phys. Rev.* B, **66**, 220504(R) (2002)

[195] *Sugawara* H., Osaki S., Saha S.R., Aoki Y., Sato H., de Haas–van Alphen Effect in Heavy Fermion Superconductor $PrOs_4Sb_{12}$. *Acta Physica Polonica* B, **34**, 1125 (2003)

[196] *Suhl* H., Matthias B.T., Walker L.R., Bardeen-Cooper-Schrieffer Theory of Superconductivity in the Case of Overlapping Bands. *Phys. Rev. Lett.*, **3**, 552 (1959)

[197] *Sun* X.F., Komiya S., Takeya J., Ando Y., Magnetic-field-induced Localization of Quasiparticles in Underdoped $La_{2-x}Sr_xCuO_4$ Single Crystals. *Phys. Rev. Lett.*, **90**, 117004 (2003)

[198] *Szabó* P., Samuely P., Kacmarcik J., Klein T., Marcus J., Jansen A.G.M., *Physica* B, **328**, 10 (2003) and *Szabó* P., Samuely P., Kacmarcik J., Klein T., Marcus J., Fruchart D., Miraglia S., Marcenat C., Jansen A.G.M, Evidence for Two Superconducting Energy Gaps in MgB_2 by Point-Contact Spectroscopy. *Phys. Rev. Lett.*, **87**, 137005 (2001)

[199] *Takegahara* K., Harima H., Yanase A., Crystal Electric Fields for Cubic Point Groups. *J. Phys. Soc. Jpn.,* **70**, 1190 (2001)

[200] *Takeuchi* T., Shishido H., Ikeda S., Settai R., Haga Y., Onuki Y., Thermal expansion and magnetostriction studies in a heavy-fermion superconductor, $CeCoIn_5$. *J. Phys.: Condens. Matter*, **14**, L261 (2002)

[201] *Tanatar* M.A., Paglione J., Nakatsuji S., Hawthorn D.G., Boaknin E., Hill R.W., Ronning F., Sutherland M., Taillefer L., Petrovic C., Canfield P., Fisk Z., Unpaired Electrons in the Heavy-Fermion Superconductor $CeCoIn_5$. *Phys. Rev. Lett.*, **95**, 067002 (2005)

[202] *Tayama* T., Harita A., Sakakibara T., Haga Y., Shishido H., Settai R., Onuki Y., Unconventional heavy-fermion superconductor $CeCoIn_5$: dc magnetization study at temperatures down to 50 mK. *Phys. Rev.* B, **65**, 180504(R) (2002)

[203] *Tayama* T., Sakakibara T., Sugawara H., Aoki Y., Sato H., Magnetic Phase Diagram of the Heavy Fermion Superconductor $PrOs_4Sb_{12}$. *J. Phys. Soc. Jpn.,* **72**, 1516 (2003)

[204] *Tewordt* L., Lifetime of Quasi-Particle in a Superconductor at Finite Temperatures and Application to the Problem of Thermal Conductivity. *Phys. Rev.*, **128**, 12 (1962), and Theory of Intrinsic Electronic Thermal Conductivity of Superconductors. *Phys. Rev.*, **129**, 657 (1963)

[205] *Tewordt* L., Fay D., Two-band theory of specific heat and thermal conductivity in the mixed state of MgB_2. *Phys. Rev.* B, **68**, 092503 (2003)

[206] Tinkham M., **Introduction to Superconductivity**, Mc-Graw-Hill, New York, 1980'

[207] *Tsuda* S., Yokoya T., Takano Y., Kito H., Matsushita A., Yin F., Itoh J., Harima H., Shin S., Definitive Experimental Evidence for Two-Band Superconductivity in MgB_2. *Phys. Rev. Lett.*, **91**, 127001 (2003)

[208] *Varma* C.M., Valence Fluctuations, Heavy Fermions and their Superconductivity. *Comments Solid State Phys.*, **11**, 221 (1985)

[209] *Vekhter* I., Houghton A., Quasiparticle Thermal Conductivity in the Vortex State of High-T_c Cuprates. *Phys. Rev. Lett.*, **83**, 4626 (1999), and *Vekhter* I., Hirschfeld P.J., Nicol E.J., Thermodynamics of d-wave superconductors in magnetic field. *Phys. Rev.* B, **64**, 064513 (2001)

[210] *Vollmer* R., Faißt A., Pfleiderer C., H. v. Löhneysen, Bauer E.D., Ho P.-C., Maple M.B., Low-Temperature Specific Heat of the Heavy-Fermion Superconductor $PrOs_4Sb_{12}$. *Phys. Rev. Lett.*, **90**, 057001 (2003)

[211] *Volovik* G.E., Superconductivity with lines of GAP nodes: density of states in the vortex. *JETP Letters*, **58**, 469 (1993)

[212] *Walker* I.R., Grosche F.M., Freye D.M., Lonzarich G.G., The normal and superconducting states of $CeIn_3$ near the border of antiferromagnetic order. *Physica* C, **282-287**, 303 (1997)

[213] *Wexler* G., The size effect and non-local Boltzmann transport equation in orifice and disk geometry. *Proc. Phys. Soc.* **89**, 927 (1966)

[214] *Wiedemann* F. and Franz R., Über die Wärmeleitungsfähigkeit der Metalle. *Annals of Physics* **89**, 497 (1853)

[215] *Wilke* R.H.T., Bud'ko S.L., Canfield P.C., Finnemore D.K., Suplinskas R.J., Hannahs S.T., Systematic effects of Carbon Doping on the Superconducting Properties of $MgB_{1-x}C_x)_2$. *Phys. Rev. Lett.*, **92**, 217003 (2004)

[216] *Xiao* H., Hu T., Almasan C.C., Sayles T.A., Maple M.B., Angular-dependent torque measurements on $CeCoIn_5$ single crystals. *Phys. Rev.* B, **73**, 184511 (2006)

[217] *Yu* R.C., Salamon M.B., Lu J.P., Lee W.C., Thermal Conductivity of an Untwinned $YBa_2Cu_3O_{7-\delta}$ Single Crystal and a New Interpretation of the Superconducting-State Thermal Transport. *Phys. Rev. Lett.*, **69**, 1431 (1992)

[218] *Yu* F., Leggett A.J., Lee W.C., Ginsberg D.M., Tensor Magnetothermal Resistance in $YBa_2Cu_3O_{7-x}$ via Andreev Scattering of Quasiparticles. *Phys. Rev. Lett.*, **74**, 5136 (1995) and *Phys. Rev. Lett.*, **75**, 3028 (1995)

[219] Ziman J.M., **Prinzipien der Festkörpertheorie**, Deutsch, Thun, 1999[2]

List of publications

Results on $PrOs_4Sb_{12}$, sample A

Seyfarth G., Brison J.P., Méasson M.A., Flouquet J., Izawa K., Matsuda Y., Sugawara H., Sato H., Phase supraconductrice de $PrOs_4Sb_{12}$: Diagramme de phase et propriétés de transport. Proceedings of "JMC 9"(poster contribution), Congrès SFP, Nancy (2004)

Seyfarth G., Brison J.P., Méasson M.A., Flouquet J., Izawa K., Matsuda Y., Sugawara H., Sato H., Multiband Superconductivity in the Heavy Fermion $PrOs_4Sb_{12}$. Proceedings of "Physik seit Einstein"(oral contribution), DPG-Tagung, Berlin (2005)

Seyfarth G., Brison J.P., Méasson M.A., Flouquet J., Izawa K., Matsuda Y., Sugawara H., Sato H., Multiband Superconductivity in the Heavy Fermion Compound $PrOs_4Sb_{12}$. *Phys. Rev. Lett.*, **95**, 107004 (2005)

Results on $PrOs_4Sb_{12}$, sample B2

Seyfarth G., Brison J.P., Méasson M.A., Braithwaite D., Lapertot G., Flouquet J., Superconductivity in $PrOs_4Sb_{12}$: on the double transition and multiband effects. *J. Magn. Magn. Mater*, to be published (oral contribution to ICM 2006, Kyoto)

Seyfarth G., Brison J.P., Méasson M.A., Braithwaite D., Lapertot G., Flouquet J., Superconducting $PrOs_4Sb_{12}$: a thermal conductivity study. *Phys. Rev. Lett.*, **97**, 236403 (2006)

Previous work in collaboration with J. Flouquet's group at SPSMS-CEA Grenoble

Méasson M.A., Braithwaite D., Flouquet J., Seyfarth G., Brison J.P., Lhôtel E., Paulsen C., Sugawara H., Sato H., Superconducting phase diagram of the filled skuterrudite $PrOs_4Sb_{12}$. *Phys. Rev.* B, **70**, 064516 (2004)

Abstract

In this thesis, we present thermal conductivity (κ) measurements on the heavy fermion superconductors $PrOs_4Sb_{12}$ ($T_c \sim 1.75$ K) and $CeCoIn_5$ ($T_c \sim 2.35$ K). After an introduction to these compounds, particular emphasis is put on the experimental technique, which has allowed reliable measurements down to 10 mK and in magnetic fields up to 6.5 T. As an original part of this work, we developed a method to fully characterize (quantitatively) the electric *and* thermal contact resistances on the setup.

A strong increase in the low temperature field dependence of κ in $PrOs_4Sb_{12}$ and $CeCoIn_5$ reveals the existence of a characteristic field scale much smaller than H_{c2}. This high field sensitivity of κ does not correspond to predictions for ordinary type II or unconventional superconductors with gap nodes, but rather supports a multiband superconductivity scenario, reminiscent of the case of MgB_2. Moreover, in $PrOs_4Sb_{12}$, the temperature dependence of κ points to fully open gaps on the whole FERMI surface, whereas strong suppression of inelastic scattering impedes any conclusion on the gap topology on $CeCoIn_5$.

Key words

$PrOs_4Sb_{12}$
$CeCoIn_5$
Heavy Fermion
Multiband Superconductivity
Thermal Transport
Contact Resistance

Résumé

Dans cette thèse, nous présentons des mesures de conductivité thermique (κ) dans les supraconducteurs à fermions lourds $PrOs_4Sb_{12}$ ($T_c \sim 1.75$ K) et $CeCoIn_5$ ($T_c \sim 2.35$ K). Après une courte introduction aux composés, nous décrivons notre technique expérimentale, qui a permis des mesures fiables jusqu'à 10 mK et dans un champ magnétique allant jusqu'à 6.5 T. Le développement d'une méthode de caractérisation (quantitative) des résistances de contact électriques *et* thermiques du montage constitue une partie originale de ce travail.

Une forte augmentation de κ avec le champ à basse température dans $PrOs_4Sb_{12}$ et $CeCoIn_5$ révèle l'existence d'une échelle de champ caractéristique beaucoup plus faible que H_{c2}. Cette haute sensibilité au champ de κ ne correspond ni aux prédictions pour un supraconducteur ordinaire de type II ni au cas où le gap présente des noeuds, mais souligne plutôt le caractère multibande de la supraconductivité, comme dans MgB_2. En outre, dans $PrOs_4Sb_{12}$, la dépendance en température de κ indique des gaps complètement ouverts sur toute la surface de Fermi, alors que dans $CeCoIn_5$ la suppression de diffusions inélastiques rend impossible une conclusion sur la topologie du gap.

Mots Cléfs

$PrOs_4Sb_{12}$
$CeCoIn_5$
Fermion lourd
Supraconductivité multibande
Transport Thermique
Résistance de contact